University of Southampton

Faculty of Engineering and Physical Sciences

Physics and Astronomy

Liquid Crystal and Meta-Surface Devices for Enhancing Light Manipulation from Visible to THz Regime

by

Eleni Perivolari

ORCID ID 0000-0003-3051-7839

Thesis for the degree of Doctor of Philosophy

October 2021

“And, when you want something, all the universe conspires in helping you to achieve it.”

— Paulo Coelho, The Alchemist

University of Southampton

Abstract

Faculty of Engineering and Physical Sciences

Physics and Astronomy

Doctor of Philosophy

Liquid Crystal and Meta-Surface Devices for Enhancing Light Manipulation from Visible to THz Regime

by

Eleni Perivolari

Liquid crystals lie at the heart of many light-switching devices. Convectional devices switch as a result of the imposition of an external voltage, leading to an electric field inside the bulk. In this thesis I investigate bistable liquid crystal-based devices with switching between states controlled by light. Such an enhanced, photoactive response can be realised by integrating liquid crystals with photoalignment or photoconductive alignment layers. The resulting liquid crystal cells, asymmetric by design, need to be monitored for the stability and uniformity, especially in the regions exposed to light. In this work, I report on an integrated, versatile model and technique to characterise their core parameters as well as more subtle effects, such as the strength of anchoring energy. The snapshot method (the so-called 'OMPA') also provides two dimensional maps of the cells' thickness, pretilt angle and uniformity. A dynamic, optically addressed, waveplate forming rewriteable twisted liquid crystal structures is then presented. The cell is bistable, with switching between states controlled by one-step illumination of a single PAAD azobenzene alignment layer with visible light. There is no requirement for electrodes or an applied field to control the dynamic behaviour. The photo-alignment properties of the layer enable reversible switching between two perpendicular alignment states at the cell surface, resulting in controllable polarization manipulation of visible and infrared light with an efficiency greater than 90%.

Towards controlling longer wavelengths i.e., THz radiation exploiting the low optical anisotropy of liquid crystals in this range, is one of the main challenges. Although, there have been several solutions incorporating semiconductors or planar metamaterials, there is still the need to incorporate external stimulus (voltage, bulky magnets, temperature). This is a considerable technological challenge, since new applications impose compact, and thin devices with the less possible complexity in their systems and experimental setups. All-optical control of liquid crystals exploiting the THz itself is one of the main challenges nowadays. Enhanced localization of THz electric field in the vicinity of metamaterials may drive liquid crystal molecules and thus control their optical properties without the need of external stimulus. Here, I present an experimental and theoretical study of liquid crystal loaded metamaterials devices capable of shifting the narrowband resonant response of metamaterials by 45 GHz when switching between two planar liquid crystal states for both Babinet complementary patterns. My study suggests that this is due to the orientational optical nonlinearity of nematic liquid crystals induced in the vicinity of metamaterials near-field 'hotspots', which prompt liquid crystal molecules to spatially re-orient along the localized electric field lines. I envisage that these findings can directly lead to the increase of the efficacy of THz modulators and other

active optical components exploiting the enhanced nonlinear light-matter interactions in liquid crystal-metamaterials hybrid structures.

Table of Contents

Table of Contents ..... **i**
Table of Tables ..... **v**
Table of Figures ..... **vii**
Research Thesis: Declaration of Authorship ..... **xxi**
Acknowledgements ..... **xxiii**
Chapter 1 1
Introduction **1**
1.1 Motivation and Outline of the Thesis 1
1.2 Liquid Crystals 2
1.2.1 Types of Liquid Crystals 3
1.2.2 Nematic Liquid Crystals 5
1.3 Optical Properties of Liquid Crystals 11
1.3.1 LCs in Electric Field 11
1.3.2 The Fréedericksz Transition 13
1.3.3 Optical Anisotropy of Nematic Liquid Crystals 15
1.3.4 Birefringence in Liquid Crystals 16
1.4 Alignment of Liquid Crystals 20
1.4.1 Rubbing: Mechanism and Applications 20
1.4.2 Photoalignment 23
1.4.2.1 Photoalignment mechanisms 24
1.4.2.2 Photoisomerization 25
1.5 Summary 28
Chapter 2 29
Characterisation of The Optical Properties of Liquid Crystal Cells **31**
2.1 Properties of Liquid Crystal Materials 31
2.2 Liquid Crystal Cells 34
2.2.1 Cell Thickness Measurement 36
2.2.2 Quality of Liquid Crystal Alignment 37
2.3 Optical Measurements 39

2.3.1 The Fréedericksz Transition Experiment (Cross-Polarized Intensity Experiment) 39
2.3.2 Modelling and Fitting the Cross-Polarized Intensity (CPI) 42
2.4 Fully-Automated Optical Systems for Large Scale Characterisation of Liquid Crystal Cells 45
2.4.1 Wide Area Mapping of Liquid Crystal Devices 46
2.4.1.1 Multiple cross-polarised intensity traces 48
2.4.1.2 Results on wide area mapping of liquid crystal cells 50
2.4.2 Two-Dimensional Snapshot Measurement of Surface Variation of Liquid Crystals 53
2.4.2.1 Optical Multi-Parameter Analyser (OMPA) 54
2.4.2.2 Mapping anchoring, pretilt and thickness LC cells 58
2.4.3 Anchoring Energy 61
2.4.3.1 The effect of the anchoring energy 61
2.4.3.2 Minimisation landscapes 62
2.4.3.3 Polar anchoring energy experimental results 63
2.5 Summary 66

Chapter 3 67

Optically Driven Bistable Liquid Crystal Waveplates 69

3.1 Introduction 70
3.2 Photo-Aligning Azobenzene Dyes (PAAD) 71
3.2.1 Preparation of PAAD films 71
3.2.2 Absorbance and light induced absorbance of PAAD materials 73
3.2.3 Radiant exposure of PAAD 77
3.3 Determination of PAAD Refractive Index Using the Iterated Ray Method 79
3.4 Dynamic Half-Wave Plates Based on Photo-Aligning Azobenzene Dyes (PAAD) 84
3.4.1 Experimental methodology 84
3.4.2 Modelling and fitting the transmitted optical contrast 89
3.4.3 Transmission for multiple probe beam wavelengths in the visible and near-infrared regimes 90

3.5 Conclusions and Future Work....94

Chapter 4 95

Liquid Crystal Devices for Manipulating Terahertz Radiation....97

4.1 Introduction....97

4.2 Terahertz Radiation – Basic Principles....98

4.2.1 The terahertz history....99

4.2.2 Applications....101

4.3 Terahertz-Time Domain Spectroscopy....102

4.3.1 Generation and detection of terahertz pulses....104

4.4 Terahertz Time Domain Scans....106

4.4.1 Terahertz spot size....111

4.5 Terahertz Properties of Nematic Liquid Crystals....113

4.5.1 High-birefringence nematic liquid crystal mixtures for terahertz applications....114

4.5.2 Evaluating liquid crystal properties for manipulating the terahertz regime....118

4.6 Liquid Crystal-Metamaterials Integrated Devices for Efficient Control of Terahertz Radiation....121

4.7 Summary....124

Chapter 5 124

Liquid Crystal-Loaded Metamaterials for Enhanced Light-Matter Interactions in The Terahertz Regime....125

5.1 Fabrication Liquid Crystal-Loaded Metamaterial Cells....125

5.1.1 Photolithography....126

5.1.2 Cell assembly of liquid crystal-loaded metamaterial devices....128

5.2 Simulated and Experimental Results of Pristine Metamaterial Samples....131

5.3 Simulated and Experimental Results of THz Liquid Crystal-Metamaterial Devices 138

5.3.1 Anomalous resonance frequency shift for positive MMs when hybridised with liquid crystals....141

5.3.2 Simulation of different angular LC re-alignment ranges 145

5.4 Modelling the Change of Liquid Crystal Birefringence Induced by Local Fields Within 'Hotspots' 146

5.5 Orientational Optical Nonlinearity of Nematic Liquid Crystals Induced by The Enhanced Light-Matter Interactions with THz Metamaterials 148

5.6 Conclusions 149

Chapter 6 149

Analytical Calculation of The All-Optical In-Plane Switching of Liquid Crystals at Terahertz Frequencies Enabled by Metamaterials 151

6.1 Introduction 151

6.2 Experimental demonstration of optical switching 153

6.3 Analytical calculation of in-plane switching 155

6.3.1 Linear approximation – Method 1 157

6.3.2 Linear approximation – Method 2 160

6.4 Discussion 162

6.5 Conclusions 163

Chapter 7 163

Conclusions and Outlook 165

7.1 Conclusions 165

7.2 Ongoing and Future Work 167

7.2.1 Investigation of twisted liquid crystal devices integrated with THz metamaterials 167

7.2.2 Diffraction Efficiency of Azobenzene Complex Dyes 168

Appendix A 172

Appendix B 174

B1. Journal and Conference publications 175

B2. Conference contributions 177

Bibliography 179

Table of Tables

Table 2-1: Material properties of nematic E7 33

Table 2-2: Splay and Bend Elastic Constants Measured for the E7-PI Cell 52

Table 2-3: Some Literature Values for the E7 Splay and Bend Elastic Constants 52

Table 2-4: Description of the samples 55

Table 2-5: Anchoring energy values from symmetric and asymmetric LC cells 64

Table 2-6: Optical parameters of symmetric planar PI - E7 cell. 65

Table 2-7: Experimental results of PEDOT:PSS – QYTN-004 cell. 65

Table 3-1: Radiant exposure specifications for PAAD materials [139]. 78

Table 3-2: Refractive Index and Thickness of PAAD-22E and ITO Layers Deposited on a Glass Slide, Obtained by Fitting the Experimental Data in Figure 3-11. 83

Table 3-3: Theoretical transmitted intensity I(λ) for a d = 6.5 μm thick E7 layer in a twisted configuration, see Equation (3.3). The E7 birefringence data was taken from Ref. [56]. 90

Table 3-4: Fitted values of the time constant τ_1 for three different types of illumination of the PAAD layer. 92

Table 4-1: Comparison of the THz properties of E7 114

Table 4-2: E7 parameters and τ_{on} at 1 THz (accuracy:+/− 5%) 115

Table 4-3: Material parameters of 1825 mixture at 25 °C. 117

Table 5-1: LC 1825 optical properties 147

Table 6-1. Specifications of LC 1825 [58] 158

Table of Figures

Figure 1-1 An illustration of the difference of the behaviour of solid, LCs and liquid. LCs flow like a liquid, but its molecules are oriented in a crystalline manner..... 2

Figure 1-2 Schematic representation of (a) nematic, (b) smectic and (c) cholesteric mesophases. 3

Figure 1-3 Defining the director in a local region of LC. 4

Figure 1-4 A diagram of a 5-cyano-biphenyl (5CB) molecule, which is a common component of LC materials. Blue represents a nitrogen atom, and grey and white are carbon and hydrogen, respectively. The elongated shape is critical to its LC phase behaviour [8]. 5

Figure 1-5 Schlieren Texture of a Nematic Films as obtained by [12] 6

Figure 1-6 Schlieren Texture of a Nematic Films as obtained by [12] 7

Figure 1-7 Three types of deformations occurring in nematics. 8

Figure 1-8 LC geometries for observing upon application of external field. Transition that cause different types of nematic deformation: splay (left), twist (centre), bend (right)..... 9

Figure 1-9 Types of LC alignment between parallel glass substrates: (a) planar, (b) homeotropic, (c) tilted, and (d) position of director, n, and easy axis in space.10

Figure 1-10 LC cells with different boundary conditions. (a) Homeotropic LC geometry. (b) Strong-boundary conditions affect the re-orientation of molecules caused by the applied electric field. (c) Soft-boundary conditions allow the applied field to perturb the orientation of the molecules at the cell boundaries. 11

Figure 1-11 Index ellipsoid for a plane polarized optical wave propagating along s in a uniaxial crystals. ne(θ) and no are the refractive indices for the extraordinary and ordinary components, respectively. 15

Figure 1-12 Schematic of a typical LC display pixel consisting of electronic driving circuit, polarizers, LC cell, colour filter, and phase plate (not shown) [16]. 17

Figure 1-13 Structural sketch of a rubbing machine. A rubbing machine consists of a roller covered by rubbing cloth, and a platform to hold the substrate. The roller or the substrate stage moves at a constant speed while the roller is rotating at

several hundreds of rpm. The gap between the roller and the stage is adjusted to change the pile impression. 20

Figure 1-14 Alignment disclination lines defect (Néel wall). 22

Figure 1-15 Alignment in a twist-reverse defect. 22

Figure 1-16 Alignment in a tilt-reverse defect. 22

Figure 1-17 Principle of photoisomerization in-plane LC alignment 27

Figure 1-18 In-plane reorientation of nematic LC exploiting the reversible photoisomerization of azobenzene dye molecules. Top schematic illustrates a planar alignment of LC towards the x axis, while bottom schematic shows a planar alignment towards the y axis. Alternating polarisation of incident light results in a reversible orientation process perpendicular to it. 28

Figure 2-1 Molecular structure of nematic LC mixture E7. 33

Figure 2-2 Schematic illustration of the LC cell structure. 34

Figure 2-3 Anti-parallel rubbing direction on the opposite sides of the LC cell to ensure a uniform planar alignment. 35

Figure 2-4 Transmission spectrum of the empty cell. Transmitted beams interfere beyond the cell, which appears in the spectrum as maxima and minima. To calculate the cell thickness, two transmission maxima with the wavelength λ_1 and λ_2 are selected from the spectra. 37

Figure 2-5 Schematic of the set up for observing the quality of planar LC cell between crossed polarizers. Director of nematic LC is parallel to the first polarizer's (P1) axis allowing the incident light to pass through the cell. After passing the first polarizer light will remain unchanged after the cell and finally be blocked by the second polarizer (P2). 38

Figure 2-6 Schematic of the set up for observing the quality of a twisted LC cell between crossed polarizers. Director of nematic LC is parallel to the first polarizer's (P1) axis allowing the incident light to pass through the cell. After passing the first polarizer light will rotate polarization triggered by the twisted LC molecules and finally transmit through the second polarizer (P2). 38

Figure 2-7 Schematic representation of the experimental setup for detecting electric field-induced Fréedericksz transition. Arrows on the polarizers (P1 and P2) indicate their polarization axes. 40

Figure 2-8 Crossed-polarized intensity as a function of the applied voltage for an E7 cell. Shaded areas indicate which parts of the curve is more sensitive to the corresponding parameters. The LC thickness is 12 μm. 41

Figure 2-9 Experimental set-up to measure the CPI at different locations of a planar LC cell. The polarizer and analyser are perpendicular to each other and at 45° to the LC alignment. The motorized, computer-controlled translation stage allows us to define the area of the cell to be examined. 46

Figure 2-10 CPI as a function of the applied voltage for an E7-PI cell. Multiple traces are measured across the surface of the cell to obtain reliable uniformity maps. The LC thickness is ~12 μm. Colour map shows the variation of thickness measured at the different spots at the cell's surface. Black colour stands for the thinner areas while yellow for thicker ones, usually spotted at the edges of the cell. ..48

Figure 2-11 PI planar cell filled with E7: spatial map of the LC (a) thickness and (c) pretilt angle; (b) and (d) are the corresponding errors. Circles are the fitted values, and the background colour map is a piece-wise cubic interpolation between them. 51

Figure 2-12 Sample schematics. (a) Planar symmetric E7 cell where both ALs are rubbed PI (PI-E7-PI). (b) Planar symmetric QYTN-004 cell, where both ALs are rubbed PEDOT: PSS (PEDOT: PSS-QYTN004-PEDOT: PSS). (c) Planar asymmetric E7 cell, where one AL is rubbed PI while the other is photoaligned PAAD-22D (PI-E7-PAAD22D). 55

Figure 2-13 Experimental setup of the OMPA instrument. A fibre coupled diode laser at 642 nm passes from a fibre port into two lenses L1 and L2 which expand and collimate the beam. The sample is located between two crossed polarizers (P1 and P2), each at 45° to the director alignment, where the light enters at normal incidence. Photodiodes, PD1 and PD2 monitor the power of the laser before and after the cell by exploiting two beam splitters (BS). Finally, the light is incident on a CCD camera, which we use as spatial resolution detector. The entire setup is enclosed to reduce the background noise to the detectors and CCD camera and reduce thermal fluctuations 56

Table of Figures

Figure 2-14 CPI trace for the asymmetric PI - PAAD-22D planar cell filled with E7. Parameter values: $K1 = 11$ pN, $K3 = 16.4$ pN, ε ‖= 19.54, ε ⊥= 5.17, $d = 7$ μm, $\theta PAAD = 0.34 \circ$, $\theta PI = 1.9 \circ$, $WPAAD = 0.21\ mJ/m2, WPI > 1000\ mJ/m2$, $\lambda =$ 642 nm, $ne = 1.7287$ and $no = 1.5182$. 57

Figure 2-15 Spatial maps of thickness and pretilt angle of symmetric cells: (a) thickness and (b) pretilt angle maps of PI – E7 cell. (c) thickness and (d) pretilt angle maps of PEDOT: PSS – QYTN-004 cell..... 59

Figure 2-16 Asymmetric PI - PAAD-22D planar cell filled with E7: spatial map of the LC (a) thickness and (b) pretilt angle..... 60

Figure 2-17 CPI traces for different values of the anchoring energy in a symmetric cell. Parameter values Parameter values: $K1 = 10.9$ pN, $K3 = 17.9$ pN, ε ‖= 19.54, ε ⊥= 5.17, $d = 12$ μm, $\theta = 2 \circ$, $\lambda =$ 642 nm, $ne = 1.7287$ and $no = 1.5182$. 61

Figure 2-18 Minimisation landscapes: in all cases the anchoring energy is along the horizontal axis and varies by +/- 30% with respect to $W0$. The vertical axes are, from left to right, the splay and bend elastic energy, and the pretilt angle. The scale of the colour bar is in arbitrary units. Parameter values: $K10 = 10.9$ pN, $K30 = 17.9$ pN, ε ‖= 19.54, ε ⊥= 5.17, $d0 = 12$ μm, $\theta 0 = 2 \circ$, $W0 = 100$ μJ/m2. 63

Figure 3-1 Spin coating of thin films..... 72

Figure 3-2 Thickness profile of PAAD-22. The minimum thickness was 30 nm at 3000 RPM and 1% w/v concentration of PAAD-22 in methanol..... 73

Figure 3-3 Absorbance of PAAD-22, 22D, 72, and 22E as measured with an UV/VIS/NIR JASCO spectrometer between 300-1500 nm. For clarity we only show the range of 300-650 nm. 74

Figure 3-4 Absorbance of PAAD-22 before (solid) and after (dash dot) illumination of 458 nm. 75

Figure 3-5 Absorbance of PAAD-22D before (solid) and after (dash dot) illumination of 458 nm. 75

Figure 3-6 Absorbance of PAAD-72 before (solid) and after (dash dot) illumination of 458 nm. 76

Figure 3-7 Absorbance of PAAD-22E before (solid) and after (dash dot) illumination of 458 nm. 76

Figure 3-8 Extrapolation of radiant exposure (E) data for PAAD-22 material. Specifications from BEAM Co (black points) used to calculate E [J/cm^2] at 405 and 532 nm (blue circles). 78

Figure 3-9 Experimental optical setup for the photo-actuation of azobenzene complex dyes before assembling the LC cell. A fibre coupled diode laser at 405 nm is used to address PAAD-22D thin films on ITO/glass substrates. The laser beam is expanded with a two lenses system (L1 & L2) to cover the surface across the PAAD film. The polarisation of the incident light beam was controlled through a half-wave plate (HWP) and a polariser (P).....79

Figure 3-10 Experimental setup for measuring the transmittance coefficients as a function of the angle of incidence of PAAD-22E isotropic thin film, $T(\theta 1)$. A He–Ne laser was used at a 632.8 nm wavelength for 1.4 mW power as measured at the surface of the sample. The polarisation of the incident light beam was controlled through a half-wave plate (HWP) and a polariser (P). To remove background noise, we used a lock-in amplifier, where an optical chopper modulated the signal. A long wave-pass trim filter (LWP) helped further in cutting down the unwanted signals. 80

Figure 3-11 Graphs showing the experimental (orange) and fitted (blue) transmission curves for an s -polarised (top) and a p-polarised (bottom) 632.8 nm beam incident on the PAAD-22E/ITO/glass system. Inset: shows the experimental geometry for s-polarised light where the electric vector points along y axis while for p-polarised light it lies in the x-z plane. 82

Figure 3-12 Schematic of a PAAD-22D – LC cell in planar and twisted states. Switching between planar and twist states is controlled by one-step illumination with visible light. 85

Figure 3-13 Schematic of the optical setup for the single beam experiment. A fibre coupled diode laser at 405 nm is used to address PAAD-22D material which passes from a fibre port to collimates the beam. The sample is located between two parallel polarisers (P1 and P2), where the light enters at normal incidence. The PAAD-22D photoaligning layer lay on the front face and the PI layer at the far face of the cell. Photodiodes, PD1 and PD2 monitor the power of the laser before and after the cell by exploiting two beam splitters (BS). Here, the single beam is used also to realign the PAAD layer. 86

Figure 3-14 Schematics of the optical setup for the pump-probe experiment. A fibre coupled diode laser at 405 nm is used to address PAAD-22D thin films on ITO/glass substrates. The laser beam is expanded with a two lenses system (L1 and L2) to cover the surface across the PAAD film and. A beam splitter (BS) along with two mirrors (M) used to direct the beam onto the sample. The polarisation of the incident light beam was controlled through a half-wave plate (HWP) and a polariser (P3). A second fibre diode laser beam is used to probe the transmitted intensity. The sample is located between two parallel polarisers (P1 and P2), where the light enters at normal incidence. Photodiodes, PD1 and PD2 monitor the power of the laser before and after the cell by exploiting a beam splitter (BS)..... 87

Figure 3-15 Co-polarised microscope images of cells aligned with green (532 nm) beam. Within each panel: 1) Initial planar state. 2) First twisted state. 3) Second planar state. 4) Second twisted state. 88

Figure 3-16 Co-polarised microscope images of cells aligned with blue (405 nm) beam. Within each panel: 1) Initial planar state. 2) First twisted state. 3) Second planar state. 4) Second twisted state. 88

Figure 3-17 Realignment dynamics of PAAD-22D-LC cells by switching between planar → twist (OFF) and twist → planar (ON) states with one step illumination with linearly polarised blue light (405 nm). 89

Figure 3-18 Results of the single beam experiments. The top and bottom rows correspond to green and blue beam illumination respectively; the left column shows the transmitted intensity as a function of time over several cycles; the right column shows the normalized asymptotic illumination intensity (parameter b in Equation (3.4)) of the twisted and untwisted states in subsequent cycles. 91

Figure 3-19 Transmitted intensity against illumination time for a green single beam, blue single beam, blue pump and red probe, and an expanded blue pump and NIR probe. **(a)** Initial twisting step; **(b)** Subsequent untwisting. The experimental error of the normalized intensity is 5%, as discussed in Section 3.3.1..... 93

Figure 3-20 Transmitted intensity against illumination time for an expanded blue beam **(a)** Relaxation dynamics for the first few twist/untwist cycles. **(b)** Asymptotic intensities at subsequent twist and untwist steps. 94

Figure 4-1 Schematic diagram showing the location of the THz region in the electromagnetic spectrum..... 99

Figure 4-2 THz-TDS setup incorporating PC antennas for both emitter and detector. A femtosecond laser beam is split into pump and probe beams. The pump beam travels via an optical delay line before exciting THz radiation in the emitter. In this example the emitter is electrically modulated by an external power supply. The THz field is collimated by a parabolic mirror before being focussed onto the detector by a second parabolic mirror. The probe beam excites carriers within the detector which are accelerated by the instantaneous THz field. The current generated by this is detected by a lock-in amplifier. 101

Figure 4-3 Schematic representation of a custom THz-TDS setup. An 800 nm Ti:Sapphire fs laser (60 fs, 80 MHz repetition rate) is used to generate THz pulses of about 1-2 ps. THz-TDS utilizes a synchronous detection method resembling a pump-probe setup with inherent high signal to noise ratio which allows accurate measurements. Briefly, the beam is split into two beams with a beam splitter. One beam is sent to the THz emitter (GaAs photoconductive antenna, PCA), where the THz pulse is generated. The THz pulse illuminates the sample with aid of a four-lens system and then is collected by the detector. The other beam (60 fs) passes through a delay line and hits detector, where it gates it, and the detector is activated. Now by varying the delay line, the short 100 fs pulse can resolve in time the longer generated THz pulse (1-2 ps). 103

Figure 4-4 An illustration of a typical photoconductive antenna (PCA). The incident laser pulse excites carriers which are accelerated by the bias voltage to generate a photocurrent. The red dot is the focused laser beam between the two biased antenna structures fabricated on a semiconductor material (GaAs) with a band-gap that matches the energy of the laser. The resulting charge separation causes dipole emission of THz frequencies 105

Figure 4-5 Time domain scans of the THz electric field of a 1.17 mm fused silica sample (red) and reference air scan (black) taken using our custom THz-TDS 106

Figure 4-6 Time domain scan of the THz electric field of the 1.17 mm fused silica sample. Black colour stands for the initial pulses, dashed blue for the window function, and red for the resulting pulses after windowing. 107

Figure 4-7 THz electric field of a 1.17 mm silica sample (red) and a reference air scan (black) after windowing. 108

Figure 4-8 THz spectra of a reference, air (black) and a sample, silica before (blue) and after (red) windowing. 109

Figure 4-9 THz spectra of a reference, silica (black) and a sample, metallic resonator (red). 109

Figure 4-10 Phase of a reference, silica (black) and a sample, metallic resonator (red). .. 110

Figure 4-11 Normalised THz spectra of the sample i.e. metallic resonator. Transmission (left) and phase (right). 110

Figure 4-12 Knife-edge experiment: The THz pulse is generated with the aid of GaAs photoconductive antenna, PCA, and then propagate through a four-lens system collected by the detector. Knife edge measurements are made along the THz beam at the focal point by varying the position of the knife edge. 111

Figure 4-13 Time scan of detected THz signal as a function of knife edge position. Black colour stands for knife edge blocking completely the THz signal. 112

Figure 4-14 Knife-edge profile of the focused THz beam against the knife edge position: experiment (dash dot red line) and fit according to the expression of *P* (solid black line). 112

Figure 4-15 Absorption coefficients for ordinary (o) and extraordinary (e) ray of the highly birefringent LC mixture 1825 [58]. 115

Figure 4-16 Extinction coefficients for ordinary (o) and extraordinary (e) ray of the highly birefringent LC mixture 1825 [58]. 116

Figure 4-17 Ordinary (no) extraordinary (ne) refractive indices and birefringence (Δn) of E7 and suspension of E7 and BaTiO3 NPs provided by [159]. 118

Figure 4-18 (a) Refractive index of LC material for different temperatures. (b) Temperature dependence of the average refractive index of LC material at 1 THz frequency. The phase transitions between the different LC phases are indicated in the graph. Provided by [225]. 119

Figure 4-19 (a) Schematic diagram of the (a) magnetically [226] and (b) the electrically THz phase shifter using a LC cell [157]. (c) Temporal waveforms of the THz pulse transmitted through the empty and LC cell at various applied voltages [157]. (d) Schematic drawing of a self-polarising THz LC component [156]. (e) Time-domain spectra of the empty cell and the LC-filled cell when applied no voltage and three specific voltages [156] 120

Figure 4-20 Comparing the transmission spectra of a gold mirror versus a gold MM. Mirror gives zero transmission, diffracting the incident light, whereas MM shows a

homogenous response absorbing at a specific frequency. MMs derive enhanced properties different from its constituent materials and often going beyond the range of properties available in natural materials.....121

Figure 4-21 (a) Schematic and microscope images of fish-scale planar MM used in [165]. (b) Transmission spectra for both empty and LC-loaded MMs [165]. (c) An artistic impression of a spatial phase modulator [240]. (d) The geometry of the COMSOL model used for simulating the operation of the spatial phase modulator [240]. (e) Simulated (solid lines) and measured (dashed lines) transmittance spectra of the spatial phase modulator presented for two limiting cases of LC uniform alignment corresponding to planar/ 0 V (blue) and homeotropic/ 20 V (red) [240]. (f) An optical microscope image of the fabricated spatial phase modulator designed to operate at a frequency of 0.8 THz [240].....122

Figure 4-22 (a) Schematic layout and geometrical parameter definition of the proposed LC-tunable fishnet THz MM [150]. (b) Reflectance, transmittance, and absorption spectra of the investigated LC-tunable THz fishnet MM characterized by W=110μm and w=40μm, for the limiting LC alignment configurations, namely along the (top panel) x− and (bottom panel) z−axis [150].....123

Figure 5-1 Schematic illustration of the D-shaped metamolecules in (a) positive and (b) negative designs. Two Babinet complementary MM patterns investigated during this thesis. The width of the patches/slits was 10 μm, and the unit cell of the arrays had the dimensions of 70 x 80 μm.....126

Figure 5-2 Photolithography etching process for fabricating positive patterns on a 300 nm thick gold film onto a 100 μm thick slab of fused quartz.....127

Figure 5-3 Photolithography lift-off process for fabricating negative patterns on a 300 nm thick gold film onto a 100 μm thick slab of fused quartz.....128

Figure 5-4 Microscope images of MM patterns in positive (top panels) and negative (bottom panels) designs. 128

Figure 5-5 Schematic of LC-loaded MM hybrid cell used in this study. 129

Figure 5-6 Schematic representation of LC alignment cases. Planar 1 case indicates that LC alignment is parallel to the polarisation of light, whereas planar 2 case when perpendicular to the polarisation of light. By exploiting this optical contrast of refractive indices, large resonance shifts can be observed in the THz regime.130

Figure 5-7 Images of the sample. (left) The resulting hybrid LC metafilms device was $2 \times 2\ cm2$. (right) The different optical transparency, switching ON (bright side) and OFF (dark side) by altering the LC alignment is evident when sample was observed through crossed-polarisers.....130

Figure 5-8 (a) Transmission spectra simulated for pristine MMs of positive D-shaped design. Inset: Image of the unit cell taken with a reflection microscope. (b) Field map shows the normalised magnitude of electric field at the resonant frequency of the positive pattern. Field localisation appears around the edges of D shaped MM geometry. (c) Normalised distribution of the surface charge density induced in the positive MM at the resonant frequency.....131

Figure 5-9 (a) Transmission spectra simulated for pristine MMs of negative D-shaped design. Inset: Image of the unit cell taken with a reflection microscope. (b) Field map shows the normalised magnitude of electric field at the resonant frequency of the negative pattern. Field localisation appears in the central part of D shaped MM geometry. (c) Normalised distribution of the surface charge density induced in the negative MM at the resonant frequency.....132

Figure 5-10 (a & b) Transmission spectra simulated for pristine MMs of positive I-shaped and C-shaped designs, respectively. Insets: Schematic drawings of the unit cells along with the resonant polarisation states. (c & e) Normalised distribution of the surface charge density induced in the positive MMs at the resonant frequency. (d & f) Field maps show the normalised magnitude of electric field at the resonant frequency. Field localisation appears around the edges of I- and C-shaped MM geometries. 133

Figure 5-11 (a & b) Transmission spectra simulated for pristine MMs of negative I-shaped and C-shaped designs, respectively. Insets: Schematic drawings of the unit cells along with the resonant polarisation states. (c & e) Normalised distribution of the surface charge density induced in the negative MMs at the resonant frequency. (d & f) Field maps show the normalised magnitude of electric field at the resonant frequency. Field localisation appears in the central part of I- and C-shaped MM geometries.....134

Figure 5-12 Transmission spectra simulated for pristine MMs of positive (top) and negative (bottom) D-, I- and C-shaped MM designs. Insets: Normalised distribution of the surface charge density induced in the MMs at the resonant frequency. ..135

Figure 5-13 Transmission spectra measured experimentally (open triangles) and simulated (thick solid lines) for pristine MMs of positive (red) and negative (blue) designs. **Insets:** Images of the unit cells and fragments of the fabricated MMs of positive (top) and negative (bottom) designs taken with a reflection microscope.....136

Figure 5-14 (a) Normalised distribution of the surface charge density (colours) and electric field lines (black arrows) induced in the positive MM at the resonant frequency. (b) Polar plot of in-plane directivity of the local electric field in positive MM averaged over the area of the unit cell. The radius corresponds to the magnitude of the average electric field (E) normalised on the incident field (E_0). (c) Same as (a) but for negative MM. (d) Same as (b) but for negative MM.. 137

Figure 5-15 (a) Simulated transmission spectra for negative MM loaded with NLC in planar 1 (red) and planar 2 (blue) configurations. (b) Same as (a) but for positive MM. 139

Figure 5-16 Orientations of LC molecules schematically shown for planar 1 and planar 2 configurations. Planar 1 configuration is always in parallel with the resonant polarisation state of the MM, whereas planar 2 is perpendicular. 140

Figure 5-17 Calculated maximum resonance shift that can be attained in positive (black points) and negative (red points) MMs at different values of LC birefringence. Insets: Schematics of MM unit cells.....141

Figure 5-18 (a) Transmission spectra measured experimentally (open squares) and simulated (solid lines) for negative MM loaded with NLC in planar 1 (red) and planar 2 (blue) configurations. (b) Same as (a) but for positive MM. 142

Figure 5-19 (a) Orientational optical nonlinearity of NLC in planar 1 configuration engaged with positive MM. Local field-induced distortions of the initial alignment assumed within the hotspots are shown schematically via the orientation of LC molecules. (b) Same as (a) but for initial planar 2 alignment of NLC.....143

Figure 5-20 (a) Transmission spectra measured experimentally (open triangles) and simulated (thick solid lines) for positive MM taking into account the effect of orientation nonlinearity of NLC in planar 1 configuration. Inset: Spatial distribution of LC alignment assumed in the simulations. Scale bar ranges from -45° (blue) to 135° (red). 0° and 90° correspond to LC molecules being parallel to x- and y-axes, respectively. (b) Same as (a) but for initial planar 2 alignment of NLC.....144

Figure 5-21 Transmission spectra of measured experimentally (open triangles) and simulated (thick solid lines) for LC-loaded positive MM in (a) planar 1 and (b) planar 2 configurations in different angular re-alignment ranges. Re-orientation of ± 45° (90°±45° and 0°±45°, respectively) found to be closer to the experiment. 145

Figure 5-22 Schematic representation of modelling the anisotropy induced to the NLC molecules in (a) planar 1 and (b) planar 2 configurations due to the charge density distribution at the surface of positive MM patterns. 146

Figure 6-1 (a) 3D view of a homogeneously aligned LC cell, which is integrated with an array of metallic resonators (metamolecules). Magnification shows the geometry of the twist deformation of LC molecules by the in-plane THz electric field. (b) Schematic representation of in-plane switching induced in a homogeneously aligned LC cell, where shaded areas and red arrows show the near-field enhancement and lines respectively. 152

Figure 6-2 (a) Experimental (dash line) and simulated (solid lines) transmission spectra of LC-loaded MM in the case of planar alignment (blue curve) and hotspot alignment (red curve) induced by orientational nonlinearity of LC. Insets illustrate schematically the alignment of LC molecules in the two cases. Twist angle, φ, shows the maximum twist deformation of LC molecules by $\pi 4$. (b) Field map shows the normalised magnitude of electric field at the resonant frequency of the positive pattern. Field localisation appears around the edges of D-shaped MM geometry with electric field lines distributing along the pink arrows. 154

Figure 6-3 Drawing field lines: (a) diverge around the metamaterial edges and (b) extend perpendicularly to the parallel plates as per [285], producing either a nonhomogeneous or a homogeneous electric field, respectively. 155

Figure 6-4 The linear approximation of $12cos2\varphi$ (black line) obtained with two methods: Method 1 (red line) and Method 2 (blue line) 157

Figure 6-5 (a) The change of twist angle, φ, within LC layer, z, for different electric field, E, values. (b) Electric field map shows the penetration depth of the near-field enhancement of MMs in the LC bulk. (c) The change of twist angle, φ, as a function of the electric field strength, E, for different penetration levels, z, above the metasurface, (z=1-5 μm). The critical electric field strength values, EC, where LC molecules are oriented in between of initial planar and 'hotspot'

alignments is shown in magenta open hexagons. (d) The estimated critical electric field strength, EC, as a function of LC thickness height, z, obtained by the linear approximation. 159

Figure 6-6 (a) The change of twist angle, φ, within LC layer, z, for different electric field, E, values. (b) The change of twist angle, φ, as a function of the electric field strength, E, for different penetration levels, z, above the metasurface, (z=1-5 μm). The critical electric field strength values, EC, where LC molecules are oriented in between of initial planar and 'hotspot' alignments is shown in magenta open hexagons. Inset shows the estimated critical electric field strength, EC, as a function of LC thickness height, z, obtained by the linear approximation. 161

Figure 7-2 Schematic representation of a twisted nematic LC cell. 167

Figure 7-3 Schematic illustration of the X-shaped metamolecules in (a) positive and (b) negative designs. The width of the patches/slits is 10 μm, and the unit cell of the arrays has the dimensions of 70 x 80 μm. 168

Figure 7-4 A 514.5 nm Ar^+ laser was used for writing the diffraction gratings and a HeNe laser at 632.8 nm was used for monitoring the diffraction efficiency (η). 169

Figure 7-5 Transmitted order is S- and P-polarisation of the reference sample: ITO coated glass. 170

Figure 7-6 Transmitted order is S- and P-polarisation of the sample: PAAD film on ITO coated glass. 171

Figure 7-7 1st diffractive orders is S- and P-polarisation of the sample: PAAD film on ITO coated glass. 172

Figure 7-8 Diffraction efficiency as calculated from 1st diffracted orders and from 0th transmitted orders for S- and P-polarisation of the sample: PAAD film on ITO coated glass 172

Research Thesis: Declaration of Authorship

Print name: Eleni Perivolari

Title of thesis: Liquid crystal and meta-surface devices for enhancing light manipulation from visible to THz regime

I declare that this thesis and the work presented in it are my own and has been generated by me as the result of my own original research.

I confirm that:

1. This work was done wholly or mainly while in candidature for a research degree at this University;
2. Where any part of this thesis has previously been submitted for a degree or any other qualification at this University or any other institution, this has been clearly stated;
3. Where I have consulted the published work of others, this is always clearly attributed;
4. Where I have quoted from the work of others, the source is always given. With the exception of such quotations, this thesis is entirely my own work;
5. I have acknowledged all main sources of help;
6. Where the thesis is based on work done by myself jointly with others, I have made clear exactly what was done by others and what I have contributed myself;
7. Parts of this work have been published as journal papers and conference contributions listed in 0.

Signature: Date:

Acknowledgements

Firstly, I would like to thank my supervisors Prof. Malgosia Kaczmarek and Dr. Vasilis Apostolopoulos for giving me the chance to do a PhD in Physics at the University of Southampton, for their guidance during my studies, for the financial support of my research and for the opportunities to represent our group at international conferences. I am very grateful to Dr. Vassili A. Fedotov for the useful discussions and the supervision of the metamaterials' part of my project, for the help with theoretical simulations with COMSOL models and with writing papers. Many thanks to Prof. Giampaolo D'Alessandro for the useful discussions and suggestions on theoretical calculations and for the help with Matlab programming. Further, I would also like to acknowledge Dr. Nina Podoliak, who has taught me how to do experiments, assisted me through my first steps in research and was always willing to discuss my results. I want to really thank Kath Leblanc, Dr. Oleksandr Buchnev, and Neil Sessions because they were so helpful during my work in the cleanroom. I am grateful to Prof. Janusz Parka, and Dr. Urszula Chodorow, for providing me liquid crystal materials and for giving me the opportunity to work in their lab. Special thanks to Dr. Luciano De Sio and to my great friend now Dr. Alexa Guglielmelli for their unconditional help and support during this Thesis, and the educational discussions about photoalignment of liquid crystals. I also thank the PhD students of our research group, namely Dr. Jon Gorecki for introducing me into THz spectroscopy, and Lewis Piper for always being there when I needed help in the lab and for his help with COMSOL. I would also like to thank the other PhD students of the THz and Liquid Crystal groups namely Nick, Tom, and Jordan, for bringing a fresh vision to some problems and having fun with me.

But most importantly, I would like to thank my parents Konstantinos and Kyriaki, and my brother, George, for their love and support during my studies and for helping me to go on and on, even if they do not understand what I do. My beloved partner Dr. Angelos Xomalis, who inspired me during all these years and taught me how exciting science is, and because he supported me more than anyone else to accomplish my studies and follow my dreams. And then my dear friends, Konstantina, Artemis, Marilena, Nikos, Loukas, and Magda, who made this journey in Southampton an unforgettable one with their love, their support and all the fun we had together.

Finally, I would like to thank everyone else I should thank but forgot to add here.

Chapter 1

Introduction

1.1 Motivation and Outline of the Thesis

Liquid crystals (LCs) lie at the heart of many light-switching devices. Three key properties underlie this capacity. The first is the LC birefringence, the nature of which depends on the relative orientation between the LC molecules and an external electric field. The second is the fact that an external field can also reorient the constituent molecules of a LC. The third is the fact that surface effects, known as anchoring, also orient the LC molecules at the surface, and given orientational molecular interactions, this effect extends into the bulk [1,2].

Therefore, LCs were arguably one of the first medium widely exploited for devices such as phase shifters and light modulators from the optical to terahertz (THz) regime due to their high optical anisotropy (birefringence). However, the THz region of the electromagnetic spectrum is considered to be technologically under-developed in comparison to the neighbouring wavelength regions due to the lack of tunable modulators. The lack of suitable materials has so far restricted the development of THz devices. Conventional LC devices exploit transparent conducting electrodes such as indium tin oxide (ITO), needed to provide voltage-controlled alignment to the LC molecules. Despite that ITO exhibits super transparency in the visible spectra, it is highly reflective in the THz region (less than 10% transmission at 0.2-1.2 THz) [3]. This project aims to investigate potential new THz modulators and phase shifters capable of being controlled remotely using only external light sources, avoiding the need of conducting electrodes at all.

Chapter 1 gives an introduction regarding the nematic LCs and their optical properties upon application of electric field. 0 explains the experimental methods used to fabricate and

characterise the multi-layered LC cells. 0 reports on the optical driven bistable waveplate for the visible and near-infrared regimes, while 0 bridges the gap between visible and THz radiation. There, a brief description of the basic principles about THz radiation and time domain spectroscopy (THz-TDS) are presented. In addition, it contains an overview of how to evaluate the properties of LCs in the THz regime. 0 explores the LC-loaded metamaterials (MMs) devices, where experimental and theoretical results are presented. 0 includes the analytical calculation of the desired electric field strength capable of switching the LC molecules in-plane caused by the near-field enhancement in the vicinity of MMs. Finally, 0 contains the conclusions and ongoing work.

1.2 Liquid Crystals

LCs are a state of matter which has a unique phase described by properties that are between those of liquid and solid states. In addition to the solid crystalline and liquid phases, LCs exhibit intermediate phases where they flow like liquids yet possess some physical properties characteristic of crystalline solids.

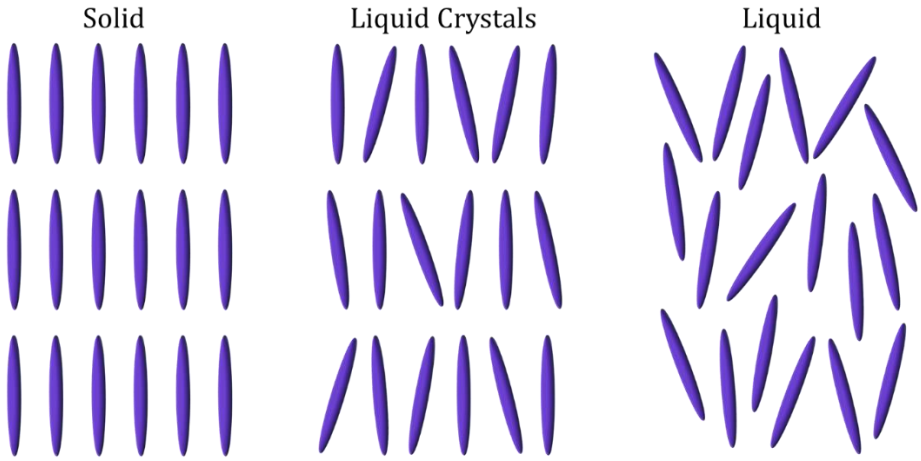

Figure 1-1 An illustration of the difference of the behaviour of solid, LCs and liquid. LCs flow like a liquid, but its molecules are oriented in a crystalline manner.

A true liquid is isotropic, meaning that its properties are uniform in all directions, where molecules are in constant random motion [1,4]. Most crystalline solids, in contrast, are anisotropic meaning that optical and other properties such as thermal and electrical conductivity vary with direction. A LC phase has many of the physical attributes of a liquid, but

its molecular units are sufficiently ordered to give rise to some anisotropy, most notably in their optical properties. Therefore, LCs can be considered crystals that have lost some or all of their positional order, while maintaining full orientational order (Figure 1-1) [5].

1.2.1 Types of Liquid Crystals

Materials that exhibit such unusual phases are often called mesogens (i.e., they are mesogenic), and the various phases in which they could exist are termed mesophases. A number of different types of molecules form LCs phases. What they all have in common is that they are anisotropic [4,6].

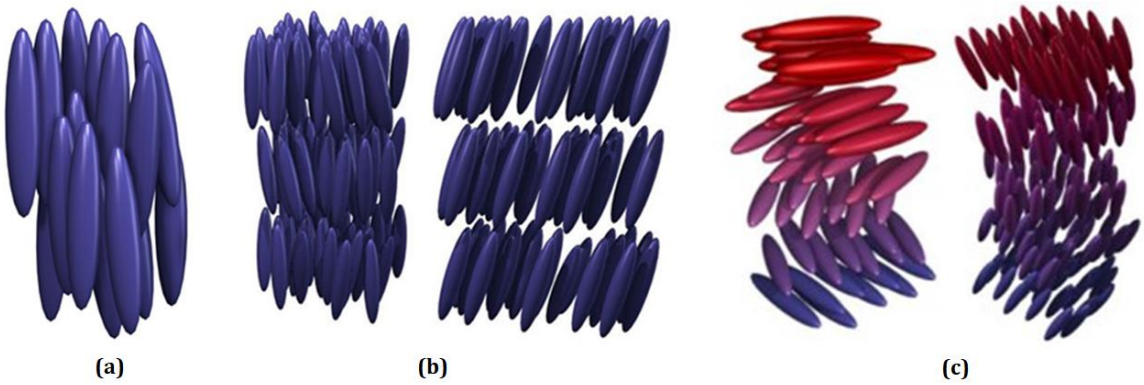

Figure 1-2 Schematic representation of (a) nematic, (b) smectic and (c) cholesteric mesophases.

The well-known ones are the thermotropics, the polymerics, and the lyotropics. The most widely used LCs and extensively studied for their linear as well as nonlinear optical properties are the thermotropics [6]. Molecules form rod-like shapes where one molecular axis is much longer than the other two. Thermotropic LC phases occur in a certain temperature phase. This type of materials has two characteristic temperatures: a temperature at which they transform from solid to LC, the so-called melting point, and a temperature at which they transform from LC to liquid, the so-called clearing point [4]. If the temperature rise is too high, thermal motion will destroy the delicate cooperative ordering of the LC phase, pushing the material into a conventional isotropic liquid phase. At too low temperature, most LC materials will form a conventional crystal. As a function of temperature, or depending on the constituents, concentration, substituents, and so on, thermotropics exist in many mesophases. These various mesophases can be characterised by the type of molecular ordering [1]. One can distinguish the positional order, that shows whether the molecules are arranged in any sort of ordered lattice and the orientational order (the so-called director axis, $\tilde{n}$), whether the molecules are

mostly pointing in the same direction. Moreover, the order can be either short-range or long-range depending on the distance between the molecules.

Figure 1-2(a-c) depicts schematically the arrangement of the elongated rod like LC molecules in the most common mesophases, nematic, smectic and cholesteric phases respectively. Nematic LC phase is a well-established one (Figure 1-2 (a)), with the word nematic originating from the Greek νήμα (nema), which means "thread". This term is derived by the thread-like topological defects observed in nematics. The molecules are positioned random like liquids, and have no positional order, but they self-align to have a long-range directional order with their long axes (roughly parallel), defined by a unit vector $\tilde{n}$, the director axis. Thus, the molecules are free to flow, but still maintain their long-range directional order. Only the nematic LCs are considered in this thesis [1,6].

Smectic LCs (Figure 1-2 (b)), unlike nematic, possess positional order and hence molecules are aligned in a pattern. In these phases, molecules act like liquids but in layers. There are many different smectic phases, all characterized by different types and degrees of positional and orientational order [1,7]. In the Smectic A phase, the molecules are oriented with their long axis normal to the plane of the layer, while in the Smectic C phase they are tilted away from it. Further, this phase can be reached at lower temperatures than the nematic phase and acquire higher viscosity ($\tilde{\gamma}$).

Cholesteric, now often called chiral nematic LCs, resemble nematic LCs in all physical properties except that the molecules tend to align in a helical manner as depicted in Figure 1-2(c). Here, the director, $\tilde{n}$, is not fixed in space as in a nematic phase but rotates throughout the sample. This property results from the synthesis of cholesteric LCs obtained by adding a chiral molecule to a nematic LC [6].

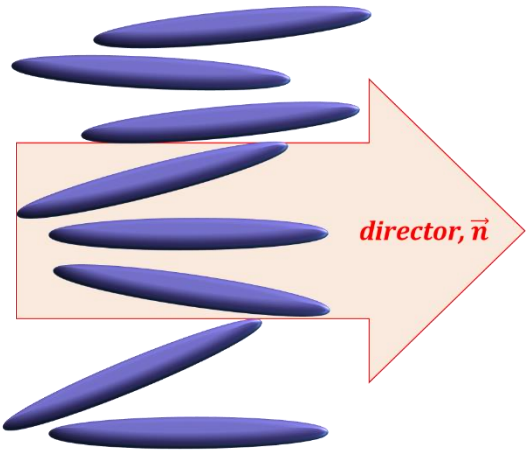

Figure 1-3 Defining the director in a local region of LC.

1.2.2 Nematic Liquid Crystals

Nematic is one of the most common LC phases. There exists long-range orientational order, where anisotropic elongated molecules (with a length between 1 and 3 nm and a width of approximately 0.1 to 0.5 nm), are aligned with their long axes along one common direction. Macroscopically a unique axis (the preferred direction) is defined in this way, the director $\hat{n}$. Nematic molecules have the same properties in the $+\hat{\boldsymbol{n}}$ and $-\hat{\boldsymbol{n}}$ directions; they are centrosymmetric [6].

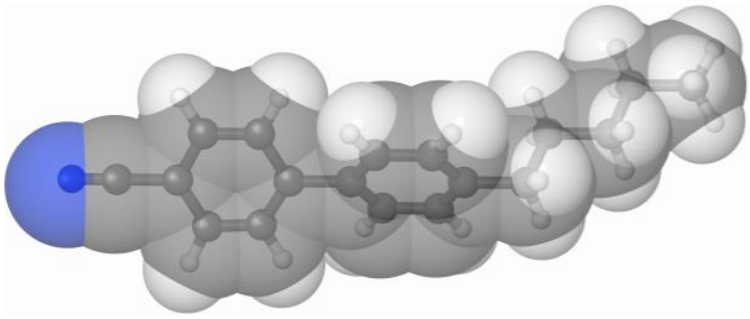

Figure 1-4 A diagram of a 5-cyano-biphenyl (5CB) molecule, which is a common component of LC materials. Blue represents a nitrogen atom, and grey and white are carbon and hydrogen, respectively. The elongated shape is critical to its LC phase behaviour [8].

To specify the amount of orientational order in such a LC phase, an order parameter is defined. This can be done in many ways, but the most useful formulation is to find the average of the second Legendre polynomial [6],

$$S = \langle P_2(cos\ \theta)\rangle = \langle \frac{3}{2} cos^2\ \theta\ -\ \frac{1}{2}\rangle. \tag{1.1}$$

The angle brackets denote averaging over all possible directions of the long molecular axes within the sample volume and also temporal averaging, while angle θ is the angle between the molecular axis and the director. A perfectly oriented system, where θ=0 for all molecules (perfectly oriented solid), the order parameter S would be equal to 1 (S=1). Whereas an isotropic liquid would have S=0. LCs typically have value of S between 0.3 and 0.8.

In elastic continuum theory, introduced over the last several decades by Oseen (1933) [9] and Frank (1958)[10], nematic LCs are described by the distribution of the order parameter tensor field, $n(\vec{r})$,

$$S_{\alpha\beta} = Q(T)\left(n_\alpha n_\beta - \frac{1}{3}\delta_{\alpha\beta}\right). \quad (1.2)$$

Here, n_α, n_β are the corresponding components of the director and $\delta_{\alpha\beta}$ is the delta function. This theory is based on the fact that director is not perfectly uniform but varies with position. In fact, it is a very rare case since surface treatments and/or external fields are usually required to obtain uniformity. The variation of director, $n(\vec{r})$, is extremely modest on a microscopic level, thus any orientational or positional order parameters are neglected. the order parameter $S_{\alpha\beta}(\vec{r})$ can be defined by the director field only. Thus, the nematic state can be entirely described in terms of the director field, $n(\vec{r})$.

When the director orientation is discontinuous, surface defects appear in the texture of nematic LC films, the so-called *Schlieren* texture [11]. These points correspond to disclination lines, as depicted in Figure 1-6. Between crossed polarizers these points are connected by dark brushes which are regions in which the director is either parallel or perpendicular to the plane of polarization of the incident light. The colors are Newton colours of thin films and depend on the thickness of the sample. Director, $n(\vec{r})$, changes its orientation continuously around a disclination. This curvature of the director costs elastic energy, thus by minimizing the free energy density one can obtain the actual configuration around the defects. An exception is the case of defects where large local spatial variations of the nematic order parameter can be observed.

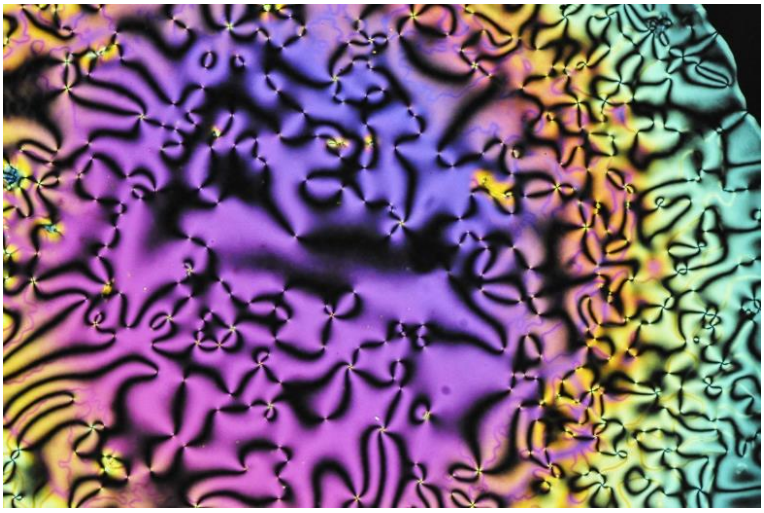

Figure 1-5 Schlieren Texture of a nematic film as obtained by [12]

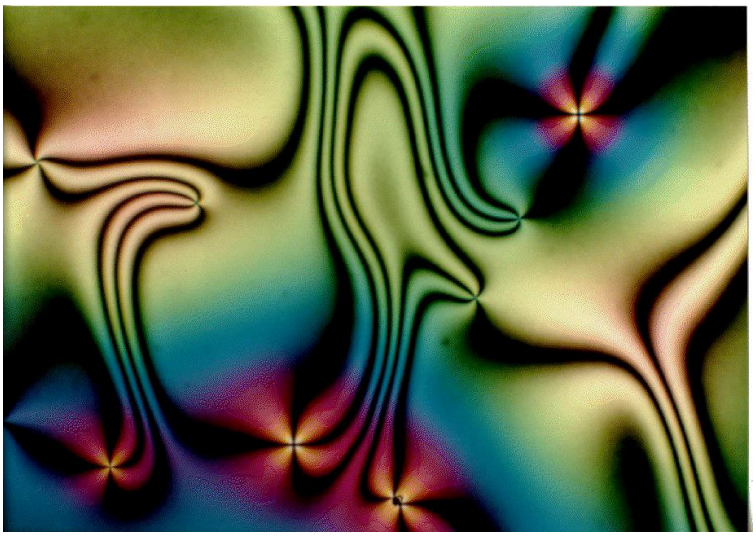

Figure 1-6 Schlieren Texture of a Nematic Films as obtained by [12]

As a result, the continuum theory is based on the phenomenological expressions that describe the free energy of a LC state. The free energy density may be expressed as a series of the order parameter. Any distortion from the orientation order leads to additional terms in free energy involving the gradient of $S_{\alpha\beta}(\vec{r})$.

Upon application of an external perturbation field, nematic LCs will undergo deformation in its bulk. Twist, splay, and bend are the main types of director axis deformations for nematics, see Figure 1-8. According to the theory first developed by Frank [10], the free-energy densities associated with these deformations are given by,

$$\text{Splay: } f_1 = \frac{1}{2}K_1(\nabla \cdot \hat{n})^2, \tag{1.3}$$

$$\text{Twist: } f_2 = \frac{1}{2}K_2(\hat{n} \cdot \nabla \times \hat{n})^2, \tag{1.4}$$

$$\text{Bend: } f_3 = \frac{1}{2}K_3(\hat{n} \times \nabla \times \hat{n})^2, \tag{1.5}$$

where, K_1, K_2, and K_3 are the splay, twist, and bend Frank elastic constants, respectively. The induced external field will create more than one forms of deformation and so the total distortion free-energy density is given by,

$$F_d = \frac{1}{2}K_1(\nabla \cdot \hat{n})^2 + \frac{1}{2}K_2(\hat{n} \cdot \nabla \times \hat{n})^2 + \frac{1}{2}K_3(\hat{n} \times \nabla \times \hat{n})^2. \tag{1.6}$$

This expression is the fundamental formula of continuum theory [1,6], which will be used in this thesis to characterise LC samples.

Splay, K_{11} **Twist, K_{22}** **Bend, K_{33}**

Figure 1-7 Three types of deformations occurring in nematics.

Phenomena such as surface alignment of nematics play an essential role in determining the behaviour of the bulk phase. Usually, plane surfaces are used in all experimental LC samples to separate the material from an external medium by some boundaries. In fact, these boundaries are responsible for inducing the preferential molecular orientation into the bulk (see Figure 1-8). There are many ways to induce the desired molecular orientation at the boundaries surface, which will be discussed later in this chapter. By the curvature elasticity surface orientation propagates far into the bulk, leading to an overall alignment of the nematic director $n(\vec{r})$. Put differently, the director is "anchored" along an easy axis produced by the nematic surface.

In order to microscopically explain the behaviour of the easy axis at various types of nematic surfaces, a number of theoretical efforts have so far been made from a Continuum, statistical mechanical, phenomenological, and elastic standpoints. The surface anchoring has been most commonly treated and understood on the basis of a phenomenological formalism due to *Rapini* and *Papoular* [13]. Therein, the simplest form of the anchoring energy density is given by:

$$f_s = \frac{1}{2} W_s sin^2\, \alpha, \tag{1.7}$$

Where, α, is the angle of the director deviation from the easy axis. In general, however, the anchoring energy depends on the director at the interface. The one associated with the rotation of the director within the plane spanned by the easy axis and the substrate normal is referred to as the "polar" anchoring energy. The one which corresponds to the rotation perpendicular to it is called the "azimuthal," "torsional," or "in-plane'' anchoring energy. The surface

anchoring is further classified, sometimes, into "strong" or "weak" anchoring according to whether or not director, $\boldsymbol{n}(\vec{r})$, can deviate from the easy axis direction.

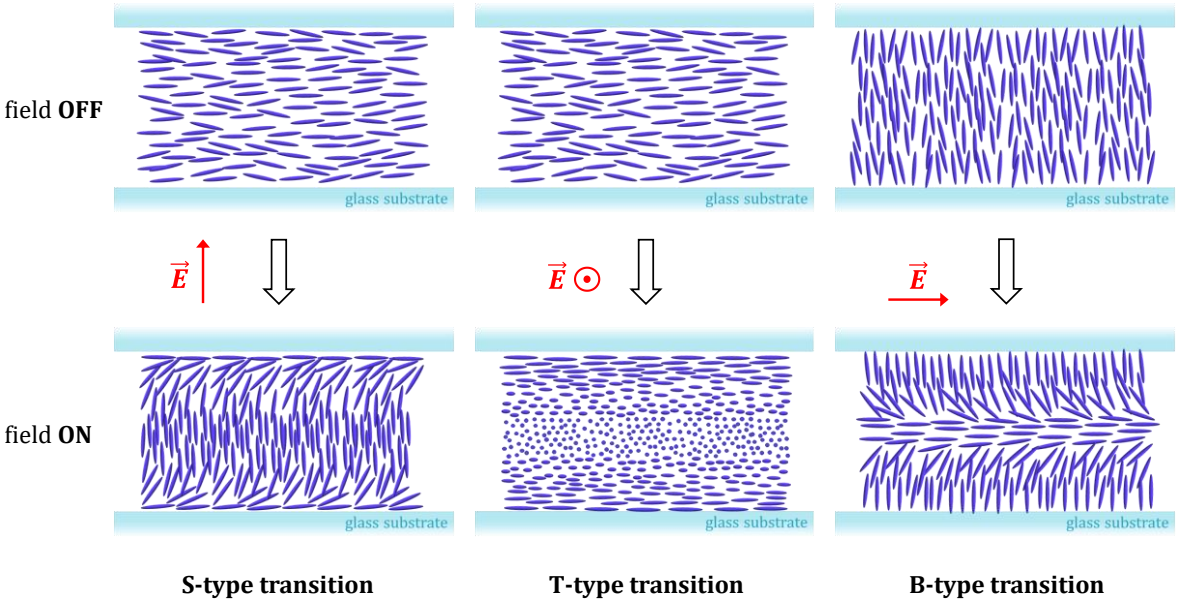

Figure 1-8 LC geometries for observing upon application of external field. Transition that cause different types of nematic deformation: splay (left), twist (centre), bend (right).

When $W_s \rightarrow \infty$ (strong anchoring) the director cannot deviate from the easy axis direction. Thus, the director field could be described by the bulk terms in the free energy functional only, and by the fixed boundary conditions. On the other hand, when W_s has a finite magnitude, typically of the order of 10^{-2} erg cm^{-2} or less, the molecules are not strongly anchored at the boundaries (weak anchoring). Both bulk and surface terms in the free energy should be considered. Sometimes, to characterize the anchoring type, a dimensionless parameter is used [14]:

$$w_i = \frac{d\, W_s}{K_i}, \tag{1.8}$$

where K_i is one of the elastic constants, depending on the sample geometry, d is the LC layer thickness. $w_i \gg 1$ and $w_i \ll 1$ correspond to strong and weak anchoring, respectively.

Therefore, the orientation of the molecules on the surface is characterised by two parameters, i.e. an easy axis and a surface anchoring energy density, W_s. The easy axis shows an equilibrium position of the director on the surface that minimizes the surface energy. For a given nematic and a substrate, the easy axis assumes either perpendicular, parallel, or slanted orientation with respect to the substrate. These configurations are referred to as homeotropic, planar, and

tilted alignments, respectively. The type of LC alignment on the plane surface is usually defined by an angle, θ, between the easy axis and the plane. Depending on this angle, the different alignment configurations could be distinguished: planar ($\theta \approx 0$), homeotropic ($\theta = \pi/2$), and tilted ($0 < \theta < \pi/2$).

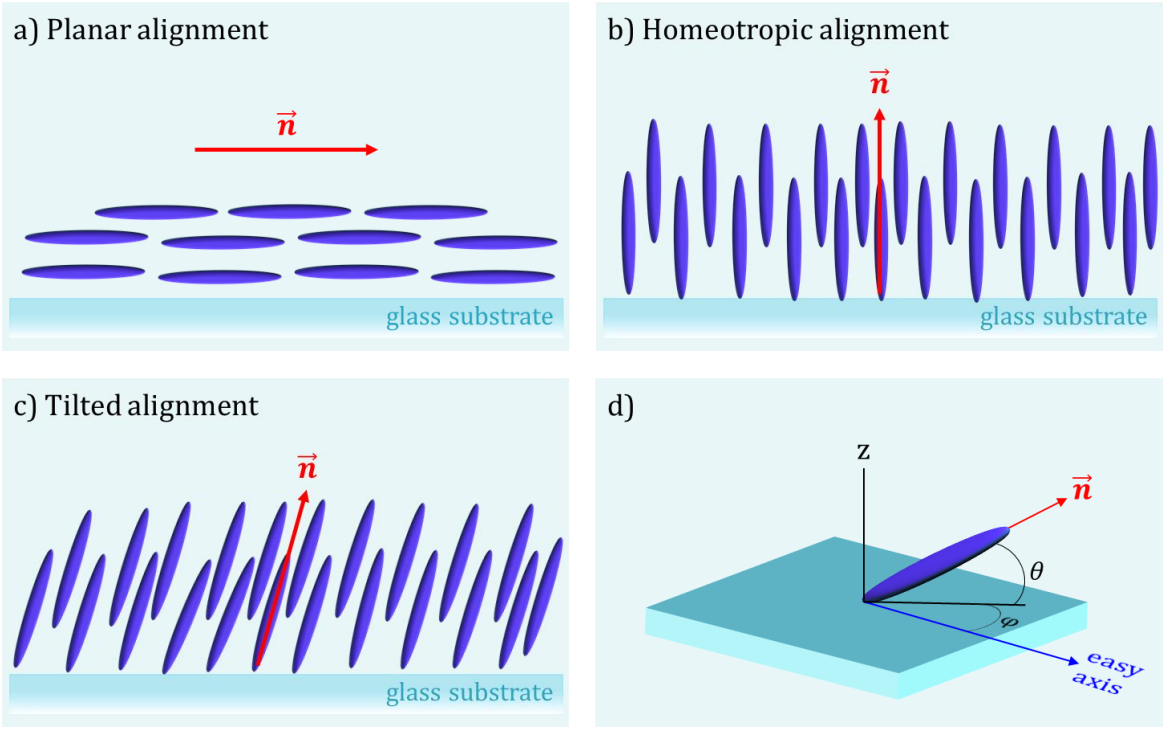

Figure 1-9 Types of LC alignment between parallel glass substrates: (a) planar, (b) homeotropic, (c) tilted, and (d) position of director, n, and easy axis in space.

There are several methods to achieve a particular alignment [7,14]. Most commonly, the planar alignment is produced by mechanical rubbing of the surface with a brush or a cloth. The rubbing creates microgrooves, which promote a well-defined orientation of the molecules on the substrate surface. The most popular technique for the homeotropic orientation is the deposition of surfactant or polymer molecules with long tails. These tails extend out vertically to the surface, inducing alignment as demonstrated in Figure 1-9. Under the strong anchoring condition, the so-called hard-boundary condition, molecules are strongly anchored to the boundary and do not respond to the applied perturbation fields (see Figure 1-10 (a, b)). On the other hand, if the molecules are not strongly anchored to the boundary, that is, the so-called soft-boundary condition, an applied field will perturb the orientation of the molecules at the cell boundaries (see Figure 1-10 (c)).

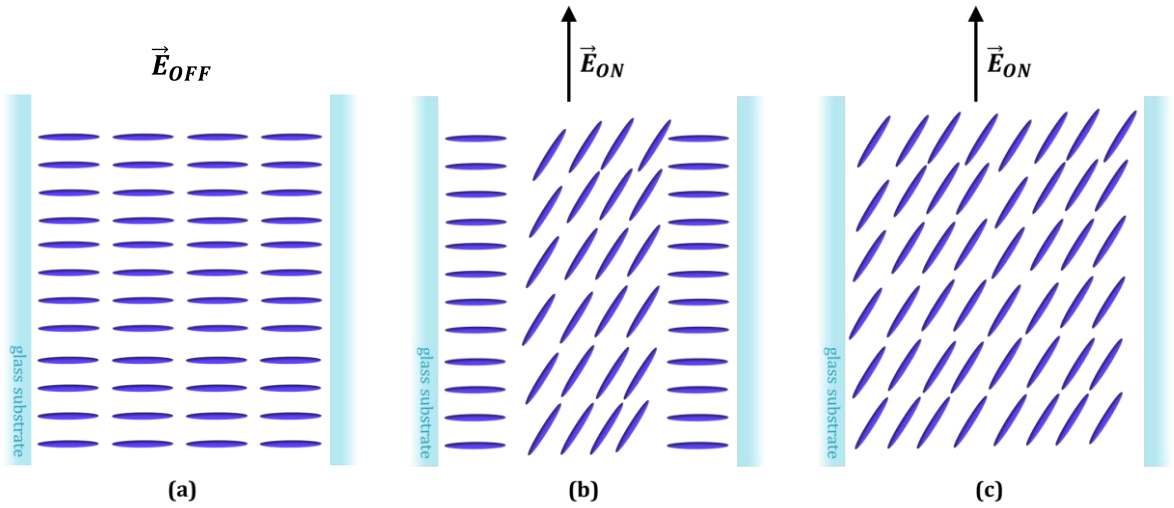

Figure 1-10 LC cells with different boundary conditions. (a) Homeotropic LC geometry. (b) Strong-boundary conditions affect the re-orientation of molecules caused by the applied electric field. (c) Soft-boundary conditions allow the applied field to perturb the orientation of the molecules at the cell boundaries.

1.3 Optical Properties of Liquid Crystals

LCs are both fluidic and anisotropic. The response of a LC to an applied field arises from the electrical polarization of the molecules. Anisotropic materials interact with the oscillating electric field of light to change the light's polarisation. LCs also interact with static electric fields. Under applied electric filed, molecules tend to rotate with their electric dipoles due to the displacement of electrons. The fluidity of LCs means that molecules are free to rotate, resulting in a tendency for the nematic director to align with the field. The LC director orientation can thus be controlled with electric fields, and in turn this can be used to control the polarisation state of the light passing through. These are the fundamentals of how a LC display (LCD) works [1,5,6].

1.3.1 LCs in Electric Field

LC can be characterised by the dielectric constants measured parallel, $\varepsilon_{\parallel}$ and perpendicular, $\varepsilon_{\perp}$ to the nematic director. Applying an external electric field, E, to a nematic of director n leads to induced electric displacement D as derived in [6],

$$D = \varepsilon_{\perp} E + \varepsilon_{\alpha} n(n \cdot E), \tag{1.9}$$

Where $\varepsilon_{\alpha} = \varepsilon_{\parallel} - \varepsilon_{\perp}$ is an anisotropy of dielectric permittivity. The electric contribution to the free energy density is:

$$f_{el} = -\frac{1}{8\pi} D \cdot E = -\frac{1}{8\pi} \varepsilon_{\perp} E^2 - \frac{1}{8\pi} \varepsilon_{\alpha} (n \cdot E)^2. \tag{1.10}$$

Only the second term depends on the director orientation with respect to the electric field. So, the first term can be omitted in the modelling of the nematic director orientation.

Equation (1.10) shows that a nematic with positive dielectric anisotropy favours alignment parallel to the field, while a nematic with negative ε_{α} favours perpendicular alignment. In nematics, the polarizability anisotropy is positive due to the rod-like shape of the molecules. This implies the polarizability is larger along the molecular axis than perpendicular to it. Therefore, the contribution of the electronic polarization to the dielectric anisotropy is also positive. The sign of the dielectric anisotropy depends on the chemical structure of the molecules. The non-polar molecules or the molecules with a relatively small angle between dipole moment and molecular axis are characterised by positive dielectric anisotropy. Negative dielectric anisotropy typically belongs to materials with a permanent dipole moment normal to the molecular axis. Materials used in this thesis exhibit positive dielectric anisotropy ($\varepsilon_{\parallel} > \varepsilon_{\perp}$).

In general, the contribution of the orientation polarization depends on the magnitude of the dipole moment and the angle between the dipole and the molecular long axis. The sign of the total dielectric anisotropy is determined by the relative magnitude of the electronic and orientation polarization. Given that the relaxation time for a confined LC is [6],

$$\tau = \frac{\gamma}{K} \left(\frac{d}{\pi}\right)^2 \tag{1.11}$$

where, γ is the rotational viscosity coefficient, K is the elastic constant and d is the cell width. A typical LC cell containing E7 mixture with 7 μm thickness would have a relaxation time of ~50ms. Most practical LC devices employ AC electric field and as such the permanent dipole has little effect on field-induced realignment as the orientation polarization cannot follow the variation of the field. This implies field-induced realignment from kHz electric fields is dominated by the induced electronic polarization. The combined dipole moment, or the induced polarization of the material, is related to the electric field by:

$$P = \varepsilon_0 \chi_e E \tag{1.12}$$

where, ε_0 is the permittivity of free space and χ_e is the electric susceptibility.

For an anisotropic medium, such as nematic LCs, the dielectric permittivity (ε), permeability (μ) and susceptibility (χ_e), are direction dependent and can therefore be defined with respect to the LC director (n). From the mathematical point of view, they become the tensor quantities. The propagation of light through nematics is considered to be magnetically isotropic but electrically anisotropic, as the magnetic anisotropy of nematics is very small (in the order of $\sim 10^{-7}$), while their dielectric anisotropy is greater than unity. Then, μ is a scalar and $\hat{\varepsilon}$ is a tensor in material equations. The dielectric permittivity tensor is symmetric, so it can be diagonalized by choosing a suitable coordinate system,

$$\hat{\varepsilon} = \begin{bmatrix} \varepsilon_x & 0 & 0 \\ 0 & \varepsilon_y & 0 \\ 0 & 0 & \varepsilon_z \end{bmatrix} \tag{1.13}$$

where, ε_x, ε_y, and ε_z are called the principal dielectric constants. If two of the principal dielectric constants are equal ($\varepsilon_x = \varepsilon_y \neq \varepsilon_z$) the medium is called a uniaxial crystal, and the principal axis z is called the optical axis. In a biaxial crystal, however, all dielectric constants are different ($\varepsilon_x \neq \varepsilon_y \neq \varepsilon_z$). Most LCs belong in the class of uniaxial crystals.

1.3.2 The Fréedericksz Transition

LCs with positive dielectric anisotropy, as the ones studied in this thesis, tend towards an alignment parallel to the direction of the external electric field. This generally true for the free bulk of the LC [1,6]. However, if a nematic LC is aligned with hard anchoring conditions as in Figure 1-8, with a field applied perpendicular to the director, molecules will be realigned only when the field strength exceeds some critical threshold value E_F. Below this critical threshold ($E < E_F$), there will be no effect on the director configuration, whereas above this value ($E > E_F$), a transition occurs. The applied field is sufficient to overcome elastic and anchoring forces opposing reorientation and the LC can begin to align with the field. This phenomenon is known as Fréedericksz transition, as it was first observed and studied by Fréedericksz in 1927 [15].

The local equilibrium configuration with an applied field greater than E_F, depends on the magnitude and direction of the field with respect to the director axis, and also the dielectric anisotropy. In addition, there is a competition between the orientation imposed by the field

and the orientation imposed by the cell boundaries. It can be easily observed in a thin LC cell aligned between plane glass slides in different geometries, as illustrated in Figure 1-8. In all cases, the electric field direction is perpendicular to the unperturbed director, forming a planar (a and b) and homeotropic configuration (c). Upon application of external electric field, the director near the boundary is dictated by the surface alignment effect and, the bulk by the applied field. As a result, LC molecules will respond to the electric field only when its value is larger than the threshold field given by [6],

$$E_F = \frac{\pi}{d}\sqrt{\frac{K_i}{\varepsilon_0|\varepsilon_\alpha|}}. \tag{1.14}$$

Then, the threshold voltage can be derived as:

$$V_F = E_F d = \pi\sqrt{\frac{K_i}{\varepsilon_0|\varepsilon_\alpha|}} \tag{1.15}$$

where d is the cell thickness, K_i is an elastic constant, $\varepsilon_0 = 8.85 \times 10^{-12}\ F/m$ is the vacuum permittivity and ε_α is the permittivity anisotropy. It is worth noting that V_F does not depend on the sample thickness d. So, the critical voltage only depends on the properties of the LC (elastic constant and dielectric anisotropy), and none of the cell parameters. On the contrary, the critical field E_F is inversely proportional to the sample thickness d. Further, the elastic constant, K_i , depends on the type of deformation (i.e. splay, twist, or bend) caused by the external field, see Figure 1-8. The work presented in this thesis considers only planar and twisted LC geometries (Figure 1-8 a and b). Complete rotation in a homeotropic cell often requires fields of magnitude several times E_F, with the field applied normal to the initial director orientation.

All reorientation effects involve competition between the elastic, anchoring, and viscous torques opposing motion, and the torque from the applied field promoting reorientation. Elastic deformations, whether splay, twist, or bend, cost energy. The dynamic behaviour in a LC always tends towards an equilibrium state which is determined by the minimization of free energy in the system [7]. However, a discussion of the hydrodynamics of LCs is beyond the scope of this work.

1.3.3 Optical Anisotropy of Nematic Liquid Crystals

An aligned nematic LC is in essence a uniaxial crystal. Hence the crystal axes are defined perpendicular and parallel to n. These directions experience different refractive indices due to the molecular structure of the LC. The effective refractive index can therefore be given by [2]:

$$n^2 = \begin{bmatrix} {n_\perp}^2 & 0 & 0 \\ 0 & {n_\perp}^2 & 0 \\ 0 & 0 & {n_\parallel}^2 \end{bmatrix} \tag{1.16}$$

Polarized light incident on the LC sample exhibit different refractive indices depending (i) on the direction of propagation and (ii) the state of polarization with respect to the director orientation. As a uniaxial crystal, the nematic LC can be characterised by two refractive indices: the ordinary, n_o, and the extraordinary , n_e, for the light polarized perpendicular and parallel to the optical axis, respectively.

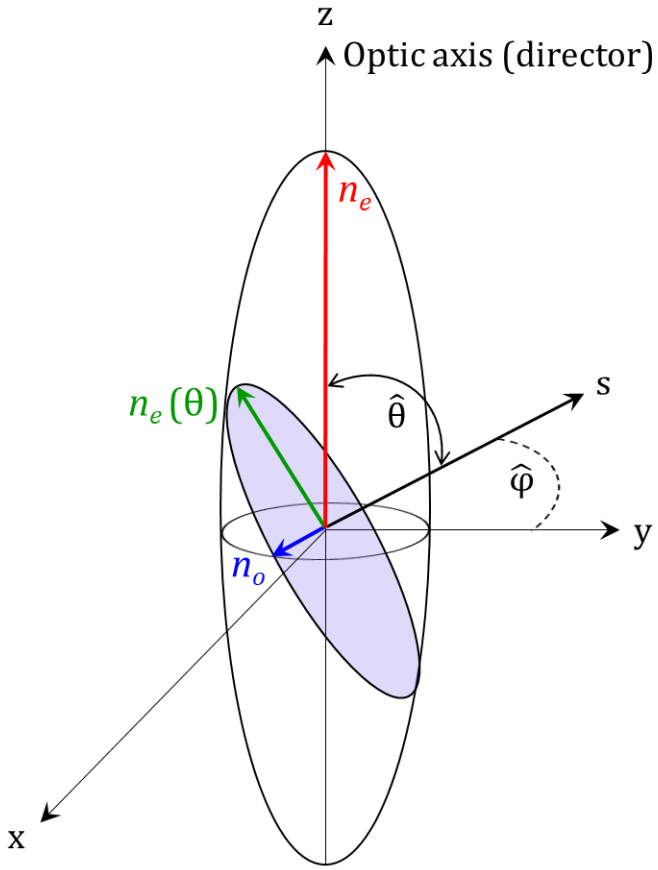

Figure 1-11 Index ellipsoid for a plane polarized optical wave propagating along s in a uniaxial crystals. ne(θ) and no are the refractive indices for the extraordinary and ordinary components, respectively.

In typical optical experiments, a light beam often propagates at a certain angle with respect to the director. Let us consider the case when the light propagates in the z direction and the director is aligned at an angle (θ_i) with respect to it. When the refractive index is independent of the direction of the propagation of light is given by,

$$n = n_o. \tag{1.17}$$

When the refractive index is dependent on the direction of the propagation of light is given by [2],

$$n = n_{eff}(\theta_i) = \frac{n_o n_e}{\sqrt{{n_e}^2 cos^2\theta_i + {n_o}^2 sin^2\theta_i}}. \tag{1.18}$$

As a monochromatic light with wavelength (λ), propagates through a nematic LC, with thickness (d), a phase lag (φ) is created between ordinary and extraordinary waves [1], which depends of the angle θ_i and is given by [2],

$$\varphi = \frac{2\pi}{\lambda}\left[n_o - n_{eff}(\theta_i)\right]d. \tag{1.19}$$

For a layer with a variable director orientation angle, $\theta_i = \theta_i(z)$, the total phase lag can be found as:

$$\Delta\varphi = \frac{2\pi}{\lambda}\int_0^d \left[n_o - n_{eff}((\theta_i(z))\right]dz. \tag{1.20}$$

The deviation of the director orientation changes the effective refractive index and the phase lag between ordinary and extraordinary components of the light propagating through the LC. This method is important for detecting the nematic reorientation, such as Fréedericksz transition, and is useful for determining of the birefringence of nematic LCs.

1.3.4 Birefringence in Liquid Crystals

Perhaps the most studied and applied property of LCs is the birefringence. With the aid of an externally applied field, one can control or realign the anisotropic LC axis, thereby controlling the effective refractive index (n_{eff}) and phase shift (δ) experienced by the light traversing the

LC. Such electro-optical processes form the basis for various optical transmission, reflection, switching, and modulation applications [7].

Essentially, the LC cells are placed within a stack of phase-shifting (phase retardation) wave plates or polarizing elements to perform various electro-optical functions, as shown in Figure 1-12 [16]. These operations usually require a phase shift, δ, on the order of π (i.e., quarter wave plate requires π/2 and half-wave plate requires π, and so on) [2]. Depending on the actual configuration, the phase shift imparted into the LC cell by,

$$\delta \sim d(\Delta n)\frac{2\pi}{\lambda} \tag{1.21}$$

where d is the path length of the light through the LC layer, Δn is the birefringence, and λ is the wavelength. Birefringence is quantified as the magnitude of the difference between the ordinary, n_o, and the extraordinary , n_e, refractive indices:

$$\Delta n = n_e - n_o. \tag{1.22}$$

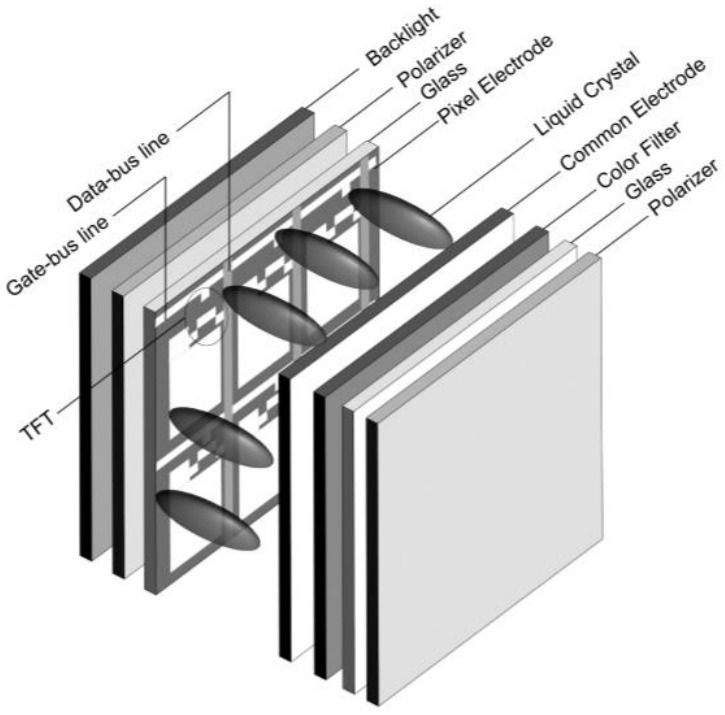

Figure 1-12 Schematic of a typical LC display pixel consisting of electronic driving circuit, polarizers, LC cell, colour filter, and phase plate (not shown) [16].

LCs are noted for their relatively large birefringence and easy susceptibility to external field perturbation. To create the required phase shift for optical application in the visible to near IR regime, only applied voltages of a few volts and a film thickness of a few microns are required. As a result, LC has enjoyed widespread and an ever-increasing demand in various optical display, switching, information, and image processing industries. Although, the quantitative description of the polarised light as propagating through LCs, is quite complex. The problem arises from the fact that the director axis within a cell is inhomogeneous and varies spatially, because of the boundary anchoring effects in response to an applied electric field (see Figure 1-8 & Figure 1-10).

In order to determine the birefringence of a LC and detect the phase lag, a typical sample is usually observed between two linear polarisers, whose transmission axes are crossed. Let us consider a planar nematic LC cell, as this geometry will be used in most of the experiments presented later. Upon characterisation, LCs are usually sandwiched between two transparent electrodes of ITO. ITO is deposited on 1 mm thick glass substrates. The cell is placed between two linear polarizers and oriented in such way to that its alignment direction makes a certain angle, φ, with the polarizer. The light beam passes through this optical system at normal incidence to cell plane and a photodiode was used to monitor the intensity of the beam after passing through the cell [2].

To define cross-polarized intensity, we assume a monochromatic plane wave which can be specified in terms of the electric field vector as:

$$E = \mathcal{E}e^{i\{(k\cdot r)-\omega t+\delta\}}, \tag{1.23}$$

where $|\mathcal{E}|$ is the electric field amplitude, $k = \frac{\omega}{v}\hat{k}$ is the wave vector, ω is the angular frequency, and δ is the phase. This wave propagates through a medium in the direction defined by unit vector $\hat{k}$ with a phase velocity $v = c/n$, where $n = \sqrt{\varepsilon\mu}$ is the refractive index of the medium. Accepting the Cartesian coordinate system, in which the direction of propagation is parallel to the *z* axis, and the director is aligned in the *x* direction, the electric field can be expressed as:

$$E = \mathcal{E}e^{i\{kz-\omega t\}}(sin\,\varphi\,\hat{x} + cos\,\varphi\,\hat{y}). \tag{1.24}$$

The polarization of the incident beam is defined by the angle φ with respect to the nematic director. The *x* and *y* components of the light experience refractive indices n_{eff} and n_o, respectively. As the beam passes through the nematic layer, it undergoes a phase lag δ between the *x* and *y* components, which results in a change of the polarization state. The electric component of the light transmitted through the cell becomes:

$$E' = \mathcal{E} e^{i\{kz\prime - \omega t\prime\}} (e^{-i\delta} sin\, \varphi\, \hat{x} + cos\, \varphi\, \hat{y}). \quad (1.25)$$

The change of the polarization state can be detected by a second polarizer, which is often called the analyser. The projection of vector E' on the analyser transmission axis is:

$$E'_{\perp} = -E'_x cos\, \varphi + E'_y\, sin\, \varphi = \mathcal{E} e^{i\{kz\prime - \omega t\prime\}} sin\, \varphi\, cos\, \varphi (1 - e^{-i\delta}). \quad (1.26)$$

Then, the normalized intensity of the beam after transmitting through the analyser, $I_{\perp}$, can be derived as follows:

$$|E'_{\perp}|^2 = \mathcal{E}^2 sin^2 \varphi\, cos^2 \varphi (2 - e^{-i\delta} - e^{-i\delta}) = \mathcal{E}^2 sin^2\, 2\varphi\, sin^2 \left(\frac{\delta}{2}\right), \quad (1.27)$$

$$I_{\perp} = \frac{|E'_{\perp}|^2}{\mathcal{E}^2} = sin^2\, 2\varphi\, sin^2 \left(\frac{\delta}{2}\right). \quad (1.28)$$

The intensity oscillates with variations of the phase lag, δ. The amplitude of oscillations depends on the angle φ, as $sin^2\, 2\varphi$. So, the intensity $I_{\perp}$ has a maximum in its amplitude of oscillations when the cell alignment direction is rotated to an angle of $\varphi = 45°$ with respect to the polarizers. Therefore, to detect the change in the phase lag, the experiment is usually run with the cell positioned at this angle with respect to the polarizers. Thus, by substituting $\varphi = 45°$ into Equation (1.28), cross-polarised intensity (CPI), $I_{\perp}$, is simplified to:

$$I_{\perp} = sin^2 \left(\frac{\delta}{2}\right). \quad (1.29)$$

This optical method is used in this thesis to measure the electric field-induced Fréedericksz transition in a LC cell with planar configuration. By applying AC electric field to the cell, the rotation of the nematic director inside the cell is observed as an intensity oscillation. The beginning of the LC reorientation happens at Fréedericksz threshold voltage when the intensity curve starts to oscillate. When the polarization of the incident beam is φ with respect to nematic director, r, the normalized intensity of the beam as detected by the photodiode when $\varphi = 45°$ is given by Equation (1.29). CPI, $I_{\perp}$, depends on the AC voltages and hence, Equation (1.29) is used to extract the change of the phase lag, δ. With the calculation of the phase lag we can determine the birefringence of LCs in the optical regime by Equation (1.21).

1.4 Alignment of Liquid Crystals

Efficient control of LC alignment results in the possibility to manipulate the effective birefringence of the LC cell and hence its optical properties. As was shown in Section 1.3, because of the anisotropy in dielectric properties of LCs, their alignment can be controlled by external electric field. Although, in the absence of external electric field, phenomena such as surface alignment of nematics play the essential role in determining the behaviour of the bulk phase. Usually, plane surfaces, such as glass substrates, are used in all experimental LC samples to separate the material from an external medium by some boundaries. In fact, these boundaries are responsible for inducing the preferential molecular orientation into the bulk. There are many ways to induce the desired molecular orientation at the boundaries surface, such as the traditional mechanical rubbing of the surface, the deposition of a polymeric surfactant with long tails extending vertically to the surface (homeotropic alignment), or the deposition of photosensitive dyes which exhibit photo-isomerisation and orient with regards to the polarisation of electric field [2,17,18]. This surface orientation propagates far into the bulk, leading to an overall alignment of the nematic director $\boldsymbol{n}(\vec{\boldsymbol{r}})$.

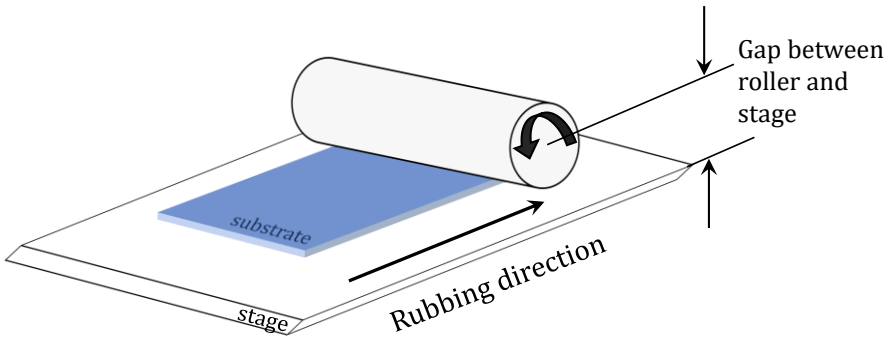

Figure 1-13 Structural sketch of a rubbing machine. A rubbing machine consists of a roller covered by rubbing cloth, and a platform to hold the substrate. The roller or the substrate stage moves at a constant speed while the roller is rotating at several hundreds of rpm. The gap between the roller and the stage is adjusted to change the pile impression.

1.4.1 Rubbing: Mechanism and Applications

Rubbing is a dominant LC alignment process, which has been reported by Mauguin almost eighty years ago. It is a well-established method to induce planar alignment to nematic LC cells, adopted by commercial manufacturers (LCD industries) [16] as well as academic researchers. The process is to rub an organic polymer coated substrate using a rotating brush or cloth with

short fibres. The rubbing creates microgrooves, which promote a well-defined orientation of LC molecules on the substrate surface. Figure 1-13 shows a typical rubbing machine consisting of a rotating drum and a substrate holding platform. Either the roller or the platform stage moves at a constant speed, while the roller is rotating at several hundreds of rpm. The gap between the roller and the stage is adjusted to change the pile impression. Rubbing must take place prior assembling the LC cell and cannot change afterwards, unless erasing the polymeric film and restart the process. These are few of its disadvantages along with the generation of dust and static electricity. Although this process has many problems, leading LC applications cannot be manufactured without it because it is a short, simple alignment process, and can be applied to a large area at low cost.

The rubbing controls both the polar and azimuthal angles (introduced in Section 1.2.2) of the LC alignment, thus it is very common to create defects and harm the optical characteristics of LC materials. However, not only the rubbing process, but also the alignment materials may affect the optical quality of LCs. For this reason, many materials have been tested as alignment layers (ALs) for rubbing, which span from polyvinyl alcohol, acrylic polymers, and vinyl polymers. Finally, high temperature polyimide (PI) prevailed as an alignment material because of its stability performance over time at elevated temperatures (possibly caused by rubbing) and superior electric characteristics. In this thesis, we also used PI as an alignment material for rubbing.

The controllable parameters of the rubbing machine are the gap between the substrate and the cylinder, the cylinder rotation speed, the stage movement velocity, and the number of times each substrate goes through the rubbing process. The most significant parameter is the gap between the cylinder and the substrate [2,18]. The gap controls the pressure of the buffing cloth on the substrate, and it affects the anchoring strength, pretilt angle, and surface morphology of the substrate. In addition, variations in the cylinder rotation speed and the stage movement velocity, may cause fluctuations in pretilt angle and unevenness in the resulted alignment. Then, alignment-related defects appear, such as disclination lines, reverse twist, and reverse tilt (see Figure 1-14, Figure 1-15, and Figure 1-16). Monitoring the rubbing status is very difficult, since evaluation of defects is possible only after assembling the substrates and observing the images of the finished cells.

Furthermore, additional problems such as, accumulation of static electricity and dust particles are a typical issue [19]. There are several ways to eliminate or control them. When rubbing a high resistance material like PI, and static electricity is generated, one can neutralize the surface by injecting ionized N_2 gas. While, to prevent possible diffusion of the dust from the rubbing cloth and alignment material, a cover hood and an exhaust fan are suggested [18].

Although, these problems are addressed, there is still the need to incorporate electrodes and external electric field into the cell design [20]. Thus, rubbing has become somewhat controversial [21,22]. Furthermore, such surfaces will not, in general, sustain bistability as new technologies require. This would only be possible if the surface alignment can itself be altered, which is completely impractical if the alignment has been achieved by rubbing [17,23,24].

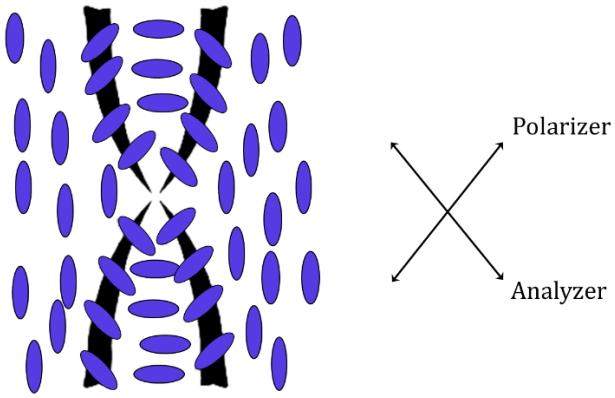

Figure 1-14 Alignment disclination lines defect (Néel wall).

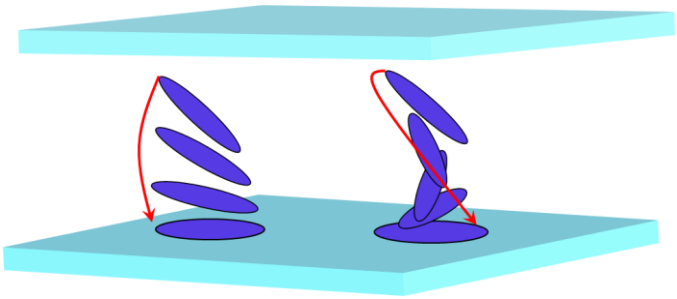

Figure 1-15 Alignment in a twist-reverse defect.

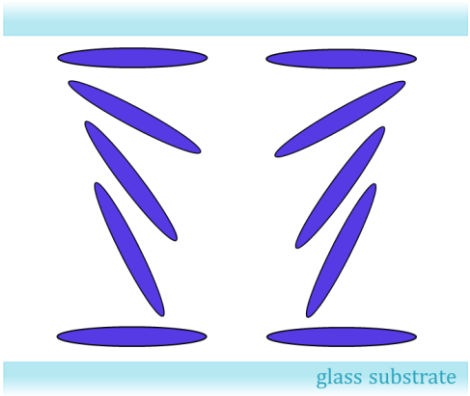

Figure 1-16 Alignment in a tilt-reverse defect.

1.4.2 Photoalignment

Photoalignment of LCs is a direct consequence of the observed photoinduced optical anisotropy and dichroic absorption in thin amorphous films [19]. In fact, the subject of light–molecule interactions have been a fascinating subject of research for a long time and is still capturing the imagination of many people. Light is responsible for the delivery of energy as well as phase and polarization information to materials systems. In this particular case, the alignment of the molecules takes place due to a partial ordering of the molecular fragments after a topochemical reaction of a photoselection (Weigert's effect) [25]. It was soon shown that these materials could provide high-quality alignment of molecules in an LC cell [26,27].

The first photo-patterned optical elements, based on polyvinyl-cinnamate films, appeared in 1977 [19], the technology became an LCD one only at the beginning of the 1990s [26,28-30]. While, the first publication on photoalignment in LCs has been reported by Ichimura in 1988 [31,32], which discussed the application of the reversible *cis-trans* isomerization of azobenzene molecular layers to the switching of the alignment of the LC layer from homeotropic to planar orientation. Ever since photoalignment has been a focus of research developing very rapidly. Gibbons et al. reported their photoalignment results in 1991 [27], where they described an azobenzene-mixed polyimide exposed to linearly polarized UV light that aligned the LC. In 1992, Schadt reported photoalignment by dimerization of poly (vinyl cinnamate) exposed to linearly polarized UV light [33]. In these projects, special photochemical reactions, such as dimerization or isomerization, were used, and only a few limited types of photoalignment materials were involved. In 1994, it was found that polyimide exposed to linearly polarized deep UV light showed LC alignment, and that a wider variety of materials could be used for photoalignment [34]. Soon after the LC photoalignment procedure was derived using cinnamoyl side-chain polymers and dye-doped polymer ALs. Moreover, Yuri Reznikov was particularly influential in developing this surface alignment technique, and his name appears on numerous patents and right papers. These date right from the technique's invention in the 1980s (see e.g. [32]) and stretch e.g. to his more recent 2012 review with Yaroshchuk [19].

Photoalignment received a lot of attention and the vast majority of new materials, techniques, and LCD prototypes have appeared because it can be used to establish multiple domains easily. In particular, the application of photoalignment to active optical elements in optical signal processing and communications is currently a hot topic in photonics research [35-39].

Photoalignment possess obvious advantages in comparison with the traditional rubbing treatment of the substrates of LC cells. Some of the benefits using photoalignment are: (i) The elimination of electrostatic charges and impurities as well as mechanical damaging of the

surface. (ii) A controllable pretilt angle and anchoring energy of the LC cell, resulting from materials' properties. (iii) The possibility to produce structures with the required LC director alignment within selected areas of the cell, and thus allowing spatial dividing (pixel) to enable novel LC configurations. (iv) New advanced applications in integrated photonic devices i.e. fibre communications, optical data processing, holography, and other fields where rubbing alignment is not possible due to the sophisticated geometry of the LC cell and /or high spatial resolution of the system. (v) The efficient LC alignment on curved and flexible substrates. (vi) There is no need of continual imposition of a voltage, causing the device to continually consume power. For static displays, in which continual updating is in principle unnecessary, this is a particular problem. It is a problem that can be overcome if the device is constructed so as to be bistable (see e.g. [40]). In this case, electric impulses alone should be sufficient to persuade a pixel to switch states.

1.4.2.1 Photoalignment mechanisms

The most common mechanism for photoalignment involves the generation of an anisotropic distribution of the molecules of the alignment materials by using the dependence of the polarization direction of the absorption of light by the molecules [19]. When the electric vector of the photons coincides with the transition moment of the molecule, the molecule absorbs light strongly, and a photochemical reaction occurs. The creation of anisotropy by using polarized light is called the Weigert effect [41] and has been known since 1920. However, the photoalignment mechanisms in some materials are not yet understood because the photochemical reactions are different in each photoalignment material. In some cases, the LC alignment direction depends on the exposure energy of the light on the photoaligning material.

Progress in the application of LC photoaligning for new, multi-layered photonic devices has resulted in the development and fundamental studies of many photoalignment mechanisms. Four of them are distinguished and extended here. The first corresponds to the photochemical reversible *cis-trans* isomerization in azo-dyes containing polymers, monolayers, and pure dye films. The second mechanism is based on pure reorientation of the azo-dye chromophore molecules or azo-dye molecular solvates due to diffusion under the action of polarized light. While the third and fourth experience topochemical crosslinking in cinnamoyl side-chain polymers, and photodegradation in polyimide materials, respectively. Processes involving azo-dyes present reversible transformations, while the other require irreversible photochemical changes [42]. In this thesis, I exploited photochemical reversible cis-trans isomerization in azo-dyes containing pure dye films (first mechanism), the so-called photoisomerization. The reversible transformation of LC's alignment along with the high purity of thin ALs suitable for multilayer integrated photonic devices, determined the choice of the mechanism.

1.4.2.2 Photoisomerization

Photoisomerization controls the LC alignment by a conformational change between *cisoid*- and *transoid*-type azobenzene functional units [38]. The principle of LC alignment by photoisomerization is shown in Figure 1-17. Azobenzene based materials exhibit strong, selective photosensitivity, and undergo photochemical isomerization transforming from their *trans*-state to the *cis*-state under subsequent illumination by UV–visible polarized light [38,43]. As the *trans*-isomers preferentially absorb UV and blue photons polarized parallel to their molecular axis, the conformation of the N = N bond changes at the centre of the molecules and transform into its *cis*-state [44]. The important phenomenon here is the absorption of the photons which depends on the angle between the molecular axis of azo-compounds and the polarization of electric field. Azobenzene molecules absorb photons the most when parallel to the electric field, and none when perpendicular to it. This results in an axis-selective anisotropic absorption and reorientation of the molecules. Thus, azo-molecules whose transition moments are parallel to the electric field of the exposed light change their conformation because of their anisotropic absorption. An azobenzene molecule whose molecular long axis is parallel to the polarization axis of the exposed light reversibly changes its conformation isomerizing *transoid*-type molecules to the *cisoid*-type which has a small absorbance for the polarized light of that orientation [45]. *Cis*-isomers are shorter than the *trans*-isomers [45](0:6 nm against 1 nm), and have different dipole moment and, hence, refractive index. Then *cisoid*-type molecules relax back into the more stable *transoid*-type with its molecular long axis orientation to be altered randomly, (Angular Hole Burning model [46,47]), through either a spontaneous relaxation or a reverse photoisomerization process [48]. The lifetime of the *cis*-state is molecule dependent, but it is, in general, relatively short lived (~ 1 s).

By addressing the azobenzene molecules with linearly polarised light for a sufficiently long time, photoisomerization cycle from *transoid,* to *cisoid,* and then back to *transoid*-type, will continue until all the molecules are oriented perpendicular to the light polarisation and they do not absorb photons anymore [42]. Therefore, the number of *transoid* molecules whose axes are perpendicular to the polarization axis increases in relative terms, and the injected LC layer becomes aligned along the molecular axis, which is perpendicular to the polarization axis.

Step 1:

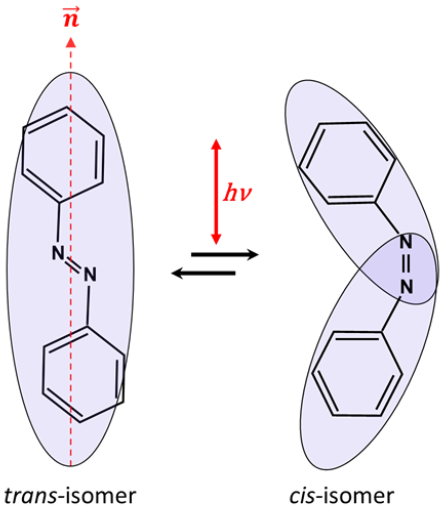

isomerization

Step 2:

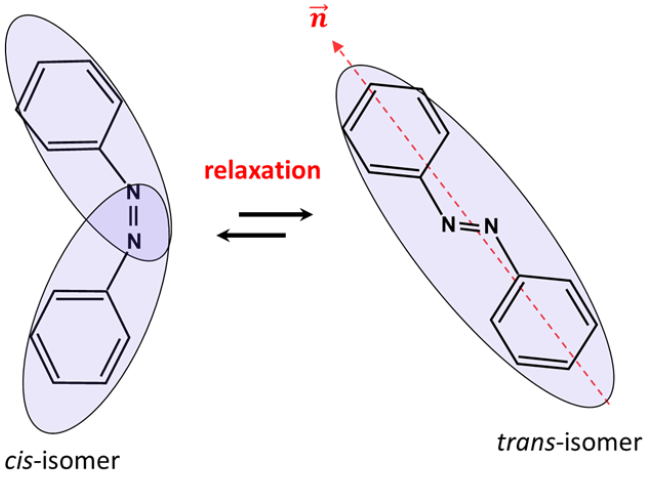

reorientation

Step 3:

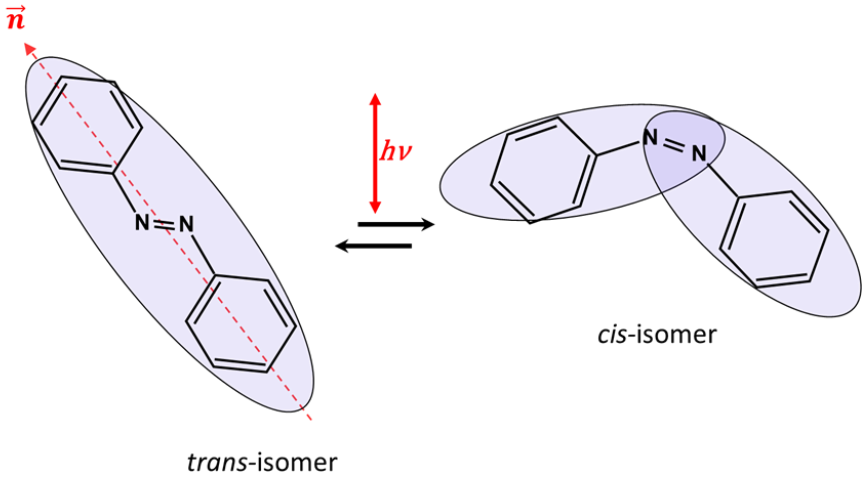

isomerization

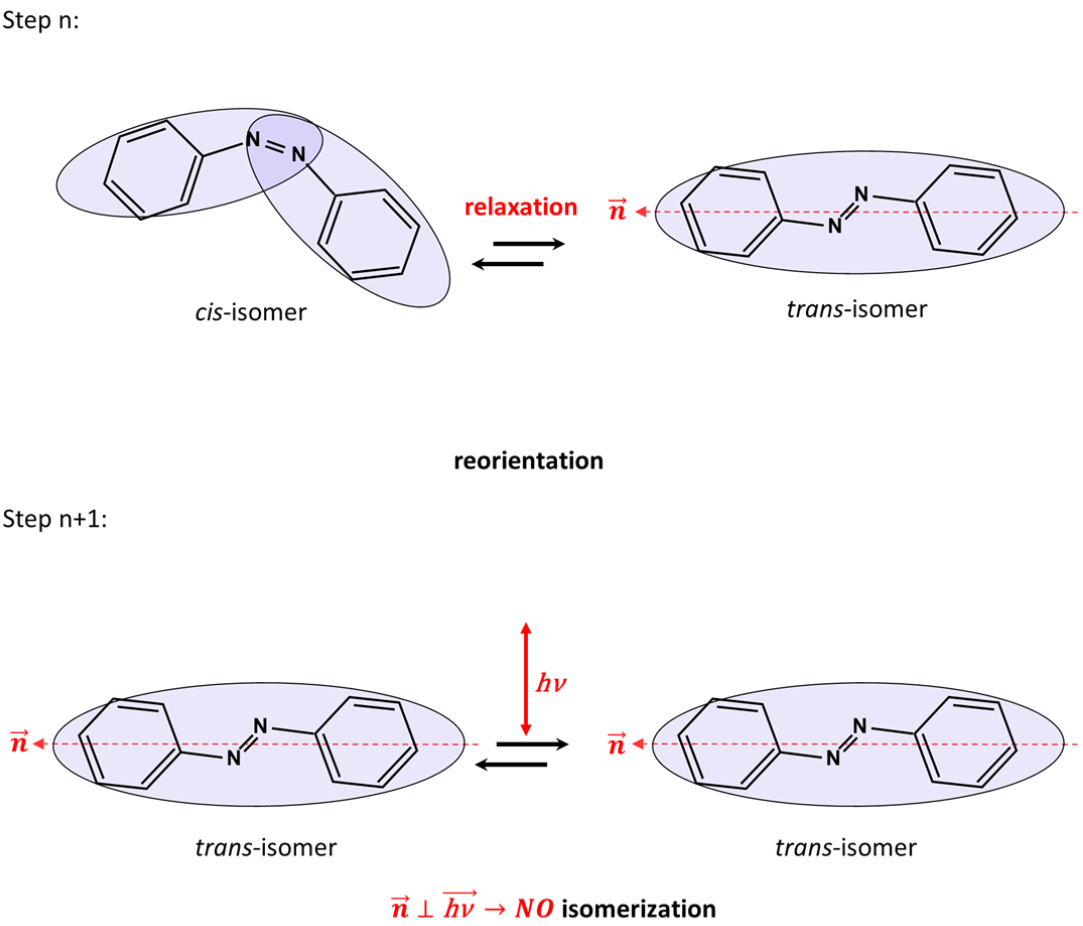

Figure 1-17 Principle of photoisomerization in-plane LC alignment

In fact, the probability that the *trans* molecules are transferred to the *cis*-state under illumination is proportional to $\cos^2\theta$, where θ is the angle between the long axis of the molecules and the polarization axis of the incident light. This means that the highest probability to isomerize is when the molecules are oriented parallel and lowest when the molecules are oriented perpendicular to the polarization of the light.

The axially anisotropic photoisomerization alone is sufficient to control the LC alignment in few seconds (<10 s) [49]. LC molecules are homogeneously aligned perpendicular to the direction of the laser polarization and remain aligned in the absence of the laser light. Furthermore, photoisomerization is a reversible process that can achieve many reproducible cycles, by changing the polarization of light. Figure 1-17 shows switching in-plane alignment of LC when the linear polarisation of light is switched from being along the x-axis to y-axis. Ichimura et al. [31] have shown that the effect of *cis-trans* isomerization is very important in many cases. The application of photo-optical regulation of LC orientation in waveguide structures [50,51], photoaddressing [52], and photorecording [53] has been proposed.

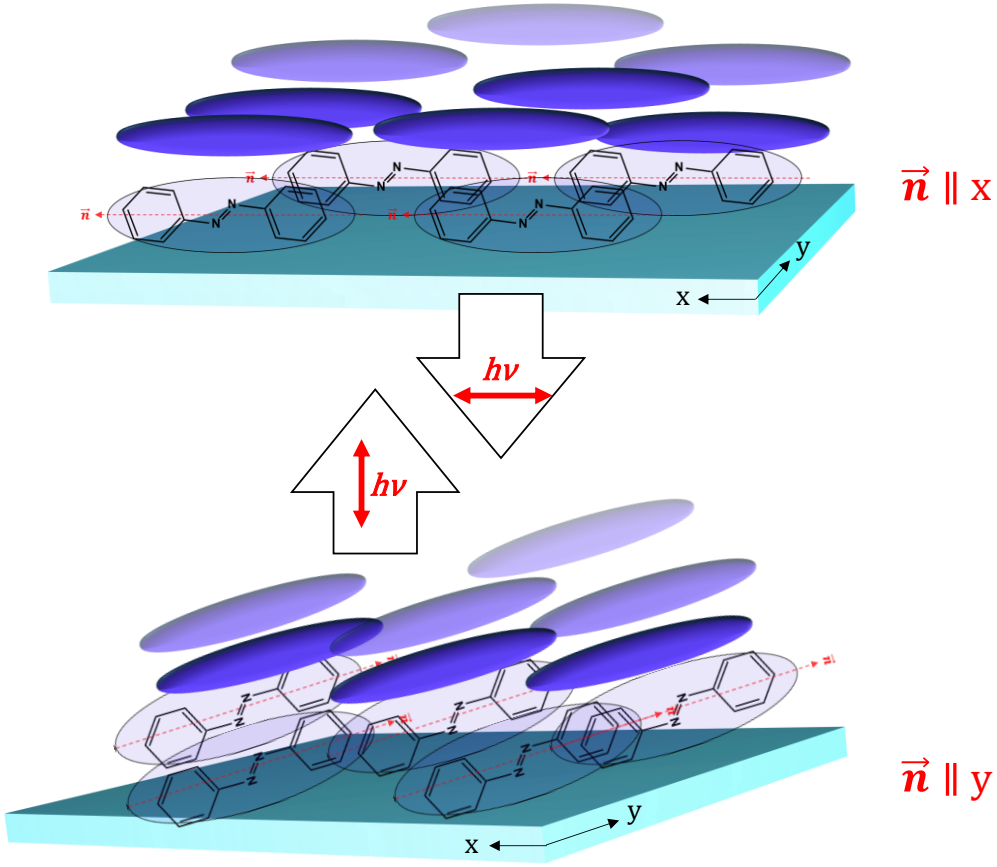

Figure 1-18 In-plane reorientation of nematic LC exploiting the reversible photoisomerization of azobenzene dye molecules. Top schematic illustrates a planar alignment of LC towards the x axis, while bottom schematic shows a planar alignment towards the y axis. Alternating polarisation of incident light results in a reversible orientation process perpendicular to it.

1.5 Summary

A LC is a phase of matter that combines the properties of both liquids and crystals. There are different liquid crystalline phases, depending on the degree of molecular order. In this work only nematic LCs are considered. This is the least ordered phase in which molecules are free to flow but demonstrate orientational order. This produces anisotropy of their electrical, and optical properties. An alignment in a nematic sample can be induced either by the surfaces (by special treatment of the boundary substrates) or by applying an external magnetic or electric field. When the alignments induced by the field and surfaces are orthogonal to each other, an effect known as Fréedericksz transition occurs in the cell. At a low field, surface-induced alignment is maintained in the sample by bulk elastic forces. The alignment preferred by the field is induced only when the field strength is higher than a threshold value.

The nematic phase can be described by the continuum theory, which deals with the nematic director, i.e. the unit vector that describes the preferable molecular orientation in the sample. There are three possible deformations of the director: splay, twist, and bend. Any of these distortions, or the influence of the external fields, are characterized by a contribution to the free energy functional. An equilibrium distribution of the director field corresponds to a minimum in the free energy.

An aligned nematic sample shows a birefringence effect. It is characterized by two refractive indices along and across the nematic director. It is possible to observe LC birefringence by placing a thin nematic sample between two crossed polarizers. This underlines the optical method of detecting LC reorientation. Any deviation of the nematic director in the sample causes a change in the refractive index encountered by the extraordinary polarized wave. This leads to a change in the phase lag between the ordinary and the extraordinary waves. Variation of the phase lag causes oscillations in the intensity of the laser beam that passes through the LC sample placed between two crossed polarizers, which can be detected experimentally. Moreover, the possibility to control LC alignment creates a sample with controllable optical properties. This has enabled LCs to find wide application in a variety of opto-electronic devices.

The most common way to align LCs is by mechanical rubbing of the surface. Rubbing creates microgrooves which promote a well defined orientation of the molecules on the substrate surface. However, rubbing must take place prior assembling the LC cell, stays fixed neglecting the possibility to reorient, and generates dust and static electricity. An alternative technique, photoalignment, has emerged from the appearance of the photoinduced optical anisotropy and dichroic absorption in thin pure dye films. Photochemical reversible *cis-trans* isomerization in azo-dyes, is the mechanism of photoalignment explored in this thesis. The method of repeated *cis-trans* photoisomerization reaction resulting in the reorientation of the backbone structure of azobenzene molecule, is used to introduce in-plane alignment to LCs exploiting UV and visible linearly polarised light.

Chapter 2

Characterisation of The Optical Properties of Liquid Crystal Cells

This chapter concentrates on describing experimental methods that are used in this thesis to fabricate LC cells and investigate their optical properties. Furthermore, it includes modelling and fitting methods used to obtain the optical properties of LC cells. It starts with the properties of LC materials mainly used in this work, however more details about each material can be found in the relevant chapters. The fabrication techniques for LC cells and the experimental methods of determining the cell characteristics, such as cell thickness and LC alignment, are included in Section 2.2. Part of this work has been published as: **Wide area mapping of LC devices with passive and active command layers.** Bennett, T., Proctor, M., Forster, J., Perivolari, E., Podoliak, N., Sugden, M., Kaczmarek, M. & D'Alessandro, G. (2017). Applied Optics, 56(32), 9050-9056. & **Two-dimensional snapshot measurement of surface variation of anchoring in LC cells.** Perivolari, E., D'Alessandro, G., Apostolopoulos, V., Brouckaert, N., Heiser, T., & Kaczmarek, M. (2021). *Liquid Crystals*, 1-11. The fabrication of LC cells, measurements, and data fitting were done by myself, I acknowledge help of Dr Nina Podoliak with sample fabrication in the first work. Other co-authors contributed with advice and/or to supervision and writing of the article.

2.1 Properties of Liquid Crystal Materials

A commercially available nematic LC, E7 (Merck Ltd.), is used in most in this thesis. E7 nematic LC is a mixture of four types of cyanobiphenyl molecules, whose content and molecular

structure is presented in Figure 2-1. It consists of 51% of 4-cyano-pentyl-4'-cyanobiphenyl molecules, 25% 4-cyano-4'-n-heptyl-bipheny, 16% of 4-cyano-4'-n-oxyoctyl-biphenyl and 8% 4-cyano-4"n-pentyl-p-terphenyl. The main component (51%) of E7 consists of 4-pentyl-4'-cyanobiphenyl (commercial name, 5CB) nematic LC molecules, which is a widely used material as mentioned earlier in Section 1.2.2 and Figure 1-4. E7 is more suitable for use in the experiments compared to 5CB, because it has a wider temperature range for the existence of the nematic phase. This extended temperature range has emerged from the addition of the other components. The nematic state of E7 exists at room temperature and specifically between -10°C and 59.8°C, while 5CB nematic phase exists between 22.5°C and 35.3°C. Below -10°C E7 crystalizes and reaches the crystalline (solid) phase, while over 59.8°C (the so-called clearing point temperature) it reaches the isotropic (liquid) phase transforming into a clear liquid from the milky diffractive one. At the lower temperatures (<-10°C), E7 molecules might inhabit one or more phases with significant anisotropic orientational structure and short-range orientational order while still having an ability to flow. While heating over the clearing point, will eventually drive E7 molecules into a conventional liquid phase characterized by random and isotropic molecular ordering (little to no long-range order), and fluid-like flow behaviour.

Table 2-1 presents some characteristics of the nematic E7, including the elastic constants, refractive indices, diamagnetic anisotropy, and dielectric constants. The relatively large anisotropy of refractive indices ($\Delta n = (n_e - n_o) \sim 0.22$, where n_e, n_o are the extraordinary and ordinary refractive index, respectively), is one of the key properties we exploit in this work.

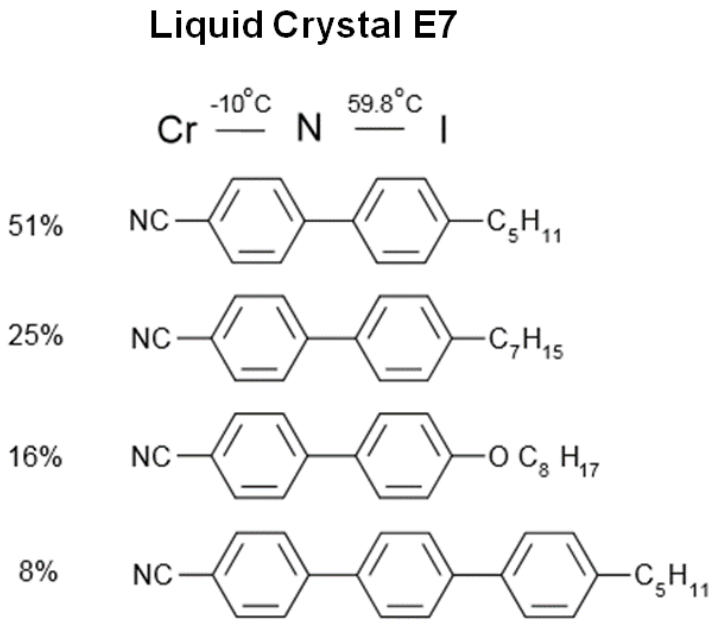

Figure 2-1 Molecular structure of nematic LC mixture E7.

Table 2-1: Material properties of nematic E7

		Liquid Crystal; E7	
Elastic constants,	K_1	11.2 [54]	
$\times 10^{-7}$ erg/cm	K_2	6.8 [54]	
	K_3	17.8 [55]	
Refractive indices,			
at 633 nm ($T = 25°C$)	n_o	1.5289 [56]	
	n_e	1.7305 [56]	
at 589.3 nm ($T = 25°C$)	n_o		1.7472*
	n_e		1.5217*
at 532 nm ($T = 25°C$)	n_o	1.5268 [56]	
	n_e	1.7512 [56]	
Dielectric constants,	$\varepsilon_\perp$	5.17 [57]	5.1*
	$\varepsilon_\parallel$	19.54 [57]	19.3*
Diamagnetic anisotropy,	χ_α	$\sim 10^{-7}$ [1]	

* E7 characteristics taken from Merck data sheet.

In this thesis, other nematic LCs were used, namely 1825 [58] and QYTN-004 [59]. LC 1825 is a complex mixture that was prepared only for THz applications and provided by the Faculty of Advanced Technologies and Chemistry in Military University of Technology in Warsaw. The mixture 1825 is a complex mixture of isothiocyanate compounds with fluorine atoms substituted in the lateral position and phenyl rings. There are also acetylene bridge group (C ≡ C) between benzene rings and one compound possess cyclohexane ring. For the synthesis of high birefringence LCs for THz applications, complex mixtures of LC molecules are required as suggested by Herman et al. On the other hand, the LC material under the commercial name QYTN-004 was produced by Qingdao QY Liquid Crystal Co and used in a side project on this thesis. The key optical property of QYTN-004 is its low reorientation voltage threshold which helped us to test our characterization methods. Characteristics of LCs 1825 and QYTN-004 will be discussed later in Chapters 4.5.1 and 2.4.2.2, accordingly.

2.2 Liquid Crystal Cells

The LC cells used in the experimental investigations of this thesis consist of two glass or quartz substrates covered with an AL, and a thin layer of LC in between them, as demonstrated in Figure 2-2. Both glass substrates were already covered with a thin layer of conductive ITO layer as electrode for potential voltage application. Two LC alignment techniques were investigated in this work, the rubbing and photoalignment techniques. Therefore, we used two different ALs for each technique.

For the rubbing we used polyimide with the commercial name Pyralin PI 2525 from HD Microsystems. The solution of PI 2525 was diluted in solvent 1methyl-2-pyrrolidinone with ratio 1:10 and then was spin coated on the glass substrate with 3000 rpm steady rotational speed to form a uniform film. To stabilize the polymer layer and evaporate the excess of solvent, the coated substrate was baked on a hot plate at 225 °C for 1 hour and left to cool down for another hour. After that, PI 2525 coated glass substrates were rubbed with a velvet cloth using a traditional rubbing machine (as described in Section 1.4.1) which allows precise control of the rubbing direction with respect to the edges of the substrate. Rubbing produces microgrooves on the PI 2525 layer which promotes the alignment of LCs in this direction. The two substrates were joined together in such a way that there were antiparallel rubbing directions on the opposite sides of the cell, as Figure 2-3 shows. This technique ensures a uniform planar alignment inside the cell without defects and twist deformations.

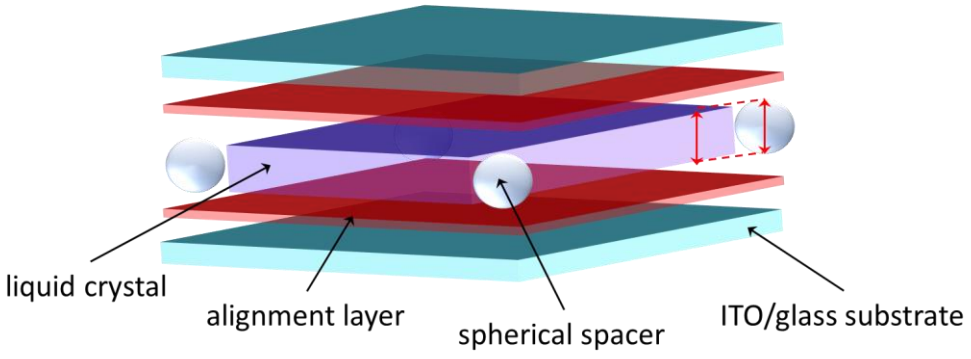

Figure 2-2 Schematic illustration of the LC cell structure.

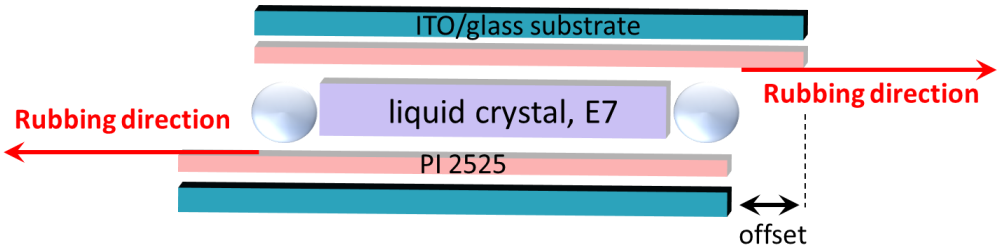

Figure 2-3 Anti-parallel rubbing direction on the opposite sides of the LC cell to ensure a uniform planar alignment.

The thickness of the LC layer is set by the size of the glass bead spacers, which was defined either 6 μm, 12 μm, or 20 μm. We dispersed spacers in ultra-violet (UV)-curing glue (Norland Optical Adhesive 61) and placed few drops on the corners of one PI 2525 coated substrate, which is then covered with second one. The two substrates are gently pressed together to obtain a monodispersed layer of spacers. The shape of the spacers is very important for the thickness uniformity since there is the possibility of aggregation during deposition which will double the thickness locally. For this reason, we used spherical spacers which are less likely to stuck together. Uniformity of the thickness gap can be controlled by just observing the interference fringes. The cell is then exposed to UV light to cure the glue.

We offset the coated substrates, as evident from Figure 2-3, not only to attach electrodes but also to fill the gap with LC. The cells are filled with LC in the isotropic phase. For this, the cell was placed on a hot stage, heated above the clearing temperature, and then filled using capillary forces. When the hot stage is switched off, the cell stays on it as it slowly cools down to room temperature. The slow cooling process ensures that there is no redistribution of molecules in LC suspensions during transition to the nematic state. In some cases, the cells are filled at room temperature with LC materials in the nematic phase. No difference in the alignment and cell homogeneity is detected in cells filled either in isotropic or in nematic phases. Each cell is then sealed around the edges with epoxy glue to prevent the LC leaking out.

With photoalignment we used a similar procedure. The photoaligning layers used in this study are based on azo-coupling of the diazonium salt of 4,4'−diaminobiphenyl−2,2−disulfonic acid with the derivatives of phenol and aniline having different numbers and positions of such pendants as -chloro, -hydroxy, -alkyl, -carboxyl groups or in the phenol ring or at the nitrogen atom in aniline. Specifically, we investigated the photoaligning azobenzene dyes (PAAD) either in powder form or in ready solutions produced by BEAM Co. Thin PAAD films were spin coated on ITO glass substrates and annealed on a hot stage for 10 minutes. Each coated substrate was then exposed to linearly polarized light to introduce the desired orientation of the PAAD molecules which will promote the alignment of LCs in this direction. Preparation and exposure

of PAAD thin films is covered in detail later in 0. The cells were assembled the same way as described earlier in this section.

2.2.1 Cell Thickness Measurement

To determine the cell thickness, I illuminate it with white light and collect the transmission through the cell which then is directed to a spectrometer (Ocean Optics USB4000) [2]. The transmission spectrum comprises fringes characteristic of a Fabry-Pérot optical cavity. Briefly, interference between the multiple reflections of light between the two partially reflecting surfaces causes transmission to vary for different wavelengths. Here, constructive interference occurs if the transmitted beams are in phase, and this corresponds to a high-transmission peak of the etalon (antinode). If the transmitted beams are out-of-phase, destructive interference occurs, and this corresponds to a transmission minimum (node). The transmission spectrum of the cell as a function of wavelength is shown in Figure 2-4. The wavelength of the spectrum maximum satisfies the condition [2]:

$$\Delta S = m_i \lambda_i, \tag{2.1}$$

where m_i is an integer. The difference between numbers m_i and m_{i+1} corresponds to the neighbouring maxima. The thickness of the cell is then related to the wavelength by [2],

$$d = \frac{m\lambda}{2n} \Leftrightarrow 2nd = m\lambda \tag{2.2}$$

For an empty cell, $n = n_{air} = 1$, and hence from Equations (2.1) & (2.2) we derive the relation between the optical path and the cell thickness which is [2]:

$$\Delta S = 2d. \tag{2.3}$$

From the wavelength dependent transmission maxima (say, λ_1 and λ_2) and number of interference cycles between λ_1 and λ_2, d can be calculated from:

$$d = \frac{m}{2n}\frac{\lambda_2\lambda_1}{\lambda_2 - \lambda_1}, \tag{2.4}$$

From the example of Figure 2-4, $\lambda_1 = 0.510\ \mu m$, $\lambda_2 = 0.574\ \mu m$, $m = 4$ and $n = 1$, so that d is calculated to be $9.148\ \mu m$. The forth maxima (i.e. λ_2, m=4) was chosen as an example. The result will be equivalent for another integer.

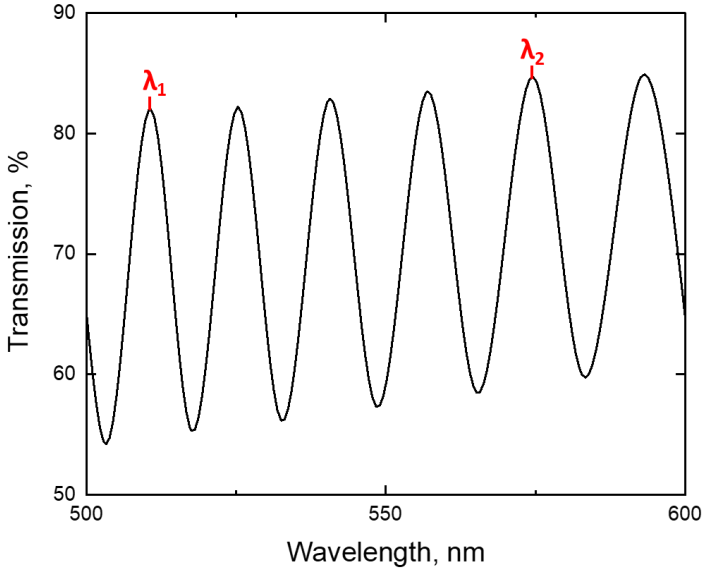

Figure 2-4 Transmission spectrum of the empty cell. Transmitted beams interfere beyond the cell, which appears in the spectrum as maxima and minima. To calculate the cell thickness, two transmission maxima with the wavelength λ_1 and λ_2 are selected from the spectra.

2.2.2 Quality of Liquid Crystal Alignment

After filling the cell with the LC material, we can inspect the alignment quality by observing the cell between two linear, crossed polarizers. Planar alignment of LC molecules indicates that the image of the crossed polarizers will change from uniform bright to uniform dark. When director is parallel or perpendicular to the polarizer's axis, then incident light encounters only one refractive index, either the extraordinary, n_e, or the ordinary, n_o, respectively. This polarization will be then blocked by the second polarizer which results in a dark cell image, as shown in Figure 2-5.

When the planar cell is neither parallel nor perpendicular to the polarizers but placed at some angle (other than 0° or 90°), the light experiences two refractive indices, the ordinary, n_o, and extraordinary, n_e. Passing through the LC, the two polarizations become out of phase and in general emerge as elliptically polarized light. Some light can therefore pass through the second polarizer, creating a bright multicoloured image. Similarly, when a twisted alignment is introduced in the cell the image of the crossed polarizers will change when the cell is rotated with respect to the polarizers' axes. In order to obtain a bright image, each alignment side of the cell must be parallel to the corresponding polarizer. There incident light passes through the first polarizer, is rotated throughout the cell, and finally passes the second crossed

polarizer too (see Figure 2-6). Otherwise, a dark image will occur since incident light after passing the first polarizer will remain unchanged after the cell and finally be blocked by the second polarizer [11]. Alignment defects such as non-uniformities in the nematic alignment, Schlieren textures (see Figure 1-5 & Figure 1-6), disclination lines, uncured glue, or dust particles are visible as bright, dark, or multicoloured nonuniform regions or spots on the crossed polarized image.

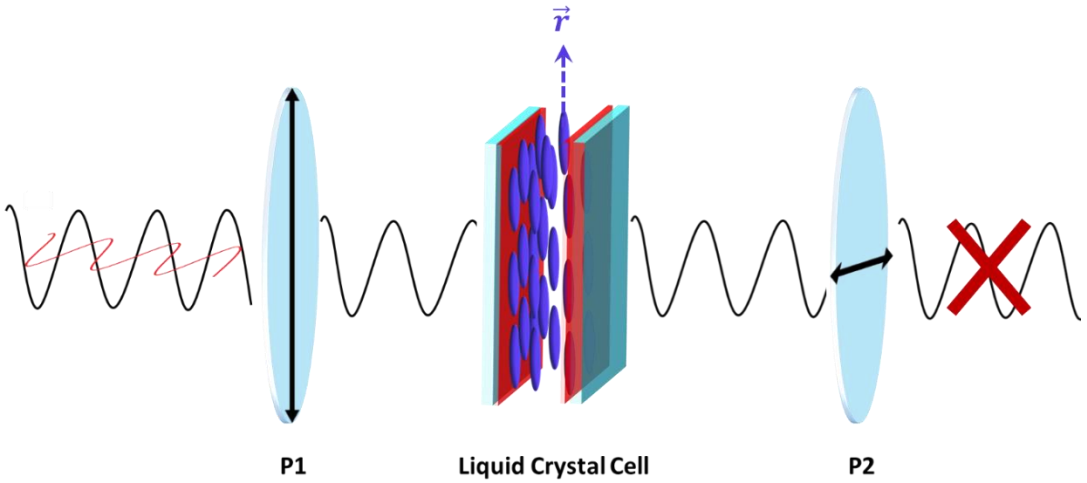

Figure 2-5 Schematic of the set up for observing the quality of planar LC cell between crossed polarizers. Director of nematic LC is parallel to the first polarizer's (P1) axis allowing the incident light to pass through the cell. After passing the first polarizer light will remain unchanged after the cell and finally be blocked by the second polarizer (P2).

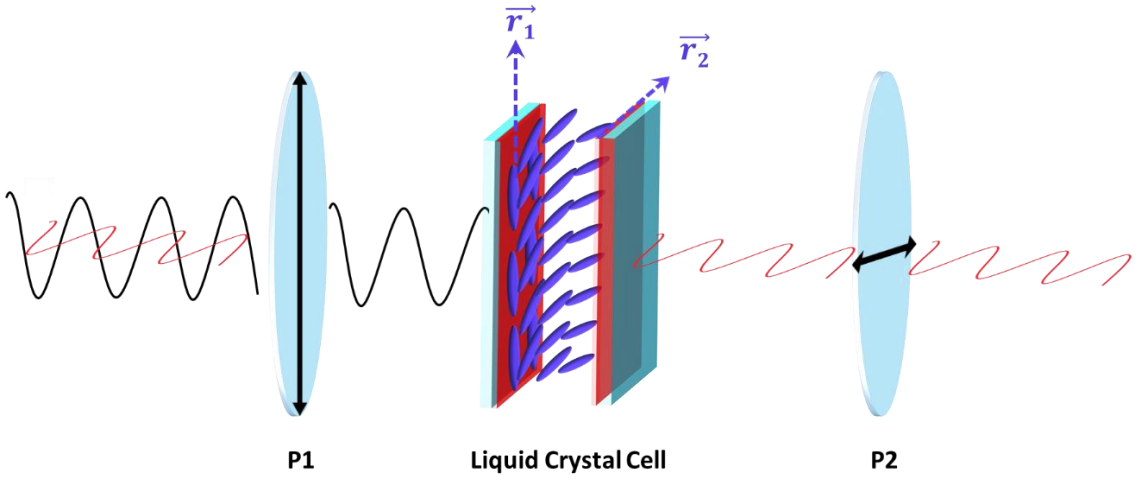

Figure 2-6 Schematic of the set up for observing the quality of a twisted LC cell between crossed polarizers. Director of nematic LC is parallel to the first polarizer's (P1) axis allowing the incident light to pass through the cell. After passing the first polarizer light will rotate polarization triggered by the twisted LC molecules and finally transmit through the second polarizer (P2).

2.3 Optical Measurements

Optical measurements in this work involve the Fréedericksz transition experiments with an AC electric field, essential when LC devices are fabricated. Furthermore, the geometry of the cell and its LC-related properties, e.g., the thickness, elastic constants, and the pretilt angle, can be characterised can be measured by several techniques. For example, it is possible to obtain extremely accurate measurements of the gap thickness of an empty cell using interferometric methods in which the cell acts as a Fabry–Perot optical cavity (see Section 2.2.2). However, this is bound to change during the filling process and during storage. While it is possible to measure variations in the LC thickness of a filled cell by simply shining white light through cross-polarizers, this measurement is unable to separate the effect of thickness variation from other effects, e.g., pretilt angle, change of anchoring energy, and deposition of surface charges. A very commonly used method to measure the cell thickness, elastic constants, and the pretilt angle, consists in measuring the Cross-Polarized Intensity (CPI) of a monochromatic light beam passing through the cell as a function of the voltage applied to the cell [1,6].

2.3.1 The Fréedericksz Transition Experiment (Cross-Polarized Intensity Experiment)

The response of LCs to an electric field was investigated by measuring the electric field-induced Fréedericksz transitions. The Fréedericksz transition is the transition from a uniform director configuration to a deformed director configuration due to application of a magnetic or electric field. As the field value is gradually increased higher than Fréedericksz transition, the director begins to rotate until its aligned with the field (see Section 1.3.2).

Here, the Fréedericksz transition experiments with an applied AC electric field are performed on the cells with the same LC mixture(E7), but with different thicknesses, different ALs (PI 2525, PAAD), and different wavelengths. They were carried out to determine the quality of LC cells with regards the thickness uniformity, the alignment uniformity, pretilt angle, and the anchoring energy. Determining such parameters was crucial for a complete characterization of LC devices used for this thesis. This will be discussed in detail in 0 .

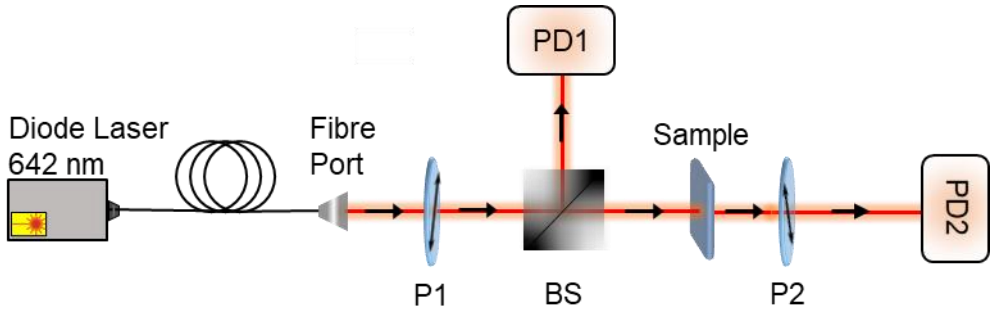

Figure 2-7 Schematic representation of the experimental setup for detecting electric field-induced Fréedericksz transition. Arrows on the polarizers (P1 and P2) indicate their polarization axes.

The experimental setup is presented in Figure 2-7. The LC cell is placed between two crossed polarizers (P1 and P2), oriented at 45° with respect to LC alignment director, where the monochromatic light enters at normal incidence. A light beam from a fibre coupled diode laser is launched through a fibre port connector which collimates the beam. Here, we show a laser wavelength of 642 nm, but other wavelengths can easily be selected by attaching a different laser to the fibre port. After propagating through the cell, the light beam is collected by a photodiode (PD2). For reference, we also monitor the intensity of light with another photodiode (PD1) just before the cell by exploiting a beam splitter (BS). The cross polarized intensity (CPI) is recorded depending on the AC voltage applied to the cell. For this, we used an Agilent 33120A waveform generator generated an AC electric field at 1kHz and with 1% accuracy in the measurement of the amplitude. The cell had conductive ITO layers that served as electrodes, so voltages at rate 1 mV/s from 0 V to 10 V were applied to the cells. An example of the normalized CPI curve measured in the nematic E7 cell is shown in Figure 2-8.

An AC voltage is applied to the cell to reorient the LC. The two polarization components of the incident light experience different phase delays when passing through the LC cell. As a result, the beam output polarization may change, causing the CPI to vary as a function of the liquid alignment and, hence, of the voltage applied to the cell. The intensity at zero field in both curves depends on maximum of the phase lag induced by the planar alignment LC layer between ordinary and extraordinary beams: $\delta = 2\pi d(\Delta n)/\lambda$, where $\Delta n = n_e - n_o$ is the birefringence of LC and d is the cell thickness. The intensity curves start to oscillate at the Fréedericksz threshold fields, at which the beginning of the LC reorientation happens. The threshold voltage in the electric field, V_F, is determined by the LC properties i.e., dielectric anisotropy ε_α, and the elastic constant K_1), as defined by Equations (1.15) and (2.5).

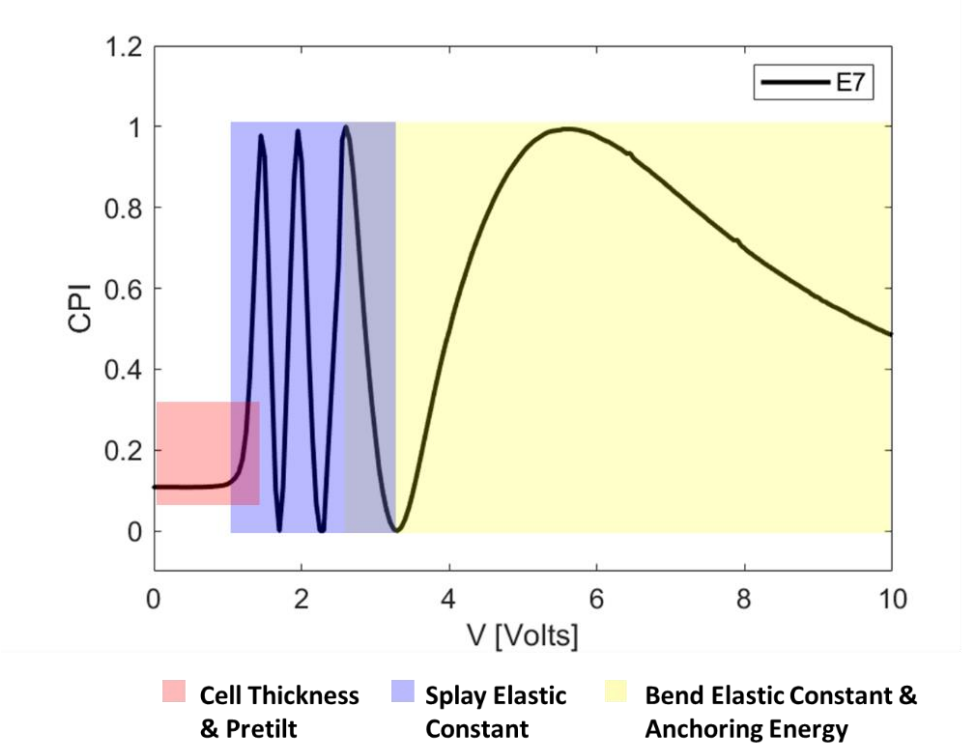

Figure 2-8 Crossed-polarized intensity as a function of the applied voltage for an E7 cell. Shaded areas indicate which parts of the curve is more sensitive to the corresponding parameters. The LC thickness is 12 µm.

$$V_F = \pi \sqrt{\frac{K_i}{\varepsilon_0 |\varepsilon_\alpha|}}. \tag{2.5}$$

The transition takes place at relatively low voltages of ~0.9 Volt. This is because the dielectric anisotropy of LC E7, which is relatively large as can be seen from Table 2-1:

$$\varepsilon_\alpha = \varepsilon_\parallel - \varepsilon_\perp = 14.4 \tag{2.6}$$

As the electric field is applied LC twists away from its initial planar direction towards the electric field and as a result the polarization of the light that exits the cell, varies allowing it to either get blocked by the second polarizer or passed through. Above the threshold voltage, this gives rise to maxima and minima intensity outputs measured and recorded by the photodiode. The complete reorientation requires a voltage of approximately 10 Volt. The complete reorientation of the LC appears as a slow reduction of the CPI to zero with increasing field.

The region below the Fréedericksz transition is mainly sensitive to the LC thickness d and the pretilt angle θ_0. The splay elastic constant K_1, plays a role in the region near Fréedericksz transition, while the bend elastic constant K_3, controls the high voltage part of the curve. The residual intensity at high fields is also associated with the anchoring effects at the cell boundaries because at $V \gg V_F$ regime, the director, except close the boundary layers, is aligned by the electric field. As a result, the Fréedericksz transition and CPI variation with AC filed experiment allows us to estimate the splay and the bend elastic constants (K_1 and K_3), the cell thickness d, and the pretilt angle θ_0. K_1 can be evaluated using the threshold voltage value, V_F. K_3 defines the rate of the LC reorientation towards the homeotropic state at a high field. The higher value of K_3 results in the slower process of reorientation, which appears in the larger spacing between the intensity oscillations in curve $I_\perp$ (V) (1.28). The exact values of K_1 and K_3 can be found by fitting the experimental cross-polarized intensity curve using a numerical model described in the next section.

2.3.2 Modelling and Fitting the Cross-Polarized Intensity (CPI)

In this section a numerical model and fitting procedure of electric field-induced Fréedericksz transition in nematic cells is described. The model is based on continuum theory which was introduced in Section 1.2.2.

Briefly, upon application of an external field, nematic LCs will undergo deformation in its bulk. Twist, splay, and bend are the main types of director axis deformations for nematics. According to the theory first developed by Frank [10], the free-energy densities associated with these deformations are given by K_1, K_2, and K_3 which are the splay, twist, and bend Frank elastic constants, respectively. The induced external field will create more than one forms of deformation and so the total distortion free-energy density is given by Equation (1.28),

$$F_d = \frac{1}{2}K_1(\nabla \cdot \hat{n})^2 + \frac{1}{2}K_2(\hat{n} \cdot \nabla \times \hat{n})^2 + \frac{1}{2}K_3(\hat{n} \times \nabla \times \hat{n})^2. \qquad (2.7)$$

This expression is the fundamental formula of continuum theory, which will be used in this thesis to fit the experimental cross-polarized intensity curve.

We model the LC alignment in the planar nematic cell using the Frank-Oseen theory [9,10]. We neglect the LC fluid motion, since only smoothly varying high frequency voltages are applied to the LC when measuring the CPI [60]. The ALs are parallel to the (x_1, x_2)-coordinate plane, while the x_3 axis is into the cell. We assume that the cell lateral variations are large with respect to the LC relaxation length so that the director n is a function only of the coordinate into the

cell, $\hat{n}$. We parameterize the LC orientation by the tilt angle $\theta(x_3)$, that the director field forms with the ALs. With this notation we can write the director field as,

$$\hat{n} = [cos(\theta), 0, sin(\theta)]. \tag{2.8}$$

The equation for the alignment of the LC cell takes the form [61]:

$$\begin{aligned} \gamma_1 \frac{\partial \theta}{\partial t} \;=\; & \frac{\partial}{\partial x_3} \left\{ \left[\frac{K_1}{2} [1 + cos(2\theta)] + \frac{K_3}{2} [1 - cos(2\theta)] \right] \frac{\partial \theta}{\partial x_3} \right\} \\ & + \frac{1}{2} sin(2\theta) \left[(K_1 - K_3) \left(\frac{\partial \theta}{\partial x_3} \right)^2 + \varepsilon_0 \, \varepsilon_\alpha \left(\frac{\partial \psi}{\partial x_3} \right)^2 \right], \end{aligned} \tag{2.9}$$

where, γ_1 is the LC rotational viscosity, K_1 and K_3 are the splay and bend elastic constants respectively , ε_0 is the vacuum permittivity, $\varepsilon_\alpha = \varepsilon_\parallel - \varepsilon_\perp$ is the dielectric anisotropy of the nematic LC, with $\varepsilon_\parallel$ and $\varepsilon_\perp$ the component of dielectric permittivity tensor parallel and perpendicular to the director, respectively.

The electrostatic potential $\psi(x_3)$ is given by the first of Maxwell's equations, which, in this geometry, can be written as:

$$\frac{\mathrm{d}}{\mathrm{d}x_3} \left[\left(1 + \frac{\epsilon_A}{\epsilon_\perp} sin^2[\theta(x_3)] \right) \frac{\mathrm{d}}{\mathrm{d}x_3} \psi(x_3) \right] = 0. \tag{2.10}$$

This can be solved explicitly [62,63] as:

$$\psi(x_3) = \int_0^{x_3} \frac{V}{1 + \frac{\varepsilon_\alpha}{\varepsilon_\perp} sin^2[\theta(\xi_3)]} \, d\xi_3 \left[\int_0^d \frac{1}{1 + \frac{\varepsilon_\alpha}{\varepsilon_\perp} sin^2[\theta(x_3)]} \, dx_3 \right]^{-1}, \tag{2.11}$$

where V is the, possibly time dependent, rms voltage applied to the cell and d is the cell thickness. The Rapini-Papoular [64] alignment conditions on Equation (2.9) are:

$$+ \left[\frac{K_1}{2} [1 + cos(2\theta)] + \frac{K_3}{2} [1 - cos(2\theta)] \right] \frac{\partial \theta}{\partial x_3} = \frac{W_d}{2} sin\big[2\big(\theta - \theta_0(0)\big)\big], \tag{2.12}$$

$$- \left[\frac{K_1}{2} [1 + cos(2\theta)] + \frac{K_3}{2} [1 - cos(2\theta)] \right] \frac{\partial \theta}{\partial x_3} = \frac{W_R}{2} sin\big[2\big(\theta - \theta_0(L)\big)\big], \tag{2.13}$$

at $x_3 = 0$ and $x_3 = d$ respectively. In these equations $\theta_0(0)$ and $\theta_0(d)$ are the AL preferred alignment direction at $x_3 = 0$ and $x_3 = d$ respectively. Similarly, W_d and W_R are the surface polar anchoring energy coefficients at $x_3 = 0$ and $x_3 = d$ respectively.

Lastly, we define the CPI to be the ratio between the output and input intensity, so that it is normalized in the interval (0, 1). Hence, the CPI is given by:

$$I(V) = sin^2\left(\frac{\pi}{\lambda}\int_0^d \left[n_0 - n_{eff}\big(\theta(x_3)\big)\right] dx_3\right) \tag{2.14}$$

where $n_{\text{eff}}(\theta)$ is the effective refractive index seen by the component of polarization in the plane of the director,

$$n_{eff}(\theta) = \frac{n_e n_o}{\sqrt{{n_o}^2\, cos^2(\theta) + {n_e}^2\, sin^2(\theta)}}. \tag{2.15}$$

Here, n_o and n_e are the optical ordinary and extra-ordinary refractive indices, respectively.

The model in Equation (2.9), has been integrated numerically in MATLAB using a spectral collocation method to discretize space [65], and an implicit variable step algorithm (MATLAB routine ode15s) to integrate in time. The solution of the electrostatic equation, Equation (2.11), and the CPI integral in Equation (2.14) were computed using a Clencurt quadrature [65]. The boundary conditions Equations (2.12)**Error! Reference source not found.** and (2.13) were solved using an approximate solution in the limit of very strong or very weak anchoring or using a Newton solver for the director at the boundary in all intermediate cases. The code was validated by successfully comparing its results with the output of a finite element implementation of the model in COMSOL Multiphysics. The alignment Equation (2.9) was implemented as a General Form PDE with a boundary flux source given by Equations (2.12)and (2.13), while the electrostatic Equation (2.10) was solved numerically using the Electrostatic module. We have not used the analytical solution of this equation, given by Equation (2.11), to ensure that the two codes were maximally independent.

After evaluating the profile of the director orientation inside the cell as described above, the optical properties of the LC are then calculated by the fitting procedure. We use the following fitting procedure for a single CPI trace, as the one shown in Figure 2-8. First, the algorithm detects all the minima and maxima and from their number obtains an approximate LC thickness. Then it fits the low voltage part of the curve (up to the first extremum) using the LC thickness and the pretilt angle as fitting parameters, while keeping the given values for elastic constants fixed. Refractive indices and dielectric constants of the LC are assumed known. These

can be either taken from the LC data sheets or measured separately. After that, we fit the whole CPI trace, taking the already found values for d and θ_0 and using K_1 and K_3 as fitting parameters.

2.4 Fully-Automated Optical Systems for Large Scale Characterisation of Liquid Crystal Cells

LCs are a material of choice in many optical devices such as displays, optical light modulators, LC light valves, diffractive waveplates and diffraction elements, waveguides, soliton channels, and lenses, to name a few [37,66-73]. In all these devices, it is essential that the geometry of the cell and its LC-related properties, e.g., the pretilt angle, are uniform across a wide area. In the case of the display industry, many steps are taken to ensure that this uniformity is reached, but in many smaller scale applications, the only viable solution is to check and monitor the uniformity and occasionally discard devices that do not satisfy appropriate quality requirements. It is therefore important to be able to easily check the wide area properties of a LC device and also to monitor its stability in time. This is a key issue also for more exotic and experimental LC devices that may include LCs doped with particles [74-77] or active ALs that may, for example, be light sensitive [78-80]. In this case, it is important not just to measure and monitor uniformity, but also to be able to do it in situ, with a minimally invasive procedure.

There are many techniques to measure some of these properties. For example, it is possible to obtain extremely accurate measurements of the gap thickness of an empty cell using interferometric methods in which the cell acts as a Fabry–Perot cavity (see Section 2.2.1). However, this is bound to change during the filling process and during storage. While it is possible to measure variations in the LC thickness of a filled cell by simply shining white light through cross-polarizers (see Section 2.2.2), this measurement is unable to separate the effect of thickness variation from other effects, e.g., pretilt angle, change of anchoring energy, and deposition of surface charges. Similarly, it is possible to use the crystal rotation method [81] to measure the pretilt, but this procedure is rather cumbersome, and it is nontrivial to obtain accurate pretilt maps. Finally, it is possible to use fluorescent confocal polarizing microscopy to obtain reliable maps of the LC alignment throughout a cell [82,83]. This is an exquisite procedure but not easy to do and requires specialized equipment and powerful computational methods.

For developing and optimising the performance of LC devices, it is important to determine the fundamental parameters of a LC material. For example, it is only through using an accurate

model that it is possible to separate the effect of pretilt and cell-gap thickness on the polarization of the light passing through a LC cell. Elastic constants have been measured and explored through different techniques, such as, for example, using the voltage induced Fréedericksz threshold in untwisted and twisted cells [84]. Another very commonly used method consists in measuring the cross-polarized intensity (CPI) of a monochromatic light beam passing through the cell as a function of the voltage applied to the cell, as discussed in Section 2.3.1.

2.4.1 Wide Area Mapping of Liquid Crystal Devices

Reliable two-dimensional maps of the device properties were obtained by a simple method based on CPI measurements at multiple locations on the surface of the device. The method provides a snapshot of device optical quality and provides a quick and precise procedure to monitor its reliability. The relevant experimental setup is presented below, in Figure 2-9.

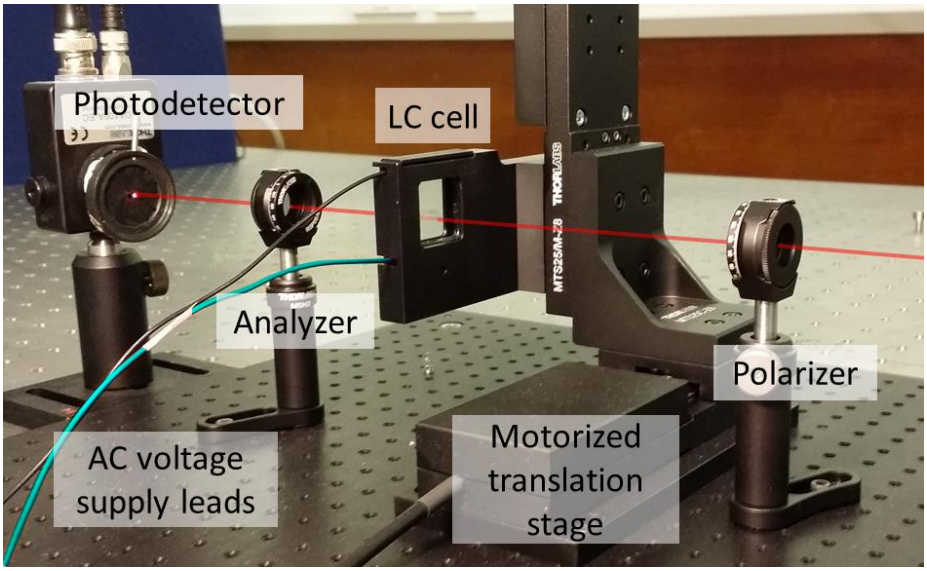

Figure 2-9 Experimental set-up to measure the CPI at different locations of a planar LC cell. The polarizer and analyser are perpendicular to each other and at 45° to the LC alignment. The motorized, computer-controlled translation stage allows us to define the area of the cell to be examined.

A light beam (1 mm beam spot size) emitted by a He–Ne laser with 632.8 nm wavelength passes through a polarizer oriented at 45° to the director alignment and enters the LC cell at normal incidence. After propagation through the cell, it passes through a second polarizer, at 90° to the first, and hits a photodiode that measures its intensity. An AC voltage is applied to the cell to reorient the LC. The two polarization components of the incident light experience different

phase delays when passing through the LC cell. As a result, the beam output polarization may change, causing the CPI to vary as a function of the liquid alignment and, hence, of the voltage applied to the cell (as described in Section 2.3.1).

The CPI as a function of voltage is measured by applying a 10 kHz AC voltage to the LC cell and ramping the voltage peak-to-peak amplitude from 0 to 20 V in incremental steps of 0.1 V. At each voltage step, the experiment controlling software analyses any transient effects by monitoring the CPI, waits until the value saturates, and then takes and averages the intensity reading over 1 s. The average CPI is recorded as a function of the rms amplitude of the applied voltage.

The cell is mounted on an assembly of two motorized translation stages from Thorlabs that move it with respect to the light beam in the plane of the cell, so that the same CPI measurement can be taken at different locations. Once the intensity has been measured for every voltage amplitude at one location on the cell, the cell is translated, and the measurement is repeated at another location in order to map the LC thickness and pretilt across the whole cell area.

Temperature plays an important role at this stage. It is crucial to keep the temperature constant for the duration of the experiment in order to have accurate estimates of the LC parameters. Although we did not use a dedicated, temperature stabilized cell holder, we took some precautions to control the ambient temperature around the set-up. Using just a simple holder allowed us to assess how critical it was to fix the temperature very precisely. We concluded that because only low laser power was required, it did not change the temperature of the sample during a single set of measurements in any considerable way. However, we note that there may have been variations in temperature between measurements for different samples.

The experiment is fully controlled by a specially developed software in MATLAB, which performs experimental apparatus control, data acquisition, and subsequent fit as described in Section 2.3.2. The software graphical user interface allows setting a range of AC voltages and coordinates on the cell surface where the measurements are taken. This technique is designed to be applicable to any prototype LC device consisting of a planar LC layer of sufficient thickness to fulfil the half-wave retardation condition for the probe wavelength. This condition, while not essential, makes the measurement procedure more robust because of the large achievable variation in the light polarization as a function of the applied voltage.

2.4.1.1 Multiple cross-polarised intensity traces

A standard LC E7 cell, in anti-parallel planar alignment was used to test our setup, as the one illustrated in Figure 2-3. We followed the procedure outlined earlier to measure the thickness, the pretilt angle, splay, and bend elastic constants across the surface of E7-PI cell.

Multiple traces are measured across the surface of the cell to obtain reliable uniformity maps with the aid of the translation stage. In particular, we measured CPI at 48 different location spots on the surface of the cell, and hence there are 48 different traces characterising the LC cell. Figure 2-10 presents the CPI traces for the 48 different sampling spots across the surface of a E7-PI cell. Although the sample size was 2 x 2 cm^2, we capture a smaller central area of the sample to avoid fabrication imperfections i.e. epoxy glue around the edges of the cell. The spatial resolution emerged from the 48 sampling spots in the smaller area (17.5 x 12.5 mm^2), is 2.2 mm along x axis and 2.1 mm along y axis. This allows us to consider each sample point in the cell as independent from its neighbours and, hence, to apply the model derived in Section 2.3.2 to each of them individually.

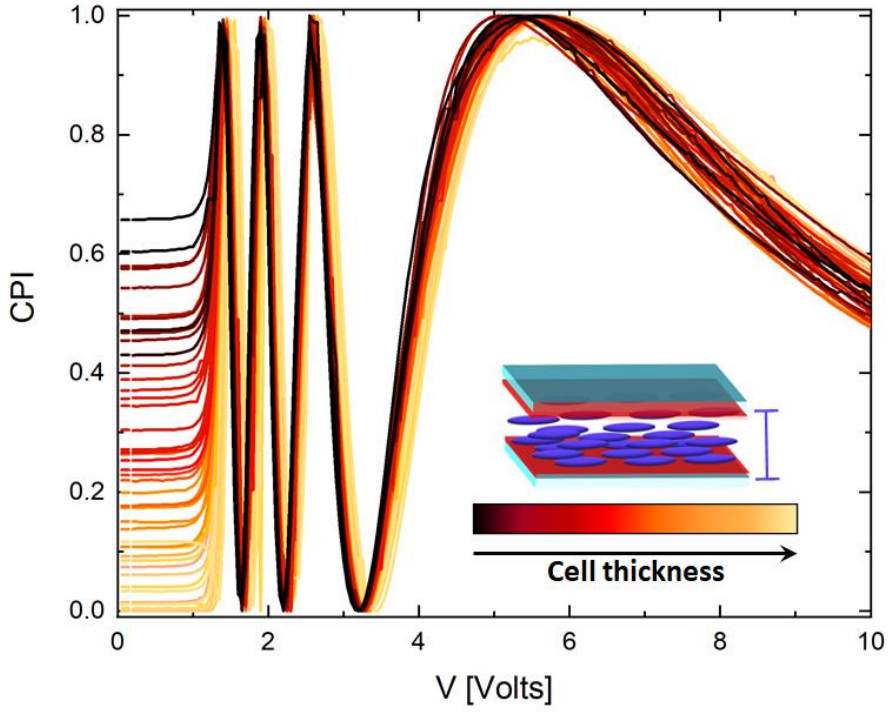

Figure 2-10 CPI as a function of the applied voltage for an E7-PI cell. Multiple traces are measured across the surface of the cell to obtain reliable uniformity maps. The LC thickness is ~12 μm. Colour map shows the variation of thickness measured at the different spots at the cell's surface. Black colour stands for the thinner areas while yellow for thicker ones, usually spotted at the edges of the cell.

In Figure 2-10 we see that CPI goes through maxima and minima as the applied voltage increases and that they approach limiting values in the high voltage region. This is because LC molecules are reoriented by the electric field and hence causes the cell to behave as a phase retardation plate. For V>10 V, all molecules are reoriented parallel to the electric field's polarization, thus no phase difference exists between the ordinary and extraordinary rays at high voltages. When applied field is reduced, partial relaxation of the molecules occur towards the initial planar alignment and optical anisotropy appears again. The first maximum (starting from the high voltage end) of the CPI curve is identified with an absolute phase retardation of π at a specific voltage (~5.4 V). Thereafter, the other extrema correspond to integral multiples of π for the phase difference of δ and consequently can be used to determine the uncertainty of $N\pi$ for V < 5.4 V. Starting from high voltage side of data plotted in Figure 2-10, the extrema can be assigned to phase differences of π, 2π, 3π, etc.

Following this procedure, we find that N=7 at the threshold voltage, $V_F \sim 0.9$ V where CPI first begins to increase. The total phase difference produced by this cell is then given by:

$$|\delta| = (N+1)\pi - 2\,tan^{-1}\sqrt{\frac{I_\perp}{I_\parallel}}, \tag{2.16}$$

where, $I_\perp$ and $I_\parallel$ correspond to perpendicular and parallel orientations of the analyser relative to the polariser given by [85].

The cell thickness is already known approximately from direct measurement to be ~ 12 μm (see Section 2.2.1). However, for a filled cell with nematic E7 it might vary. The starting point of the CPI curve is determined by the initial phase lag, that is, in the zero pretilt approximation, $\delta_{max} = 2\pi d(n_e - n_o)/\lambda$. There, we can estimate the cell thickness variation at the different sampling spots from the relatively large birefringence of E7 ($\Delta n = n_e - n_o = 0.22$). Although, the phase lag uncertainty of about 0.7π, results in cell thickness uncertainty of 1 μm which is obvious for $V < V_F$, as demonstrated in Figure 2-10 by a colour map. Colour variations show the change of thickness measured at the different spots at the cell's surface. Black colour stands for the thinner areas while yellow for thicker ones, usually spotted at the edges of the cell. This is a direct consequence of the phase lag, which is larger for thicker LC areas, as discussed above. Therefore, by plotting multiple CPI traces we can have a first approximation of cell thickness uniformity. It is clear from our data that we have a small variation since the number of extrema remains N=7 for all traces.

To obtain the two-dimensional uniformity maps of thickness and pretilt angle, we performed statistical data analysis on the multiple CPI traces. For this we use the fitting procedure for a single CPI trace (see Section 2.3.2). Briefly, the program detects firstly all the minima and

maxima (N) and from their number obtains an approximate LC thickness. Then it fits the low voltage part of the curve (up to the first extremum) using the LC thickness and the pretilt angle as fitting parameters, while keeping the given values for elastic constants fixed. Refractive indices and dielectric constants of the LC are assumed known. These can be either taken from the LC data sheets or measured separately. After that, we fit the whole CPI trace, taking the already found values for d and θ_0 and using K_1 and K_3 as fitting parameters. The fitting procedure for multiple traces is an extension of the single trace algorithm as described in [60].

2.4.1.2 Results on wide area mapping of liquid crystal cells

I have followed the procedure outlined earlier and tested it with a planar cell filled with E7 nematic LC and PI as ALs. I have obtained reliable maps of the LC thickness and the pretilt angle, as well as the values of the elastic constants. Moreover, by performing a boot-strapping statistical analysis coupled with multiple measurements, I obtained error bars on all the measured parameters. This technique requires some prior information about the cell and the LC, for example, the type of alignment (planar, homeotropic, twisted, etc.), of LC (e.g., nematic, cholesteric), and its dielectric anisotropy (negative or positive) and birefringence. Its principles are, however, quite general and require "just" developing a new fitting model of the CPI. For example, here, I have used a Frank–Oseen model for the alignment of a nematic LC. A ferroelectric LC would require a different model, but other aspects of the methodology described here would remain unchanged. In particular, the statistical analysis discussed in [60] can be applied without any changes, provided that the temperature of the samples can be maintained constant. Therefore, even though the cell considered here is a planar one, there is no obstacle in principle to using different types of cells, e.g., twist. We will come back to this point in the conclusions.

A typical thickness map is shown in Figure 2-11(a) for a PI-E7 cell. As expected from the multiple CPI traces graph (see Figure 2-10), the thickness is smaller in the centre of the cell, probably due to the squeezing of the cell when sealing it. Figure 2-11(c) presents a typical example of a LC cell with a pretilt of approximately 3°. At first sight, the pretilt map look less structured than the thickness map. However, it is important to notice that the angle variation is very small. In this case for the PI-E7 cell, the variation is less than 1°.

The error maps, shown in Figure 2-11(b) and (d), indicate that the estimation error, both on the thickness, δd, and on the pretilt angle $\delta\theta_0$, are in general small and uniform: the thickness and pretilt variations are of the order of a few nanometres and a few tenths of degrees, respectively. The only glaring exception is the location at coordinates (5,2.5) mm. The much larger error at this location is not due to an imperfection in the cell (which is clearly absent in the plots on the left-hand side of this figure). It is caused, instead, by the limitation of fitting the

CPI. In the CPI trace shown in Figure 2-8, the value at V = 0 is well away from 0 and 1: a small perturbation of the cell or LC parameters (as in the bootstrapping procedure) will not qualitatively change this graph. However, in the case of the location at coordinates (5,2.5) mm in Figure 2-11(b) and (d), the CPI at V = 0 is very close to 1. A small perturbation can, in this case, create or remove a maximum from the CPI trace, thus changing the graph qualitatively. This perturbation significantly increases the error in the estimate, even though it remains small and does not affect conspicuously the mean, i.e., the thickness and pretilt plotted in Figure 2-11(a) and (c), respectively.

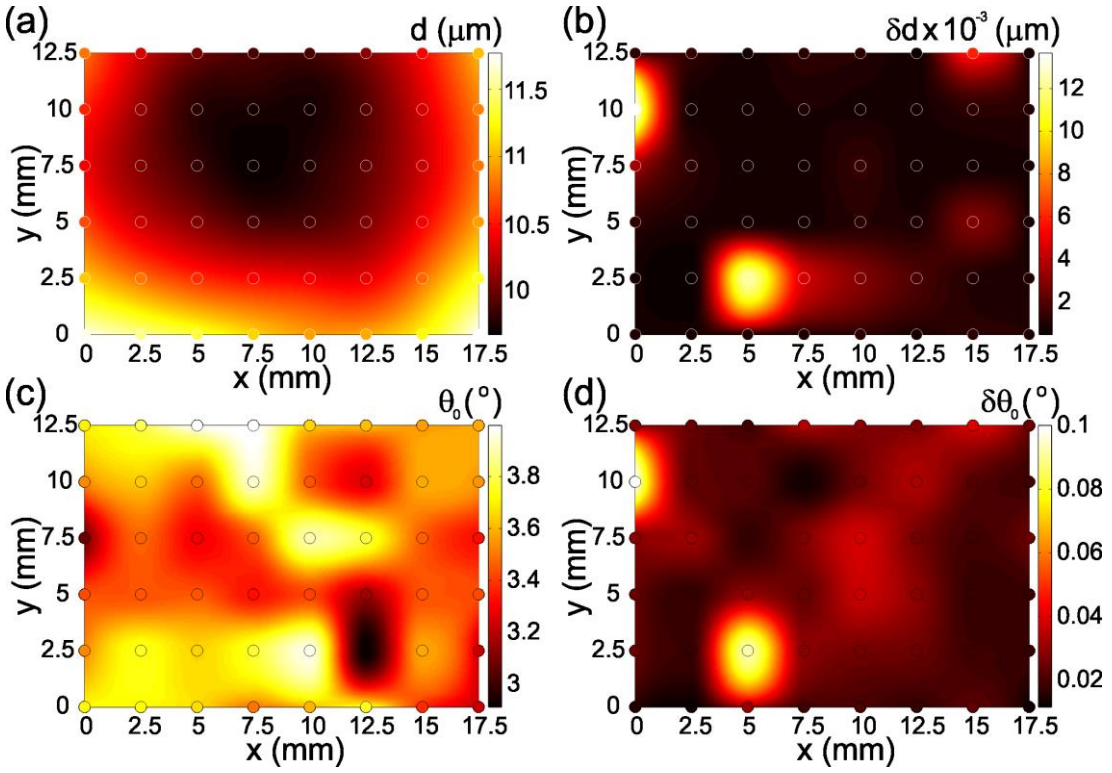

Figure 2-11 PI planar cell filled with E7: spatial map of the LC (a) thickness and (c) pretilt angle; (b) and (d) are the corresponding errors. Circles are the fitted values, and the background colour map is a piece-wise cubic interpolation between them.

Finally, the estimates of the splay and bend elastic constants and their errors are listed in Table 2-2. We discuss here only the case of E7, for which there is more literature material. Firstly, we note that the values of the E7 elastic constants are compatible with other estimates that have appeared in the literature, summarized in Table 2-3. The second observation is that the error estimates are smaller than the differences in the values of K_1 and K_3 that I have measured or that have been reported in the literature. This is caused by the fact that there are many systematic errors that are not included in the measurement process. Four errors are discussed here as examples.

Table 2-2: Splay and Bend Elastic Constants Measured for the E7-PI Cell

LC cell	K_1 [pN]	K_3 [pN]
E7-PI	10.7 ± 0.02	16.2 ± 0.03

The first is temperature. Applying a standard error propagation technique to the temperature dependence formulas [86] for K_1 and K_3 shows that a 1°C temperature variation around room temperature induced a percentage error in $K_{1,3}$ of more than 1%. Another effect is that the glass slides of the cell form a Fabry–Perot cavity: changing the alignment of the LC moves the light in and out of resonance with the cavity and, hence, modulates the CPI. Because the LC thickness is not uniform, the cell sides are curved: they are nearly parallel in the cell centre but more at an angle near the cell boundaries. Hence, the quality of the Fabry–Perot cavity and, therefore, the CPI modulation, are position dependent.

The third effect to consider is more significant for the measurements of K_3. As illustrated in Figure 2-8, this parameter is determined by the large voltage amplitude part of the CPI trace. For these voltage values, most of the LC in the bulk is aligned with the electric field, and the only significant alignment variations are near the boundaries. It is likely that surface effects, like surface anchoring energy, charge deposition, and dust, affect these measurements more significantly than those of K_1, whose value is determined by the LC deflection in the bulk.

Table 2-3: Some Literature Values for the E7 Splay and Bend Elastic Constants

Reference	K_1 [pN]	K_3 [pN]
Raynes *et al.* (1979) **[57]**	11.7	19.5
Raynes *et al.* (2003) **[54]**	11.2	18.6
Trabi *et al.* (2008) **[87]**	10.5	15.2
Chen *et al.* (2015) **[88]**	10.8	17.5

The fourth and last effect is the role that the thickness of the polymer AL plays on the voltage dropped across the LC layer. The voltage amplitude V(t) that appears in Equation (2.11) is the voltage applied to the LC layer. However, the value used in the parameter fitting is the voltage applied to the whole cell, because this is the only parameter we can measure. In general, the two voltages are very close one to the other, because the polymer layer is extremely thin with respect to the LC layer. For example, for a PI cell, the two thicknesses are approximately 20 nm

and 12 μm. However, this may not always be the case. For example, in P3HT (photoconductive polymer layers) [89] cells, the equivalent of these two layers might have thickness of 100 nm and 6 μm, respectively. This implies that we are slightly overestimating the voltage applied to the LC layer in the P3HT cells and, hence, also the magnitude of the elastic constants, as confirmed by the values reported in Table 2-2.

At this point someone may ask: Why bother with the error bars reported in Table 2-2? The point I wish to make is that they are not an estimate of the error on the "true" value of the splay and bend elastic constant. They are, instead, a measurement of the reproducibility of the cell fabrication process, provided that the measurements are temperature controlled. If the fabrication process is such that the systematic errors are controlled, in the sense that they are the same for all cells, then we expect that the measured values of the elastic constants will fall within the estimated error bars.

2.4.2 Two-Dimensional Snapshot Measurement of Surface Variation of Liquid Crystals

Photoaddressable command layers for LCs with photoconductive [90-93], photoalignment [94-97] and, more recently photovoltaic layers [98-101], promise new application areas of LCs, e.g. in telecommunications and organic electronics. They also offer an increased level of control, such as the contactless LC alignment provided by photoalignment. This avoids the deposition of charge or dust on the substrates caused by rubbing. However, the photosensitivity of the cell command layers can also cause the pretilt and anchoring to change in the regions exposed to optical or electric fields [97,102,103]. This is particularly relevant for photoaligned LC cells, as the strength of anchoring can depend on the duration of light exposure [104]. There is, thus, a need for a quick and comprehensive characterisation technique and model to be able to map the uniformity of the cells, and their pretilts and anchoring energy on both surfaces, as well as monitor any changes with time or illumination.

There are many different methods reported in the literature to measure individual properties of LC cells. For example, their thickness and uniformity can be obtained by the wave retarder rotational method [105] or by the phase compensation method (PCM) [106]. The pretilt angle can be characterised by spectroscopic ellipsometry [107] or the crystal rotation method [108]. The measurement of the anchoring energy relies on various techniques, such as the light-scattering [109], the wedge-cell [110], the retardation vs. voltage (RV) methods [111], electrical measurements [112], as well as a reflective method [113]. Several of these experimental methods can only work if the LCs are placed in specially prepared cells and are not well suited to characterise more advanced LC devices, with different or multiple layers on

the substrates [114]. All of them address one single spot on the surface of the cell, or they assume that the cell has uniform properties.

To address these issues and obtain quick and reliable estimates of a gamut of LC parameters, I used a single spot measurement and obtain two-dimensional maps of a range of LC and cell parameters. The particular strength of our method presented in this chapter, is that it can capture, at the same time, the parameters that strongly influence the response of LCs to external fields, such as elastic constants, viscosity, cell thickness, pretilt, as well as weaker and finer parameters, such as the strength of polar anchoring. While subtle, polar anchoring plays a major role in applications, for example bistable displays [115], e-books [116], and biological sensors [117]. It is also at the heart of the new LC physics of particle-like LC configurations, like skyrmions and torons [118], that can form complex topological structurers.

In this project, I built on the previous work described in Section 2.4.1 [60,63] and extend it in two directions that are suitable to new LC devices and physics. First, I use the whole cell measurements to estimate the average polar anchoring energy. The second development direction addresses one of the defining features of modern photosensitive cells: they are often asymmetric, with different ALs on the input and output facet. Here, I restrict the consideration only to planar nematic LCs, but in principle, this method can be adapted to other LC alignments.

2.4.2.1 Optical Multi-Parameter Analyser (OMPA)

The measurements were performed with the aid of a fully packaged and bespoke optical setup that we call the Optical Multi-Parameter Analyser (OMPA). It performs a computer-controlled CPI measurements and real-time data analysis and fitting. For the fitting process, prior information about a set of complementary LC parameters, namely dielectric permittivities, and refractive indices, of the LC material is required. This is typically provided on LC specification sheets.

In order to verify the validity of our method, we measured three different LC cells that cover a range of LCs and ALs. Two of these samples were symmetric, i.e., with the same AL on both substrates (AL_x-LC-AL_x), while the third type was asymmetric, i.e., with different ALs (AL_x-LC-AL_y). In asymmetric cells in which one substrate is known, it is possible to use this method to estimate the pretilt and anchoring energy of the unknown substrate.

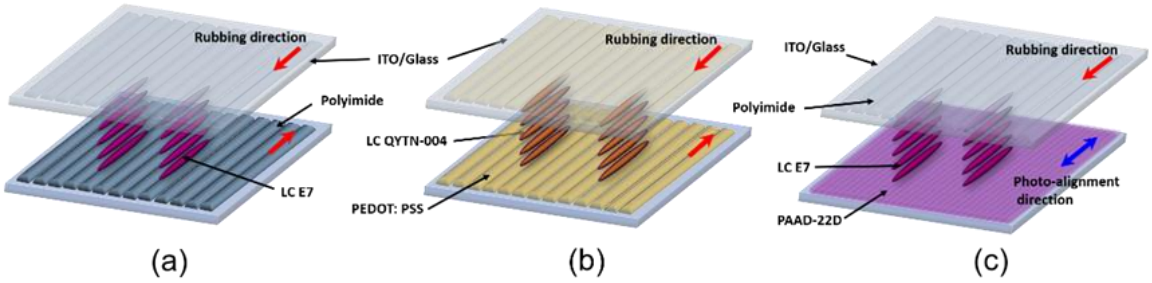

Figure 2-12 Sample schematics. (a) Planar symmetric E7 cell where both ALs are rubbed PI (PI-E7-PI). (b) Planar symmetric QYTN-004 cell, where both ALs are rubbed PEDOT: PSS (PEDOT: PSS-QYTN004-PEDOT: PSS). (c) Planar asymmetric E7 cell, where one AL is rubbed PI while the other is photoaligned PAAD-22D (PI-E7-PAAD22D).

Initially, a standard, reference LC cell was prepared consisting of the nematic E7, and two glass substrates coated with ITO conductive layers and with rubbed polyimide (PI), to produce an anti-parallel planar alignment of the LC (see Figure 2-12(a)). This technique ensures a uniform planar alignment inside the cell without defects and twist deformations. The substrates had size 2 cm x 2 cm and were held together with UV-cured glue. The thickness of LC layer was controlled by 6 μm spacers. The cells were filled through capillary forces with the LC in the isotropic phase and sealed along the perimeter of the cell. The choice of LC layer was driven by the availability in the literature of its physical, electrical, and optical properties so that we could benchmark our measurements and results.

Table 2-4: Description of the samples

Experimental samples	Liquid crystal material	AL 1	AL 2	Thickness (d), [μm]
Symmetric cell 1	E7	PI	PI	6
Symmetric cell 2	QYTN-004	PEDOT: PSS	PEDOT: PSS	6
Asymmetric cell 1	E7	PI	PAAD22D	7

As a counterpart to the standard LC nematic material and ALs (E7 and PI) used in the first test system that is known to have relatively strong anchoring energy, the second type of test cells included a less well-known LC mixture and AL. We used a LC with low reorientation voltage threshold, QYTN-004 from Qingdao QY Liquid Crystal Co. The two identical ALs consisted of a conductive polymer poly(3,4-ethylenedioxythiophene) polystyrene sulfonate, PEDOT:PSS (commercial name CPP105D) as AL, coated over ITO glass substrates. The sample area was 1

cm x 1 cm, and the thickness of LC was set by 6 μm spacers (see Figure 2-12(b)). PEDOT:PSS is a popular material used as an electrode in both the cells with flexible substrates [119,120] and in the cells with photovoltaic layers [121,122].

Finally, our third sample was an asymmetric LC cell. For reliability, we kept the nematic E7 as LC layer and PI as one of the ALs. The other was coated with a photoaligning azobenzene dye (PAAD-22D) provided by the Beam Co (see Figure 2-12(c)). PAAD materials were demonstrated as effective for LC alignment by one-step illumination with visible light [115]. To control the thickness of the LC layer we used 7 μm spacers. For clarity,

Table 2-4 summarises the specifications of the experimental samples.

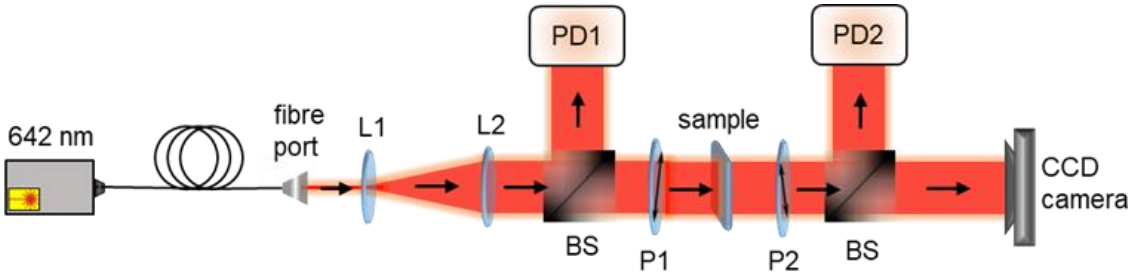

Figure 2-13 Experimental setup of the OMPA instrument. A fibre coupled diode laser at 642 nm passes from a fibre port into two lenses L1 and L2 which expand and collimate the beam. The sample is located between two crossed polarizers (P1 and P2), each at 45° to the director alignment, where the light enters at normal incidence. Photodiodes, PD1 and PD2 monitor the power of the laser before and after the cell by exploiting two beam splitters (BS). Finally, the light is incident on a CCD camera, which we use as spatial resolution detector. The entire setup is enclosed to reduce the background noise to the detectors and CCD camera and reduce thermal fluctuations.

The OMPA characterizes LC devices by measuring the CPI across the whole cell area as a function of the frequency and voltage amplitude applied to the cell. It provides the capability to capture a snapshot of the LC device with its ALs and determine its key properties. The experimental apparatus is shown in Figure 2-13. A light beam from a fibre coupled diode laser is launched through a fibre port connector which collimates the beam. Two lenses (L1 and L2) expand and collimate the beam in order to cover a wide area of the cell (diameter ~1 cm). Here, I have used a laser wavelength of 642 nm, but other wavelengths can easily be selected by attaching a different laser to the fibre port. The sample is located between two crossed polarizers, each at 45° to the director alignment, and the light enters at normal incidence. After propagating through the cell, the light beam is collected by a CCD camera. Data from neighbouring pixels are averaged so that the image collected has effective pixels of

approximately one millimetre in size. Over the 10 cm distance between the cell and the detector, diffraction expands the effective pixel diameter by less than 10%. Therefore, to a good approximation the CCD camera acts as a spatial resolution detector and each effective pixel corresponds to a single spot in the surface of the cell, allowing us to draw maps of the cell thickness, pretilt angle and of the anchoring energy. When the two polarization components of the incident light pass through the cell, they experience different phase delays that are function of the LC alignment. I change this by applying an AC voltage to the cell and measure the CPI as a function of it. I monitor the power of the laser before and after the cell using two beam splitters to redirect a fraction of the beam intensity to two photodiodes. Finally, the entire setup is enclosed to reduce the background noise to the detectors and CCD camera and thermal fluctuations. If needed, it is possible to enclose the LC cell in a temperature stabilised holder. This was not required for the measurements reported here, but it is essential when studying temperature effects on the LC parameters.

The experiment is fully managed by a MATLAB code [123,124], which controls the measuring apparatus, data acquisition and performs the data analysis using the model described in Section 2.3.2 [60]. OMPA collects pointwise data across the cell and fits the elastic constants, the pretilt angle, the anchoring energy, and the cell thickness.

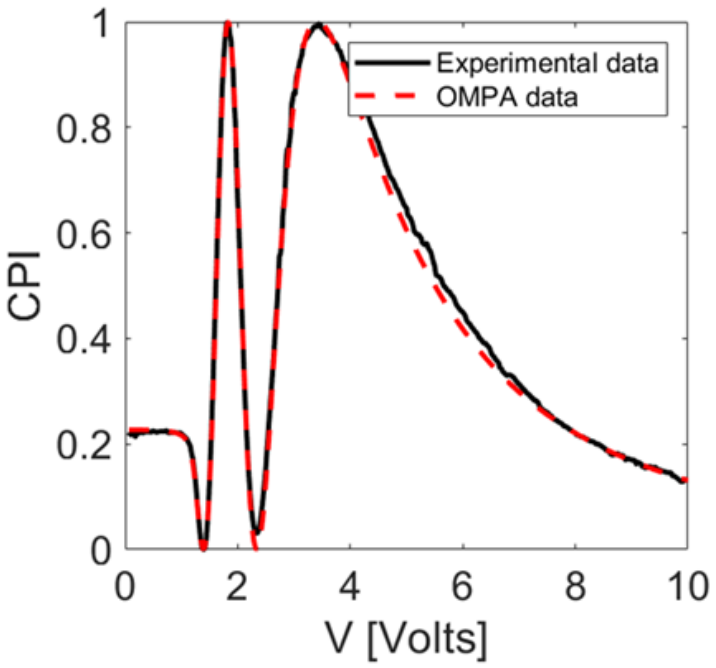

Figure 2-14 CPI trace for the asymmetric PI - PAAD-22D planar cell filled with E7. Parameter values: $K_1 = 11$ pN, $K_3 = 16.4$ pN, $\varepsilon_{\parallel} = 19.54$, $\varepsilon_{\perp} = 5.17$, $d = 7$ µm, $\theta_{PAAD} = 0.34°$, $\theta_{PI} = 1.9°$, $W_{PAAD} = 0.21\ mJ/m^2$, $W_{PI} > 1000\ mJ/m^2$, $\lambda =$ 642 nm, $n_e = 1.7287$ and $n_o = 1.5182$.

The fitting procedure is as follows. The cell thickness, pretilt, splay elastic constant and anchoring energy are fitted using the part of the CPI trace between 0 V and the first extremum. I then keep the cell thickness and pretilt fixed and fit all the other parameters using the entire trace. I use the MATLAB function *lsqcurvefit* to minimise the distance between the experimental and numerical CPI traces. The fitting of multiple traces is done in a similar manner [60,63].

The quality of the fit is determined by visual inspection of the traces (see Figure 2-14 for an example) and by estimating the error bars on the LC parameters, e.g. the elastic constants, that are measured at multiple locations (see Ref. [60,63]) for a detailed error analysis of the measurement process). I have also verified the impact of potential errors in the values of the LC dielectric permittivities and refractive indices. A 1% variation of any of these parameters produces changes in the fitted parameters by at most, 2%. In principle the OMPA can also detect a set of Leslie viscosities, but we do not demonstrate this feature in this paper since it is included in previous work [63]. The software graphical user interface allows us also to set the range of AC voltages and specify the region of the cell surface where the measurements are to be taken. In our experiment, the CPI as a function of voltage is measured by applying a 10 kHz AC voltage to the LC cell and ramping the voltage peak-to-peak amplitude from 0 to 20 V in incremental steps of 0.1 V. OMPA experimental apparatus is straightforward. It is seamlessly connected to the accompanying integrated model and code (described in Section 2.3.2), which in spite of its complexity, outputs the fitted parameters in clear and easy to follow way. Thus, the monitoring for any changes can be easily achieved.

2.4.2.2 Mapping anchoring, pretilt and thickness LC cells

We have analysed 3.5 x 3.5 mm2, and 7 x 7 mm2 areas of the two symmetric cells, PI - E7 (see Figure 2-15 (a and b)) and PEDOT: PSS - QYTN-004 (Figure 2-15 (c and d)), respectively. This translates into 5 x 5 and 8 x 6 points measured across the cell along the x and y axis. The spatial resolution emerged from the 25 sampling spots, is 0.7 mm along x and y axes, while for the 48 sampling spots, is 0.88 mm along the x axis and 1.2 mm along the y axis. These measurements show that the cell surface parameters, like the pretilt angle, vary over a millimetre scale, much larger than the LC relaxation length. This allows us to consider each sample point in the cell as independent from its neighbours and, hence, to apply the model derived earlier in this thesis to each of them individually.

Typical maps of the thickness and the pretilt angle of the PI-E7-PI cell are shown in Figure 2-15 (a, b). Here, we capture the edge of the cell where clearly thickness variation can be seen. The cell is thinner in the centre and thicker at the edges with a variation of 0.5 μm and average of 4.9 μm. This is most likely due to the excess of pressure applied in the centre of the cell when

sealing the edges. The fact that the LC thickness varies, highlights not only the difficulty on fabricating uniform LC cells, but also the importance of mapping the thickness profile. A similar behaviour is displayed by the thickness map of symmetric PEDOT: PSS – QYTN-004 sample (Figure 2-15 (c)). The cell is thinner in the centre and thicker at the edges, with a variation between 5.5 - 6 µm and average of 5.7 µm. These data should be compared with the spacer size used in these cells which is 6 µm for both samples.

The pretilt angle map of E7 (Figure 2-15 (b)) has an average value of 1.89° ± 0.06°, while Figure 2-15(d) presents the pretilt map of PEDOT: PSS – QYTN-004. A visual inspection of this cell showed that the alignment was only correct at the central part of the cell. This is confirmed by this pretilt map: in the inner region the pretilt is very uniform with an average value of 1.28° ± 0.08°. Outside this region, both the pretilt value and, more importantly, its fluctuations are larger, reflecting the poor visual quality of the cell there.

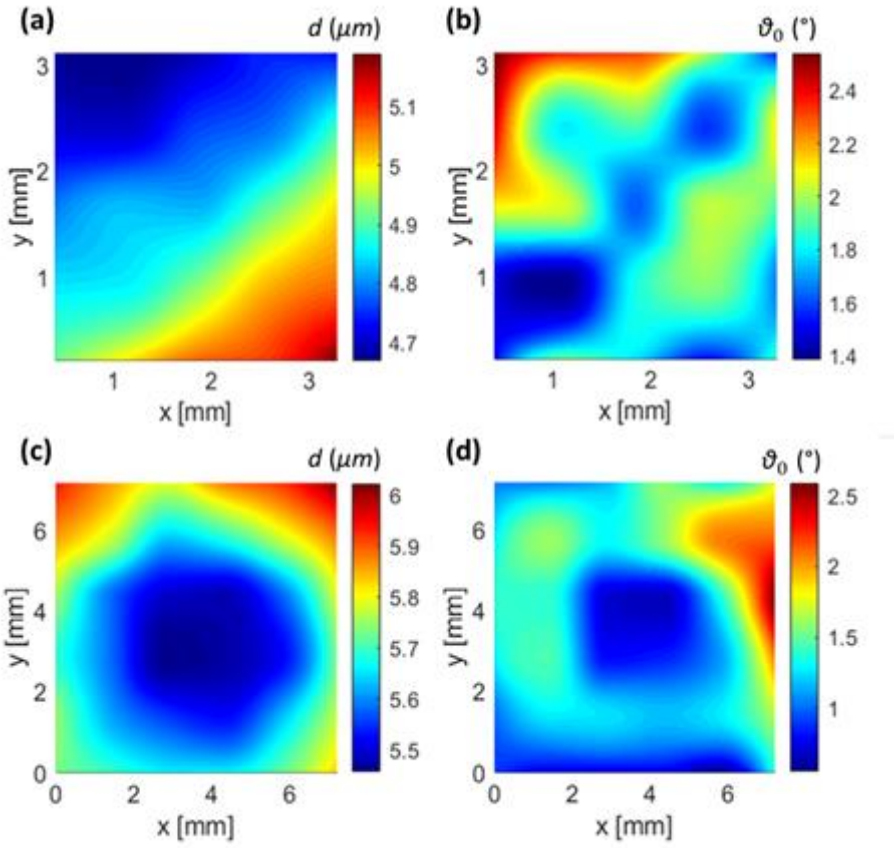

Figure 2-15 Spatial maps of thickness and pretilt angle of symmetric cells: (a) thickness and (b) pretilt angle maps of PI – E7 cell. (c) thickness and (d) pretilt angle maps of PEDOT: PSS – QYTN-004 cell.

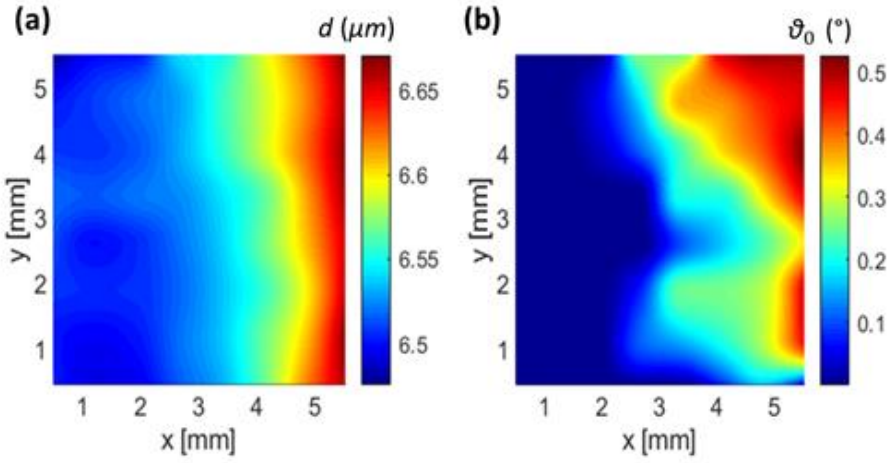

Figure 2-16 Asymmetric PI - PAAD-22D planar cell filled with E7: spatial map of the LC (a) thickness and (b) pretilt angle.

The CPI trace responds only to the average alignment properties of the cell. It is however possible to use it in an asymmetric cell, provided that one layer has already been characterised with the same LC as the one used in the asymmetric cell. Briefly, for an asymmetric LC measurement (AL_x-LC-AL_y), I fix the pretilt angle and anchoring energy of the known layer ALx and fit those of the unknown layer AL_y. This process is completely automated by the OMPA software. As it is ultimately a subtraction measurement, the error in this procedure is intrinsically higher than for a symmetric cell, but it allows the analysis of cells where one layer has to be different from the other, e.g. photovoltaic cells [125].

The asymmetric cell that I tested here, is a PI – E7 – PAAD-22D (Figure 2-12 (c)) where the known layer AL_x is a standard rubbed PI and the layer to be fitted, AL_y, is a photoaligning azobenzene dye layer. In this example I extracted the optical parameters for PI from the symmetric cell PI – E7, that we measured earlier (Figure 2-15 (a, b)). In Figure 2-16, I present maps of the cell thickness and of the PAAD layer pretilt. Both maps are very uniform, with few exceptions in specific points close to the boundaries. The average thickness (Figure 2-16(a)) is 6.55 μm ± 0.01, while average pretilt (Figure 2-16(b)) is 0.16° ± 0.02°. Essentially, the spatial variations (Figure 2-16(a, b)) occur due to fabrication imperfections at the right-side edge of the cell. PAAD-22D is aligned using a 450 nm laser [115]. In order to keep the intensity sufficiently high we could not expand the beam to an area larger than approximately 7 mm in diameter.

2.4.3 Anchoring Energy

2.4.3.1 The effect of the anchoring energy

In principle, the polar anchoring energy affects the alignment of the LC at all values of the voltage applied to the cell, and its strength can be deduced from the changes in LC reorientation with increasing electric field. Small values of the anchoring energy weaken the LC molecule binding to the AL, thus making it easier for the electric field to tilt the molecular axis. However, for intermediate values of the anchoring energy we expect that the binding to the AL layer will be weakened mainly at large voltage values. In this case, the LC axis is parallel to the electric field across most of the cell and there is a considerable bending of the director field near the cell sides that strains the molecular attachment to the surface thus amplifying the effect of not having an infinitely strong anchoring. We can verify this by comparing CPI traces computed for four different values of the anchoring energy, logarithmically spaced between 10 μJ/m^2 and 10 mJ/m^2 a range that stretches from very weak to very strong anchoring (see Figure 2-17). The difference between the three largest values of the anchoring energy is insignificant at low voltage, while it is well visible at high voltage, especially if the anchoring is not too strong. It is only when the anchoring is very weak that the low voltage region is affected.

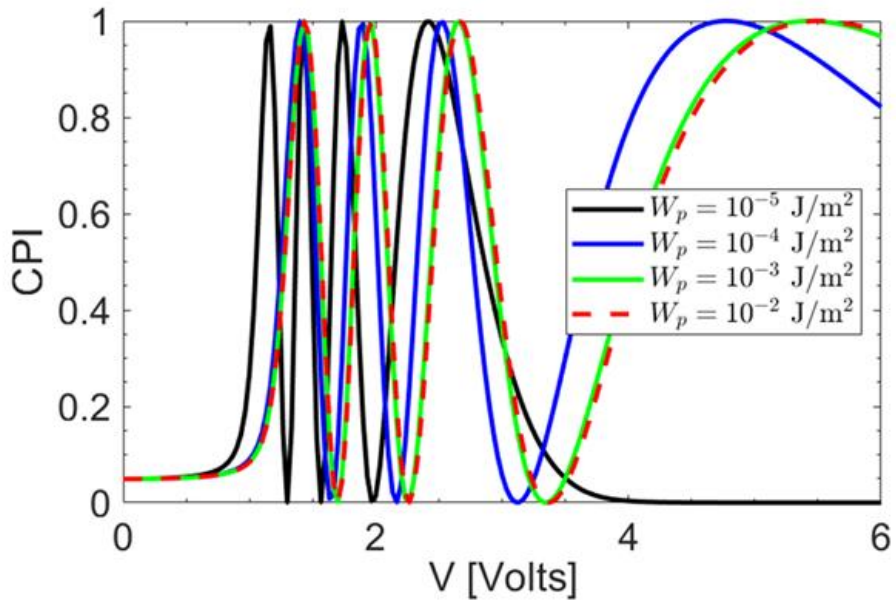

Figure 2-17 CPI traces for different values of the anchoring energy in a symmetric cell. Parameter values Parameter values: $K_1 = 10.9$ pN, $K_3 = 17.9$ pN, $\varepsilon_{\parallel} = 19.54$, $\varepsilon_{\perp} = 5.17$, $d = 12$ μm, $\theta = 2°$, $\lambda = 642$ nm, $n_e = 1.7287$ and $n_o = 1.5182$.

2.4.3.2 Minimisation landscapes

It is clear that the anchoring energy has an effect on the CPI and so, in principle, it should be possible to determine its value by fitting experimental CPI traces. In practice, however, its effect is small and so it may not be possible to determine its value accurately. For example, in the specific case of the traces in Figure 2-17, it is immediately clear that even a minimal amount of noise would make the traces that correspond to anchoring energy of 10 mJ/m^2 and 1 mJ/m^2 indistinguishable. In other words, the stronger the anchoring, the harder it is to obtain an accurate measure [111,112].

Another factor that can contribute to the poor quality of a parameter measurement, even if the fit is excellent, is the presence of degeneracies between parameters. This is a well-known problem in parameter fitting. To check whether fitting the anchoring energy is possible, i.e. to verify that there are no quasi-degeneracies, I have inspected the minimisation landscape around a known solution. I have fixed a set of LC and cell parameters, indicated by a superscript 0, as in $K_1^{(0)}$, $K_3^{(0)}$, etc., and have computed the corresponding CPI trace, $I\left(\mathrm{V_j}; K_1^{(0)}, K_3^{(0)}, d^{(0)}, \theta_0^{(0)}, W^{(0)}\right)$, where V_j is the *j*-th voltage value at which the CPI trace is evaluated, $\theta_0^{(0)}$ indicates the common value of the two pretilt angles and $W^{(0)}$ the common value of the two anchoring energies (we assume for simplicity that the cell is symmetric). I have then varied two parameters, for example the bend elastic constant and the anchoring energy, and computed the corresponding CPI trace, $I\left(\mathrm{V_j}; K_1^{(0)}, K_3, d^{(0)}, \theta_0^{(0)}, W\right)$. Finally, I have computed the distance between the two traces,

$$D(K_3, W) = \sum_{j=1}^{N} \left[I\left(V_j, K_1^{(0)}, K_3^{(0)}, d^{(0)}, \theta_0^{(0)}, W^{(0)}\right) - I\left(V_j; K_1^{(0)}, K_3, d^{(0)}, \theta_0^{(0)}, W\right) \right]^2 \tag{2.17}$$

where *N* is the total number of voltage values used. This is the function that is minimised when fitting the LC parameters, in this case the bend elastic constant and the anchoring energy at the two sides of the symmetric cell. Parameters are independent if $D\left(K_3^{(0)}, W^{(0)}\right)$ is an isolated minimum. I have plotted the distance, Equation (2.17), as function of three different combinations of parameters in Figure 2-18, forming minimization landscapes. The anchoring energy (*W*) is along the horizontal axis and varies by +/- 30% with respect to $W^{(0)}$. The vertical axes are, from left to right, the splay and bend elastic energy, and the pretilt angle. In all cases there is an isolated minimum, confirming that the anchoring energy can indeed be fitted. The

region of the minimum in the left and in the middle of the plots is elongated, indicating that the estimate on the anchoring energy can be changed significantly just by a relatively small change in either of the elastic energies. The region of the minimum in the rightmost plot, instead, is more symmetric indicating that the pretilt and the anchoring energy are to a good approximation independent one of the other. The minimisation landscapes offer only a local analysis of the best fit, as is the case for the covariance matrix method to estimate correlations between parameters. It is always possible that there may be other local minima in the landscape, especially when varying all the parameters. I tried to avoid this pitfall of all high-dimension minimisation methods by repeating the fitting of the experimental CPI traces using different initial guesses of the fitting parameters.

In summary, this analysis shows that it is possible, in principle and in practice, to fit the polar anchoring energy values from the very weak to strong regime. The precision of the fit may be affected by errors in the estimates of the elastic energy coefficients; the more precisely these are known, the more accurate the estimate of the anchoring energy will be. If the LC system is in a very strong anchoring regime, the accurate value cannot be extracted, but in fact, this is not a significant limitation. In this regime the LC alignment is, by definition, not sensitive to the accurate value of the anchoring energy.

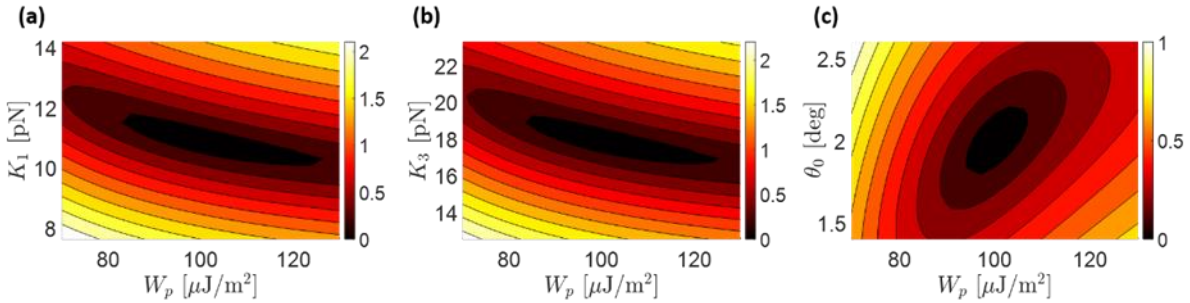

Figure 2-18 Minimisation landscapes: in all cases the anchoring energy is along the horizontal axis and varies by +/- 30% with respect to $W^{(0)}$. The vertical axes are, from left to right, the splay and bend elastic energy, and the pretilt angle. The scale of the colour bar is in arbitrary units. Parameter values: $K_1^{(0)} =$ 10.9 pN, $K_3^{(0)} = 17.9$ pN, $\varepsilon_{\parallel} = 19.54$, $\varepsilon_{\perp} = 5.17$, $d^{(0)} = 12$ µm, $\theta^{(0)} = 2°$, $W^{(0)} = 100$ µJ/m2.

2.4.3.3 Polar anchoring energy experimental results

As discussed earlier, the polar anchoring energy effects are small and, hence, sensitive to noise in the measurement process. Moreover, they are mostly detectable in the large voltage amplitude part of the CPI trace. For these voltage values, most of the LC in the bulk is aligned with the electric field, and the only significant alignment variations are near the boundaries.

Surface anomalies, like charge deposition, and dust, affect these measurements more significantly than those of the elastic constants, thickness and pretilt angle, whose value are related to the LC bulk properties, thus, adding to the noise on the measurement. To compensate for this, I have measured the polar anchoring energy averaged over the cell area. Our measurements are summarised in Table 2-5.

Table 2-5: Anchoring energy values from symmetric and asymmetric LC cells

Measured LC cells	**Average Polar Anchoring Energy on the photoactive layer [mJ/m^2]**
Symmetric 1: PI-E7	> 1
Symmetric 2: PEDOT: PSS-QYTN-004	23 ± 11
Asymmetric 1: PI-E7-PAAD22D	0.26 ± 0.01

The average polar anchoring energy of the standard symmetric PI-E7 cell is > 1 mJ/m^2, the upper bound of our detection window (see Figure 2-17). While in the case of the complex LC mixture of QYTN-004 on PEDOT:PSS, the average polar anchoring energy is 23 ± 11 mJ/m^2. In order to calculate the polar anchoring energy of the asymmetric PI – E7 – PAAD-22D cell, we exploited the optical parameters for PI from the symmetric cell PI – E7 (see Figure 2-15). The resulting average polar anchoring energy of E7 on PAAD-22D is 0.26 ± 0.01 mJ/m^2, a weaker alignment that on PI.

As the results in Table 2-5 demonstrate, the method presented here captured different anchoring strengths for a set of LC systems. Strong anchoring was measured for the reference cell (PI-E7), as expected, and a reduced anchoring was observed for the photoaddressable cells with photoalignment (PAAD) [104] and for a system with an organic conductor (PEDOT:PSS)[36]. While the anchoring is lower in those cells than in the test cell with PI, it nevertheless remained in the regime associated with strong anchoring.

The selection of a PI – E7 symmetric cell for our first set of measurements was driven by the availability of the E7 parameter values in the literature, making it the best candidate to calibrate the OMPA instrument. The literature parameter values together with those fitted by the OMPA are listed in Table 2-6. It is evident that even for this popular LC there are relatively few measurements, and none as comprehensive as those provided by the OMPA. As shown in Table 2-6, the OMPA measurements are in line with the literature ones. We also note that the

spread of values for the anchoring energy is quite significant, reflecting the difficulty in measuring this parameter.

Table 2-6: Optical parameters of symmetric planar PI - E7 cell.

Source	K1 [pN]	K3 [pN]	Pretilt Angle [°]	Polar Anchoring Energy [mJ/m^2]
Literature	11.2 [126]	18.6 [126]	-	-
	10.8 [127]	17.5 [127]	-	-
	11.7 [128]	19.5 [128]	2 [128]	-
	11.5 [129]	18.2 [129]	-	-
	-	-	1.5 [130]	-
	-	-	-	0.3 [131]
	-	-	-	0.8 [132]
	-	-	-	1 [133]
OMPA measurements	11.6 ± 0.2	17.8 ± 0.1	1.9 ± 0.1	> 1

The average measurements for QYTN-004 on PEDOT:PSS are summarised in Table 2-7. These are the first measurements that I am aware of this low threshold voltage LC. Polar anchoring energy revealed a weaker behaviour than E7 on PI (23 ± 11 mJ/m^2). This highlights the importance of being able to estimate the average value and fit both strong and weak anchoring energy responses, especially when characterising newly synthesised LC materials. In the case of the PI – PAAD-22D asymmetric cell, I have used the values listed in Table 2-6 to fix the alignment properties of E7 on PI and have fitted the pretilt angle and anchoring energy on the PAAD-22D side. The most surprising feature of this measurement is the relative weakness of the anchoring energy of E7 on PAAD-22D, with respect to PI (0.26 ± 0.01 mJ/m^2 and > 1 mJ/m^2 respectively). Usually photoaligned azo-dye layers provide comparable anchoring energy with the rubbed LC alignment on PI [134].

Table 2-7: Experimental results of PEDOT:PSS – QYTN-004 cell.

Source	K1 [pN]	K3 [pN]	Pretilt Angle [°]	Polar Anchoring Energy [mJ/m^2]
OMPA measurements	10.08 ± 0.14	16.0 ± 0.4	1.28 ± 0.08	23 ± 11

This difference can be explained by non-optimum alignment of PAAD-22D layer, as observed in our earlier work [115]. The strength of anchoring at a photoalignment layer depends on the quality and uniformity of the film [134,135]. As shown here, the maps obtained for this cell indeed indicate some lack of uniformity. This is an additional, important feature of this method, i.e. that it is capable of detecting the lack of uniformity or stability over time, as commonly observed when dealing with new LC or alignment materials.

For azobenzene based PAAD ALs, the anchoring energy can be varied considerably by changing the UV exposure time and irradiation dose of azo-dyes [135]. In particular, the optimum anchoring energy is obtained when irradiation dose of a UV pump beam (365 nm) is higher than 1 J/cm^2 [136]. I have used a longer wavelength (450 nm) and a weaker irradiation dose (0.22 J/cm^2). The second factor that affects the film quality is its thickness: very thin films may lack continuity and form islands. It is known that even very thin (e.g. 1 nm) layers of azo-dyes can be used to align LC, but with significantly reduced strength [15]. The thickness of the PAAD-22D layer in the asymmetric cell was estimated to be approximately 15 ± 10 nm, while it normally spans from 75 to 150 nm [137]. This larger thickness is likely to lead to smoother films with stronger anchoring.

2.5 Summary

This chapter described the experimental methods I used during my thesis to fabricate and characterise LC cells. In these experiments, LCs are tested in planar LC cells. Cell thickness uniformity of empty cells was ensured by the interferometric method (Fabry-Pérot, optical cavity), whereas for the filled cells we exploit the cross-polarized intensity experiment (Fréedericksz transition experiment). The former is based on the response of LCs to the applied electric field. Thus, by measuring the electric field-induced as a function of the CPI transmitted through the cell, I characterise the optical properties of LC materials. The cell thickness, the pretilt angle, the polar anchoring energy and the elastic constants are some of these optical properties I was interested to determine.

To obtain quick and reliable estimates of a gamut of LC parameters, I used a fully automated and compact optical instrument (OMPA). OMPA allows an interactive determination of a range of LC cell parameters, from a single spot measurement and in real time. The particular strength of the method presented in this chapter, is that it can capture, at the same time, the parameters that strongly influence the response of LCs to external fields, such as elastic constants,

viscosity, cell thickness, pretilt, as well as weaker and finer parameters, such as the strength of polar anchoring.

Enhanced, photoactive response can be realized by integrating LCs with photoalignment or photoconductive ALs. Such cells, asymmetric by design, need to be monitored for the stability and uniformity, especially in the regions exposed to light. Here, the method adopted was fast, robust, reproducible, and represents an accurate model and technique for characterising symmetric and asymmetric LC cells based on CPI measurements. This optical method can capture the subtle contribution to the phase lag from anchoring on the substrates and use it to determine its strength when the dielectric anisotropy and birefringence of LC are known. I tested this approach on cells with a single photoalignment layer as well as on a system with organic conductors.

In addition, the two-dimensional maps of uniformity of the cells were obtained, showing spatial variation of the thickness and of the pretilt angle, both important parameters for determining long term stability of LC devices. My measurements have focused on planar LC cells with voltage inactive layers. However, the technique I have presented can easily be extended to more complicated cell configurations. For example, including photoconductive or photovoltaic layers requires only to change Equation (2.11) in a relatively simple way, while modelling the effect of light-induced alignment changes requires only modest modifications of the boundary conditions, namely Equations (2.12) and (2.13). This flexibility, coupled with the ease and speed of measurement, make OMPA method an ideal tool for the characterisation of novel photoaddressable LC geometries.

Chapter 3

Optically Driven Bistable Liquid Crystal Waveplates

In this chapter, I present the methodology for the construction of optically controlled, dynamic half-wave plates, created using the photo-aligning properties of PAAD materials. The experimental results on the optical characteristics of the cells are interpreted within the framework of a simple theory. This LC system can efficiently control the transmission and polarisation of light in the visible and near-infrared (NIR) region. It is bistable, with state-switching achieved by addressing the PAAD layer with visible light, a process that is reversible and reproducible for multiple cycles. In some of the work presented here, the realignment is provided by the probe beam itself. In other experiments, the transmission of a probe beam is monitored, whilst the realignment is carried out by a pump beam at a different wavelength. This work goes beyond that on previous azo and PAAD systems, where typically, the alignment geometry has been fixed for the duration of the life of the cell, while here the alignment is re-addressable. Part of this work has been published as: **Optically controlled bistable waveplates.** Perivolari, E., Gill, J. R., Podoliak, N., Apostolopoulos, V., Sluckin, T. J., D'Alessandro, G., & Kaczmarek, M. (2018). Journal of Molecular Liquids, 267, 484-489. The fabrication of photo-addressable LC samples, and measurements were done entirely by me. I acknowledge help from Dr Jordan Gill with data fitting and assistance of Dr Nina Podoliak with experimental setups. Other co-authors contributed with advice and/or to supervision and with writing of the article.

3.1 Introduction

LCs are valuable materials for many light-switching applications [14,18]. A disadvantage, at least under some circumstances, of conventional (e.g., 1970s–2000) LC devices is that their operation requires the continual imposition of a voltage, causing the device to continually consume power. For static displays, in which continual updating, is in principle, unnecessary, this is a particular problem. It is, however, a problem that can be overcome if the device is constructed so as to be bistable [40]. In this case, electric impulses alone should be sufficient to persuade a pixel to switch states.

Assembling a bistable device is no simple matter, though. Take, for example, the widely used ZBD device [40]. Its operation requires that one of the surfaces be carefully engineered to possess a particular kind of grooves, enabling more than one LC configuration to be stable in the neighbourhood of the interface.

In simpler cases, rubbing of an AL takes place (see Section 1.4.1) which is a traditional, and somewhat uncontrolled technique. Disadvantages for commercial and technological applications, such as the accumulation of static charges, the generation of dust particles, and simply the need to incorporate electrodes and an external voltage into the cell design are well known [19]. Furthermore, such surfaces will not, in general, sustain bistability. This would only be possible if the surface alignment can itself be altered, which is completely impractical if the alignment has been achieved by rubbing.

An alternative to the rubbing technique is photopolymerization of an AL. In this method, polarised light is used to align polymer molecules in the surface layer adjacent to the LC [26,27]. In turn, the surface LC molecules align in accordance with the molecules of the polymer layer. Yuri Reznikov was particularly influential in developing this surface alignment technique, and his name appears on numerous patents and right papers. These date right from the technique's invention in the 1990s [26,28-30] and stretch e.g. to his more recent 2012 review with Yaroshchuk [19]. Photoalignment is a much more controlled and reproducible procedure than rubbing, and has the important, extra advantage is the reorienting of a surface layer after a cell's construction. This provides the possibility of bistability without an elaborately engineered surface layer, but rather by the ability to reversibly replace one surface orientation with another.

3.2 Photo-Aligning Azobenzene Dyes (PAAD)

During my thesis, I investigated LC cells coated with an AL of PAAD-22D, a photo-aligning azobenzene dye (PAAD) from BEAM Co. In general, various different azo-compound materials form films with thickness varying from 20 nm to 500 μm and have been used as photoaligning materials for LCs for the last 30 years. PAAD materials have demonstrated themselves to be capable of forming high resolution patterns, enabling their use for polarisation gratings and spiral phase wave-plates, and to be effective in the alignment of LCs. They also require low exposure energies and have an absorption spectrum extending past 400 nm.

Like all azobenzene-based ALs, the molecules of the PAAD-22D layer are able to convert efficiently between their trans and cis states when subject to UV and visible light illumination (see Section 1.4.2). The effect of this illumination is similar to that of an electric field in a direction perpendicular to the incident light and its polarisation, in that the molecules tend to align along this axis. The mechanism is slightly different to that of an external field, however, which simply rotates the molecules [46,47]. Rather, according to the 'angular hole-burning model', starting in the thermally stable trans state, the azo-molecules absorb photons and transform into their metastable cis state. They subsequently return, with a random orientation, through either a spontaneous relaxation or a reverse photoisomerization process (see Figure 1-17). The absorption of the photons depends on the angle their electric field makes with the PAAD molecules, with photons absorbed preferentially by molecules parallel to the electric field. It follows that by addressing the PAAD with linearly polarised, visible light for a sufficiently long period of time, the orientation of the PAAD molecules moves towards a population that is entirely perpendicular to the incident electric field (since these are non-absorbing).

3.2.1 Preparation of PAAD films

The photoaligning layers (PAAD) used in this thesis are based on azo-coupling of the diazonium salt of 4,4'−diaminobiphenyl−2,2−disulfonic acid with the derivatives of phenol and aniline having different numbers and positions of such pendants as -chloro, -hydroxy, -alkyl, -carboxyl groups or in the phenol ring or at the nitrogen atom in aniline. In fact, I investigated four different versions of PAAD complex dyes, namely PAAD-22, 22D, 22E, and 72 either in powder form or in ready solutions produced by BEAM Co. All four variations are based on the same chemical composition. They were developed with the aim of shifting the absorption band away from the ultraviolet and into the visible region of the spectrum (towards 532 nm), while

maintaining their stability and uniformity. In earlier works, several versions of PAAD [25], [26] were studied for their contact angle and photoalignment properties with LCs. They show different wetting properties on glass and ITO coated glass substrates which affect the films' thickness and uniformity. In addition, they show differences in the wavelengths of their absorption spectrum, with some forming either narrow or broad and single or double peaks.

Thin films of PAAD dyes were fabricated by dissolving the dye powder in methanol at a concentration of 1% g/ml and then sonicating for 5 minutes, until a clear solution was obtained. Previously, other solvents were tested such as water, toluene, and heptane, however these solvents were not able to dissolve the dye powder. Dimethylformamide (DMF) has been also tested, showing promising results, and hence finally used by the BEAM Co to produce ready solutions of PAAD in DMF (1% g/ml). Thereafter, thin films of PAAD were deposited on the substrate by spin coating as shown in Figure 3-1.

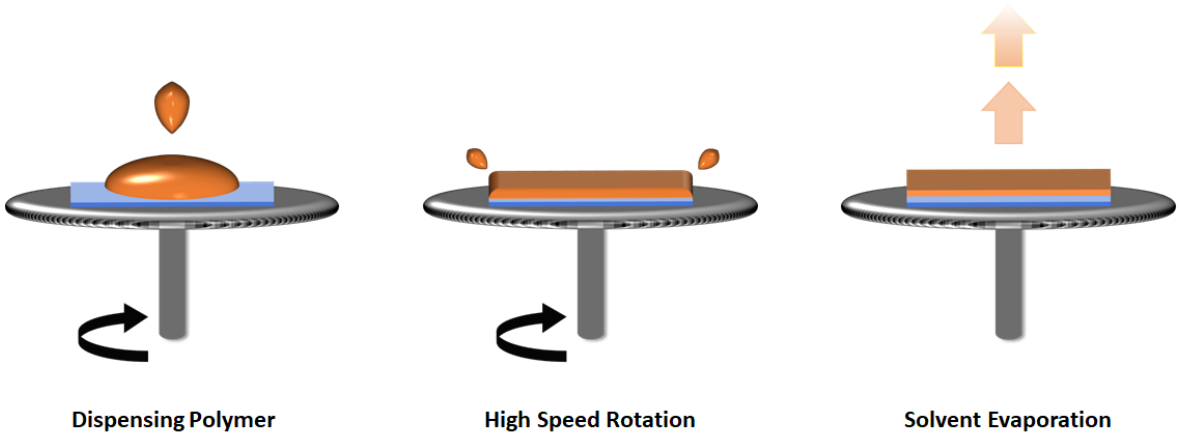

Figure 3-1 Spin coating of thin films.

During my experiments, I used indium titanium oxide (ITO) on glass as substrate, which is extensively used for LC cells. Basically, the choice of ITO coated glass substrates was based on the fact that they offer better adhesion for the hydrophobic PAAD materials, demonstrating more uniform and smooth films compared to glass [49]. Therefore, we deposited PAAD films on 30 nm ITO on glass (1 mm) and annealed on a hot stage at 90°C for 10 minutes. Further, in order to determine the thickness ranges we can achieve by spin coating, I tried different rotation speeds (rounds per minutes -RPM) and different concentrations of the PAAD solution in methanol. Specifically, I used 1500, 2000, 3000, and 4000 RPM and 1%, 2%, and 5% w/v concentrations. The thicknesses of all the films were measured with profilometry (KLA Tencor P-16 Stylus Profiler) in all the stages of the experiments. An example of thickness profile for the PAAD-22 material, is presented in Figure 3-2. The maximum thickness was obtained for the maximum concentration, 5% w/v and the minimum rotation speed, 1500 RPM which is 280 ± 50 nm. However, for concentration of 5% w/v, the resulting films were not uniform, and

roughness was very high as the large error reveals. In addition, for concentration 1% and 2% w/v, the differences were minor and thus we fixed our recipe to 1% w/v and 3000 RPM, where the film thickness was 30 ± 10 nm. Each coated substrate was then exposed to linearly polarised light to introduce the desired orientation of the PAAD molecules which will promote the alignment of LCs in this direction (see Section 1.4.2).

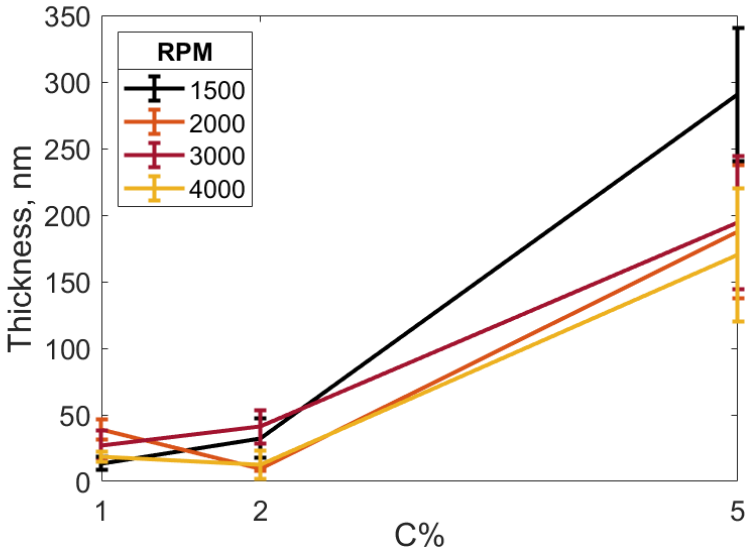

Figure 3-2 Thickness profile of PAAD-22. The minimum thickness was 30 nm at 3000 RPM and 1% w/v concentration of PAAD-22 in methanol.

3.2.2 Absorbance and light induced absorbance of PAAD materials

Absorbance (A), also known as optical density [138], is the quantity of light absorbed by a solution. Therefore, spectrophotometry is a method to measure how much a chemical substance absorbs light by measuring the intensity of light as a beam of light passes through sample solution. The basic principle is that each compound absorbs or transmits light over a certain range of wavelength. The absorbance is defined by Beer-Lambert law [138],

$$A = -log10\frac{I_T}{I_0}, \tag{3.1}$$

Where I_T, is the intensity of the incident light, and I_0, is the intensity of that light after it passed through the sample. In other words, $\frac{I_T}{I_0}$, is the transmittance of the sample. To determine the absorbance the intensity between a reference and a sample need to be measured.

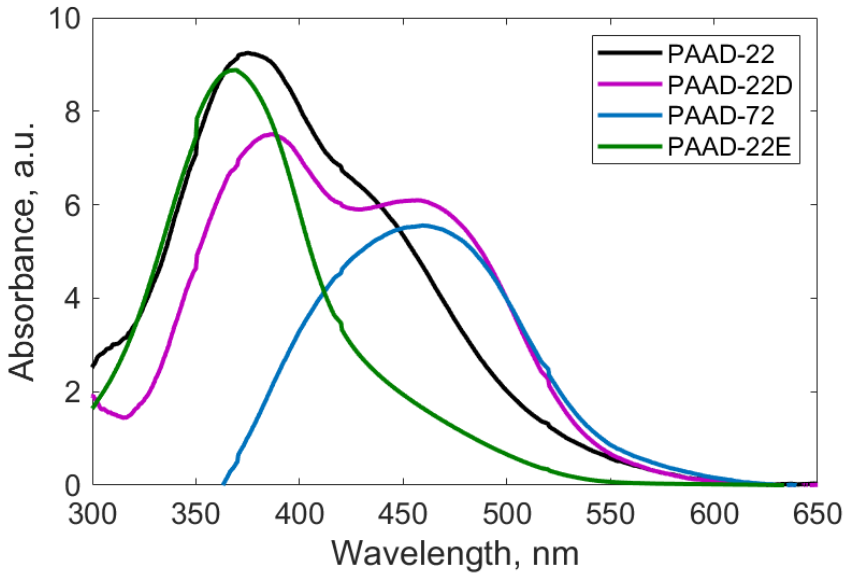

Figure 3-3 Absorbance of PAAD-22, 22D, 72, and 22E as measured with an UV/VIS/NIR JASCO spectrometer between 300-1500 nm. For clarity we only show the range of 300-650 nm.

Here, I measured the absorbance of four different PAAD materials, namely PAAD-22, 22D, 22E, and 72. The aim was to determine the photosensitivity of these materials in order decide the proper wavelength for the optimum photoalignment results. Samples were measured when deposited on ITO coated glass substrates with a spectrometer using unpolarised light (UV/VIS/NIR JASCO). The error of the system is approximately 2%. The materials were characterised between 300-1500 nm. For clarity, we only show the range of 300-650 nm, as presented in Figure 3-3 above.

Typical of azobenzene derivatives, the trans state is more stable and is the dominant isomer before UV and visible light irradiation. Briefly, the spectral properties of azobenzene are attributed to the two lowest electronic transitions of the trans states, the so-called π-π* and the n-π* transitions. Photoisomerization occurs when exciting the π-π* and the n-π* transitions, with π-π* transition exhibiting a stronger absorption band for the trans isomers. This mainly because of azobenzene molecular symmetry where overlap between n and π* orbitals is poor. To this extend n-π* transitions require less energy (ΔE) and hence the absorption maximum corresponds to longer wavelengths than the π-π* transition.

In Figure 3-3, PAAD-22 and 22D show broader absorption spectra, with the latter exhibiting two distinct peaks, at 387 and 459 nm, and the former showing the main peak at 377 nm and a shoulder at ~423 nm. The main absorption peak for PAAD-22E appears at 368 nm, and for PAAD-72 at 461 nm showing a narrowband absorption spectra. There the main peak corresponds to the stronger π-π* absorption band while the second to the weaker n-π* band.

The maximum wavelength of the π-π* absorption band is influenced by the linking functionality (i.e. ether or ester group) between the azobenzene and the headgroup. Thus, the main absorption peak for the different PAAD compounds appears to be shifted.

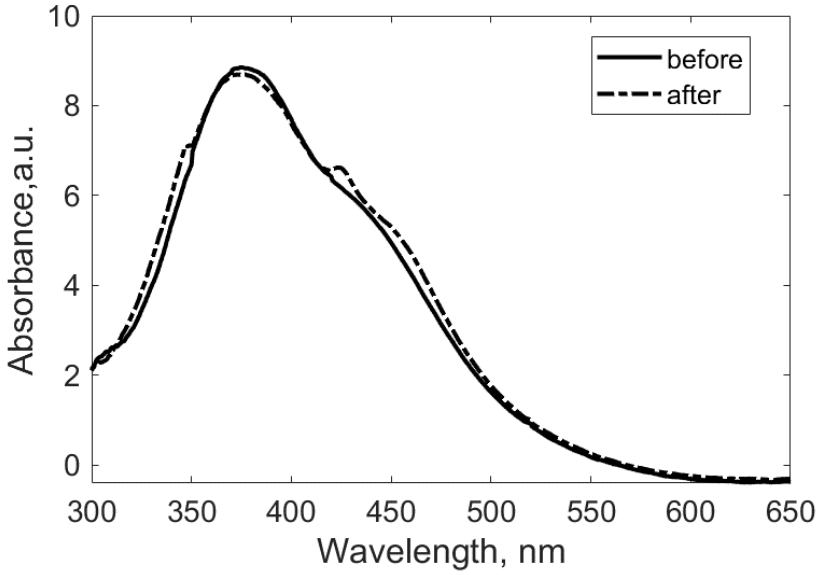

Figure 3-4 Absorbance of PAAD-22 before (solid) and after (dash dot) illumination of 458 nm.

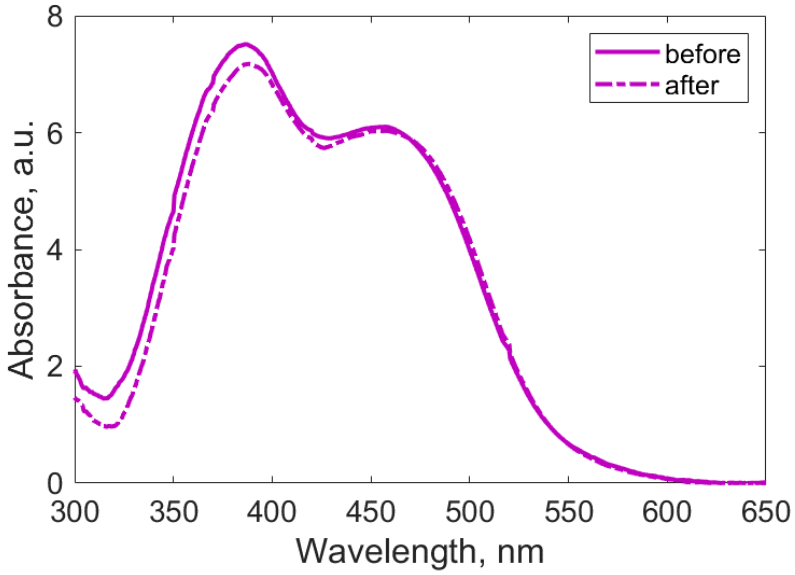

Figure 3-5 Absorbance of PAAD-22D before (solid) and after (dash dot) illumination of 458 nm.

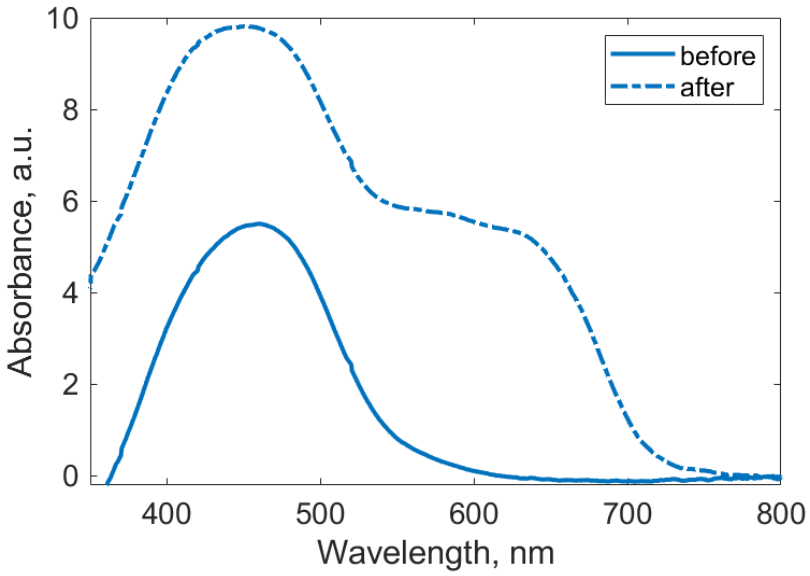

Figure 3-6 Absorbance of PAAD-72 before (solid) and after (dash dot) illumination of 458 nm.

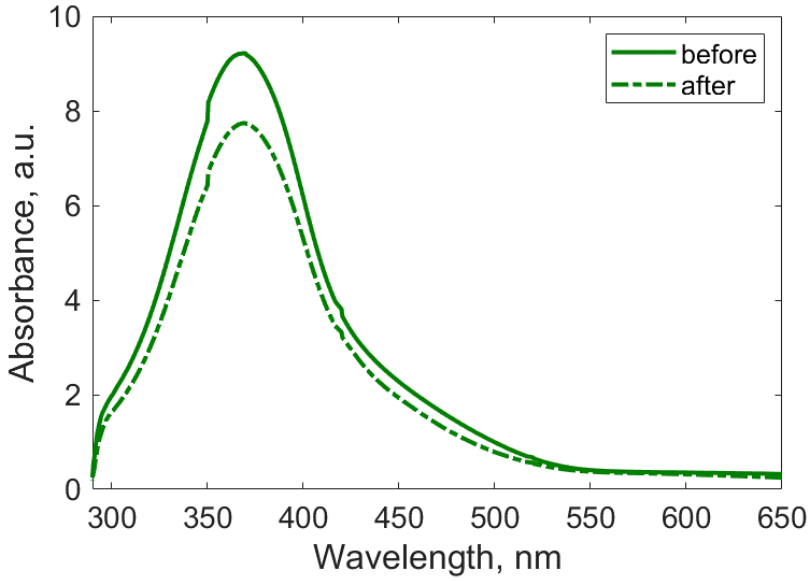

Figure 3-7 Absorbance of PAAD-22E before (solid) and after (dash dot) illumination of 458 nm.

To determine the photosensitivity of PAAD materials we measured then the absorption spectra after illuminating them with a 458 nm polarised diode laser (14 mW) with 1 mm^2 spot size for 1 minute. The absorption spectra of PAAD materials after illumination is presented in Figure 3-4, Figure 3-5, Figure 3-6, and Figure 3-7 for PAAD-22, 22D, 72, and 22E respectively. Post illumination a reduction in the π-π* band is expected, whereas the n-π* shall become more intense [19]. In fact, the absorption of PAAD-22 is slightly reduced while a second peak appears

at 426 nm. For PAAD-22D there is a 4.5% absorbance decrease at 386 nm, maintaining its two distinct peaks while for PAAD-22E there is decrease of 16% at 368 nm. Interestingly, this is not the case for PAAD-72. PAAD-72 appears to be the most sensitive to light from all the PAAD materials, since after illumination, its absorbance has increased by 44%. In addition, a second peak arises at ~608 nm, thus making the absorption spectra broader for this specific material. These results suggest that the azobenzene molecules are converted into cis isomers in all solutions, allowing one to estimate the proportions of the trans and cis configurations.

Given the above-mentioned absorption spectra measurements for the different PAAD materials, I conclude that PAAD-22D is the most stable material after illumination maintaining its initial absorption peaks with the less losses. But most importantly, it absorbs more at longer wavelengths in the visible regime i.e., >400 nm compared to the other PAAD materials.

3.2.3 Radiant exposure of PAAD

Photo-isomerisation of PAAD complex dyes is induced by their irradiation with UV or visible polarised light, as discussed in Section 1.4.2.2. There, anisotropy, and birefringence are induced in azobenzene-containing materials. Normally photoinduced birefringence increases with exposure time until it reaches a stable maximum value. When the illumination is discontinued, the maximum value may change slightly until it reaches stability due to thermal reorientation of azobenzene groups. The induced birefringence reduces over time, but depending on the material, the relaxation may be fast or slow [42]. Factors affecting the exposure time (t) required to reach the maximum value of birefringence include the thickness of the film (d), the irradiation wavelength (λ) and power (P), and the spot area of the laser beam (A). The exposure time can then be extracted by:

$$E\left[\frac{J}{cm^2}\right] = P\,[W] * \frac{t\,[s]}{A[cm^2]}. \tag{3.2}$$

Information about the radiant exposure, E, were retrieved by BEAM Co materials' specifications (see Table 3-1) [139]. There is information only for PAAD-22 and 72 materials, because PAAD-22D and 22E share the same type of the polymer backbone and the structure of the azo chromophore with PAAD-22 material, and hence the same specifications.

In my experiments I was interested in blue light at 405 and 458 nm, and in green light at 532 nm, avoiding UV irradiation sources (<400 nm). This will allow devices for real-life applications. The wavelength, 458 nm was chosen because there occurs the maximum absorption for the selected band, while 405 nm exhibits similar radiance exposure with UV

light yet visible. On another hand, 532 nm lies at the edge of the absorption spectra allowing the investigation of the photoinduced properties of PAAD-22D at longer wavelengths where the material absorbs the less. However, the radiant exposure information for these specific wavelengths was not included in the company's specifications. Therefore, I extrapolated the data between 325 and 540 nm in order to calculate the exposure time needed for the specific wavelengths, as shown in Figure 3-8. The calculated radiant exposure values for 405 nm and 532 nm are 0.22 J/cm^2 and 7.48 J/cm^2 respectively.

Table 3-1: Radiant exposure specifications for PAAD materials [139].

Material	**λ_{max}**	**E [J/cm^2]**			
		λ=325 nm	λ=365 nm	λ=458 nm	λ=488 nm
PAAD-22	366 nm	0.3	0.5	0.8	2.4
PAAD-72	423 nm	-	-	0.06	0.3

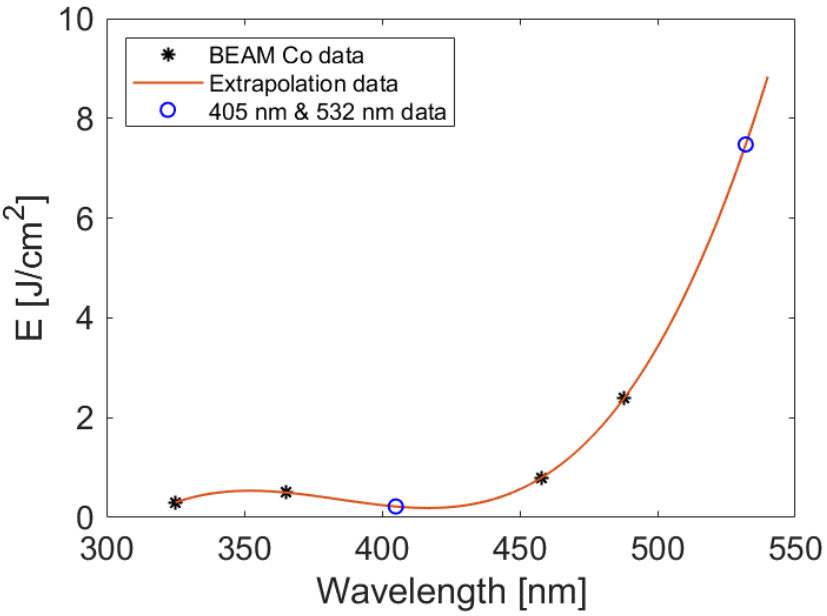

Figure 3-8 Extrapolation of radiant exposure (E) data for PAAD-22 material. Specifications from BEAM Co (black points) used to calculate E [J/cm^2] at 405 and 532 nm (blue circles).

Photo-alignment of PAAD-22D films occurred with the aid of the following optical setup, demonstrated in Figure 3-9. A fibre coupled diode laser at 405 nm for 14 mW passes from a fibre port into two lenses L1 and L2, which expand and collimate the beam to cover the surface across the film. The polarisation of the incident light beam was controlled through a half-wave

plate (HWP) and a polariser (P). Finally, the laser light beam of a diameter of 1 cm is incident on the PAAD film at normal incidence. The resulting alignment of PAAD molecules will be perpendicular to the polarisation of light (here horizontal). The exposure time is calculated by Equation (3.2) to be: $t = 12\ s$, which is the recommended exposure time for PAAD ALs before assembling the LC cell. To ensure a uniform alignment across the PAAD coated surface, each area of the sample was illuminated under the same conditions.

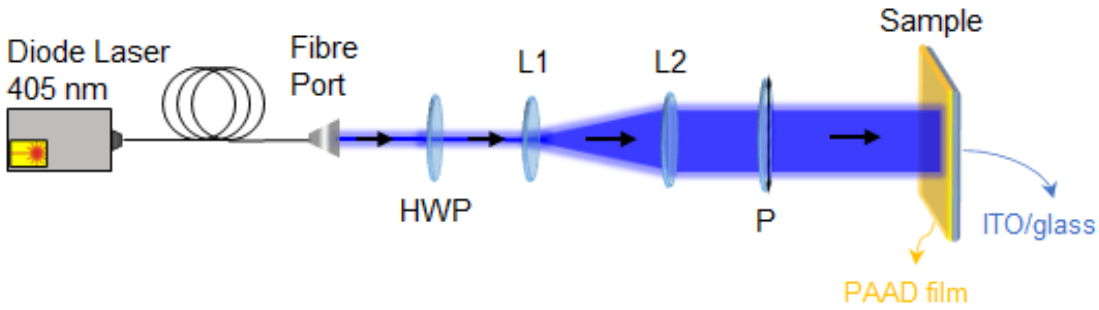

Figure 3-9 Experimental optical setup for the photo-actuation of azobenzene complex dyes before assembling the LC cell. A fibre coupled diode laser at 405 nm is used to address PAAD-22D thin films on ITO/glass substrates. The laser beam is expanded with a two lenses system (L1 & L2) to cover the surface across the PAAD film. The polarisation of the incident light beam was controlled through a half-wave plate (HWP) and a polariser (P).

3.3 Determination of PAAD Refractive Index Using the Iterated Ray Method

Here, I present the Iterated Ray Method, a highly efficient and accurate algorithm for computing the reflection and transmission coefficients of layered structures [140]. It is based on the intuitive picture of rays being partially transmitted and reflected at each interface and uses series sums of each reflection and transmission coefficient to build an efficient recursive algorithm for the total reflectance and transmittance of the multi-layered structure. The introduction and the more detailed information about this model is covered in the paper by *Gill J. R. et al.* in [140].

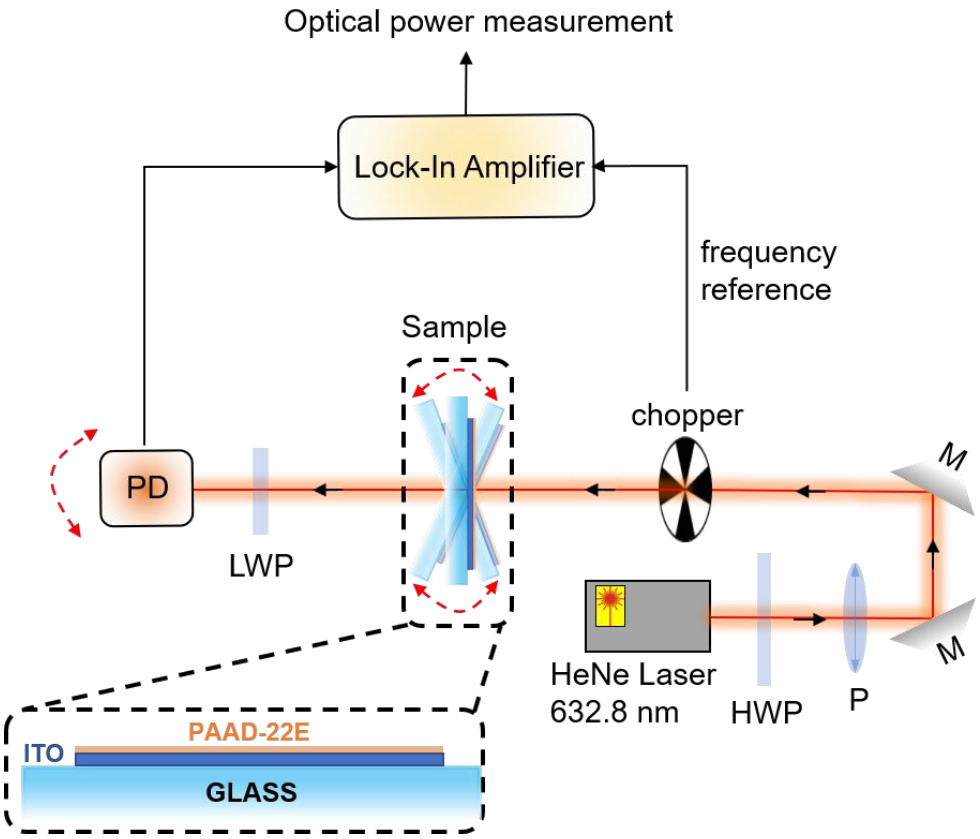

Figure 3-10 Experimental setup for measuring the transmittance coefficients as a function of the angle of incidence of PAAD-22E isotropic thin film, $T(\theta 1)$. A He–Ne laser was used at a 632.8 nm wavelength for 1.4 mW power as measured at the surface of the sample. The polarisation of the incident light beam was controlled through a half-wave plate (HWP) and a polariser (P). To remove background noise, we used a lock-in amplifier, where an optical chopper modulated the signal. A long wave-pass trim filter (LWP) helped further in cutting down the unwanted signals.

In this thesis, I have used the Iterated Ray Method to obtain the intrinsic properties (i.e., refractive index and film thickness) of isotropic PAAD layers in their unaligned state. The material that we investigated in this work has the commercial name PAAD-22E (BEAM Co.), with absorbance peak at 375 nm. Thin films of PAAD-22E dyes were fabricated as described in section 3.2.1. PAAD-22E compound has the narrowest absorption band making the sample less sensitive to other wavelengths.

To monitor the transmittance of incident light through the samples, a He–Ne laser at 632.8 nm and 1.4 mW was used as a probe. The choice of the probe wavelength was due to the low absorption of the PAAD films at 632.8 nm (see Figure 3-7), minimizing any realignment effects as the probe passes through the PAAD-22E films. The polarisation of the probe was controlled with the aid of a polariser (P) and a half-wave plate (HWP), as depicted in Figure 3-10. Finally, with the aid of two mirrors (M), we controlled and focused the beam on the sample.

The incident angle and polarisation of the probe beam were varied to monitor the transmittance of the s- and p-polarised outputs (see Inset

Figure 3-11). In order to achieve this, the sample was held in a rotation stage. The stage consisted of a 360° rotating base with a holder to keep the sample cantered on the stage's rotational axis (as depicted in Figure 3-10, the axis points out of the image). In this way, the incident light remained focused on the same spot of the sample as the stage was rotated, enabling us to monitor the transmission of the same spot of the sample for all of the different angles of incidence (depicted by the red dashed arrows around the sample in Figure 3-10). After propagating through the sample, the transmitted light was collected by a photodiode (PD), which measured its intensity.

In order to remove background noise, I used a lock-in amplifier and an optical chopper. The amplifier increased the signal-to-noise ratio, and the chopper was used to modulate the signal and provide a reference frequency. Further unwanted background signals were then filtered with a long wave pass trim filter (LWP) placed before the PD. The experiment was fully controlled by MATLAB software, which performed experimental apparatus control, data acquisition, and subsequent data normalization with respect to the reference data. Finally, to reduce the experimental noise, we also averaged the data points at opposite incident angles, as the transmission across isotropic layers is symmetric about normal incidence.

To form the theoretical model for comparison with the experimental results, the Iterated Ray Method was applied to the five-layer system (air/PAAD-22E/ITO/glass/air) to calculate the transmittance as a function of the angle of incidence. The refractive indices and thicknesses of the PAAD and ITO layers were unknown, and these are the four fitting parameters used in the fitting/optimization routine. This did not form the entire model, however. From standard Fabry–Perot theory, as well as that of the Iterated Ray Method, we see that the large thickness of the glass layer (approx. 1 mm) induces many rapid oscillations of the transmitted intensity as a function of the incidence angle. At least, this is the case for an incident plane wave.

In the experimental data, however, the oscillations are averaged out by the filtering due to the finite size and coherence of the Gaussian laser beam. It was therefore also necessary to smooth the theoretical transmission data $T(\theta_1)$ using a Gaussian filter, which was calibrated by fitting the transmission data of single glass slide. We note that the resonant effects of the glass are still evident in the narrow region near normal incidence (see the small sharp peaks in the experimental transmitted intensity visible in

Figure 3-11). In this region the phase difference between neighbouring emerging rays (and hence the overall transmission) varies with angle of incidence on a far slower scale, and, consequently, the averaging is less effective.

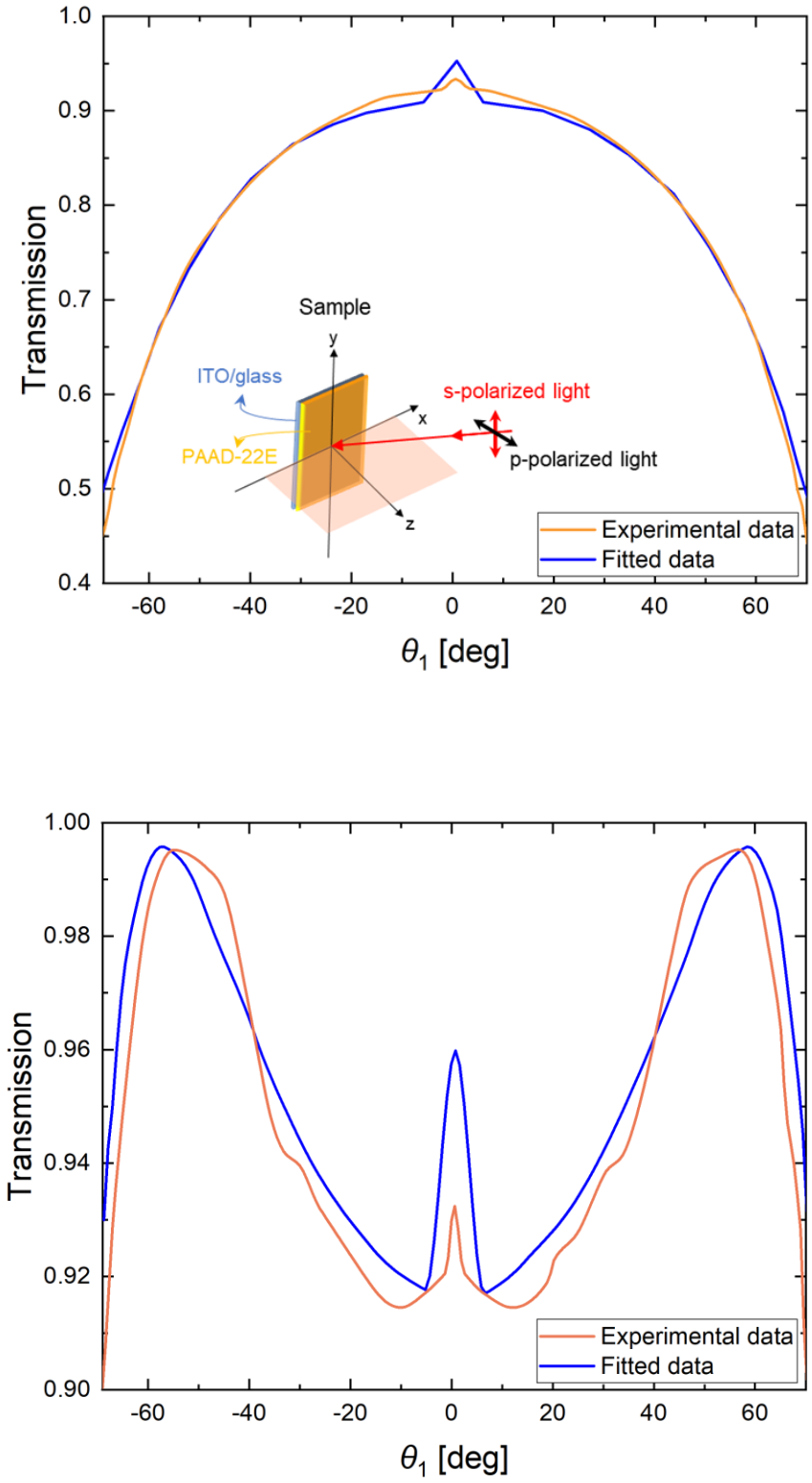

Figure 3-11 Graphs showing the experimental (orange) and fitted (blue) transmission curves for an s -polarised (top) and a p-polarised (bottom) 632.8 nm beam incident on the PAAD-22E/ITO/glass system.

Inset: shows the experimental geometry for s-polarised light where the electric vector points along y axis while for p-polarised light it lies in the x-z plane.

The Iterated Ray Method solution plus the Gaussian averaging formed the complete theoretical model. This model was used in a MATLAB minimization routine to fit to the experimental data and obtain values for the unknown refractive indices and thicknesses. In the fitting process, we excluded the data points for incident angles larger than ±56° due to the steep slope of the data. The steep slopes meant that while the experimental and theoretical curves could be very close to one another, the errors between the two in the least squares sense (difference vertically) could lead to enormous errors and make successful fitting impossible. We also ran the fitting in two stages, first fitting the larger angles of incidence for the PAAD and ITO parameters and then fine-tuning the glass thickness to fit the centre region where the glass resonance effects were observable.

The experimental and best fit curves are shown in

Figure 3-11, and the fitted parameters are shown in

Table 3-2. The ITO thickness given by the fitting process is consistent with the specifications of ITO/glass substrates offered by many manufacturers, usually in the 100–200 nm range. The refractive index is also in good agreement with values in the literature, e.g., 1.87 [141]and 1.78 [142]. The thickness and refractive index of the PAAD-22E layer are consistent with the values of 45 ± 20 nm and 1.8 ± 0.1 found in [49], in which samples created using the same method were studied, and the thickness and refractive index were found using profilometry and ellipsometry, respectively.

Table 3-2: Refractive Index and Thickness of PAAD-22E and ITO Layers Deposited on a Glass Slide, Obtained by Fitting the Experimental Data in Figure 3-11.

Material	Refractive Index, n	Thickness [143]
PAAD-22E	1.73	27
ITO	1.85	142

Before concluding this section, we would like note that the PAAD film analysed here was placed on a glass substrate that contributed significantly to the shape of the transmitted light

intensity. This is a different geometry from ellipsometry studies, which are instead based on detecting polarisation changes in the light reflected by the thin film. The aim of the experiment examined here was to analyse the PAAD film on the same type of substrate and conditions in which it would be used once in a liquid-crystal cell, wave plate, or other component. Our analysis is, thus, inspecting a more realistic and practical photo-alignment system. This imposed severe constraints on the fitting procedure because of the need to average over the multiple Fabry–Perot resonances in the glass substrate. We have used a very fine angular resolution of around 0.04° to capture the oscillations of the theoretical transmission and ensure the convergence of the averaging process. The fact that we have been able to do this on a standard desktop in a reasonable time is further confirmation of the computational efficiency of the Iterated Ray Method.

3.4 Dynamic Half-Wave Plates Based on Photo-Aligning Azobenzene Dyes (PAAD)

In this section I discuss the experimental setup and the procedure followed to measure the change in the transmittance of the PAAD-LC cells in both planar and twisted states. I also present a mathematical model and the expected results for the experiment, along with the fitting procedure to model the PAAD realignment dynamics. In Section 3.4.3 I present my results for the transmitted intensity for multiple probe beam wavelengths in the visible and NIR region. Finally, in Section 3.5, I provide a brief discussion of this work and draw some conclusions.

3.4.1 Experimental methodology

The LC cell was formed by two glass slides filled with the commercially available and widely used nematic LC E7 in the isotropic phase, as described in section 2.2. Both slides also received an additional coating: polyimide (PI) for one, and PAAD-22D for the other, as shown in Figure 3-12. This was done to investigate the transition from the planar to twisted LC configurations.

Two sets of experiments were carried out, which I will refer to as the single beam and pump-probe experiments. The optical setups are shown in Figure 3-13 and Figure 3-14, respectively. In all cases, the cell was placed between parallel polarisers (P1 and P2) and a probe beam. The probe was used with a photodiode detector (PD) to determine the LC alignment. The cell was positioned with the initial LC alignment lying vertically. The PAAD-22D photoaligning layer lay

on the front face and the PI layer at the far face of the cell. In the single beam experiments, the probe beam was either green light (λ = 532 nm, E = 7.5 J/cm^2) or blue light (λ = 405 nm, E = 0.22 J/cm^2), and had diameter 1 mm. These wavelengths were suitable not only to observe transmission, but also to rotate the easy axis on the PAAD layer surface. The pump-probe experiments involved transmission by either red light (λ = 632.8 nm) or NIR (λ = 808 nm) beams. Light at these wavelengths is not able to rotate the PAAD molecules and the resulting LC surface alignment. In this case, a blue pump beam with polariser (P3) was used to switch between surface alignments, independently of the probe. In all experiments, the measured transmitted intensity was normalized by taking its ratio with respect to that transmitted through a second planar cell. This second cell was identical to the first in all respects, except for the fact that the PAAD layer had been replaced by a second PI layer. The experimental error of the normalized intensity is 5%. We also monitored the probe power to correct for any fluctuations.

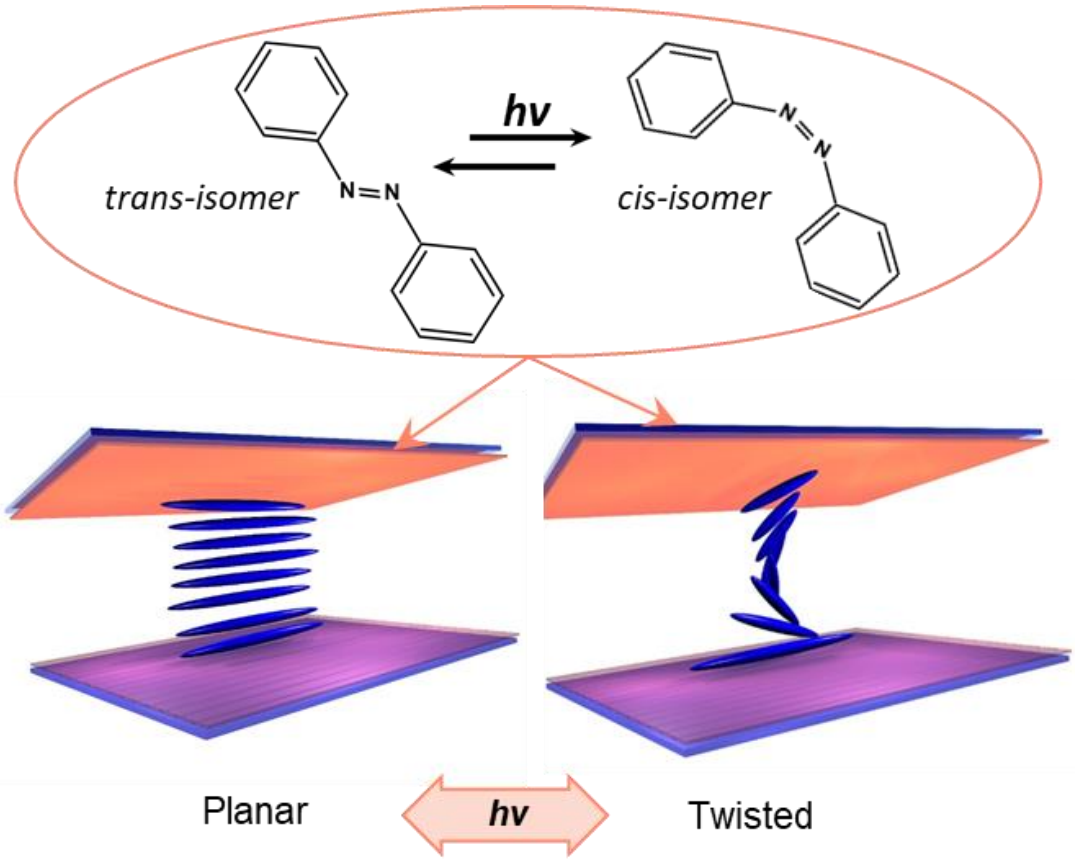

Figure 3-12 Schematic of a PAAD-22D – LC cell in planar and twisted states. Switching between planar and twist states is controlled by one-step illumination with visible light.

In the single beam experiment, the cell was initially in the planar state, schematically shown in Figure 3-12. We have verified the quality of the alignment by checking the cell through cross-

polarisers (see the top left panels of Figure 3-15 and Figure 3-16). At set times, we inserted a half-wave plate (as shown in Figure 3-14) in front of the laser to rotate its polarisation by $\pi/2$ and also rotated P1 by the same amount, causing the polarisation of the single beam to likewise rotate. The polariser P2 followed the polariser P1 so as to remain parallel at all times. Rotating P1 switched the PAAD layer alignment, leading to the $\pi/2$ rotation of the surface alignment that the PAAD layer imposes on the LC. This realigned the LC molecules adjacent to the PAAD layer (hence altering the bulk alignment, also), causing the cell to switch from a planar to a twisted state, shown in Figure 3-12. By this same mechanism, subsequent back and forward rotations of P1 and P2 then switched the cell repeatedly between the planar (ON) and twisted (OFF) states, as demonstrated in Figure 3-17.

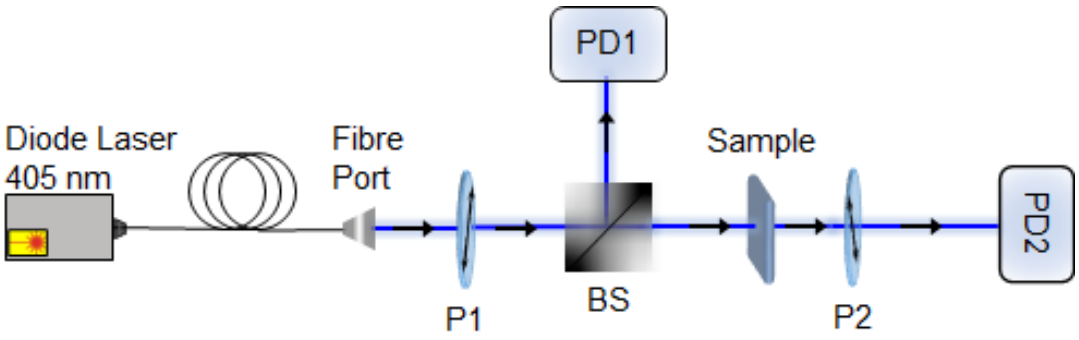

Figure 3-13 Schematic of the optical setup for the single beam experiment. A fibre coupled diode laser at 405 nm is used to address PAAD-22D material which passes from a fibre port to collimates the beam. The sample is located between two parallel polarisers (P1 and P2), where the light enters at normal incidence. The PAAD-22D photoaligning layer lay on the front face and the PI layer at the far face of the cell. Photodiodes, PD1 and PD2 monitor the power of the laser before and after the cell by exploiting two beam splitters (BS). Here, the single beam is used also to realign the PAAD layer.

The experiments consisted of this cycling between planar and twisted states while using the photodiode to observe the changing transmission characteristics of the cell as a function of time. In the planar state the transmission is close to unity. In the twisted state the transmission is close to, but not exactly, zero, except when further destructive interference between ordinary and extraordinary beams in the LC cell requires it. Immediately after rotating the polarisers, there is a relaxation process, as the transmission heads towards its new equilibrium. The experiments also involved measuring transmission at different points across the cell.

In the pump-probe experiments the procedure changed. This is because beams at 632.8 nm and 808 nm wavelengths do not realign PAAD effectively. As a result, the pump beam and polariser (P3) were added to the setup. The pump beam was used to address the PAAD layer, with the orientation of P3 dictating the PAAD alignment, and the transmission of the red (632.8 nm) and NIR (808 nm) probe beams was then measured (in the presence of the pump beam).

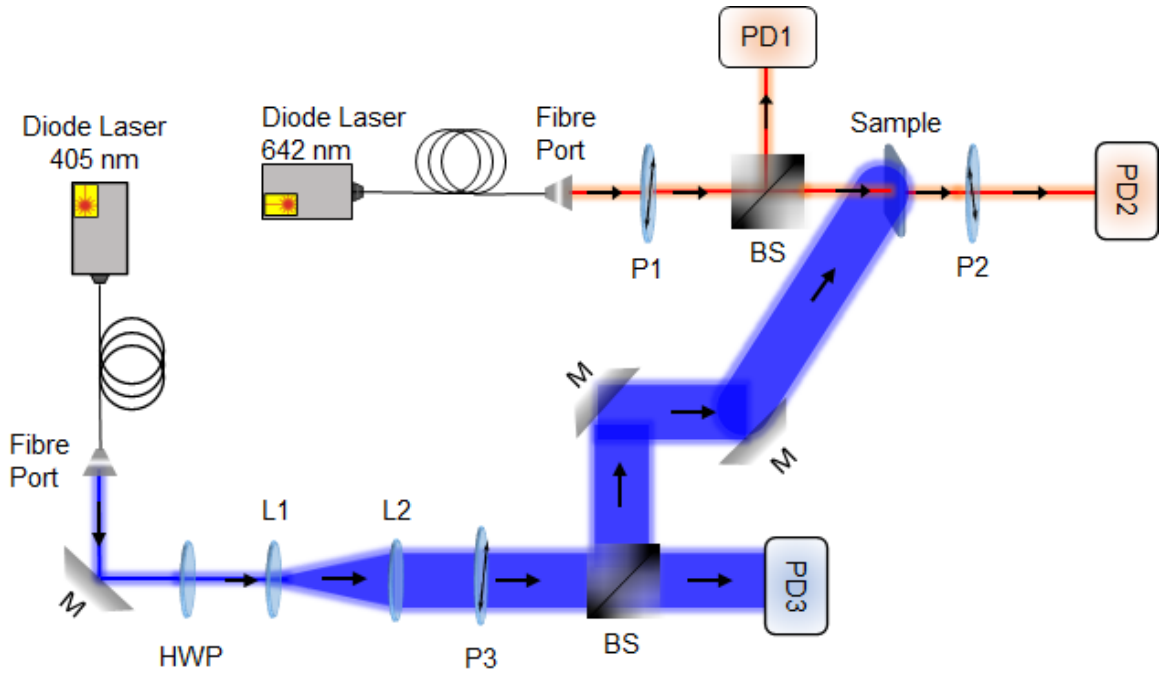

Figure 3-14 Schematics of the optical setup for the pump-probe experiment. A fibre coupled diode laser at 405 nm is used to address PAAD-22D thin films on ITO/glass substrates. The laser beam is expanded with a two lenses system (L1 and L2) to cover the surface across the PAAD film and. A beam splitter (BS) along with two mirrors (M) used to direct the beam onto the sample. The polarisation of the incident light beam was controlled through a half-wave plate (HWP) and a polariser (P3). A second fibre diode laser beam is used to probe the transmitted intensity. The sample is located between two parallel polarisers (P1 and P2), where the light enters at normal incidence. Photodiodes, PD1 and PD2 monitor the power of the laser before and after the cell by exploiting a beam splitter (BS).

The diameters of the red at 632.8 nm and NIR at 808 nm probe beams were 1 and 5 mm, respectively; the corresponding blue (405 nm) pump beam diameters were 1 and 10 mm. The larger pump diameter ensured that the NIR (808 nm) beam probed only the centre of the pump beam, ensuring almost uniform alignment. We remark that expanding the pump beam necessarily reduced its intensity, requiring longer, but still experimentally feasible, exposure times for equilibration. The uniform PAAD reorientation experienced by the expanded beam presented procedural advantages in terms of data analysis. A final experiment returned to the single beam set-up discussed above, but now with the expanded blue beam. This allowed for

the study of the realignment dynamics for a beam with a more uniform intensity, as opposed to its original Gaussian profile.

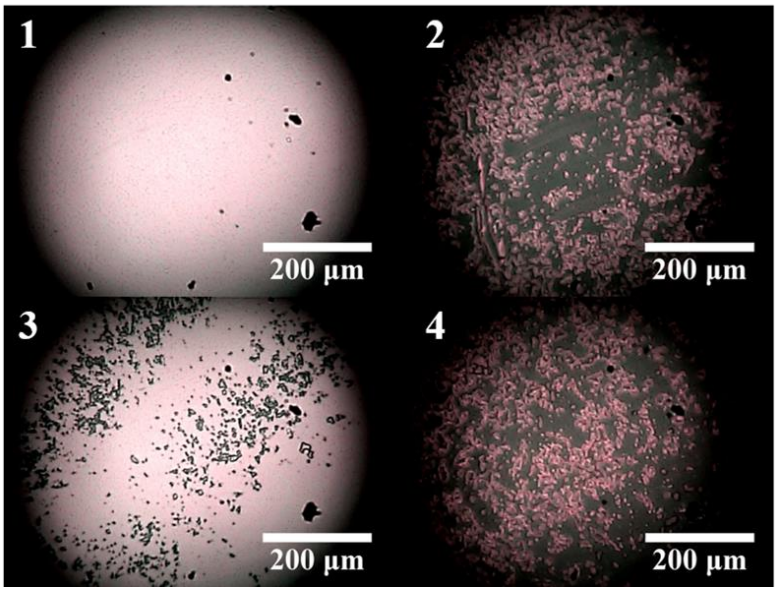

Figure 3-15 Co-polarised microscope images of cells aligned with green (532 nm) beam. Within each panel: 1) Initial planar state. 2) First twisted state. 3) Second planar state. 4) Second twisted state.

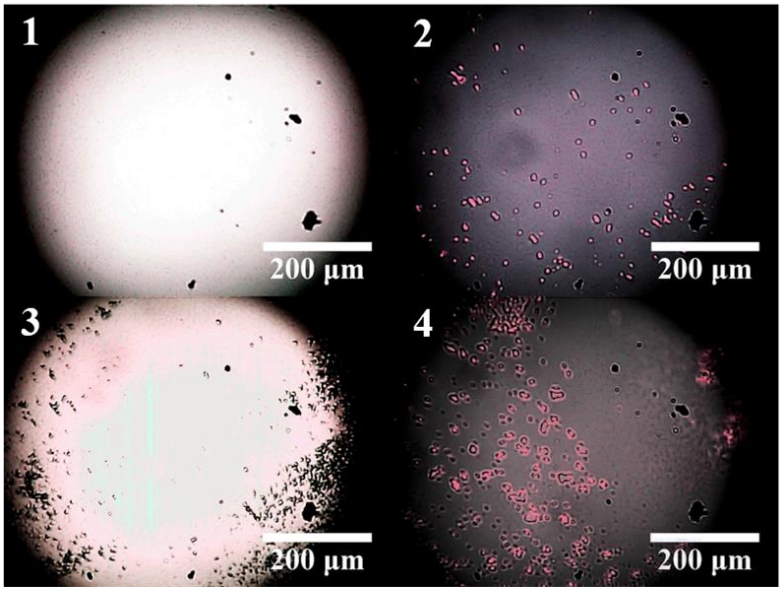

Figure 3-16 Co-polarised microscope images of cells aligned with blue (405 nm) beam. Within each panel: 1) Initial planar state. 2) First twisted state. 3) Second planar state. 4) Second twisted state.

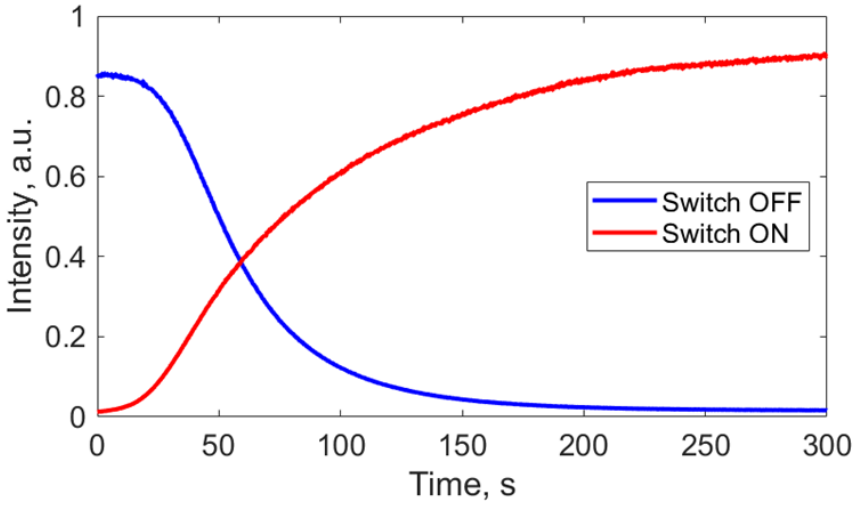

Figure 3-17 Realignment dynamics of PAAD-22D-LC cells by switching between planar → twist (OFF) and twist → planar (ON) states with one step illumination with linearly polarised blue light (405 nm).

3.4.2 Modelling and fitting the transmitted optical contrast

Twisted cells are normally used in the Mauguin limit [144], $2\Gamma/\pi \to 0$, with $\Gamma = 2\pi/\lambda\,\Delta nd$. Here λ is the incident light wavelength, Δn the LC birefringence, and d the LC layer thickness. In this limit, the twisted cell rotates the polarisation of transmitted light by $\pi/2$ and the transmitted intensity for parallel polarisers P1 and P2 is strictly zero. However, there are corrections to this null result when the ratio is merely small. The Jones matrix approach [18], yields an expected transmitted intensity:

$$I(\lambda) = \left(\frac{\pi}{2\Theta}\right)^2 sin^2\Theta, \tag{3.3}$$

where,

$$\Theta = \left[\frac{\pi^2}{4} + \left(\frac{\Gamma}{2}\right)^2\right]^{\frac{1}{2}}. \tag{3.4}$$

Substituting the experimental values into Equation (3.3) yields the values shown in Table 3-3. From these we can see that in a perfectly twisted configuration, the cells used in our experiments should have an optical contrast that is larger than 99% when probed by green and blue light, and that is about 98% and 94% at the red and NIR wavelengths, respectively. We also want to be able to determine the dynamics of the PAAD alignment process. We first

normalize the transmitted intensity data for the cells with respect to planar and twisted reference cells. These cells are of the same thickness and fabricated using two PI ALs. The transmission I(t) is then modelled using the empirical functional form:

$$I(t) = b + \alpha_1 e^{-t/\tau_1} + \alpha_2 e^{-t/\tau_2}. \quad (3.5)$$

The parameter b is the asymptotic intensity, I(t → ∞). The optical contrast is the difference between the intensities in the twisted and untwisted states. Experimentally this varies slightly from step to step, but it is fairly constant after an initial transient, see Figure 3-18(b) and (d). There are two time constants, τ_1 and τ_2 ("fast" and "slow", respectively). In practice we find that with the expanded pump beam a single time constant suffices. Thus, τ_1 seems to reflect the effect of the joint PAAD-LCs dynamics, while τ_2 is a semi-empirical approximation to an average of a multiscale relaxation process over different points in the cell, caused by the non-uniform intensity of the aligning beam. The link between the time constants and the PAAD and LC dynamics, however, remains to be investigated more fully.

Table 3-3: Theoretical transmitted intensity I(λ) for a d = 6.5 μm thick E7 layer in a twisted configuration, see Equation (3.3). The E7 birefringence data was taken from Ref. [56].

λ [143]	**I**
405	0.7%
532	1.0%
632.8	2.1%
808	5.8%

3.4.3 Transmission for multiple probe beam wavelengths in the visible and near-infrared regimes

Figure 3-15 and Figure 3-16, shows microscope images of a cell during two cycles of the twist and untwist alignments, addressed with green and blue light, respectively. Each image is taken at a different point in the cell. Step 1 corresponds to the initial planar state, step 2 to the first twisted state, step 3 to the second planar state, and step 4 to the second twisted state. The

images are taken with the cell between parallel polarisers; the bright regions correspond to the planar state and dark regions to the twisted state. The twisting and untwisting were achieved using a single external laser source as described in Section 3.2.3. It can clearly be seen that the blue beam provides a better alignment than the green, and that in both cases the structures formed are not completely uniform. Moreover, there is a noticeable, although not dramatic, change between the initial PAAD alignment through a cycle of realignment and subsequent alignment.

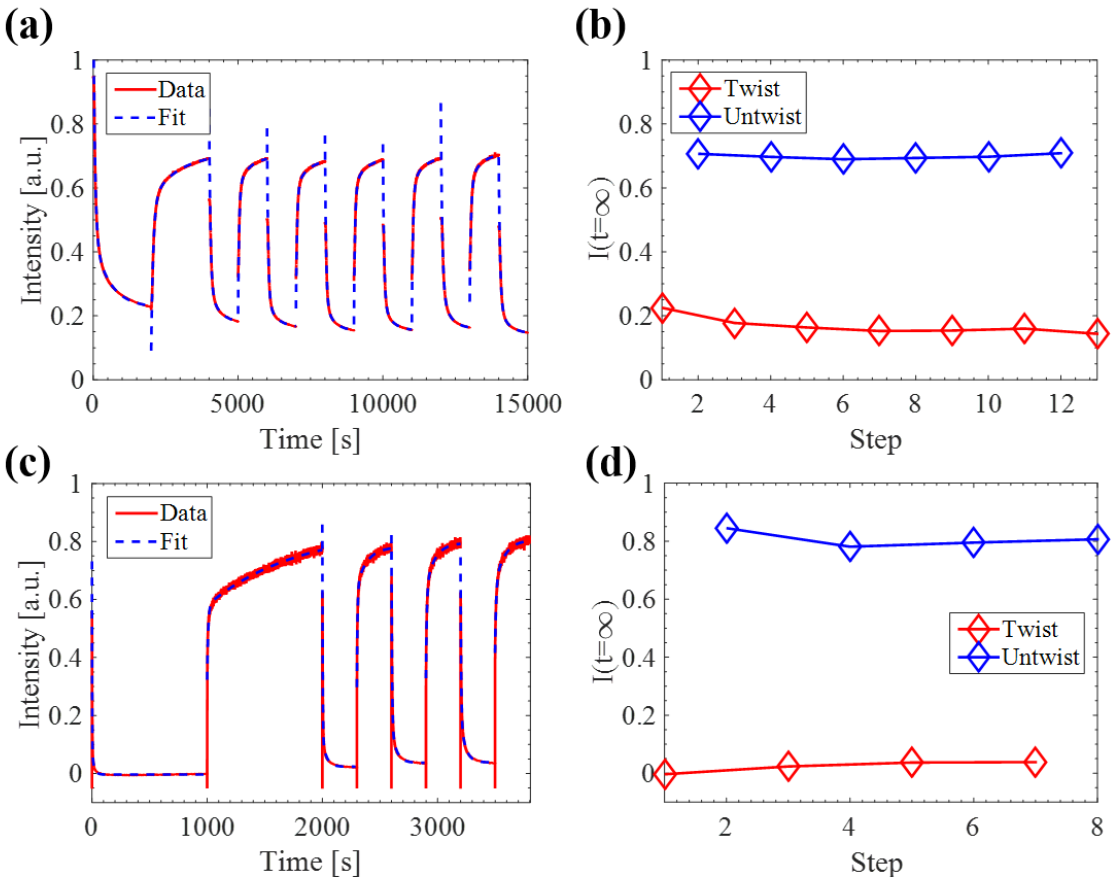

Figure 3-18 Results of the single beam experiments. The top and bottom rows correspond to green and blue beam illumination respectively; the left column shows the transmitted intensity as a function of time over several cycles; the right column shows the normalized asymptotic illumination intensity (parameter b in Equation (3.4)) of the twisted and untwisted states in subsequent cycles.

One can compare this qualitative analysis with the quantitative analysis in Figure 3-18. Figure 3-18(b) and (d) shows the degree of alignment in these cycles in both the green and blue beam cases, respectively. The degree of alignment reached in each step seems to be rather similar, but not identical, especially for the first cycle, consistent with the images in Figure 3-15 and Figure 3-16. The transmittance of the recovered planar state is up to 70% with green light and up to 90% with blue light (in comparison with the reference planar cell). The contrast ratio is

approximately 55% and 80%, respectively. I note that the contrast ratio measurement for the blue beam may be affected by the normalization procedure I have followed: the PAAD layer absorbs part of the blue beam, while its replacement PI layer in the reference cell does not. Therefore, the normalized intensity curves in Figure 3-18(c) cannot reach 1 and the contrast ratio measured is an underestimate of the "real" ratio.

A similar picture appears when considering the dynamics, which is presented in Figure 3-18(a) and (c) for the green and blue beams, respectively. There seems to be a single initial anomalous cycle in which the relaxation process differs from the relaxation processes in subsequent cycles. The relaxation processes in the later cycles repeat reproducibly. I can regard the first anomalous cycle as a transient. The physics of this transient is not yet understood, although I might regard it as being analogous to work-hardening processes in stressed defected alloys. Moreover, the relaxation time is much quicker for the blue beam (compare Figure 3-18(a) and (c) and see Table 3-4). This is to be expected because the blue beam wavelength lies closer to the absorption peak of PAAD-22D. I observed that the same quality of photoalignment could not be achieved by illuminating with a green beam even for extended periods of time. Although the switching times seem large occurring in several seconds (see Figure 3-18 (a) and (c)), keep in mind that the cells are relatively thick, ~12μm and visible pump light lies on the edge of the absorption band of PAAD materials. Nevertheless, large switching times may find use in large-scale applications such as smart windows in trains and buildings. To summarize, these devices are dynamic and switchable with reproducible properties, enabling the control of the transmission and polarisation of the probe beam using only an external light source.

Table 3-4: Fitted values of the time constant τ_1 for three different types of illumination of the PAAD layer.

PAAD illumination	**τ_1 [s]**
Narrow green, 532 nm	46
Narrow blue, 405 nm	5.8
Expanded blue, 405 nm	59

The blue beam provides both faster and better quality photoalignment and was thus used as the photoaligning agent in the pump-probe experiments with red (632.8 nm) and NIR (808 nm) probe beams. Two experiments were carried out, with standard and expanded blue pump beams, respectively. The results of this are shown in Figure 3-19. Figure 3-19(a) shows the first twisting step and Figure 3-19(b) the subsequent untwisting. The equivalent single green and blue beam data are shown for comparison. The NIR data is taken with an expanded blue pump

beam, as explained in Section 3.4.1. The pump intensity was consequently much reduced, and the NIR relaxation process is much slower.

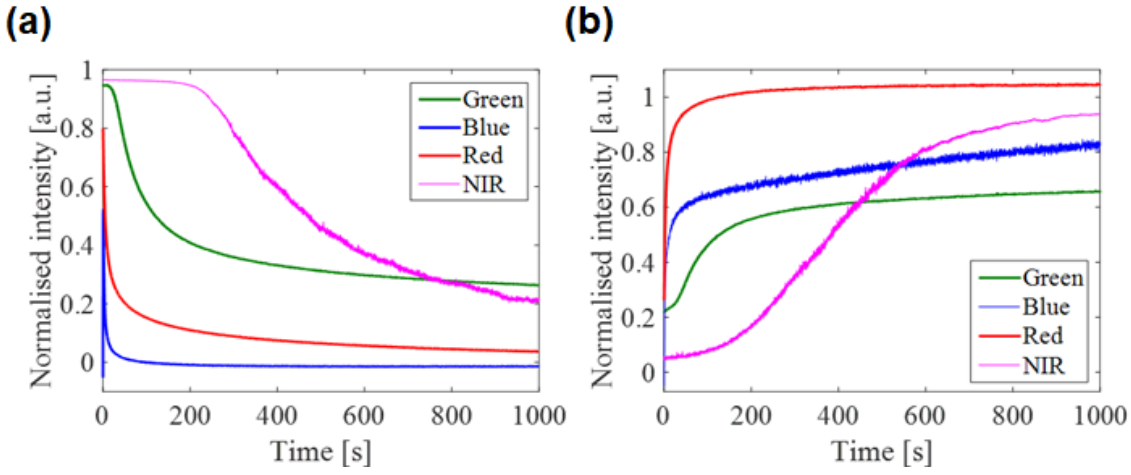

Figure 3-19 Transmitted intensity against illumination time for a green single beam, blue single beam, blue pump and red probe, and an expanded blue pump and NIR probe. **(a)** Initial twisting step; **(b)** Subsequent untwisting. The experimental error of the normalized intensity is 5%, as discussed in Section 3.4.1.

The final set of experiments used the expanded blue pump beam in the single beam set up. In this case, again, the loss of intensity due to the increased beam size resulted in much longer realignment times (see Figure 3-20 and Table 3-4). Importantly, though, the expanded single blue beam relaxation data could be analysed using only a single exponential, as opposed to the two needed for the narrow beam experiments. I thus conclude that the second time constant was in fact the result of the difference in intensities, and hence alignment speeds, between the inner and outer beam, due to its Gaussian profile.

The contrast ratio for the red beam is nearly 100% (compare the two red curves in Figure 3-19). As the red beam twist is driven by a narrow blue pump beam, this indicates that the measured contrast ratio of the single blue beam experiment is indeed affected by absorption in the PAAD layer, as discussed above in the analysis of Figure 3-15 and Figure 3-16. In the NIR beam experiment, the slow time dynamics, and problems in maintaining its stability for such long times did not allow us to reach an asymptotic state and measure the contrast ratio.

The slow dynamics caused by the low intensity of the expanded blue beam has left me with two open problems: (i) the NIR and expanded blue beam have different dynamics (compare Figure 3-19 and Figure 3-20); (ii) the contrast ratio of the expanded blue beam, see Figure 3-20(b), is approximately 65%, much lower than the narrow blue beam. Both effects may be

due to an interplay between the LC and PAAD dynamics and may also be affected by a poorer realignment of the PAAD layer. Both aspects require further study.

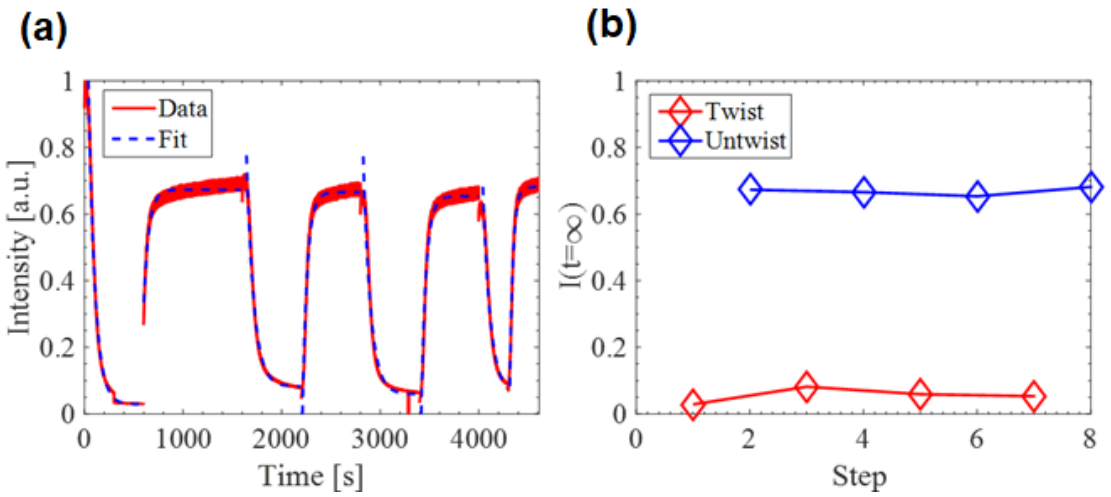

Figure 3-20 Transmitted intensity against illumination time for an expanded blue beam **(a)** Relaxation dynamics for the first few twist/untwist cycles. **(b)** Asymptotic intensities at subsequent twist and untwist steps.

3.5 Conclusions and Future Work

Work previously carried out on PAAD and other azo-based material systems focused on fixed geometries, with UV used to set the alignment [19]. In this thesis, I demonstrated the feasibility of using a PAAD-22D photoalignment layer to fabricate a dynamic system capable of forming rewritable twisted LC structures. The system is all-optically controlled and uses only visible light. There is no requirement for electrodes or an applied field to control the dynamic behaviour. In doing so, I was able to create dynamic half-wave plates for efficiently controlling the transmission and polarisation of light. The PAAD was addressed with green and blue light, with blue proving itself to provide much faster and better-quality alignments. Addressing the same point of the cell, the transmitted intensity of the initially planar cell was repeatedly recovered to approximately 90% after many twist and untwist steps. I have also demonstrated that, with the use of a blue pump beam, the transmission of both red and NIR probe beams can be modulated selectively, with greater than 90% efficiency in the case of the red beam. However, some questions still remain, concerning the precise physics of the relaxation process, the extent of the re-writability, and the anomalous nature of the early cycles of the rewriting process. Future work plans include the investigation of PAAD optical axis exploiting the Ray

Iterated Method [140] and the diffraction efficiency of photo-induced gratings (see Section 7.2.2).

Chapter 4

Liquid Crystal Devices for Manipulating Terahertz Radiation

In this chapter I give an introduction to the subject of THz and LCs. The motivation of this work is the lack of devices to control and manipulate the THz radiation which markedly delays the improvement of THz technology. This thesis aims to develop new systems for future LC-based devices for manipulating THz radiation. LCs were arguably one of the first materials used to control visible and infrared light. However, this is not the case with THz range. LCs have low optical anisotropy in THz frequencies and their thickness, which must be thinner than several hundreds of microns make them impractical as they cannot build the required phase changes for the THz wavelength. Here, I present alternative systems where LCs are functionalised to enhance their performance characteristics in the THz regime. Basic principles about THz radiation and TDS are also included in this chapter. Part of this work has been published as: **Anomalous resonance frequency shift in LC-loaded THz MM.** Perivolari, E., Fedotov, V. A., Kaczmarek, M, and Apostolopoulos, V. (2021). arxiv:2106.12346. Experimental data characterising the profile of THz beam as well as data obtained from TDS got by me. I acknowledge Dr Urszula Chodorow for the data for LC material 1825 [58] (e.g. see 4.5.1, Figure 4-15 and Figure 4-16), however graphs are created by myself.

4.1 Introduction

Over the past thirty years, THz technology has undergone remarkable growth with intense interests for applications in time-domain spectroscopy [145], imaging [146], and biomedical

[147,148] applications. These applications require a variety of active and passive THz optical elements such as polarisers, attenuators, switches, modulators, and phase shifters, which are rarely explored up to now [149-154]. The birefringence of LCs is well known and extensively utilized in optical systems for control and manipulation of visible, and infrared wave beams. Although, LC optical cells are unable to control the intensity of THz radiation, because they cannot be thicker than several hundred microns due to the difficulty to control the LC bulk alignment of such thickness. They also require bulky magnets [155] or a driving voltage in excess of 100 V [156,157].

To improve their optical properties, new LC mixtures have been synthesised altering the chemical structure of existed and well-known materials to create LCs appropriate to manipulate the THz regime [58,158,159]. However, refractive index does not change significantly. An intriguing way of improving the performance characteristics of LCs in the THz regime has emerged from their integration with semiconducting or MM structures [160-162]. Despite that semiconductors have proven to be broadband, these solutions have suffered from a number of drawbacks. In particular, semiconductor-based THz modulators have a very small active area and are able to modulate transmission by only a few percent and partly require cryogenic temperatures [163,164]. On the contrary, when the enhanced light-matter interaction of narrowband MM resonances is combined with an optically thin layer of a LC, which is too weak to produce any noticeable transmission effect alone, can yield a very efficient polarisation control of THz radiation [165,166]. This thesis aims to investigate new THz modulators and phase shifters based on active nano-structured plasmonic MM hybridised with a LC cell.

4.2 Terahertz Radiation – Basic Principles

THz radiation has a wavelength of 30 μm (30 THz) to 3 mm (100 GHz) sitting between microwaves and the long wave edge of far-infrared as shown in Figure 4-1, these frequencies correspond to energies from 40 meV to 0.4 meV. For many years, this frequency band has been remained unexplored. In fact, before the 1970's THz radiation proved a largely inaccessible region between electronic and photonic technologies. The reason for this is that conventional electronic oscillator devices could not function efficiently above ~300 GHz as the devices become unresponsive due to transistor performance above the cut-off frequency [167]. Semiconductor based optical devices also struggle to function efficiently as the energy band gap for THz is small (below 10 meV) compared to the phonon energy of the lattice, and

electronic transitions at room temperature cannot be defined [168]. The difficulties in reaching this region of the electromagnetic spectrum led scientists to coin the term 'THz Gap'.

Though difficult to generate and manipulate, the THz region holds a great deal of interest for scientific research and other practical applications. The vibrational and rotational modes of many atoms exist within this region and many chemical species have strong, unique absorption lines [169]. This has enabled the detection and study of various chemical species, which has made the THz region relevant to a wide breadth of scientific fields such as submillimetre astronomy [170], atmospheric studies [171,172] and molecular spectroscopy [173,174]. In recent decades many THz generation techniques have been explored and developed, increasing our understanding and use of these frequencies and gradually bridging the THz gap between optics and electronics.

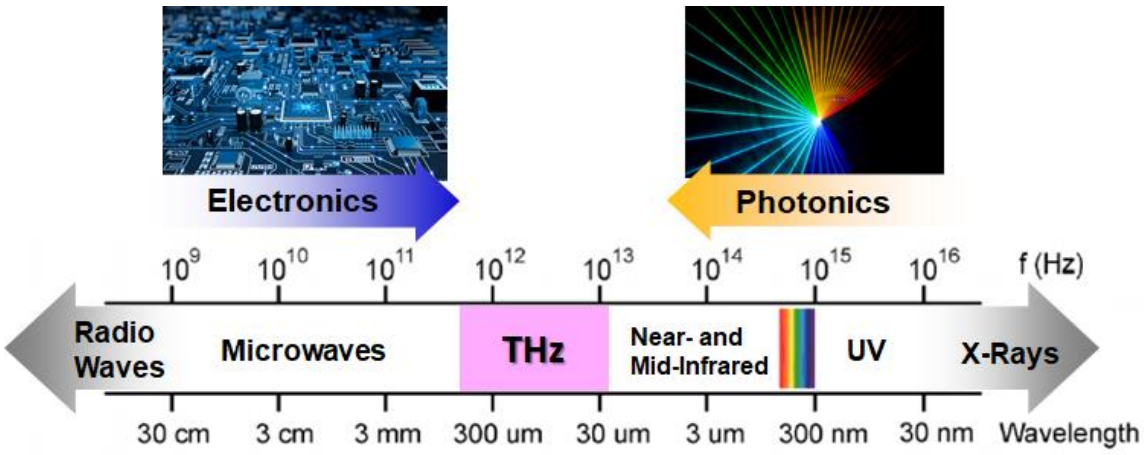

Figure 4-1 Schematic diagram showing the location of the THz region in the electromagnetic spectrum.

4.2.1 The terahertz history

THz history starts before the invention of ultrafast optical lasers, where broadband THz radiation was primarily generated through thermal sources, such as thermal lamps. These sources produce THz radiation as part of their black body spectrum, however, this emission is incoherent and suffers from a low signal-to-noise ratio (SNR) [175]. Other sources used for accessing the far-infrared spectrum included gyrotrons, klystrons and synchrotrons, which were capable of producing megawatts of power up to 300 GHz [176]. The use of molecular vapour lasers allowed access to coherent THz sources [177]. Detection was limited to devices such as bolometers and Golay cells, which are still used for the detection of continuous-wave (CW) THz. Fourier transform spectrometers were also used, however they were found to function best for frequencies above 5 THz [178].

A significant milestone for broadband THz generation and detection was demonstrated after the development in nonlinear optics and semiconductors in the 1960's due to the invention of the laser. New fields of photonics and optoelectronics were born, and shorter optical pulses were created by investigating new mode-locking mechanisms, such as the mode-locked Nd:glass laser. It was this laser that was used by Auston [179] and Lee [180] in the mid 1970's for optically pumping photoconductive switches on Si and semi-insulating gallium arsenide (SI-GaAs). Around the same time two other groups were conducting research towards generating far-infrared pulses from nonlinear crystals [181,182]. As laser pulses grew shorter photoconductive switches could be activated faster, leading to the generation of 1.6 ps THz pulses by Auston et al., in 1984 [183]. The pulses generated were then detected by another photoconductive 'Auston' switch on the opposite side of a dielectric slab, thus giving birth to modern THz science. In the same year Auston investigated nonlinear rectification for generating THz [183] and soon after demonstrated its use for spectroscopy [143]. The past 20 years have seen a significant progress in the THz regime also with the addition of THz quantum cascade lasers (QCLs) and frequency combs [184].

In the late 1980's and early 1990's, many advances took place in the field of THz science. *De Fonzo* demonstrated single cycle THz pulses propagating through air before detection [185]. Shortly afterwards *van Exter et al.* demonstrated a system for pump-probe spectroscopy which would become the typical standard for THz spectrometer design [186]. The system, based on a synchronous emission and detection scheme, was similar to that shown in Figure 4-2. The pulses from an ultrafast laser were split into a pump and probe beam. The pump beam was focussed between two electrodes separated by 5 μm fabricated on the surface of a semiconductor, acting as an 'emitter'. An applied bias was used to accelerate the carriers generated by the pump pulse, creating a dipole parallel to the material surface which radiates on a picosecond time scale [187]. The THz pulse generated is focussed by a sapphire lens onto a collimating parabolic mirror. The pulse is then focussed onto a second, unbiased 'detector' antenna by another parabolic mirror and sapphire lens. The probe pulse from the laser is directed onto the 'detector' antenna in the same manner as the pump pulse is aligned onto the 'emitter' antenna. The carriers produced by the probe pulse are accelerated by the THz field present at that moment. As the laser pulses and carrier lifetimes are much shorter than the THz pulse the carriers in the detector antenna see the THz as a DC field. By measuring the current produced in the detector antenna it is possible to deduce the strength of the THz field at that time. Delaying the optical pulse which excites the THz pulse by way of a mechanical delay line allows the THz field variation with time to be measured. Electrically gating the emitter allows for a lock-in amplifier to increase the SNR. By applying a Fourier transform onto the data both the amplitude and phase information of the pulse can be found.

In the succeeding years THz science and technology has developed and matured. The invention of the self-mode-locked Ti:sapphire laser in 1991 [184] (which could produce pulses below 100 fs) helped the spread of THz research. Research continued towards increasing the detectable bandwidth range, with Wu et al. demonstrating detection with a flat frequency response over an ultrawide bandwidth with nonlinear crystals [188]. The work accomplished in these early years led to the development of the THz time domain spectrometer (THz-TDS), a system still commonly used for research and commercial purposes. These systems offer a high SNR and, as the electric field of the THz pulse is directly measured, can also provide phase information which gives THz-TDS a major advantage for spectroscopy. Today THz technology is employed in a wide and varied range of fields.

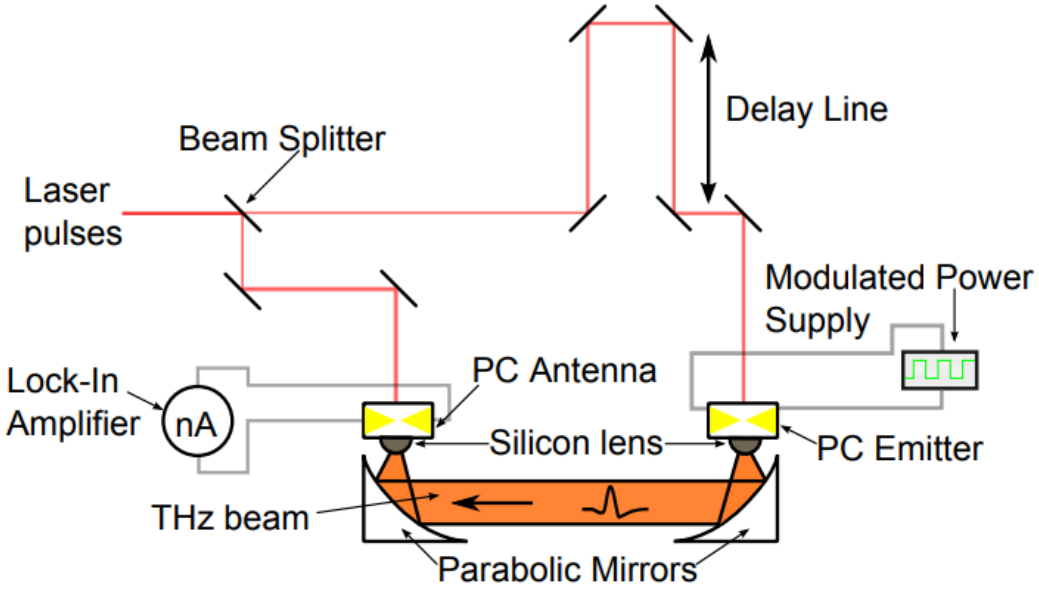

Figure 4-2 THz-TDS setup incorporating PC antennas for both emitter and detector. A femtosecond laser beam is split into pump and probe beams. The pump beam travels via an optical delay line before exciting THz radiation in the emitter. In this example the emitter is electrically modulated by an external power supply. The THz field is collimated by a parabolic mirror before being focussed onto the detector by a second parabolic mirror. The probe beam excites carriers within the detector which are accelerated by the instantaneous THz field. The current generated by this is detected by a lock-in amplifier.

4.2.2 Applications

THz radiation finds uses in applications ranging from security screening and spectroscopy, to medicine and art conservation due to its unique properties. Many materials that are opaque at visible frequencies are transparent in the THz region, such as plastics, ceramics, clothing,

and paper [24]. In the case of dielectrics, absorption is dominated by optical phonons with energies above that of THz radiation [175].

Unlike X-Rays, THz radiation is non-ionising and does not damage DNA. This makes it useful as imaging technique for biological and medical applications. In fact, THz imaging has been used for the in–vivo study of human skin tissue, obtaining tomographic information and mapping the hydration content of the samples [189]. Reflection scans of human skin have shown it is possible to differentiate between scar tissue, healthy and diseased skin, allowing detection of the spread of skin cancers [190]. The use of THz in 3D dental imaging has also been studied [191]. This allows the measurement of enamel thickness on teeth and the identification of subsurface features. This method is non-destructive and negates the need for invasive drilling or the health risks associated with dental X-rays.

The low absorption of several materials to THz makes it ideal for security applications. THz radiation can be safely used in airports and public spaces for scanning due to its non-ionising nature. There are now mm-wave full body scanners installed in some airports for detecting weapons and illicit materials, but these devices have raised concerns about privacy [192].

Further, THz has proved a useful tool even in the art world for the process of restoration. Many tools such as X-Ray fluorescence, IR spectroscopy and photographic examinations have been used to study paintings but either prove to be limited in detail or potentially damaging [193]. THz radiation has been demonstrated as a non-destructive method [194], able to reveal details about the paint layers, materials and can even be used for tomography of the painting through raster scanning. As canvas was expensive artists would often paint over previous or unfinished work to save money. Hidden paintings can be revealed by THz scanning techniques, as well as damage and forgeries [195].

Finally, the characterisation of an impressive range of materials in the THz regime has been an important component in the rapid development of THz technologies. Materials, such as LCs [196], nanocomposites [197], MMs [198] have been characterised in THz regime and should promise for THz devices for controlling and manipulating THz radiation, such as phase shifters and THz modulators.

4.3 Terahertz-Time Domain Spectroscopy

A milestone for THz science was the demonstration of the generation of freely propagating broadband, single cycle pulses from photoconductive antenna (PCA) by D. H. Auston et al. [183]

in 1984. These sources directly led to the application of THz-TDS. THz-TDS generates broadband THz radiation in the form of a THz pulse, it also measures the time dependent electric field of the THz pulse. If the THz pulse is incident on a material, then that material will modify the time dependent electric field of the THz pulse according to its optical constants in the THz region. Material parameter extraction is a method of determining the optical constants of the material from its modification to the THz electric field recorded by a THz-TDS.

THz-TDS employs a synchronous detection scheme resembling a pump-probe setup with inherent high SNR which allows for accurate measurements. As the electric field is directly measured within THz-TDS it is not only possible to measure the amplitude information but also the phase which gives it a major advantage over other spectroscopy systems. THz emitters used in THz-TDS can be broadly divided into two classes. Those based on non-linear frequency conversion of a femtosecond laser spectrum to the THz frequency range and those based on semiconductor photoconductivity. In this thesis, for the generation and detection of THz radiation the latter technique is used.

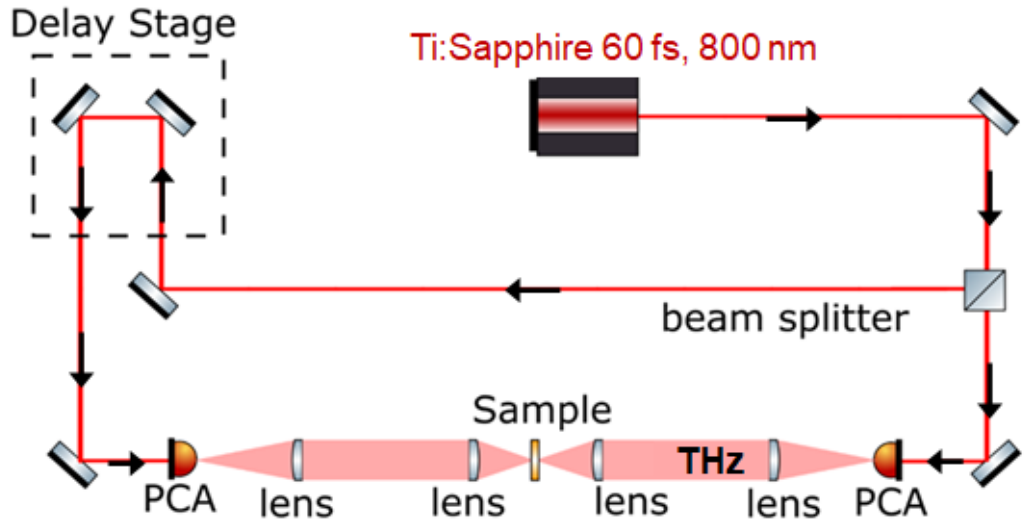

Figure 4-3 Schematic representation of a custom THz-TDS setup. An 800 nm Ti:Sapphire fs laser (60 fs, 80 MHz repetition rate) is used to generate THz pulses of about 1-2 ps. THz-TDS utilizes a synchronous detection method resembling a pump-probe setup with inherent high signal to noise ratio which allows accurate measurements. Briefly, the beam is split into two beams with a beam splitter. One beam is sent to the THz emitter (GaAs photoconductive antenna, PCA), where the THz pulse is generated. The THz pulse illuminates the sample with aid of a four-lens system and then is collected by the detector. The other beam (60 fs) passes through a delay line and hits detector, where it gates it, and the detector is activated. Now by varying the delay line, the short 60 fs pulse can resolve in time the longer generated THz pulse (1-2 ps).

Figure illustrates a schematic of the THz-TDS setup mainly used during this thesis. Briefly, I used a custom THz-TDS system based on a Ti:Sapphire near-IR, 60 fs laser with GaAs photoconductive (PCA) emitter and detector [199-201]. The beam of the ultrafast femtosecond laser is split into two beams with a beam splitter. The one beam is sent to the THz emitter, where the THz pulse is generated. The THz pulse then propagates through the four system lenses to the detector, which we use to collimate and focus the beam. These lenses are the so-called Tsurupica lenses, which are transparent in the THz and optical regime with similar refractive indices. The other beam is sent to the detector, where it gates it, and the detector is activated and can record the THz electric field at a small point in time relative to the length of THz pulse. Thus, the delay stage is used to change the optical length between the beam splitter and the detector (either increase it or decrease it). Thereafter, the THz electric field can be mapped out in time by the detector. The emitter is optically (by chopper) modulated, and a lock-in amplifier is used for the detection of the THz electric field, which is increasing the SNR. With a Fourier transform the information of the phase and the amplitude can be determined. For spectroscopy applications the sample is placed within the THz beam path (among the four lenses) and a trace of the THz electric field is measured. This measurement is compared with a reference scan made without any sample present allowing for both amplitude and phase information of the materials transfer function to be measured using algorithms that model the system [202]. THz-TDS have been widely used for determining the complex refractive indices of materials and calculating the dispersion and the absorption of different materials in the THz regime [203,204].

4.3.1 Generation and detection of terahertz pulses

In THz-TDS the most commonly used emitters and detectors consist of a photoconductive semiconductor (PCS) and two electrodes with some μm gap in the middle [183,200,201]. Semiconductors such as GaAs (gallium arsenide) have been used for photoconductive THz generation and detection [205]. These antennas usually have a bandwidth spanning from 100 GHz to 2-3 THz in transmission mode as GaAs absorbs above 3 THz [205].

A schematic of a PCA is shown in Figure 4-4, it consists of a photoconductive semiconductor with a gold structure deposited on the top to form the antenna. The semiconductor is excited by an optical pulse which is focused between the antenna gap to produce carriers. A titanium sapphire (Ti:S) ultrafast laser is usually used to excite carriers across the band-gap of GaAs. The ultrafast Ti-Sapphire pulse (800 nm), which must be focused on the semiconductor gap, is suitable with the band-gap of GaAs (870 nm) for the generation of THz pulse.

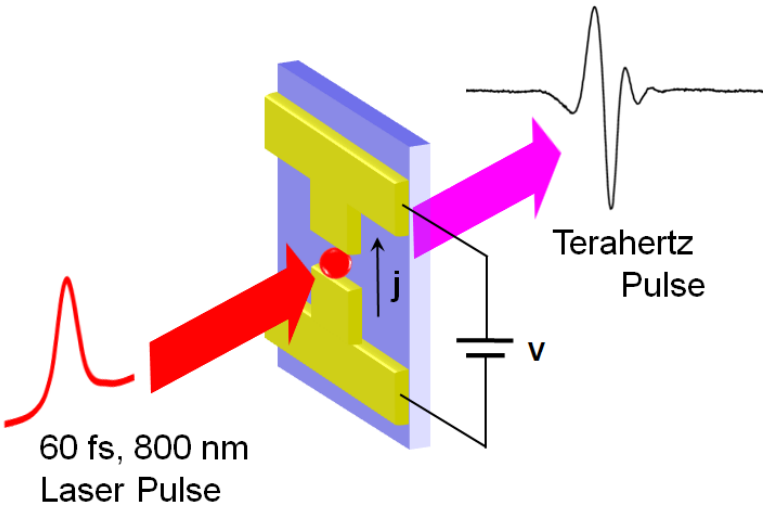

Figure 4-4 An illustration of a typical photoconductive antenna (PCA). The incident laser pulse excites carriers which are accelerated by the bias voltage to generate a photocurrent. The red dot is the focused laser beam between the two biased antenna structures fabricated on a semiconductor material (GaAs) with a band-gap that matches the energy of the laser. The resulting charge separation causes dipole emission of THz frequencies.

The carriers are accelerated by an electric field which is provided by a bias voltage. For emission an electric field in the region of 100 kV cm^{-1} is applied to the electrodes across the antenna gap. The production and acceleration of the carriers within the semiconductor creates a rising photocurrent which decays after some time due to the recombination of the electrons with the holes. The rise and fall of the photocurrent produce a time varying electric dipole which radiates a broadband THz pulse.

For the detection of THz radiation GaAs PCA is used, similarly to the one used as emitter. In principle the photoconductive detection is the reverse of the generation method [206]. The antenna is now unbiased and illuminated from the laser pulse which generates the photocarriers. These photocarriers are then accelerated by the incident THz electric field. The produced current can be measured across the antennas gap by a lock-in amplifier and is proportional to the strength of the THz electric field. Because the carrier lifetime and the laser pulse length are shorter than the THz pulse, the carriers see the THz field as a DC electric field. Therefore, by varying the delay path between the THz and optical pulses the variation of the THz field can be mapped out in time. The resulting pulse is the convolution of the THz electric field and the time dependent conductivity of the PCA detector.

4.4 Terahertz Time Domain Scans

In THz-TDS time dependent measurements both the amplitude and phase of the THz electric field are recorded using our custom THz-TDS shown in Figure 4-3. Should a material be present in the THz beam path the THz electric field will be modified due to the dielectric properties of the material. This allows the determination of optical properties for a material over the THz bandwidth. Figure 4-5 shows two time dependent measurements of the THz electric field. The reference scan in black is a time domain scan for the electric field of a THz pulse passing through air and the sample scan in red is a time domain scan for the electric field of a THz pulse passing through a 1.17 mm fused silica sample.

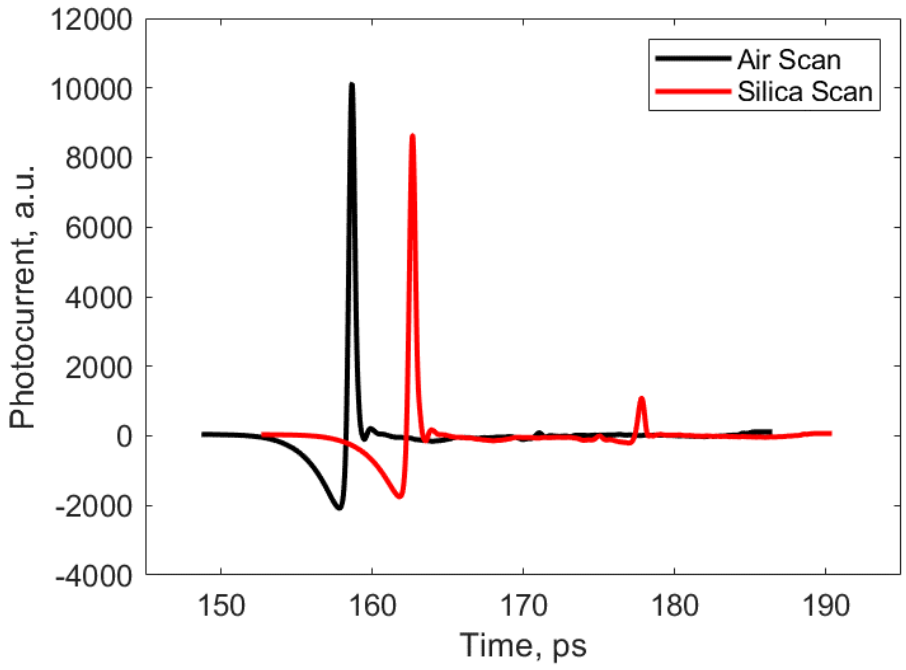

Figure 4-5 Time domain scans of the THz electric field of a 1.17 mm fused silica sample (red) and reference air scan (black) taken using our custom THz-TDS.

By comparing the differences between the sample (i.e., silica) and reference (i.e., air) scans, it is possible to determine information about the sample such as the refractive index. This can be determined by the time difference (Δt) between the main pulse in the reference and the sample scan as follows:

$$n_a = 1 + \frac{c\Delta t}{d}, \tag{4.1}$$

where d is the sample thickness and c is the speed of light in vacuum. The time difference is proportional to the sample's thickness. Here, the sample pulse is delayed by 7 ps with respect to the reference pulse and the amplitude of the main pulse is reduced as THz partially absorbed by the material. Ideally, we neglect the reflection pulses which follow the main ones, to avoid having oscillations in the THz scans as they complicate the data analysis. For this I use a double exponential window function to truncate experimental data. The window function starts after the main THz pulse to remove reflections as depicted in Figure 4-6. After the window function, the data is replaced with zeros, and the original data length is kept because consistent frequency resolution between scans is important to divide the two scans.

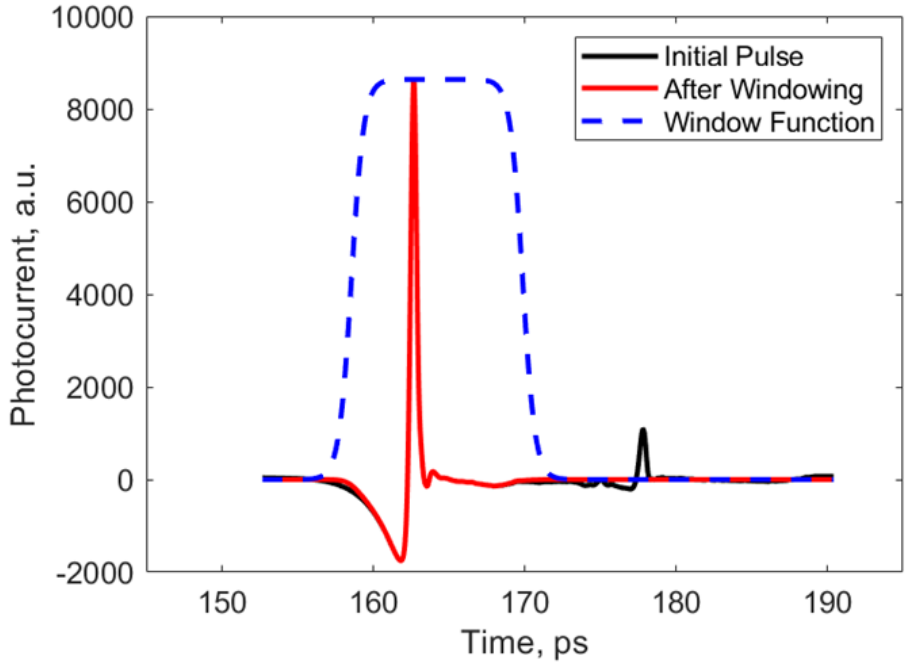

Figure 4-6 Time domain scan of the THz electric field of the 1.17 mm fused silica sample. Black colour stands for the initial pulses, dashed blue for the window function, and red for the resulting pulses after windowing.

The etalon effect of the sample has been demonstrated as a method for frequency calibration of THz-TDS [89] by comparing the transmission spectra of thin sample with a Fabry-Perot etalon model. It is crucial for the accuracy of our results to reduce the oscillations of the etalon effect of the experimental data, caused by the etalon effect. This way it will be easier to observe the absorption peaks and dips of the amplitude. Oscillations in the frequency domain can be given by:

$$\Delta f = \frac{c}{2n_a d} \tag{4.2}$$

where c is the speed of light in a vacuum, n_a is the refractive index of the etalon and d is the etalon thickness. For an etalon with average refractive index of 2.0 (quartz) [207], thickness 1.17 mm, the free spectral range is 64 GHz which is the same frequency as the oscillations observed in Figure 4-8.

Thereafter, the amplitude and the phase of the spectra is found by first taking the Fourier transform of the individual THz scans and then taking the natural logarithm of the Fourier transforms, which separates the amplitude and phase of the spectra into real and imaginary components. The amplitude and phase of the spectra are shown in Figure 4-9 and Figure 4-10 respectively.

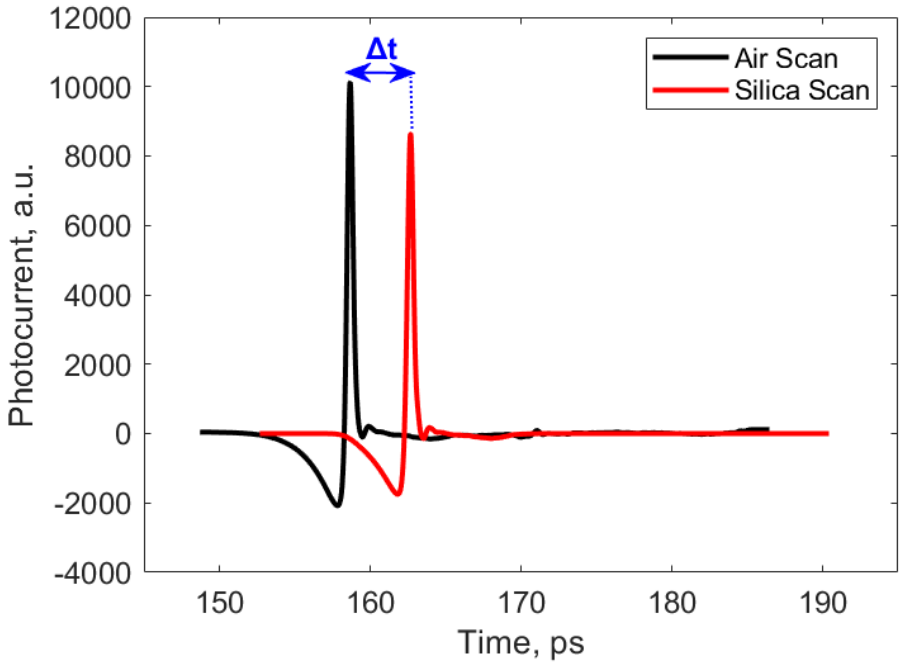

Figure 4-7 THz electric field of a 1.17 mm silica sample (red) and a reference air scan (black) after windowing.

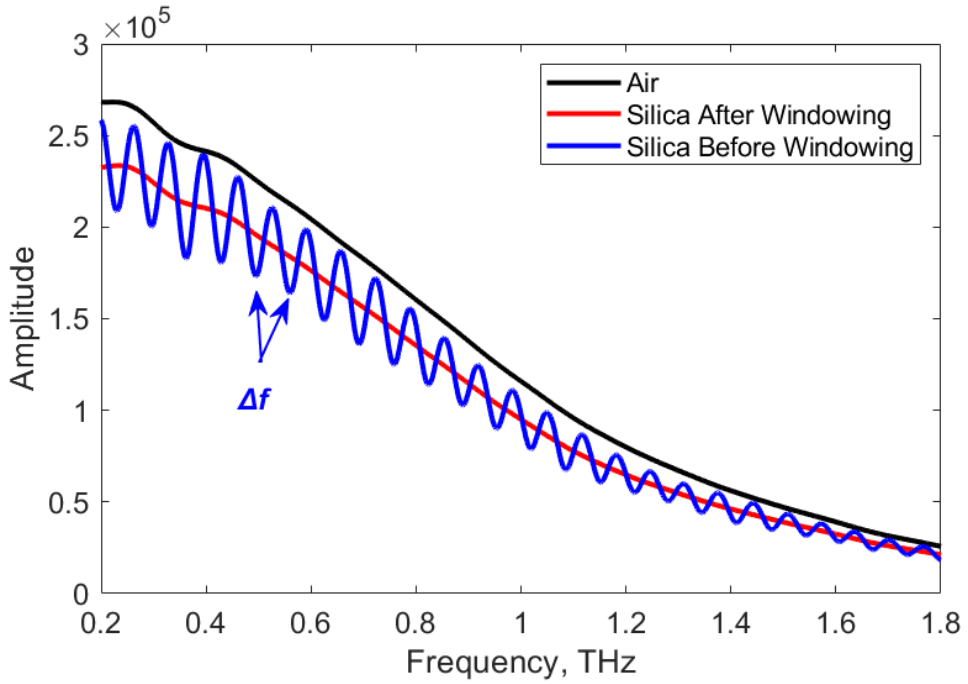

Figure 4-8 THz spectra of a reference, air (black) and a sample, silica before (blue) and after (red) windowing.

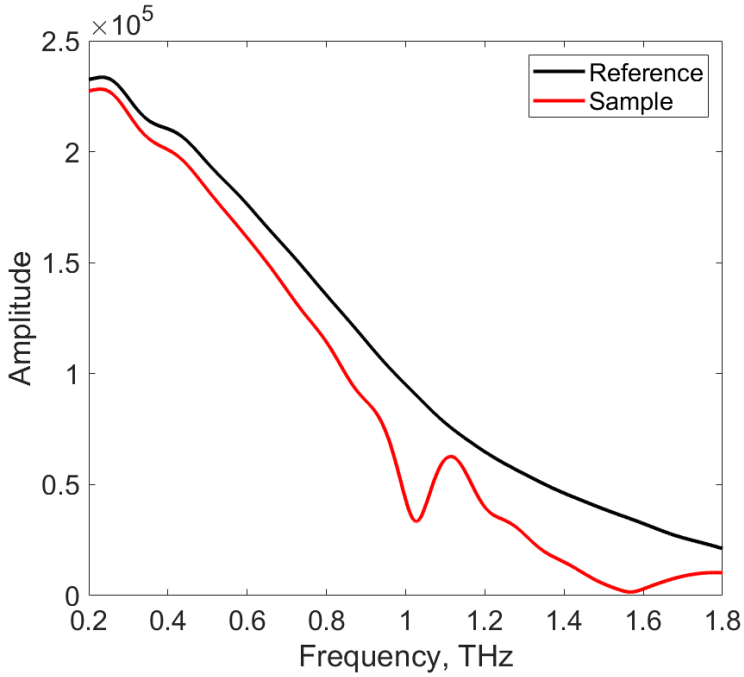

Figure 4-9 THz spectra of a reference, silica (black) and a sample, metallic resonator (red).

In the transmitted frequency there are peaks and dips in the amplitude which indicate absorption within the system. To observe visually these changes in absorption it is more

practical to normalise the sample's amplitude with respect to the reference. Although, silica does not exhibit any resonances in the frequency range of the spectrometer to observe and hence Figure 4-9 and Figure 4-10 present the results of a resonator, i.e., sample, and silica is used as a reference. Finally, by dividing the amplitude of the reference from the sample and by subtracting the phase information about transmission and phase can be extracted (see Figure 4-11). This is a standard analysis process I used to obtain THz properties.

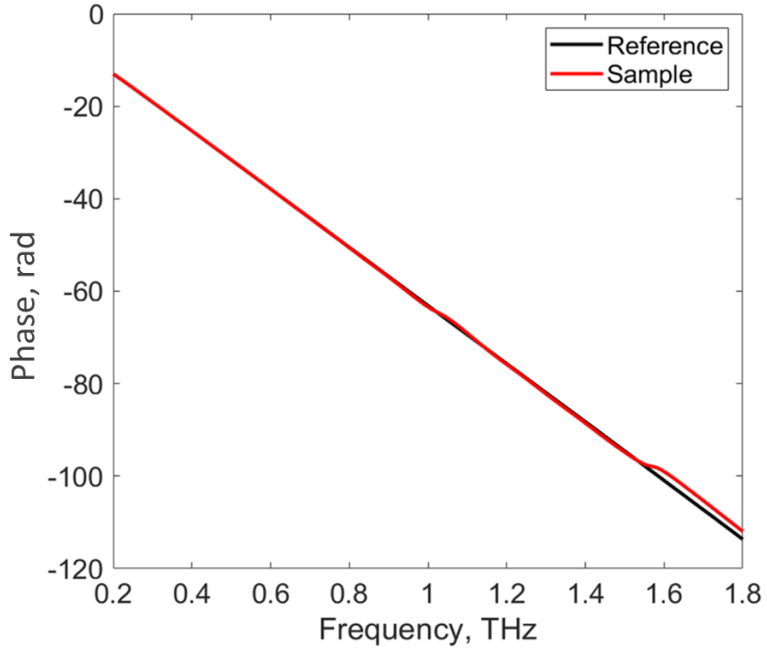

Figure 4-10 Phase of a reference, silica (black) and a sample, metallic resonator (red).

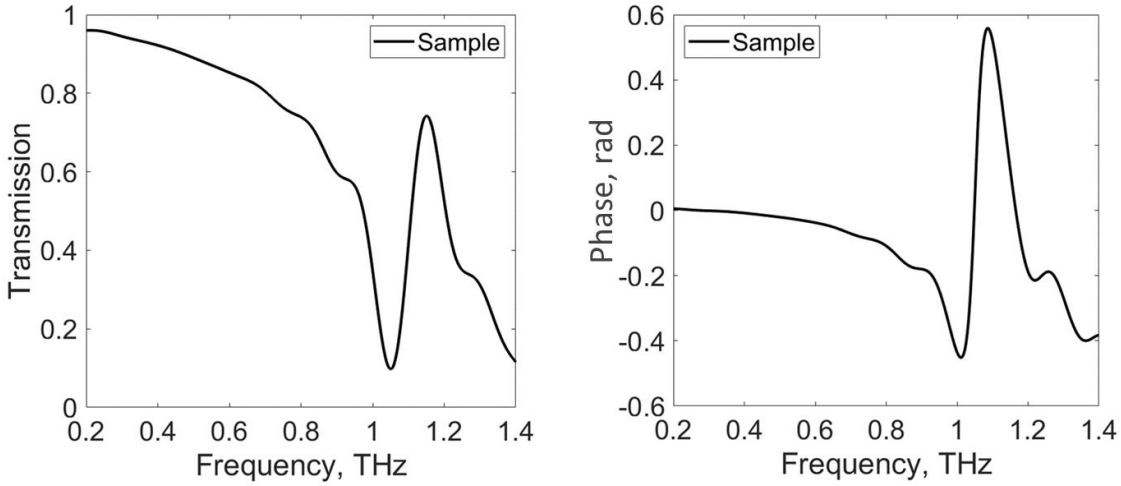

Figure 4-11 Normalised THz spectra of the sample i.e. metallic resonator. Transmission (left) and phase (right).

4.4.1 Terahertz spot size

The knife-edge experiment is a measurement of the waist of a laser beam near the focus of a lens. In particular, this technique is a beam profiling method that allows for quick, inexpensive, and accurate determination of beam parameters. Briefly, a knife-edge moves perpendicular to the direction of propagation of the laser beam, and the total transmitted power is measured as a function of the knife-edge position [208]. A schematic of the experimental setup is shown in Figure 4-12.

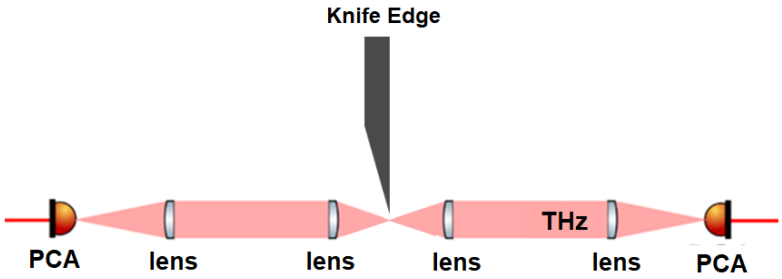

Figure 4-12 Knife-edge experiment: The THz pulse is generated with the aid of GaAs photoconductive antenna, PCA, and then propagate through a four-lens system collected by the detector. Knife edge measurements are made along the THz beam at the focal point by varying the position of the knife edge.

To define the beam profile, multiple time dependent measurements of the THz-TDS took place (see Figure 4-13). Knife edge measurements were made at 3 mm intervals along the THz beam among the Tsurupica lenses using a blade mounted on an x-y translation stage. The transmitted THz amplitude was read from a lock-in amplifier and the position of the knife edge was recorded from the x-y stage.

The normalised transmitted power as measured during one knife-edge scan in the x direction is presented in Figure 4-14. The experimental data appear in the red dash dot line while the fit in the black solid line. When the knife-edge located at 0 mm, is where I cut the power in half, which means I reached the centre of the beam. As a consequence, this is the exact position I should locate my sample in order to achieve the higher response. To fit the data, I used the following expression [209]:

$$P = P_0 + \frac{P_{max}}{2}\, erf\left(\frac{\sqrt{2}(x - x_0)}{w}\right) \tag{4.3}$$

where P_0, is the background power, P_{max}, the maximum power, x_0 the centre position of the Gaussian intensity profile, and erf is a standard error function. The beam radius w, is obtained by the fitting procedure at 5.1 mm, precisely.

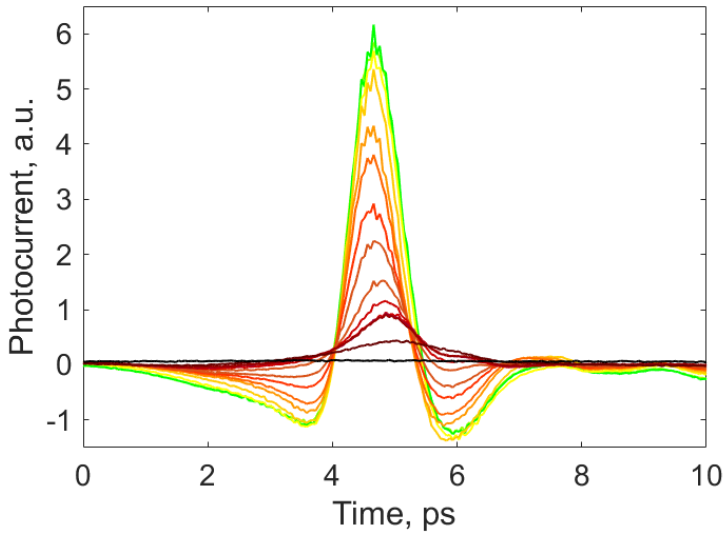

Figure 4-13 Time scan of detected THz signal as a function of knife edge position. Black colour stands for knife edge blocking completely the THz signal.

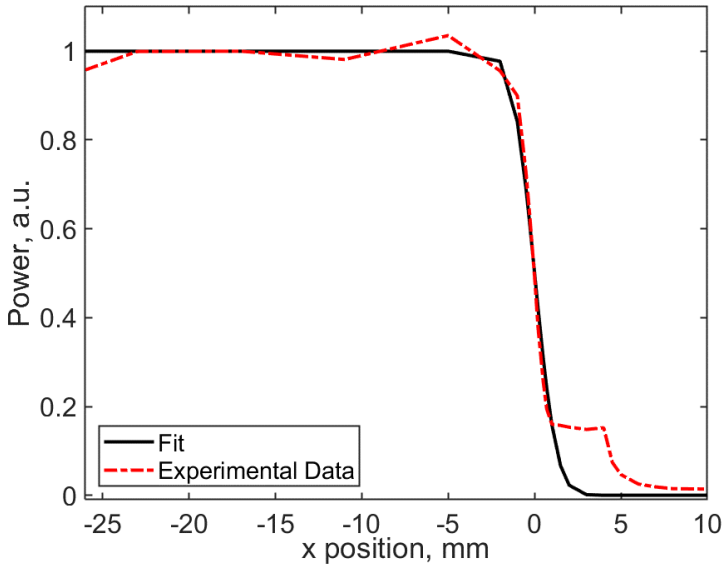

Figure 4-14 Knife-edge profile of the focused THz beam against the knife edge position: experiment (dash dot red line) and fit according to the expression of *P* (solid black line).

4.5 Terahertz Properties of Nematic Liquid Crystals

In recent decades, THz applications ranging from spectroscopy of chemicals and explosives to bio-medical imaging of breast cancer and skin diseases have been explored [210-212]. For these and other applications using THz waves, optical devices such as waveplates and polarisers are essential components. LCs have been studied for various applications at visible frequencies, such as displays, tunable optical elements, communications, signal processing and beam steering, because they typically have large birefringence, and the orientation of the LCs can be externally controlled by electric or magnetic devices. LCs also provide an attractive option for optical devices at THz frequencies: phase shifters, Fabry-Perot filters, polarisers, phase gratings, Bragg switches and tunable MMs have already been demonstrated and proposed [213-217]. However, the practical implementation of these devices is hampered by the relationships between birefringence, thickness and LC switching time. For example, the performance of a phase shifter is determined by the following equation relating the phase (δ) to the thickness (d) and birefringence (Δn) of the LC for a particular wavelength (λ):

$$\delta = 2\pi \cdot \Delta n \cdot d/\lambda \tag{4.4}$$

Therefore, a phase shift of π at 1 THz (λ = 0.3 mm) for a typical birefringence of 0.15 would require an LC layer 1 mm thick (see Table 4-1). In comparison, the same phase shift at visible frequencies (e.g. green light at 550 nm) requires an LC layer only 1.8 μm thick. As a result, the absorption of the LC at THz frequencies becomes an important consideration. Furthermore, the response times increase with increasing thickness, such that the turn-on (τ_{on}) and turn-off (τ_{off}) times are given by the following equations [71,218,219]:

$$\tau_{off} = \gamma_1 d^2/K_x\pi^2 \tag{4.5}$$

$$\tau_{on} = \tau_{off}/|(V/V_{th})^2 - 1| \tag{4.6}$$

$$V_{th} = (K_x/\varepsilon_0\Delta\varepsilon)^{1/2} \tag{4.7}$$

where $\Delta\varepsilon$ and V are the dielectric anisotropy of the LC mixture and the switching bias voltage of the cell respectively, γ_1 is the rotational viscosity and K_x is the appropriate expression for the elastic constant of the LC mixture, which is dependent upon the alignment of the LC cell. Vth (see Equation (1.15)) is known as the threshold voltage of the LC cell. Given the squared

dependency on thickness for both turn-on and turn-off times, fast devices at THz frequencies will require relatively high birefringence materials. Whilst the birefringence of LC mixtures is well documented at visible frequencies, very little is known about their properties in other frequency regions, including at THz frequencies. In order to develop fast and efficient optical devices based on LCs, it is essential to understand their optical and mechanical properties as the ordinary and extraordinary refractive indices, n_o and n_e, and viscosity.

4.5.1 High-birefringence nematic liquid crystal mixtures for terahertz applications

Optical anisotropy, namely birefringence imposed by the commercial LCs [58,220] is not sufficient for THz frequencies as discussed previously in Section 4.5. Here, I discuss the endeavours from many research groups to overcome these limitations by exploring novel high-birefringence nematic LCs suitable for THz applications.

Table 4-1: Comparison of the THz properties of E7

	Group (year)	Frequency, THz	n_e	n_o	α_e, cm^{-1}	α_o, cm^{-1}
E7	Jewell et al 2008 [216]	0.2-1.2	1.76	1.61	1.7	2.6
	Yang et al 2010 [221]	0.3-2.0	1.70	1.57	5.0	15.6
	Park et al 2012 [158]	0.2-2.0	1.74	1.59	4.2	14.3

Briefly, LC materials containing unsubstituted cyclohexylbenzene and bicyclohexyl benzene isothiocyanates, biphenyl-, fluoro-substituted terphenyl-, tolane- and phenyl-tolane isothiocyanates LCline compounds were investigated due to their high-birefringence, high polarity, and low viscosity [222,223]. By combining several components one can control the properties of resulting liquid crystalline mixtures, such as birefringence, viscosity, refractivity indices, dielectric permittivity, and elastic constants in accordance with requirements for various display and non-display applications. In order to determine the material properties of LCs THz-TDS is used. These measurements can determine parameters, such as refractive indices, birefringence, or absorption. LC E7 is among the first commercial nematic materials examined in the THz region [221] (see Table 4-1 and Table 4-2).

Table 4-2: E7 parameters and τ_{on} at 1 THz (accuracy:+/− 5%)

	γ_1, mPa·s	$\Delta\varepsilon$	K_{11}, pN	K_{22}, pN	τ_{on} at 1 THz, s
E7	282.8 [224]	13.8	11.1	17.1	2.36

Investigated nematic LC mixtures: 1870, 1852A, 1867, and 1825 are new materials and were synthesized in the Institute of Chemistry in the Military University of Technology (PL) [58]. The measurements were made at room temperature to obtain THz material properties such as refractive indices and absorption coefficients. Investigated materials have wide temperature range of nematic LC phase. In this thesis, I have exploited the LC mixture 1825 with the transition from nematic to isotropic phase proceeded at 136.0 °C. The specific material processes the largest birefringence (0.4) in the THz range of 0.2 – 3.0 THz compared to the other LC mixtures [58]. In fact, at 1.5 THz the extraordinary and ordinary refractive indices are 1.951 and 1.574, accordingly.

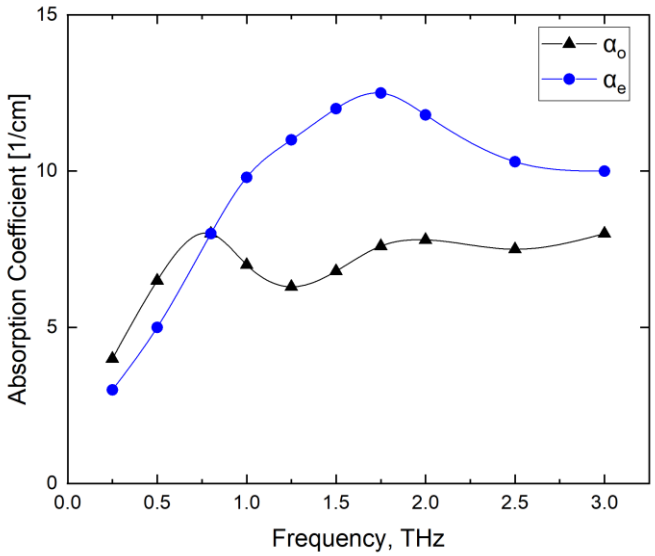

Figure 4-15 Absorption coefficients for ordinary (o) and extraordinary (e) ray of the highly birefringent LC mixture 1825 [58].

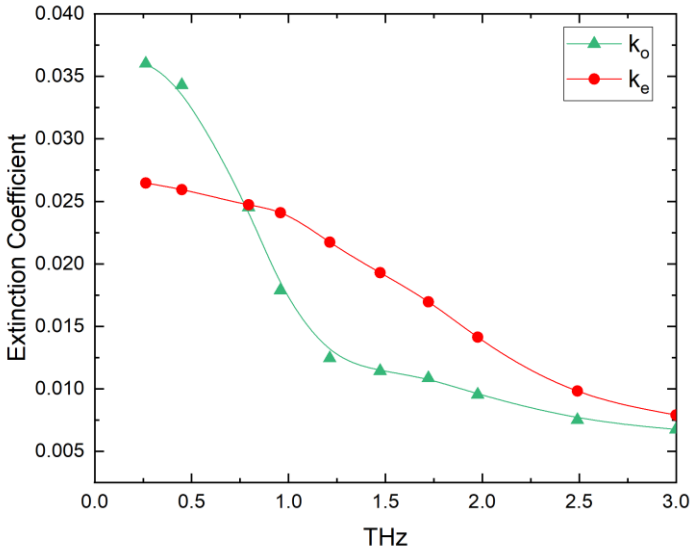

Figure 4-16 Extinction coefficients for ordinary (o) and extraordinary (e) ray of the highly birefringent LC mixture 1825 [58].

In addition, the absorption coefficients are presented in Figure 4-15, as obtained by [58]. Thereafter, by following the progressive wave equation of a plane wave of frequency (f) propagating through a solid with velocity (v) in a direction defined by (x), the electric field (E) is described as:

$$E = E_0 exp\{i2\pi f[t - (x/v)]\} \tag{4.8}$$

where, E_0 is the incident electric field vector and $\{i2\pi f[t - (x/v)]\}$ is the displacement at time t after a disturbance, created by the electric field at a point situated at x along the line of propagation. Since the velocity of propagation through the solid of complex refractive index $n_{eff} = n - ik$ is related to the speed of light in a vacuum by $v = c/n_{eff}$, then:

$$\frac{1}{v} = \frac{n}{c} - \frac{ik}{c} \tag{4.9}$$

Therefore, substituting 1/v into Equation (4.8):

$$E = E_0 exp(i2\pi f) exp\left(\frac{-i2\pi xn}{c}\right) exp\left(\frac{-i2\pi fkx}{c}\right) \tag{4.10}$$

where, $\left(\frac{-i2\pi fkx}{c}\right)$ is a measure of the damping factor, or extinction coefficient (k). As the power (P) or intensity of an incident wave through a solid is the conductivity (σ) of the solid multiplied by the square of the electric field vector ($P=\sigma E^2$), then using the damping factor term, the fraction of the incident power that has propagated from position (o) to a distance (x) through the material with conductivity (σ) is given by:

$$\frac{P(x)}{P(0)} = \frac{\sigma E^2(x)}{\sigma E^2(0)} = exp\left(\frac{-4\pi fkx}{c}\right) \tag{4.11}$$

from which the absorption coefficient (α) can be expressed in terms of the extinction coefficient (k) as:

$$\alpha = \frac{4\pi fk}{c} \tag{4.12}$$

As the velocity of light in a vacuum, $c = f\lambda$, then $\alpha = 4\pi k/\lambda$, and the power or intensity is $P = P_o exp^{-\alpha x}$. This equation is known as Bouguer's law or Lambert's law of absorption, by which radiation is absorbed to an extent that depends on the wavelength of the radiation and the thickness and nature of the medium. Reflecting on the absorption coefficient measurements, we calculated the extinction coefficient (k) and present the data for LC 1825 in Figure 4-16. Evidently the material's losses are negligible indicating an efficient performance in THz. Further, material's parameters such as elastic constants and viscosity are also presented as determined by [58]

Table 4-3: Material parameters of 1825 mixture at 25 °C.

	T [°C] N→I	**T [°C] C→N**	**Δε**	**K_{11} [pN]**	**K_{22} [pN]**	**K_{33} [pN]**	**K_{TN} [pN]**	**Γ [mPa s]**	**γ [mPa s]**
1825	136	-12	17.0	12.5	7.4	32.1	16.8	31	284

Following the optical and physical parameters of LC 1825, we can calculate the threshold voltage capable of switching homogeneously aligned nematic LCs (Fréedericksz transition) by Equations (1.14) and (1.15). Given the data from Table 4-3 we calculate,

$$V_{th} = V_F = \sqrt{\frac{\pi^2 K_{11}}{\varepsilon_0 \Delta\varepsilon}} = 0.9\ V \tag{4.13}$$

4.5.2 Evaluating liquid crystal properties for manipulating the terahertz regime

Alternative methods to increase the birefringence of the LC materials without changing their chemical structure are discussed in this section.

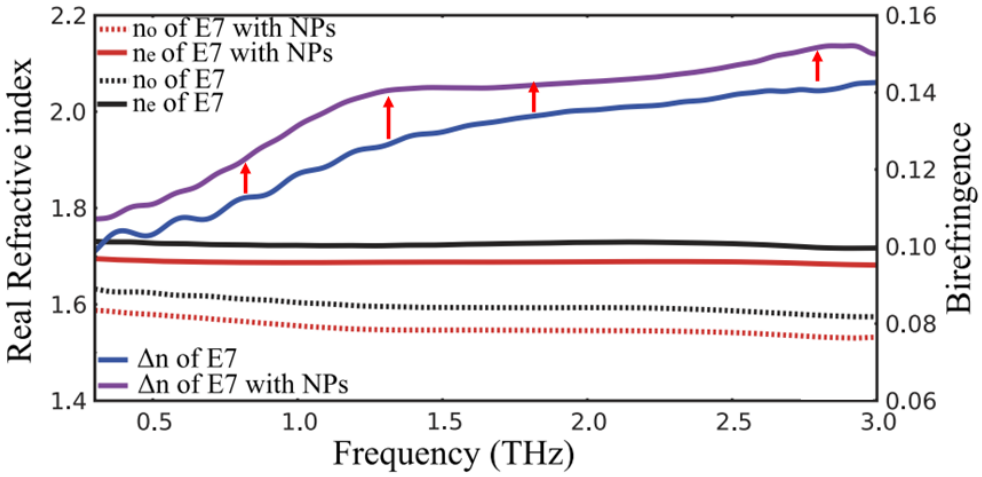

Figure 4-17 Ordinary (no) extraordinary (ne) refractive indices and birefringence (Δn) of E7 and suspension of E7 and BaTiO3 NPs provided by [159].

It has been already reported that in the optical spectrum a hybrid LC and nanoparticle (NP) mixture, with a low concentration of ferroelectric NPs, can improve the birefringence of the material and decrease the Fréedericksz transition threshold voltage [77,79]. Doping of the LC with NPs, with size between 10-100 nm, can lead to significant increase of the dielectric anisotropy and of the birefringence of the suspension without disturbing the LC alignment at expense of higher losses though. The enhancement of LC parameters is caused by the ferroelectricity of NPs, which produces large dipole moments, and thus large electric fields between the NPs. As an example, Figure 4-17 presents the refractive indices and birefringence for the commercial nematic LC E7 doped with $BaTiO_3$ NPs between 0.3 to 3 THz. The hybrid mixture shows an increase of up to 10% in birefringence in comparison with the pure E7.

Therefore, enhanced birefringence can be observed without synthesis of new LC mixtures capable of manipulating the THz regime.

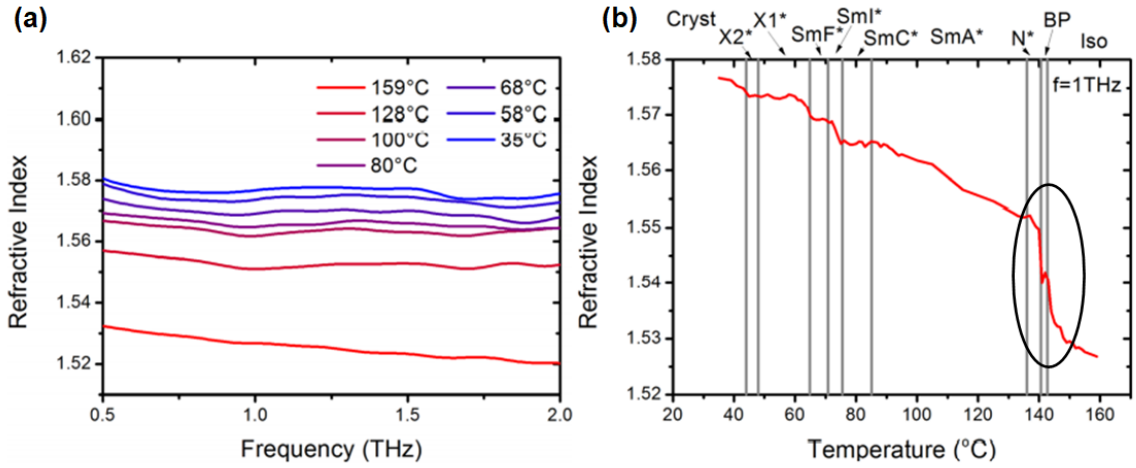

Figure 4-18 (a) Refractive index of LC material for different temperatures. (b) Temperature dependence of the average refractive index of LC material at 1 THz frequency. The phase transitions between the different LC phases are indicated in the graph. Provided by [225].

Increase of the refractive index of LC materials in the THz regime has also been reported upon variation of the temperature [225]. In fact, it is shown that phase transitions (i.e., from nematic to isotropic) that are correlated with structural ordering at different dimensions clearly reflect in the THz refractive index. There, the optical properties such as refractive index and birefringence, and also the dielectric permittivity are very sensitive to phase transitions and hence depend on temperature. This effect is investigated at THz frequencies using THz-TDS. From Figure 4-18 (a), it can be clearly seen that refractive index of LC material varies with temperature. Nevertheless, for all temperatures the refractive index does not vary significantly over the frequency range considered but shows a rather flat dependence.

Further, Figure 4-18 (b) depicts n at 1 THz as a function of temperature passing through all the LC phases from the isotropic liquid to the crystalline state. One can clearly observe pretransition effects in the isotropic phase between 160 and 140 °C, due to increased orientational and positional fluctuations.

Despite the proven advantage of hybrid LC structures, these solutions suffer from a number of drawbacks. In particular, refractive index does not change significantly in order to manipulate THz light when in a relatively thin layer. Conventionally, new technologies impose compact, thin devices of few µm which seems unrealistic here. Accordingly, variation of temperature limits the range of applications and complicates the alignment of LC molecules. Among to the mainstream solutions, room temperature LC phase shifters have also been demonstrated. The

phase shift is achieved by electrically or magnetically controlling of the effective refractive index of LC layer, as depicted in Figure 4-19 (a) [226]. The magnetic field aligned the LC for a cell as thick as 1.5 mm, while the electric field with driving voltage of 100V aligned a nematic LC E7 of 1.83 mm (see Figure 4-19 (b, c)) [157]. Great attention has been further attracted by sub-wavelength metal grating that acts as both transparent electrodes and a built-in THz polariser to control the input waves' polarisation. In fact, a highly-compact self-polarising phase shifter is demonstrated by electrically tuning the effective birefringence of a nematic LC cell. Metal grating polarisers ensure a good polarising efficiency in the range of 0.2 to 2 THz and a phase shift of more than π/3 is achieved in a 256 μm-thick cell (see Figure 4-19 (d, e)) [156].

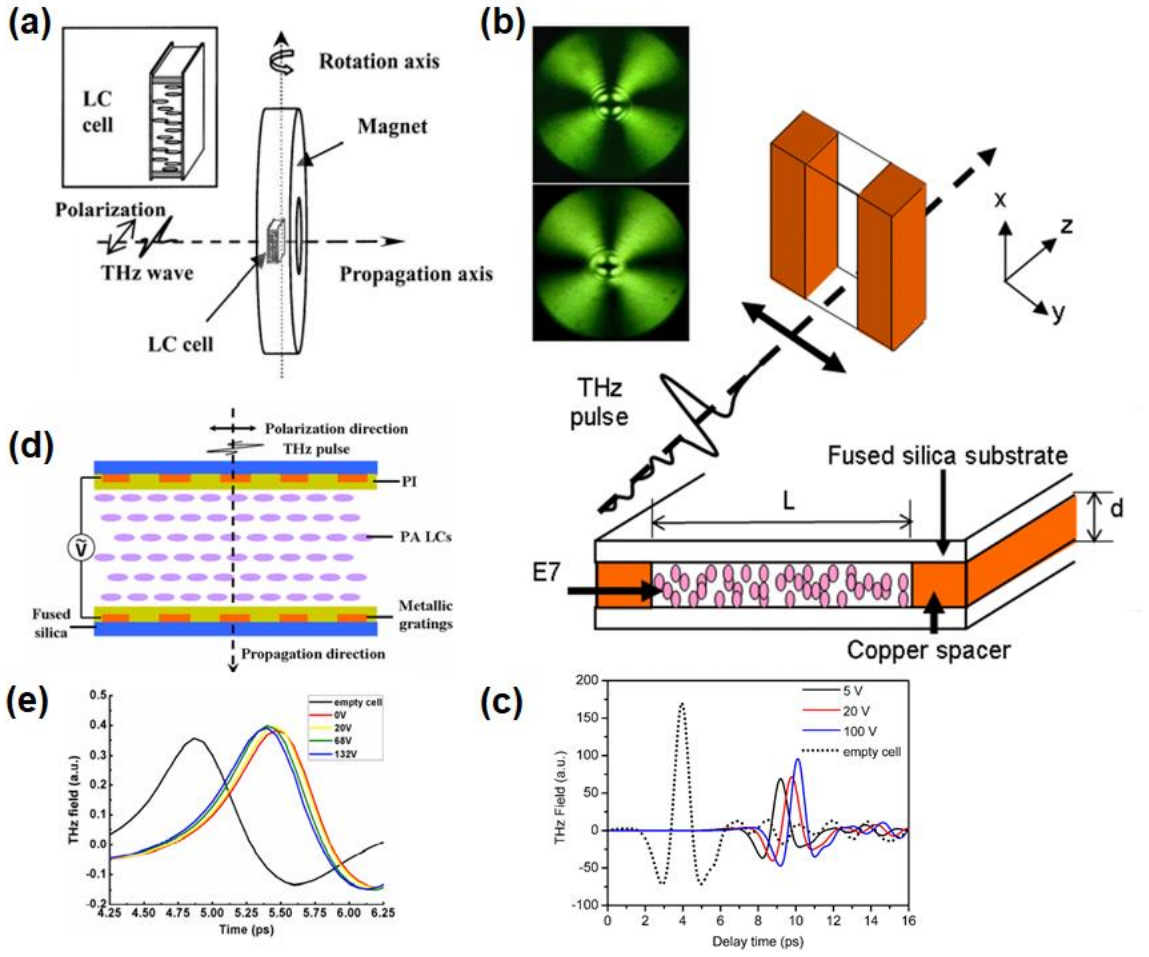

Figure 4-19 (a) Schematic diagram of the (a) magnetically [226] and (b) the electrically THz phase shifter using a LC cell [157]. (c) Temporal waveforms of the THz pulse transmitted through the empty and LC cell at various applied voltages [157]. (d) Schematic drawing of a self-polarising THz LC component [156]. (e) Time-domain spectra of the empty cell and the LC-filled cell when applied no voltage and three specific voltages [156].

4.6 Liquid Crystal-Metamaterials Integrated Devices for Efficient Control of Terahertz Radiation

Engineering artificial materials, the so-called MMs [227], are becoming one of the mainstream solutions for the THz technology [228-230]. Electromagnetic MMs have advanced rapidly and had a major impact in technologies spanning from RF and microwave technologies to photonics and nanophotonics [231].

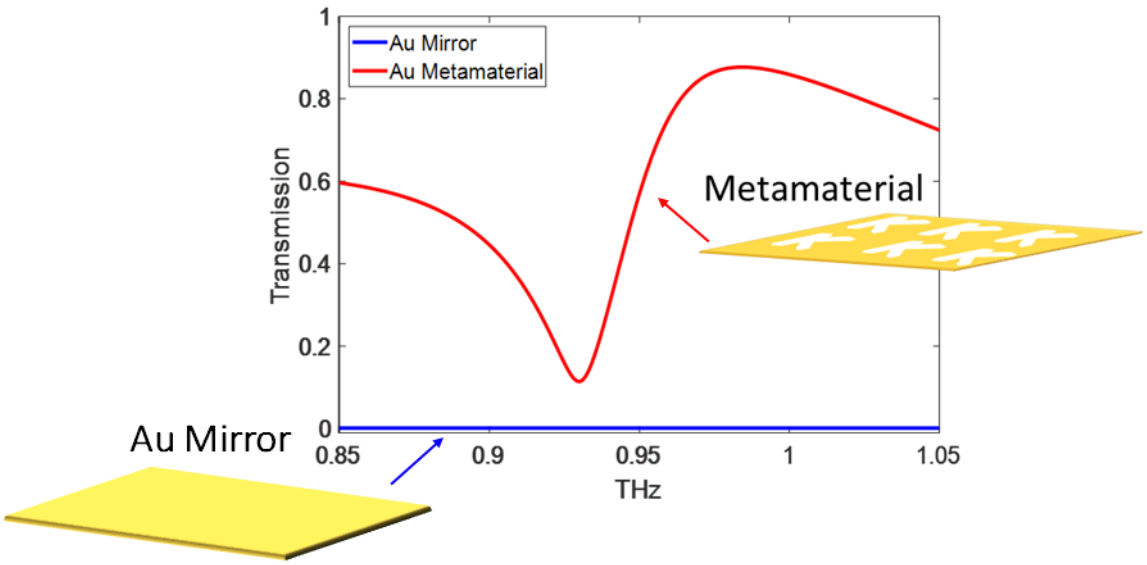

Figure 4-20 Comparing the transmission spectra of a gold mirror versus a gold MM. Mirror gives zero transmission, diffracting the incident light, whereas MM shows a homogenous response absorbing at a specific frequency. MMs derive enhanced properties different from its constituent materials and often going beyond the range of properties available in natural materials.

In principle, MMs represent a special class of low-dimensional artificial photonic media—periodically structured metallic surfaces and thin films that can transmit, reflect, and absorb light with no diffraction. They derive novel or enhanced properties from structuring on the sub-wavelength scale. Thus, MMs show a homogenous response, different from its constituent materials and often going beyond the range of properties available in natural materials (see Figure 4-20). Its name is derived from the Greek word μετά = meta, meaning "beyond", i.e., beyond-materials. The MMs concept not only has brought to life such exotic optical effects as artificial magnetism [232,233], negative refraction [234], and cloaking [235], but also enabled dramatic enhancement of light-matter interaction leading to amplified absorption [236], asymmetric transmission [236], giant polarisation rotation [237], and slow light [238,239].

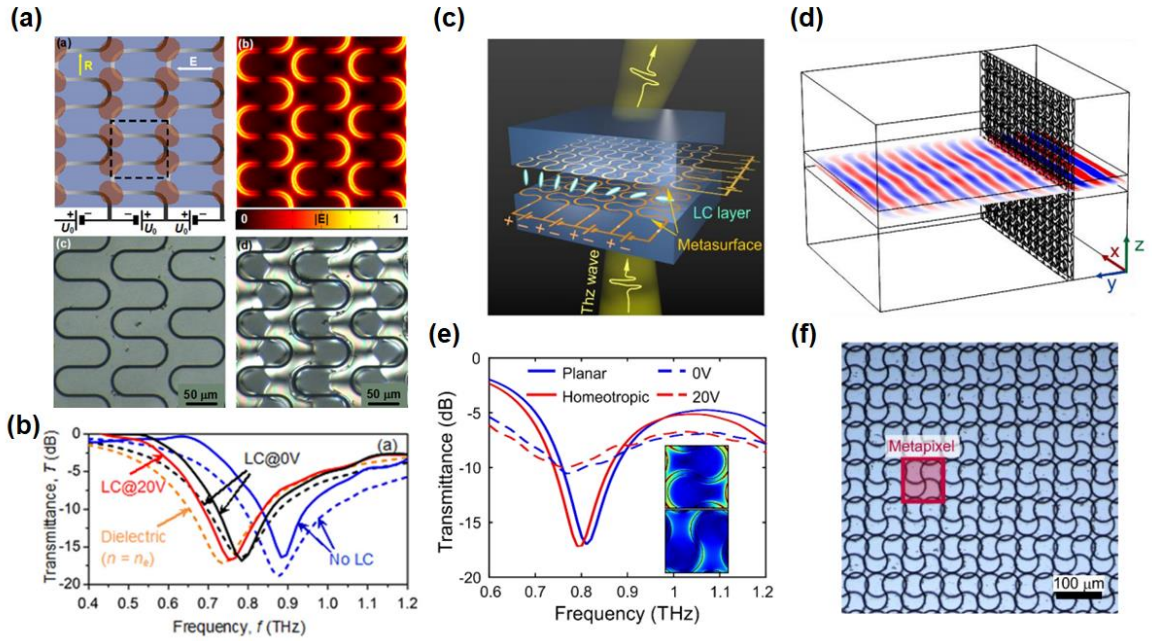

Figure 4-21 (a) Schematic and microscope images of fish-scale planar MM used in [165]. (b) Transmission spectra for both empty and LC-loaded MMs [165]. (c) An artistic impression of a spatial phase modulator [240]. (d) The geometry of the COMSOL model used for simulating the operation of the spatial phase modulator [240]. (e) Simulated (solid lines) and measured (dashed lines) transmittance spectra of the spatial phase modulator presented for two limiting cases of LC uniform alignment corresponding to planar/ 0 V (blue) and homeotropic/ 20 V (red) [240]. (f) An optical microscope image of the fabricated spatial phase modulator designed to operate at a frequency of 0.8 THz [240].

The key to the enhanced light-matter interaction in MMs is a narrowband resonant response, which can be engineered in metallic MMs at virtually any frequency within the THz band taking the advantage of very large dielectric constants of metals. Although the frequencies of MM resonances are determined by the structure of MMs and, therefore, are fixed by the design, they can be tuned with the help of functional materials integrated into the fabric of MMs. Nematic LCs were arguably the first functional media successfully exploited for active control of MMs [241,242], offering an easy-to-implement control mechanism based on reversible refractive index change [6].

LC-loaded MMs have since become a very popular and well-researched artificial material system with many applications across the electromagnetic spectrum, and in particular, in the THz domain [161,243-249]. For example, efficient active control of THz radiation has been demonstrated by *Buchnev et al*, [165], by using an actively controlled large-area planar MM (metafilm) hybridized with a 12 μm thick layer of a LC (see Figure 4-21 (a)). Active control was introduced through in-plane electrical switching of the LC, which enabled to achieve a reversible single-pass absolute transmission change of 20% and a phase change of 40° at only

20 V, as shown in Figure 4-21 (b). Further, the concept of a spatial phase modulator for correcting THz wavefronts in transmission has been introduced by *Fedotov et al.* [240]. It exploited a combination of resonant planar MMs and ultra-thin LC layers, as depicted in Figure 4-21 (c). With a LC thickness of 12 μm the suggested spatial light modulator is capable of changing the phase of transmitted THz wavefronts by applying a driving voltage of ~20 V (see Figure 4-21(c)).

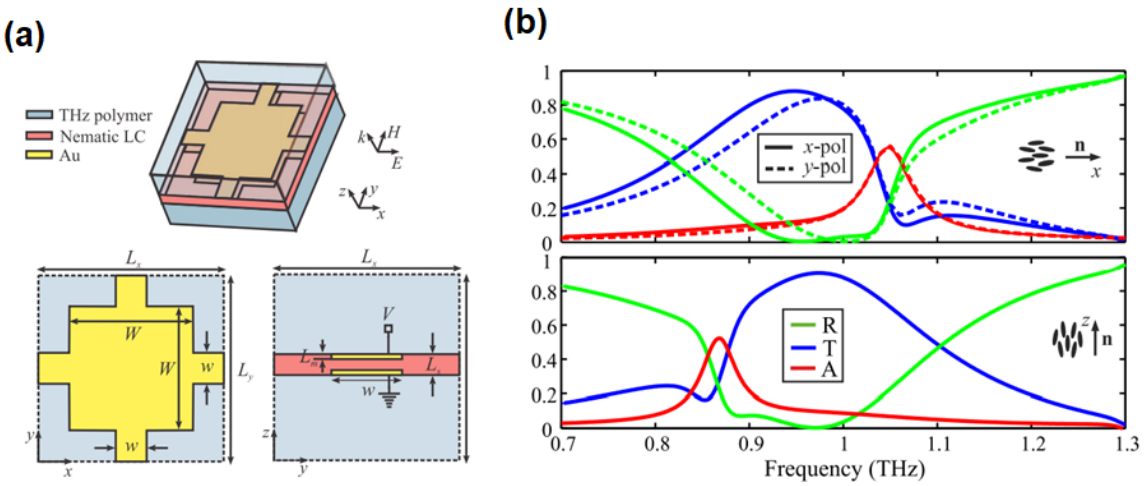

Figure 4-22 (a) Schematic layout and geometrical parameter definition of the proposed LC-tunable fishnet THz MM [150]. (b) Reflectance, transmittance, and absorption spectra of the investigated LC-tunable THz fishnet MM characterized by W=110μm and w=40μm, for the limiting LC alignment configurations, namely along the (top panel) x– and (bottom panel) z–axis [150].

Similarly, tunable THz fishnet MMs based on thin nematic LCs have been demonstrated by *Zografopoulos et al.* [150]. There, a nematic LC layer is introduced between two fishnet metallic structures, forming a voltage-controlled MM cavity, as illustrated in Figure 4-22 (a). Tuning of the nematic molecular orientation is shown to shift the magnetic resonance frequency of the MM and its overall electromagnetic response. A shift higher than 150GHz is predicted for common dielectric and liquid crystalline materials used in THz technology and for low applied voltage values. In fact, 10 V were used to switch the nematic LC and tune the magnetic resonance of MMs in the THz range (see Figure 4-22 (b)).

Although LCs behave well in the THz frequency range when integrated with plasmonic MMs, they still need externally applied electric field and driving voltage and, hence they pose a considerable technological challenge. In this thesis, we aim to investigate LC-loaded THz MM devices which exploit the enhanced localized electric field derived from MMs instead of external electric or magnetic field, to tune the molecular orientation of LCs. For this we used planar MMs with asymmetric structural elements that offer narrow transmission in the THz

regime. The appearance of such narrow resonances is attributed to the excitation of, otherwise inaccessible, symmetric current modes (‘‘trapped modes’’), through weak free-space coupling, which is provided by the structural symmetry breaking. These asymmetric MMs had enabled in the past the engineering of high-Q Fano resonances [238] and served as a building block for one of the first MM-based sensing platforms [250].

4.7 Summary

This Chapter described an intriguing way of improving the performance of LCs in the THz regime. LCs, which are too weak to produce any noticeable transmission effect alone can yield to a very efficient radiation control mechanism when combined with the strong resonant response of a THz planar MM. The suggested LC-loaded MM hybrid enables the control of both intensity and phase of transmitted THz radiation. However, the mainstream solutions suffer from several drawbacks, such as the incorporation of electrodes and driving voltage, or bulky magnets, or temperature, to control the birefringence of LC and hence tune the narrowband resonant response of MMs throughout the electromagnetic spectrum. This a considerable technological challenge, since new applications impose compact, and thin devices with the less possible complexity in their systems and experimental setups. All-optical control of LCs exploiting the THz itself is one of the main challenges nowadays. Enhanced localization of THz electric field in the vicinity of MMs may drive LC molecules and thus control their optical properties without the need of external stimulus.

Chapter 5

Liquid Crystal-Loaded Metamaterials for Enhanced Light-Matter Interactions in The Terahertz Regime

In this chapter I show that hybrid LC MM devices still hold surprising and unexplored effects. In particular, I report that THz metallic MMs with Babinet complementary patterns do not necessarily exhibit the same frequency tuning range when integrated with a nematic LC. I also show that the extent of the difference is controlled by two opposing effects: (i) mismatch between LC alignment and the direction of local electric fields induced in the MMs, and (ii) orientational (Kerr) optical nonlinearity of nematic LCs. Integration of nematic LCs with metallic MMs enables the enhancement of such nonlinearity to the level that it can be engaged using low-intensity experiments in the THz domain. Part of this work has been published as: **Anomalous resonance frequency shift in LC-loaded THz metamaterials.** Perivolari, E., Fedotov, V. A., Kaczmarek, M, and Apostolopoulos, V. (2021). arxiv:2106.12346. The fabrication of MMs, their integration with LC cells, along with measurements and modelling were done entirely by myself. I acknowledge Dr Vassili Fedotov for the design of MMs. Other co-authors contributed with advice and/or to supervision and writing of the article.

5.1 Fabrication Liquid Crystal-Loaded Metamaterial Cells

The design of MMs we chose for this study is based on a D-shaped metamolecule (see Figure 5-1) – a derivative of the asymmetrically-split ring resonator, which in the past had enabled

the engineering of high-Q Fano resonances in MMs [238] and served as a building block for one of the first MM-based sensing platforms [250]. Briefly, this new type of MMs composed of asymmetrical designs exhibit unusually strong high-Q resonances and provided for extremely narrow transmission with respect to the typical and conventional MMs. Such narrow resonances are especially important when combining with the low optical anisotropy of LCs in the THz regime, because there will be less losses and it will be easier to track even the smallest change of the transmission spectra.

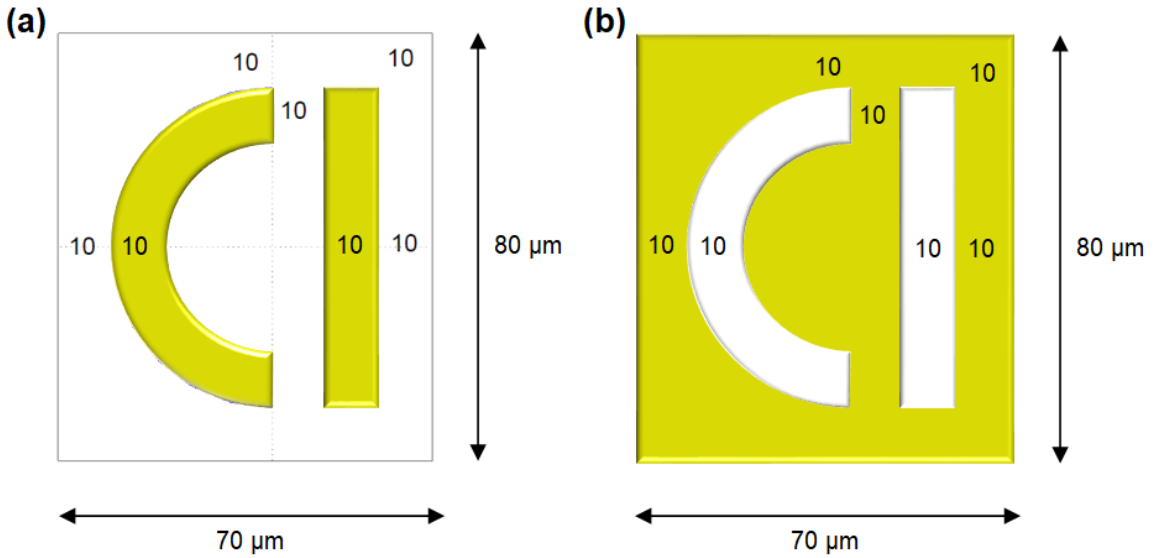

Figure 5-1 Schematic illustration of the D-shaped metamolecules in (a) positive and (b) negative designs. Two Babinet complementary MM patterns investigated during this thesis. The width of the patches/slits was 10 µm, and the unit cell of the arrays had the dimensions of 70 x 80 µm.

5.1.1 Photolithography

A standard photolithography process [251] was followed to transfer the asymmetric D-shaped metamolecule on a mask to a quartz substrate (1.17 mm). Here, I investigated two Babinet complementary patterns where featured arrays of such metamolecules formed, respectively, by metal patches (positive MM) and slits in a metal screen (negative MM), as shown in Figure 5-1 [252]. The width of the patches/slits was 10 µm, and the unit cell of the arrays had the dimensions of 70 µm × 80 µm. Positive patterns were etched using UV photolithography on a 300 nm thick gold film onto a 100 µm thick slab of fused quartz as illustrated in Figure 5-2. An additional layer of chromium 5 nm thick was also deposited in the interface of quartz and gold for better adhesion [253]. Chromium and gold metallic films were deposited beforehand by a thermal evaporator (Bob Edwards FL-400 Auto 306). A positive photo-resist, namely s1813, was spin coated onto the gold film with 500 rpm for 5 s and 5000 rpm for 50 s, in order to create a uniform thin layer and annealed on a hot plate at 90 °C for 10 minutes. In

photolithography, a mask or "photomask" is a square glass plate with a patterned emulsion of metal film on one side. The mask is aligned with the substrate, so that the pattern can be transferred onto its surface. Once the mask has been accurately aligned with the substrate surface, the photoresist is exposed through the pattern on the mask with a high intensity UV light at 402 nm.

Here I used a positive photoresist: when the resist is exposed with UV light, the underlying material is to be removed. In these resists, exposure to the UV light changes the chemical structure of the resist so that it becomes more soluble in the developer. The exposed resist is then washed away by the developer solution, leaving windows of the bare underlying material. The mask, therefore, contains an exact copy of the pattern which is to remain on the wafer. Hard-baking is the final step in the photolithographic process before etching. This step is necessary in order to harden the photoresist and improve its adhesion to the gold surface to protect it during the etching process. Dry etching took place then to remove the 'unprotected' areas of gold [254]. The unexposed photoresist is then washed away resulting in the final nanostructured MM patterns.

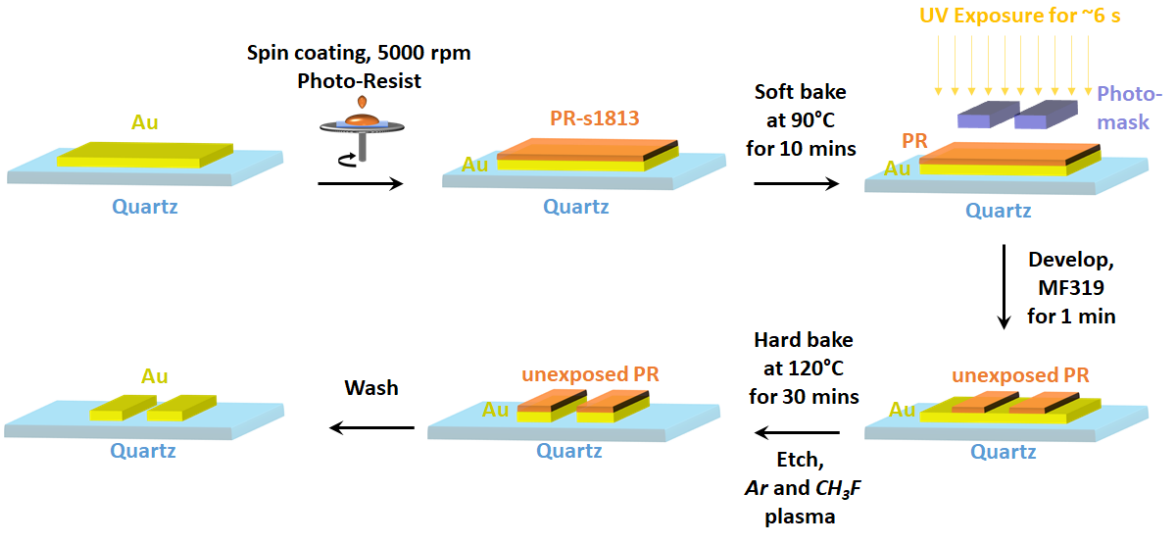

Figure 5-2 Photolithography etching process for fabricating positive patterns on a 300 nm thick gold film onto a 100 μm thick slab of fused quartz.

Negative MM patterns were fabricated with the so-called 'lift-off' process using the same high-resolution photolithography (see Figure 5-3). The basic difference here, is that metal deposition is the final step rather the first. Therefore, after developing the photoresist I deposited the 5 nm of chromium and 300 nm of gold layers by thermal evaporation, which covered both 'protected' and 'unprotected' areas. Finally, by washing off the unexposed photoresist, the opposite pattern from the mask - the negative MM pattern will be created.

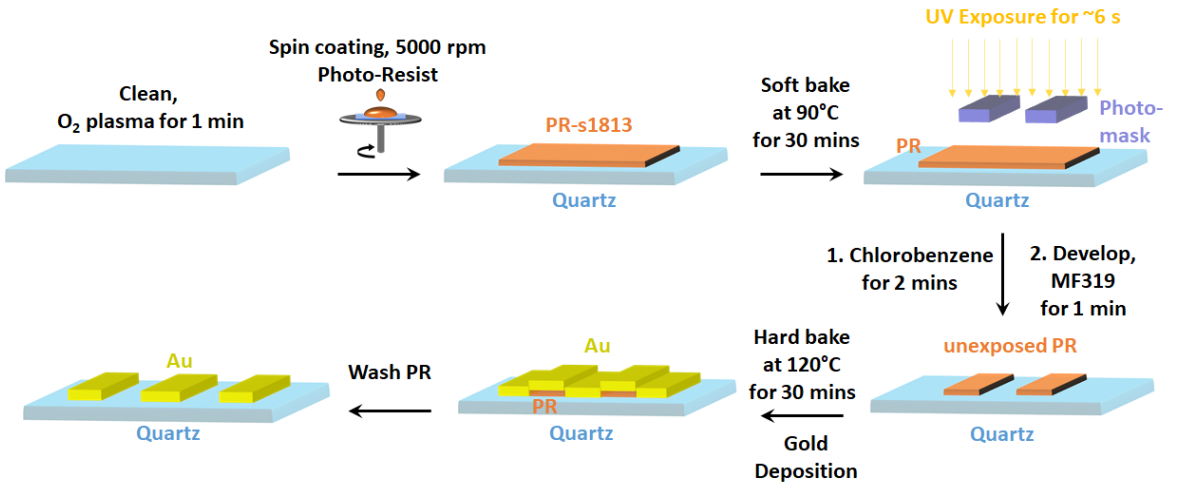

Figure 5-3 Photolithography lift-off process for fabricating negative patterns on a 300 nm thick gold film onto a 100 µm thick slab of fused quartz.

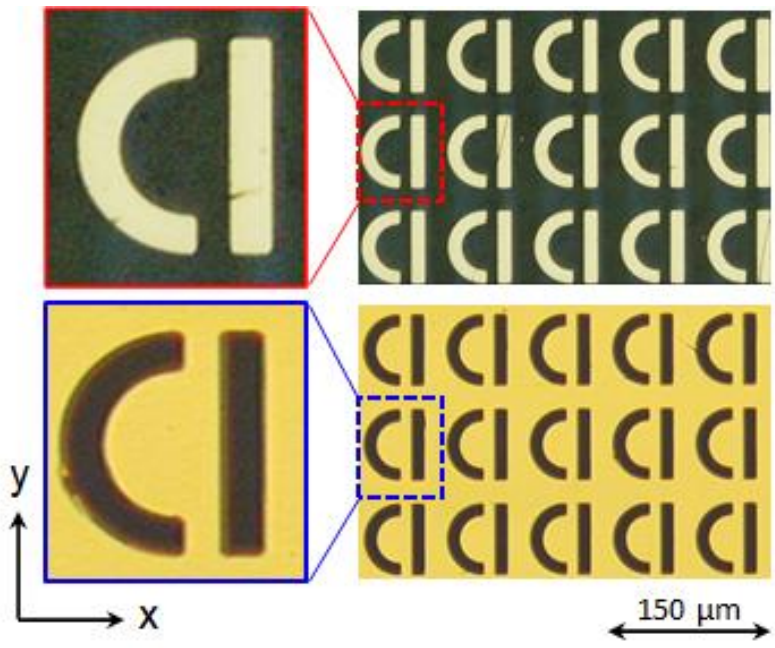

Figure 5-4 Microscope images of MM patterns in positive (top panels) and negative (bottom panels) designs.

5.1.2 Cell assembly of liquid crystal-loaded metamaterial devices

LC-loaded MM cells fabricated following a standard cell assembly process, as described in Section 2.2. MM was functionalised with a nematic LC 1825 (by Military University of Technology in Warsaw [58], see Section 4.5.1) via the planar cell arrangement, where a 20 µm thick layer of the LC was sandwiched between the MM and a pristine slab of fused quartz (1.17

mm thick) (see Figure 5-5). The surface of the MM and the surface of the quartz slab facing the LC were both coated with a thin film (~30 nm) of uniformly rubbed polyimide (PI-2525 from HD MicroSystems). Such a film acted as an AL, which promoted the orientation of LC molecules near its surface in the direction of rubbing.

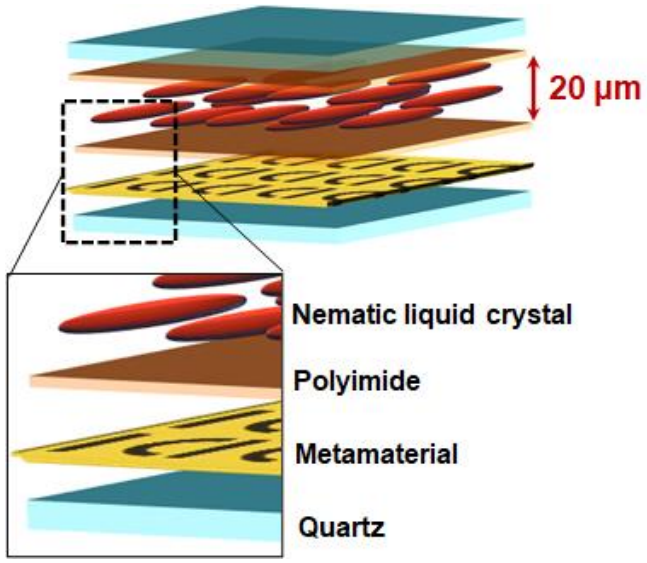

Figure 5-5 Schematic of LC-loaded MM hybrid cell used in this study.

LC 1825 exhibits high birefringence (i.e., ~0.38) meaning that its effective refractive index will be different for the two orthogonal polarisation states of THz light. The extraordinary part of the refractive index will follow the director of LC and hence it will be parallel to the molecular alignment.

By taking advantage of this effect here I investigated two alignment cases, one where the LC is oriented along the polarisation of light (the so-called planar 1 case) and another one where the LC is oriented perpendicular to the polarisation of light (the so-called planar 2 case). By comparing these two extreme LC configurations (planar 1 and planar 2) where the contrast of the effective refractive index would be the maximum, one can obtain the biggest resonance shift concerning the given birefringence. Thus, a greater refractive index contrast will lead to a larger resonance shift.

Practically, to minimise fabrication inconsistencies and compare the THz transmission of planar 1 and 2 alignment cases, I obtained in the same device both LC configurations as schematically shown in Figure 5-6. In fact, I defined positive and negative metafilms into two sections and rubbed each of them orthogonally to each other. Top coated silica substrates were also rubbed with the same aspect and sealed to be in parallel with the rubbing orientation of

the coated metasurface. The resulting hybrid LC metafilm devices were $2 \times 2\ cm^2$ in size as illustrated in Figure 5-7.

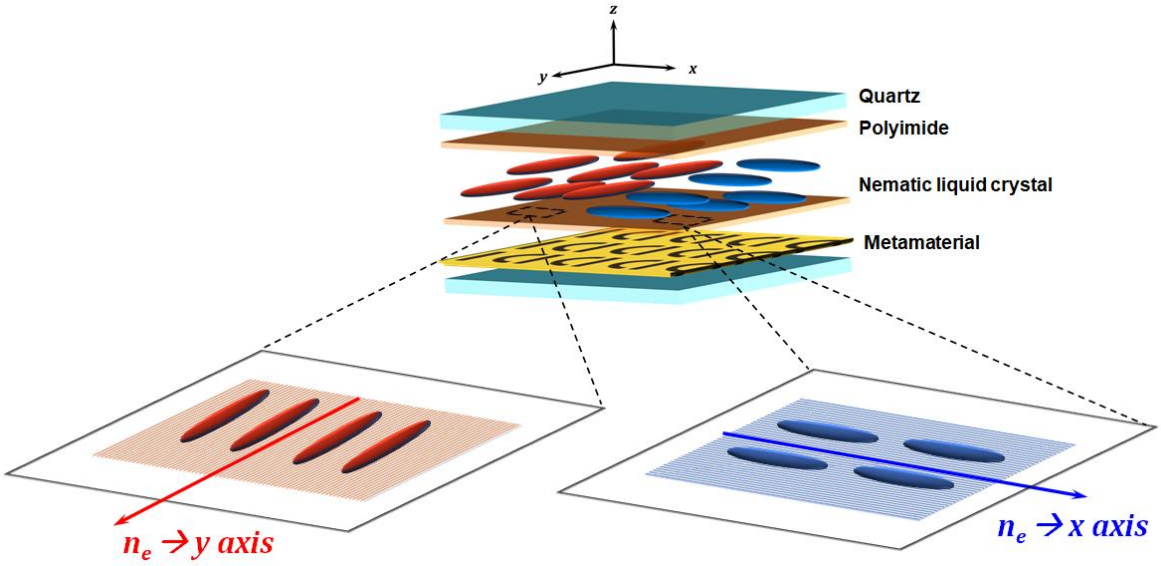

Figure 5-6 Schematic representation of LC alignment cases. Planar 1 case indicates that LC alignment is parallel to the polarisation of light, whereas planar 2 case when perpendicular to the polarisation of light. By exploiting this optical contrast of refractive indices, large resonance shifts can be observed in the THz regime.

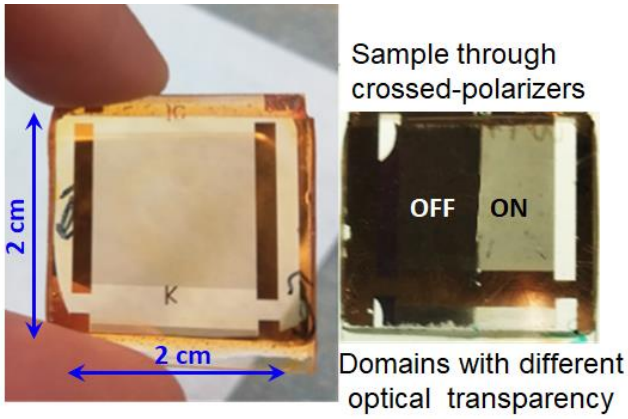

Figure 5-7 Images of the sample. (left) The resulting hybrid LC metafilms device was $2 \times 2\ cm^2$. (right) The different optical transparency, switching ON (bright side) and OFF (dark side) by altering the LC alignment is evident when sample was observed through crossed-polarisers.

5.2 Simulated and Experimental Results of Pristine Metamaterial Samples

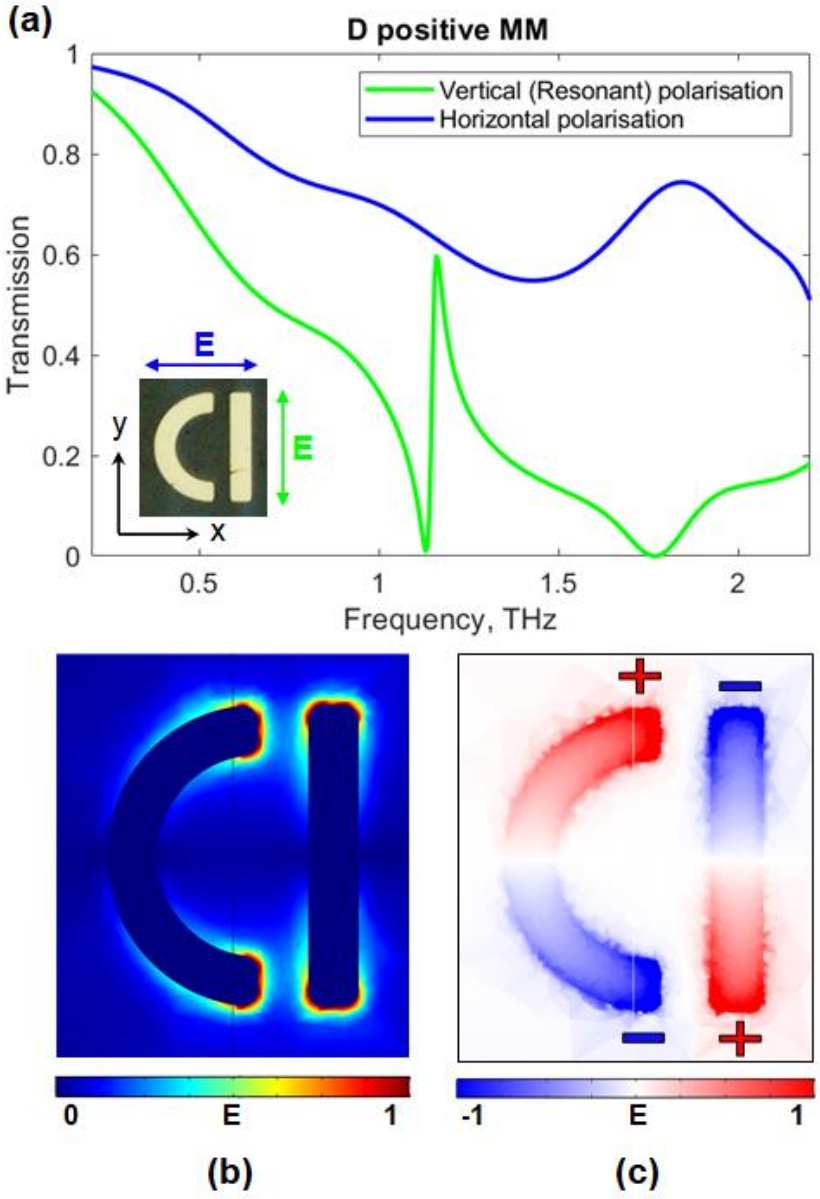

Figure 5-8 (a) Transmission spectra simulated for pristine MMs of positive D-shaped design. Inset: Image of the unit cell taken with a reflection microscope. (b) Field map shows the normalised magnitude of electric field at the resonant frequency, 1.2 THz, of the positive pattern. Field localisation appears around the edges of D shaped MM geometry. (c) Normalised distribution of the surface charge density induced in the positive MM at the resonant frequency.

Figure 5-8 (a) and Figure 5-9 (a) show the transmission spectra of both MMs (positive and negative) simulated in COMSOL 5.5 Multiphysics for normally incident linearly polarised plane

waves, assuming that the patterns were cut in a 300 nm thick gold film [255] and supported by a 100 μm thick slab of fused quartz with the refractive index of 2 [256]. The spectra reveals the presence of Fano resonances for both positive and negative MMs, featuring the characteristic asymmetric profile [257,258] with a sharp roll-off centred at around 1.17 THz and 1.22 THz, respectively.

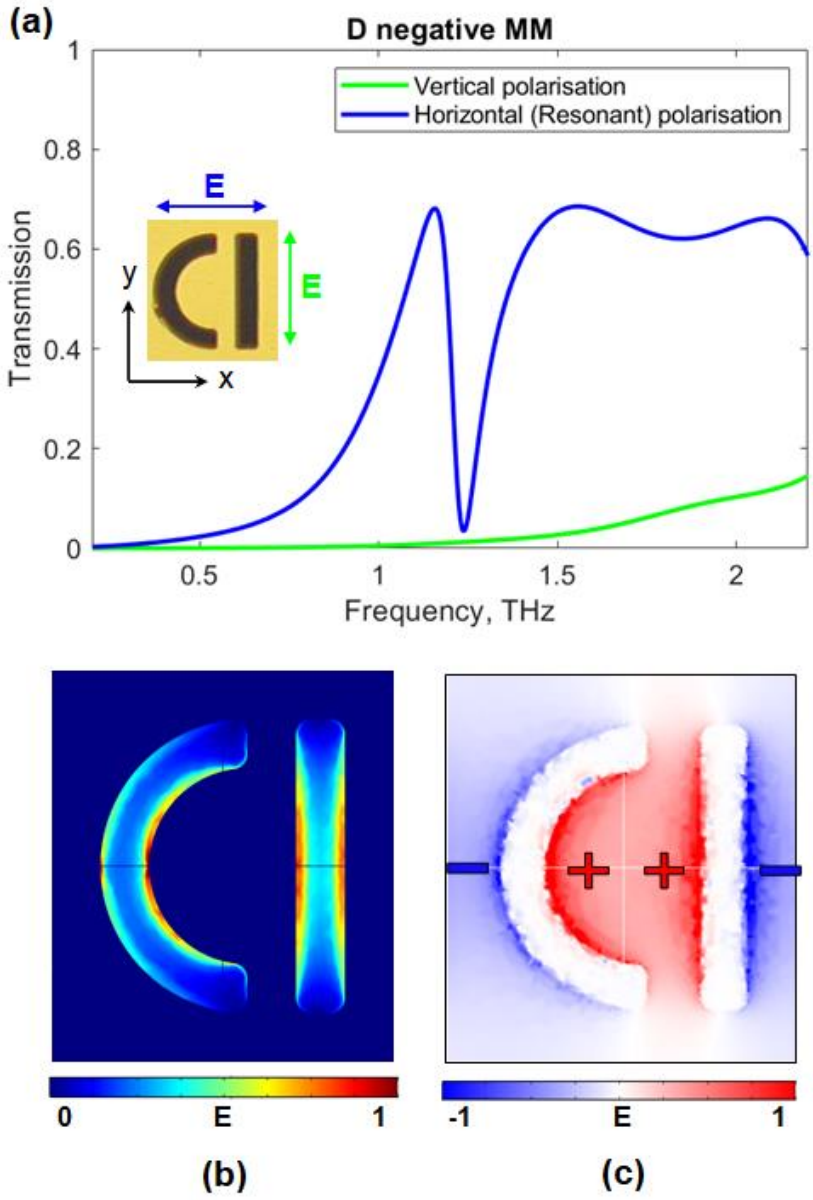

Figure 5-9 (a) Transmission spectra simulated for pristine MMs of negative D-shaped design. Inset: Image of the unit cell taken with a reflection microscope. (b) Field map shows the normalised magnitude of electric field at the resonant frequency of the negative pattern. Field localisation appears in the central part of D shaped MM geometry. (c) Normalised distribution of the surface charge density induced in the negative MM at the resonant frequency.

The origin of the Fano resonance arises from the constructive and destructive interference of a narrow discrete resonance with a broad spectral line [259]. Broad line corresponds to symmetric current mode of the metamolecule which is an electric dipole. Narrow line corresponds to anti-symmetric current mode which is a magnetic dipole/electric quadrupole. Thus, the Fano line here results from the interference between the dipole and magnetic dipole/electric quadrupole modes as shown in Figure 5-8 (c) and Figure 5-9 (c).

To engage Fano resonances the polarisation was set parallel to the straight segments of the metamolecules for positive MM (y-polarisation), and perpendicular to the straight segments of the metamolecules for negative MM (x-polarisation), as illustrated in the insets to Figure 5-8 (a) and Figure 5-9 (a). The transmission spectra simulated for the orthogonal polarisations were featureless, as expected.

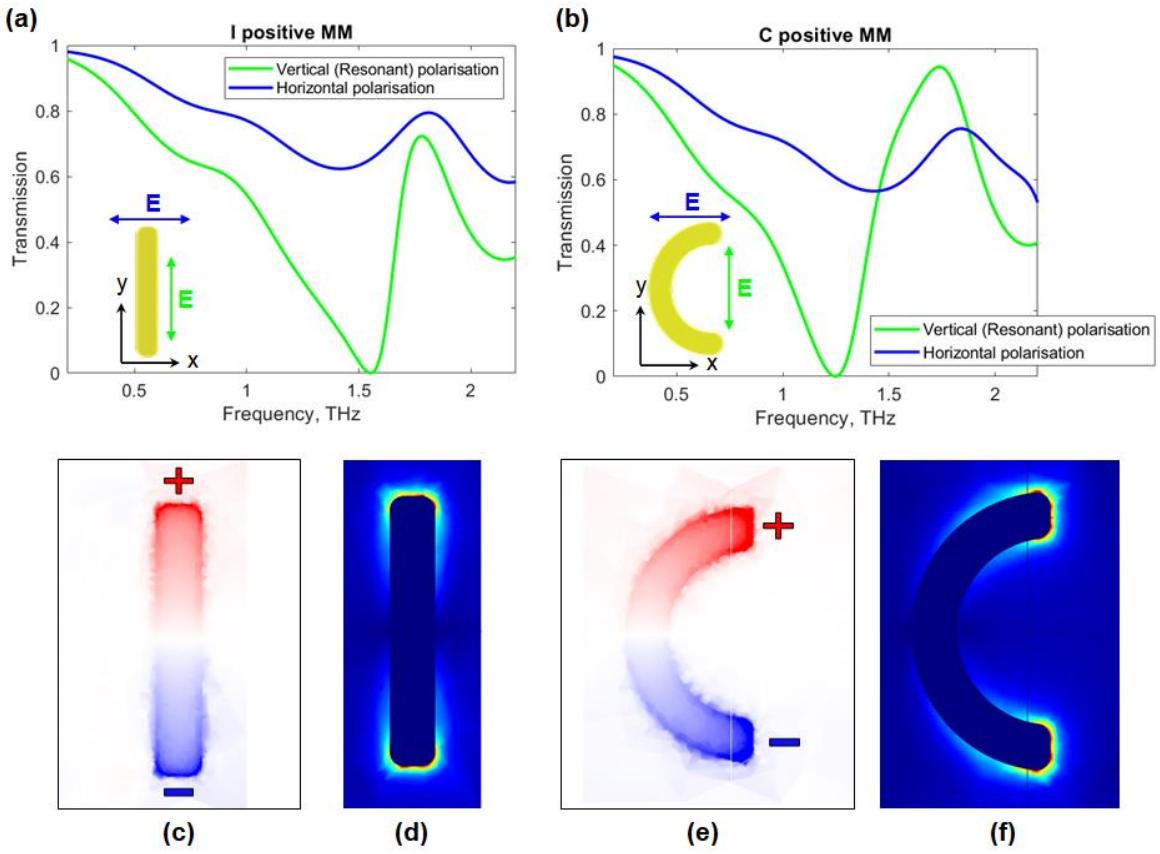

Figure 5-10 (a & b) Transmission spectra simulated for pristine MMs of positive I-shaped and C-shaped designs, respectively. Insets: Schematic drawings of the unit cells along with the resonant polarisation states. (c & e) Normalised distribution of the surface charge density induced in the positive MMs at the resonant frequency. (d & f) Field maps show the normalised magnitude of electric field at the resonant frequency. Field localisation appears around the edges of I- and C-shaped MM geometries.

Both resonances result from the excitation of the so-called trapped modes [238], where the charge oscillations induced in the two segments of the D-shaped metamolecule occur in anti-phase (see Figure 5-8 (c) and Figure 5-9 (c)). Conventional MMs are often composed of subwavelength particles that are simply unable to provide large-volume confinement of electromagnetic field necessary to support high-Q resonances. As recent theoretical analysis showed, high-Q resonances involving 'trapped' modes are nevertheless possible in MMs, if certain small asymmetries are introduced in the shape of their structural elements.

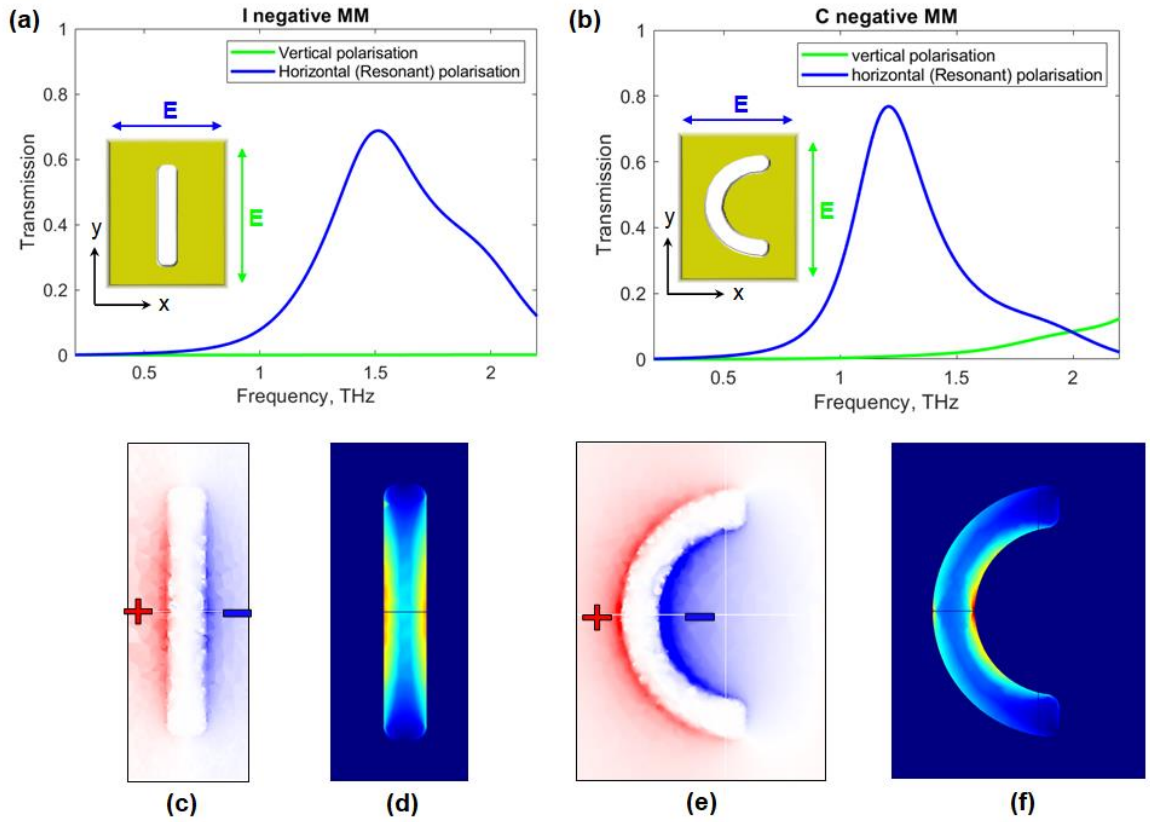

Figure 5-11 (a & b) Transmission spectra simulated for pristine MMs of negative I-shaped and C-shaped designs, respectively. Insets: Schematic drawings of the unit cells along with the resonant polarisation states. (c & e) Normalised distribution of the surface charge density induced in the negative MMs at the resonant frequency. (d & f) Field maps show the normalised magnitude of electric field at the resonant frequency. Field localisation appears in the central part of I- and C-shaped MM geometries.

To investigate the strong mode coupling between the electric dipole and magnetic dipole/electric quadrupole moments, a partition of D-shaped MM structural elements was studied which involves 'I-shaped' and 'C-shaped' MM patches and slits (positive and negative MM designs respectively), as shown in the insets of Figure 5-10 and Figure 5-11. Figure 5-10

(a) and Figure 5-11 (a) show the transmission spectra of the I- and C-shaped MM designs. Indeed, a broader resonant transmission is observed. At frequencies 1.67 THz and 1.44 THz I- and C-shaped positive MMs exhibit their fundamental resonance where the wavelength of excitation is twice the length of MM segment. Accordingly, the fundamental resonance for negative patterns appears at 1.51 THz and 1.21 THz. My calculations show that in the case of D-shaped MM an antisymmetric current mode (quadrupole mode) can dominate the usual symmetric one (dipole mode), as shown in Figure 5-12

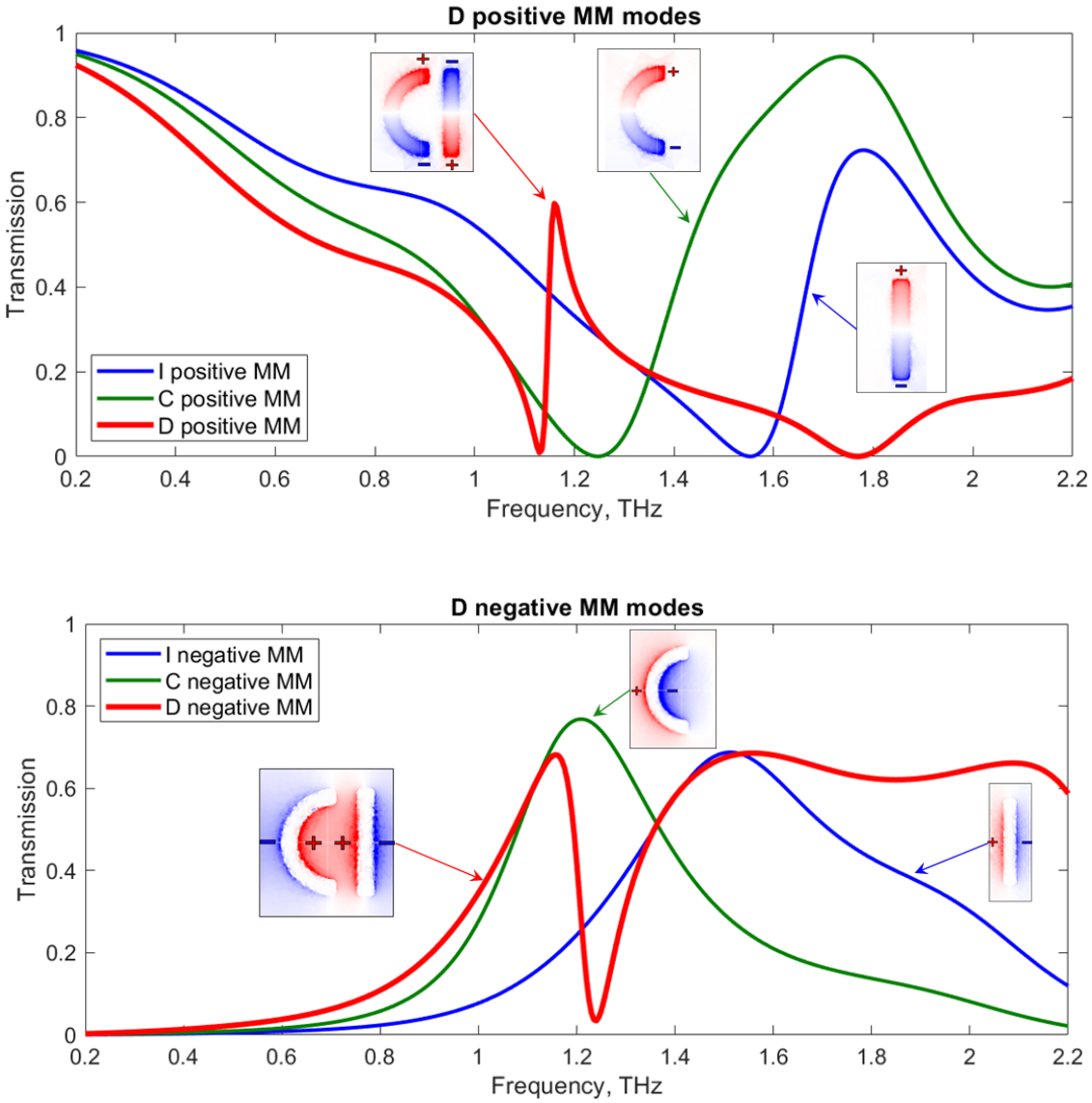

Figure 5-12 Transmission spectra simulated for pristine MMs of positive (top) and negative (bottom) D-, I- and C-shaped MM designs. Insets: Normalised distribution of the surface charge density induced in the MMs at the resonant frequency.

Antisymmetric current mode produces very weak scattered electromagnetic fields, which dramatically reduces radiation losses. Indeed, both the electric and magnetic dipole radiation

of currents oscillating in the neighbouring segments is cancelled, since currents have almost the same amplitude (see Figure 5-8(c) and Figure 5-9(c)). On the contrary, currents in usual dipole modes (see Figure 5-11(c, e) and Figure 5-12(c, e)) oscillate in phase, but excitation of one dominates the other which yields lower Q-factors for this type of the response. Therefore, by combining the symmetric dipole modes of structures 'I' and 'C', producing the 'D-shaped' MM, the two parts are excited in antiphase yielding to a high-Q transmission resonance. In Figure 5-12 the Fano resonance arises by the interference of the I- and C-shaped MMs, as it is clearly shown from both MM patterns which combine the transmission spectra of their fundamental ones.

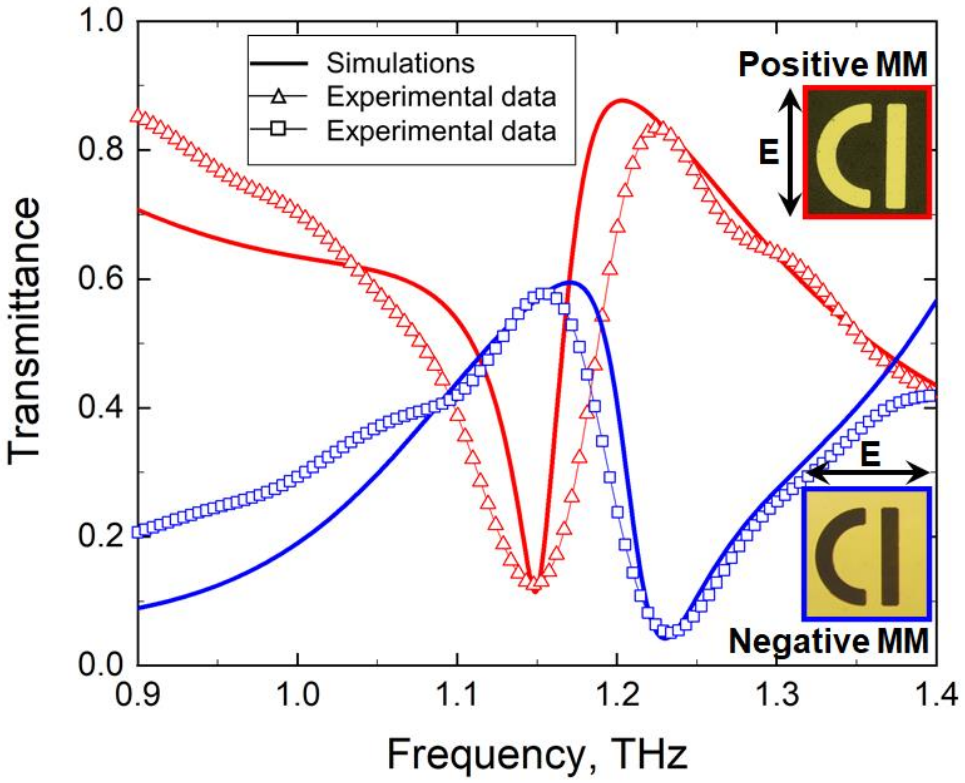

Figure 5-13 Transmission spectra measured experimentally (open triangles) and simulated (thick solid lines) for pristine MMs of positive (red) and negative (blue) designs. **Insets:** Images of the unit cells and fragments of the fabricated MMs of positive (top) and negative (bottom) designs taken with a reflection microscope.

To confirm simulations, I fabricated the exact copies of the above MMs and characterised their spectral response at normal incidence using a conventional low-power THz-TDS setup, which featured a micro-dipole based photoconductive antenna excited with 10 mW of ultrafast (100 fs) 780 nm laser and measurement based on the Pockels effect [260]. The patterns of the MMs were etched using UV photolithography (see Section 5.1.1) in a 305 nm thick metal film, which

had been deposited beforehand by thermal evaporation onto 1.17 mm thick fused quartz substrate. The film had a 300 nm thick layer of gold and a 5 nm thick layer of chromium added to ensured adhesion between gold and quartz. The overall size of the fabricated samples was 16 mm × 16 mm. The THz beam was focussed onto the samples to a 5 mm large spot, which guaranteed the absence of beam clipping and diffraction at the edges of the samples upon illumination. The measured transmission spectra of the pristine positive and negative MMs are shown in Figure 5-13. The plot reveals a very good agreement between the experimental and modelled data confirming high quality of the fabricated MM samples.

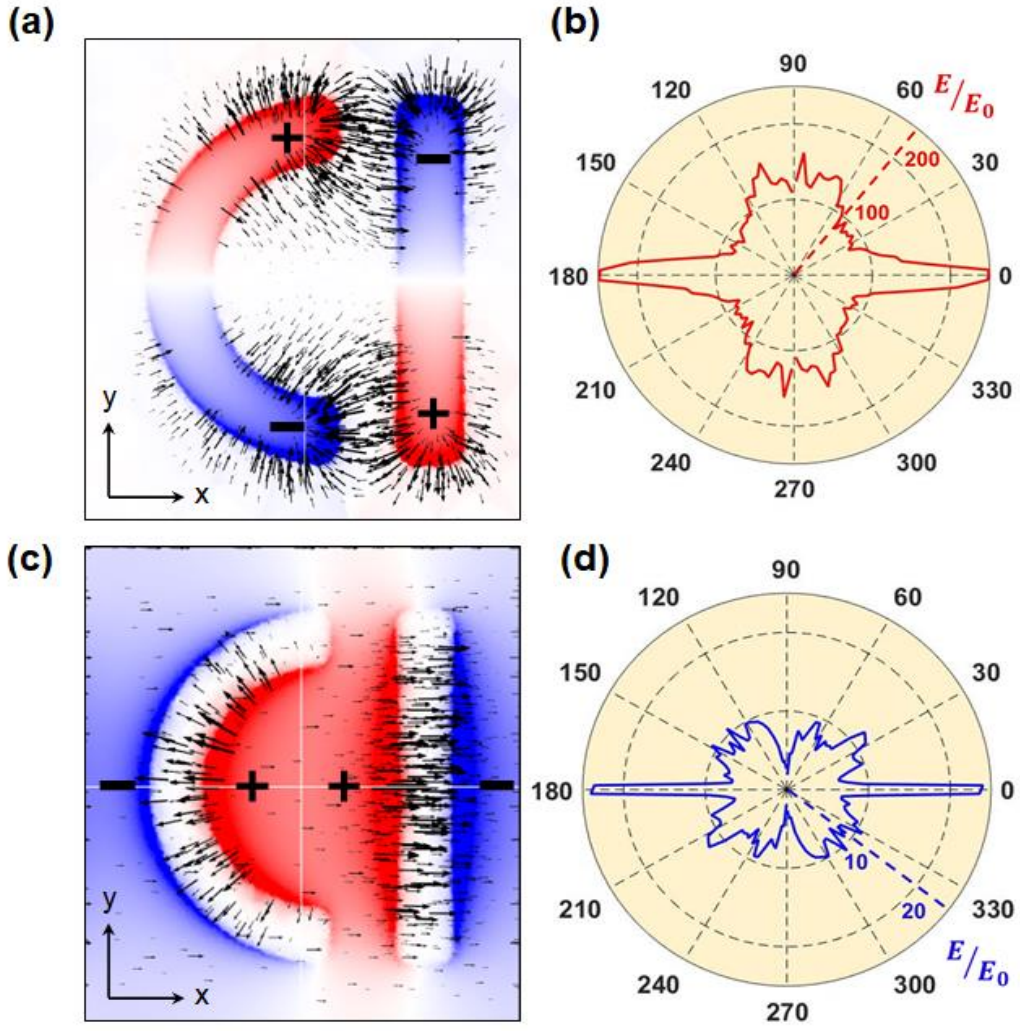

Figure 5-14 (a) Normalised distribution of the surface charge density (colours) and electric field lines (black arrows) induced in the positive MM at the resonant frequency. (b) Polar plot of in-plane directivity of the local electric field in positive MM averaged over the area of the unit cell. The radius corresponds to the magnitude of the average electric field (E) normalised on the incident field (E_0). (c) Same as (a) but for negative MM. (d) Same as (b) but for negative MM.

However, we note that the corresponding distributions of the electric field differ substantially for the positive and negative MMs. The 'hotspots' of the electric field appear to localise around the ends of the metal patches in the positive MM, and within the central areas of the slits in the negative MM. As a result, the extent of the in-plane divergence of the local field in the two cases is also very different. Indeed, in the positive MM the field lines are seen to fan out within the hotspots, spanning nearly all directions (see Figure 5-14 (a)), while in the negative MM they stretch across the slits and, thus, align predominantly along the *x*-axis (see Figure 5-14 (c)).

The difference becomes more apparent when analysed in terms of the directivity of the local field averaged over the area of a unit cell (see diagrams in Figure 5-14 (b) and (d)). Clearly, in the case of the negative MM the directivity collapses around the x-axis and is only perturbed by four small diagonal side lobes generated by the curved segment of the metamolecule. In the case of the positive MM, however, the directivity features four broad main lobes oriented along the x- and y-axes. We argue that such a directional anisotropy of the local field, which arises near the surface of the MMs becomes an important factor in the presence of optically anisotropic materials (such as nematic LCs), affecting differently the tuneability of Babinet complementary MMs.

5.3 Simulated and Experimental Results of THz Liquid Crystal-Metamaterial Devices

Babinet complementary patterns of a spectrally tunable MM incorporating a nematic LC are normally assumed to exhibit the same tuning range. However, here I will show that positive MMs when hybridised with nematic LCs can achieve larger frequency tuning range than what seems to be possible in theory.

To demonstrate it first numerically, I introduced in my model a layer of an optically anisotropic dielectric, which represented a nematic LC in the planar state. It had the thickness of 20 μm, typical for conventional LC optical cells, and was placed on top of the MMs, fully encompassing their structure (see Figure 5-5). The ordinary and extraordinary refractive indices of the LC were assumed to be $n_{\mathrm{o}} = 1.574 - i0.017$ and $n_{\mathrm{e}} = 1.951 - i0.024$, corresponding to the refractive indices of highly birefringent LC 1825 at 1 THz [261] (see Section 4.5.1).

Figure 5-15 (a) and (b) compare the simulated transmission spectra of the complementary MMs with two different planar configurations of the LC aligned, respectively, parallel (planar

1) and perpendicular (planar 2) to the incident polarisation, as discussed in Section 5.1.2. For convenience I include in Figure 5-16 a schematic representation of LC configurations.

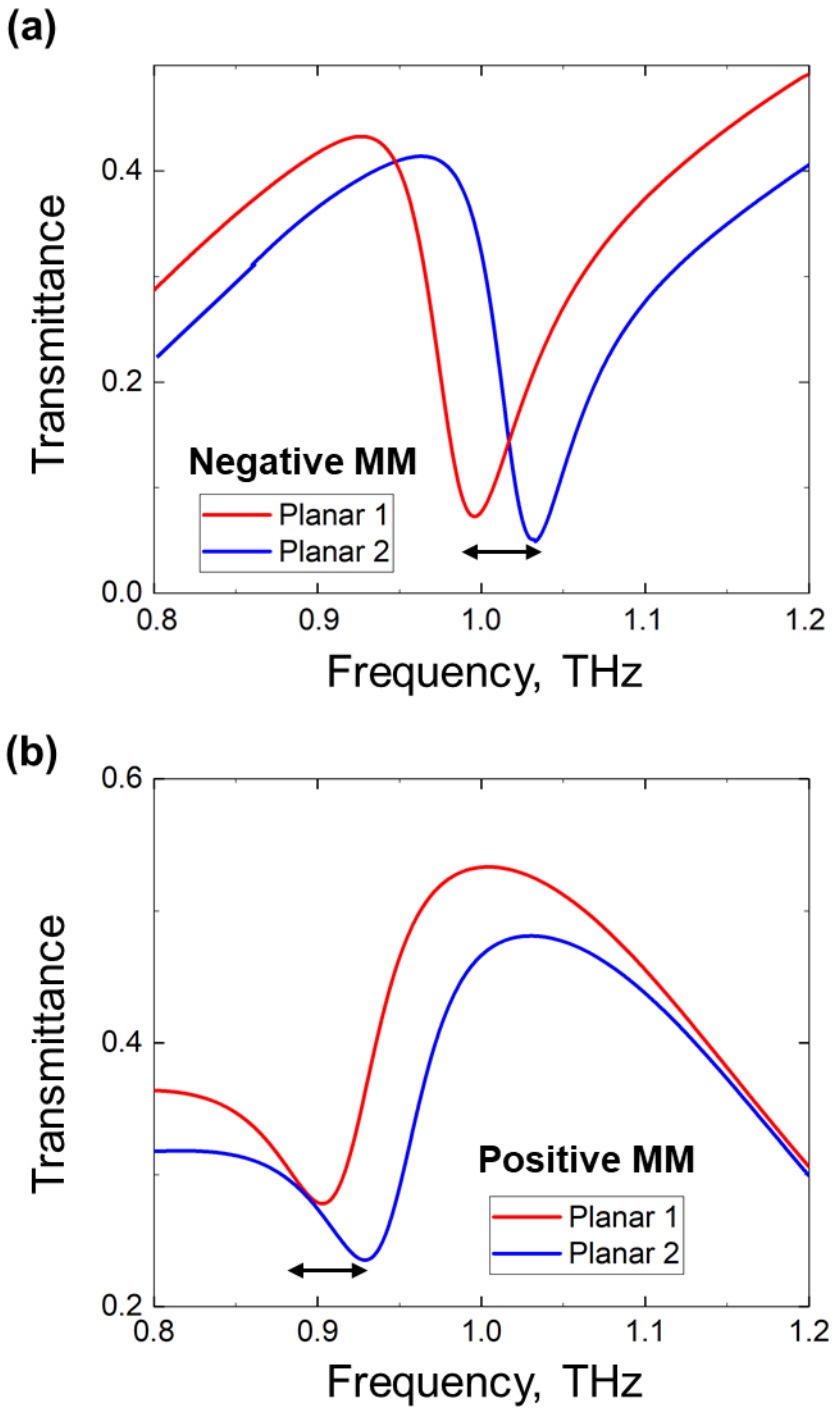

Figure 5-15 (a) Simulated transmission spectra for negative MM loaded with NLC in planar 1 (red) and planar 2 (blue) configurations. (b) Same as (a) but for positive MM.

Evidently, upon switching the LC between planar 1 and planar 2 configurations, the resonance of the positive MM exhibits a spectral shift some 20 GHz (~ 50%) smaller than that of the

negative MM. This is the manifestation of the effect of the mismatch between the direction of the local field and LC alignment, which we referred to above. Here, the tendency of the local electric field to oscillate along two orthogonal directions in the positive MM (see diagram in Figure 5-14 (a)) makes the supported electromagnetic mode less sensitive to alignment of the LC (and, correspondingly, anisotropy of its refractive index) and therefore results in a spectrally narrower tuning range.

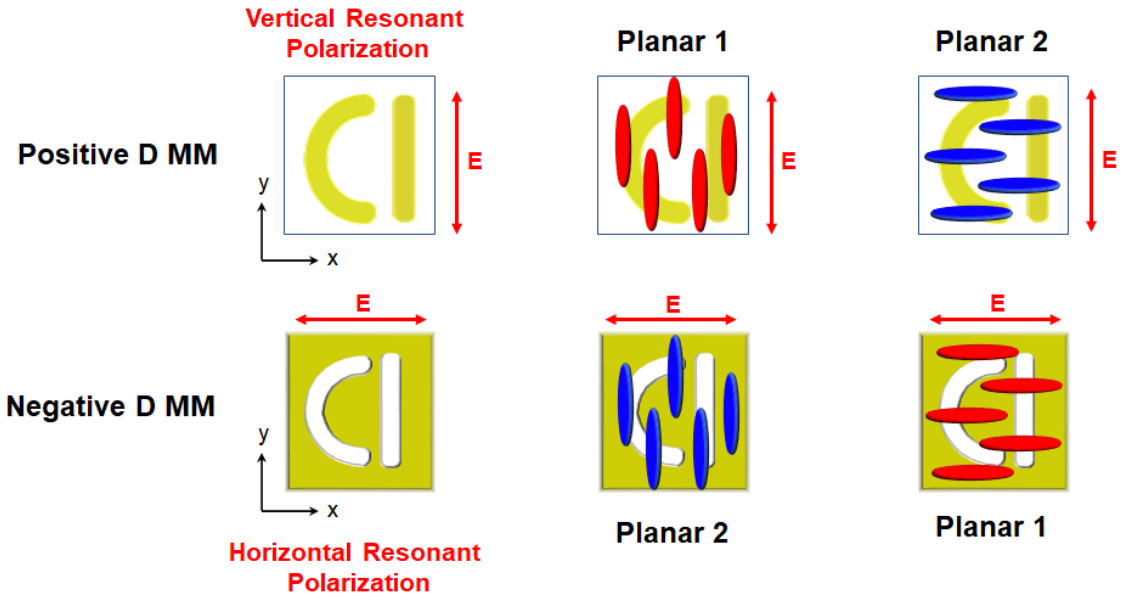

Figure 5-16 Orientations of LC molecules schematically shown for planar 1 and planar 2 configurations. Planar 1 configuration is always in parallel with the resonant polarisation state of the MM, whereas planar 2 is perpendicular.

Here, the extent of the effect is demonstrated in Figure 5-17 by comparing the maximum frequency shifts exhibited by resonances of the complementary MMs for different values of LC birefringence, $\Delta n = n_e - n_o$. In my modelling Δn varied in the range from 0.2 to 0.38, where the limits correspond to the birefringence of two different LCs, E7 [262] and 1825 [261,263] at 1 THz. The values of Δn within this range were calculated based on n_e and n_o interpolated linearly between those of E7 and 1825. The data points in Figure 5-17 mark the difference between the resonance frequencies calculated for planar 1 and planar 2 states. As expected, the frequency shift becomes smaller for both MMs as the value of the birefringence decreases towards 0.2, yet the positive MM exhibits consistently smaller shifts than the negative MM for the entire range of Δn. In other words, it is rather expected to obtain smaller shifts with positive MM designs hybridised with a thin layer of LC.

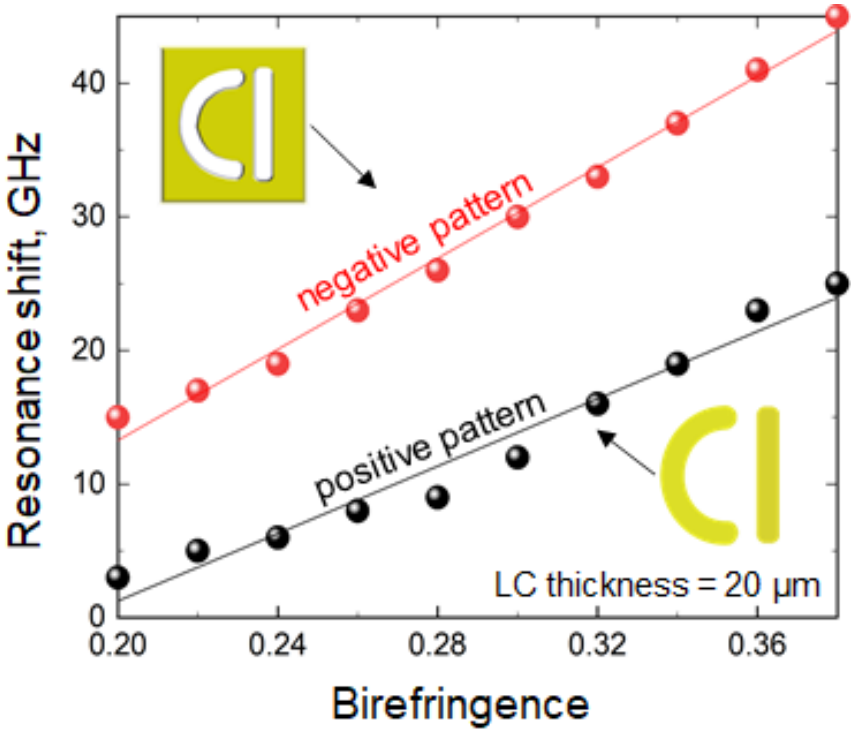

Figure 5-17 Calculated maximum resonance shift that can be attained in positive (black points) and negative (red points) MMs at different values of LC birefringence. Insets: Schematics of MM unit cells

5.3.1 Anomalous resonance frequency shift for positive MMs when hybridised with liquid crystals

The transmission spectra of LC-loaded MMs, as measured experimentally with our THz-TDS setup, are presented in Figure 5-18 (a) and (b) in open squares. Clearly, the locations of the resonance exhibited by the negative MM in the presence of differently aligned nematic LC (i.e., in planar 1 and planar 2 configurations) agree very well with the predictions of our model, with the spectral separation reaching the expected 45 GHz. In the case of the positive MM, however, a good spectral overlap between the experimental and modelled data is seen only for the LC in planar 2 configuration. Surprisingly, switching the LC to planar 1 configuration red-shifts the measured transmission spectrum of the positive MM by about 20 GHz further than what seems to be allowed from the simulation. As a result, the frequency tuning range obtained experimentally for the positive MM widens to 43 GHz, which practically negates the large difference in the expected tunability of Babinet complementary MMs which has been expected by the simulation.

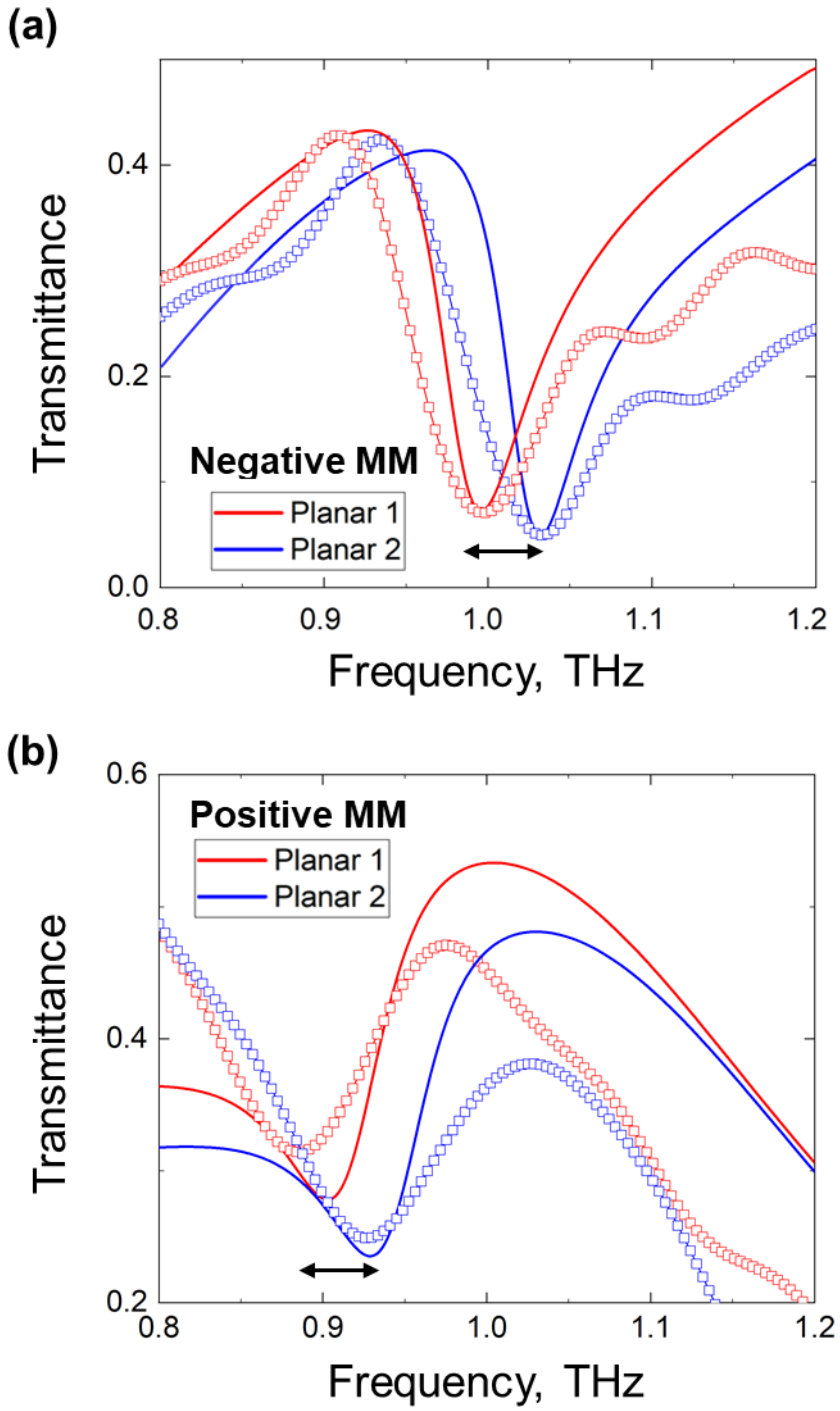

Figure 5-18 (a) Transmission spectra measured experimentally (open squares) and simulated (solid lines) for negative MM loaded with NLC in planar 1 (red) and planar 2 (blue) configurations. (b) Same as (a) but for positive MM.

We reason that the larger red-shift of the MM spectrum could have resulted only from a better match between the direction of the local electric field and the orientation of LC molecules, since that would effectively increase the refractive index of the LC perceived by the resonant electromagnetic mode of the metamolecules. To this end we note that the directional spread of

the local field in the positive MM is largest around the y-axis (see diagram in Figure 5-14 (b)) and, hence, matching the spread with local distortions of the LC will have the biggest impact for planar 1 alignment – exactly where the outcomes of our simulations and experiment disagree the most.

To demonstrate the plausibility of this hypothesis I re-modelled the response of the positive MM assuming that the LC aligned itself in the direction of the local field within the hotspots (where the divergence of the field is strongest), and such distortions were confined to a distance of 5 μm away from the edges of the metamolecules and 1 μm above their plane (see Section 5.4). I further assumed that changes in LC alignment there were limited to (-45°) – (+45°) range of angles, which corresponded to the angular spread of the local field we noted above. For the directions outside the spread the orientation of LC molecules was gradually restored to the background alignment (i.e., planar 1 configuration), as schematically illustrated in Figure 5-19 (a) and (b).

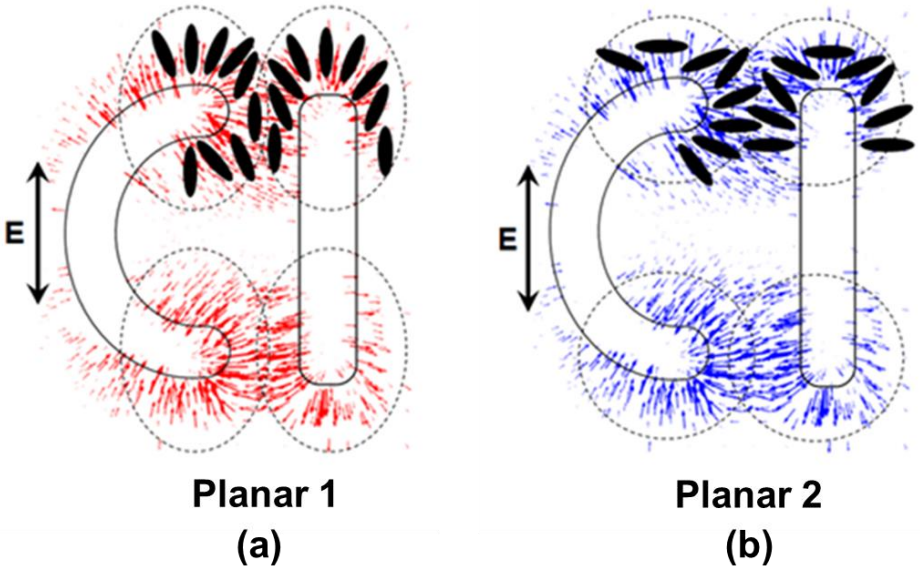

Figure 5-19 (a) Orientational optical nonlinearity of NLC in planar 1 configuration engaged with positive MM. Local field-induced distortions of the initial alignment assumed within the hotspots are shown schematically via the orientation of LC molecules. (b) Same as (a) but for initial planar 2 alignment of NLC.

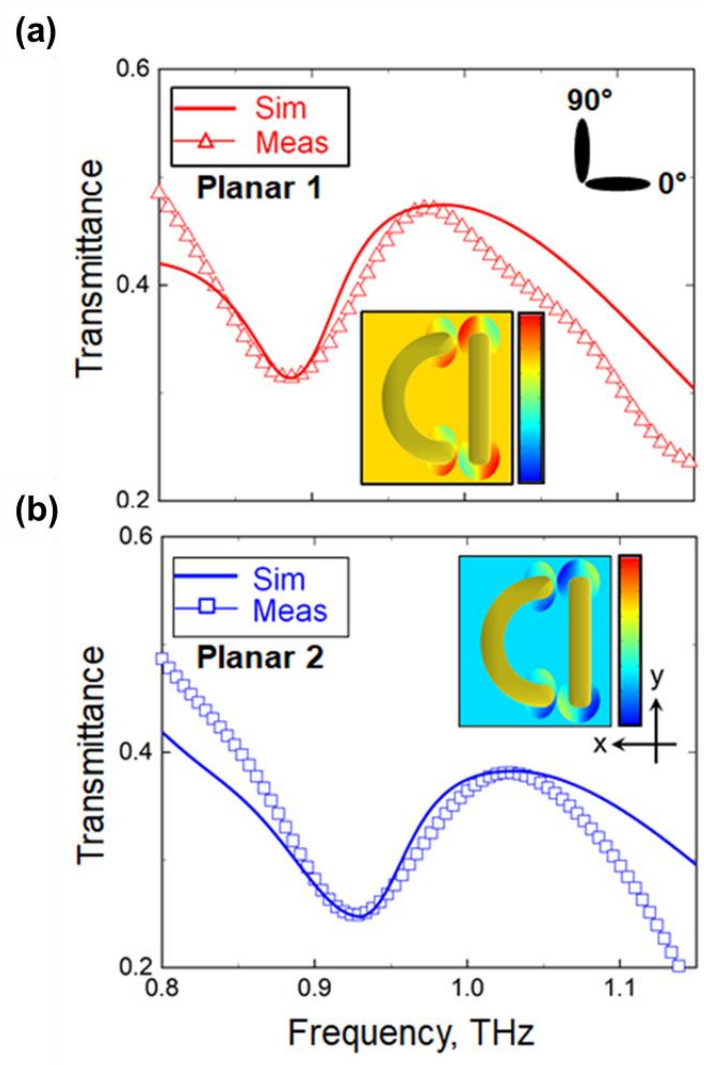

Figure 5-20 (a) Transmission spectra measured experimentally (open triangles) and simulated (thick solid lines) for positive MM taking into account the effect of orientation nonlinearity of NLC in planar 1 configuration. Inset: Spatial distribution of LC alignment assumed in the simulations. Scale bar ranges from -45° (blue) to 135° (red). 0° and 90° correspond to LC molecules being parallel to x- and y-axes, respectively. (b) Same as (a) but for initial planar 2 alignment of NLC.

The transmission spectrum of the positive MM calculated using our modified model is presented in Figure 5-20 (a), where it is compared with the spectrum measured experimentally. Evidently, this time the predicted and the actual locations of the MM resonance coincide. Moreover, a very good agreement between the simulated and experimental data is now seen in terms of the amplitude of the MM transmission as well.

As a further test of this hypothesis, I also modified the model of the positive MM with the LC featuring planar 2 alignment. Localised distortions of the alignment were introduced in the model in the same way as in the planar 1 case except that the re-orientation of LC molecules was traced relative to the x-axis (see Figure 5-20 (b)). What I found was that even in the planar

2 case (where the theory and experiment had agreed qualitatively) assuming re-alignment of the LC within the hotspots dramatically improved the accuracy of our model and enabled us to achieve nearly perfect quantitative agreement between the calculated and measured spectra (see Figure 5-20 (b)).

5.3.2 Simulation of different angular LC re-alignment ranges

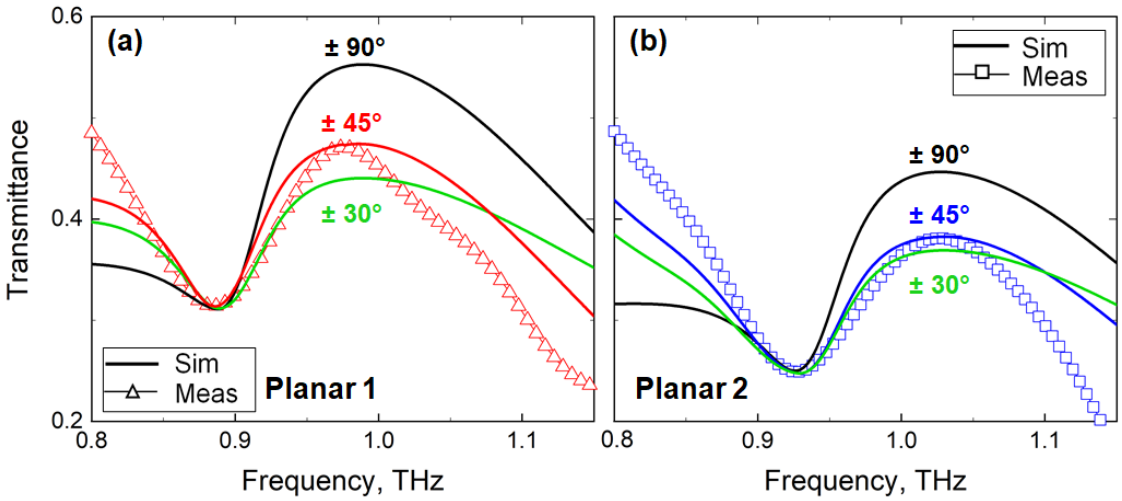

Figure 5-21 Transmission spectra of measured experimentally (open triangles) and simulated (thick solid lines) for LC-loaded positive MM in (a) planar 1 and (b) planar 2 configurations in different angular re-alignment ranges. Re-orientation of ± 45° (90°±45° and 0°±45°, respectively) found to be closer to the experiment.

For clarity different angular re-alignment ranges are simulated for both planar 1 and planar 2 cases to match the experimental data. Evidently, re-orientation of ± 45° (90°±45° and 0°±45°, respectively) found to be closer to the experiment as shown in Figure 5-21. A re-orientation of ± 90° opposes the initial strong surface anchoring energy of the rubbing and hence, it seems unnatural to obtain a re-orientation of such range. Indeed, as it is shown in the graph, re-orientation of ± 90° possesses larger transmittance than the experimental data. On the other hand, a smaller re-orientation range of ± 30° shows a weaker response. Thus, I conclude that the best fit is derived from the re-orientation range of ± 45°. For clarity, more alignment scenarios were investigated, however none fitted the experimental results (see 0).

5.4 Modelling the Change of Liquid Crystal Birefringence Induced by Local Fields Within 'Hotspots'

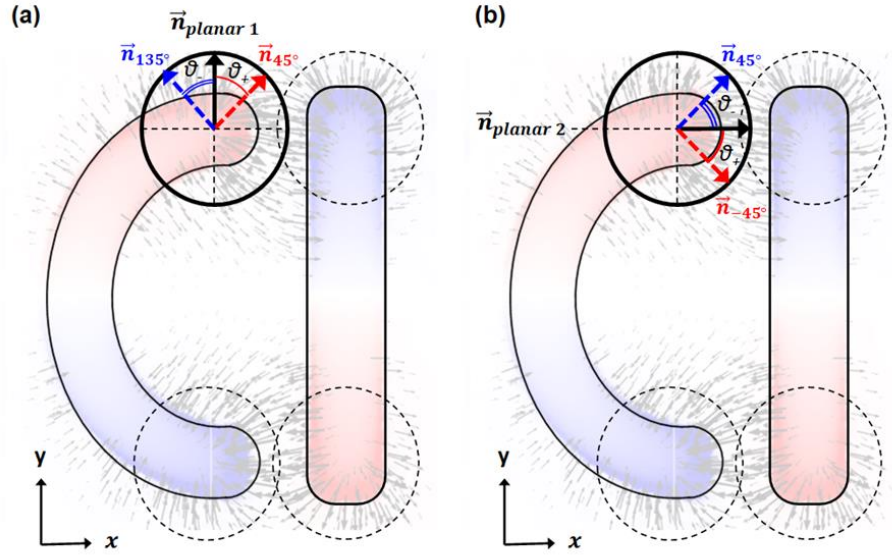

Figure 5-22 Schematic representation of modelling the anisotropy induced to the NLC molecules in (a) planar 1 and (b) planar 2 configurations due to the charge density distribution at the surface of positive MM patterns.

The hotspots are localised at the ends of the metal patches in the positive MM, as schematically shown in Figure 5-22. The layer of the LC covering the MM was assumed to be aligned along the y-axis, except in the hotspots, where maximum localisation of electric field occurs. Birefringent materials such as the LC experience double refraction, whereby light is split, depending on the incident polarisation, into two, i.e. ordinary (n_o) and extraordinary (n_e) polarisations. The extraordinary one is parallel to the LC director, $\vec{n}$, of LC molecules, pointing along the y-axis, which is the resonant polarisation. This leaves the ordinary to be parallel to the x-axis direction. In order to model such optical behaviour, a diagonal optical anisotropy must be introduced in our calculations as well as a full tensor relative permittivity approach. Here, tensor refers to a 3-by-3 matrix that has both diagonal ($\epsilon_{xx}, \epsilon_{yy}, \epsilon_{zz}$) and off-diagonal ($\epsilon_{xy}, \epsilon_{xz}, \epsilon_{yx}, \epsilon_{yz}, \epsilon_{zx}, \epsilon_{zy}$) terms, as shown below.

$$\epsilon = \begin{bmatrix} \epsilon_{xx} & \epsilon_{xy} & \epsilon_{xz} \\ \epsilon_{yx} & \epsilon_{yy} & \epsilon_{yz} \\ \epsilon_{zx} & \epsilon_{zy} & \epsilon_{zz} \end{bmatrix} \tag{5.1}$$

NLCs belong to the uniaxial crystals' category, where only the diagonal elements of permittivity tensor are nonzero. This means that $\epsilon_{xx} = \epsilon_{zz} = {n_o}^2 - {k_o}^2 + 2in_ok_o \; and \; \epsilon_{yy} = {n_e}^2 - {k_e}^2 + 2in_ek_e$. The material used in this study, LC 1825, was fully investigated by Chodorow, U., et al. [261], who provided the following characteristics which we used in the simulations:

Table 5-1: LC 1825 optical properties

LC1825	**1.5 THz**
$\boldsymbol{n_o}$	1.574
$\boldsymbol{n_e}$	1.951
$\boldsymbol{k_o}$	7 $[1/cm]$
$\boldsymbol{k_e}$	12 $[1/cm]$
$\boldsymbol{\Delta n}$	0.38

So, for planar 1 configuration we introduced the following relative permittivity tensor with diagonal elements.

$$\epsilon = \begin{bmatrix} \epsilon_{xx} & 0 & 0 \\ 0 & \epsilon_{yy} & 0 \\ 0 & 0 & \epsilon_{zz} \end{bmatrix} \tag{5.2}$$

To model the spatial variation of optical anisotropy as specified in Figure 5-20 (a, c), we introduced an off-diagonal transverse anisotropy in the XY plane. When the $\vec{n}$ of LC lies and rotates in the XY plane, making an angle of ϑ with the x-axis (see Figure 5-22), the diagonal components ($\epsilon_{xx}, \epsilon_{yy}, \epsilon_{zz}$) and off-diagonal components ($\epsilon_{xy}, \epsilon_{yx}$) are nonzero.

$$\epsilon = \begin{bmatrix} \epsilon_{xx} & \epsilon_{xy} & 0 \\ \epsilon_{yx} & \epsilon_{yy} & 0 \\ 0 & 0 & \epsilon_{zz} \end{bmatrix} \tag{5.3}$$

In that case, ϵ_{yy} is governed by the extraordinary refractive index, because $\vec{n}$ lies along the principal y-axis, while ϵ_{xx} and ϵ_{zz} are governed by the ordinary refractive index. The off-diagonal elements $\epsilon_{xy}, \epsilon_{yx}$ are derived from the multiplication of the matrices as stated below.

$$\epsilon = \begin{bmatrix} cos(\vartheta) & -sin(\vartheta) & 0 \\ sin(\vartheta) & cos(\vartheta) & 0 \\ 0 & 0 & 1 \end{bmatrix} \begin{bmatrix} \epsilon_{xx} & 0 & 0 \\ 0 & \epsilon_{yy} & 0 \\ 0 & 0 & \epsilon_{zz} \end{bmatrix} \begin{bmatrix} cos(\vartheta) & sin(\vartheta) & 0 \\ -sin(\vartheta) & cos(\vartheta) & 0 \\ 0 & 0 & 1 \end{bmatrix} =$$

$$\begin{bmatrix} (\epsilon_{xx})cos^2(\vartheta) + (\epsilon_{yy})sin^2(\vartheta) & (\epsilon_{xx})sin(\vartheta)cos(\vartheta) - (\epsilon_{yy})sin(\vartheta)cos(\vartheta) & 0 \\ (\epsilon_{xx})sin(\vartheta)cos(\vartheta) - (\epsilon_{yy})sin(\vartheta)cos(\vartheta) & (\epsilon_{yy})cos^2(\vartheta) + (\epsilon_{xx})sin^2(\vartheta) & 0 \\ 0 & 0 & \epsilon_{zz} \end{bmatrix} \tag{5.4}$$

To model the distortions of LC alignment within the hotspots, we isolated the areas around the edges of MM and built the tensor for each area individually. For convenience, we set a new origin (x_0, y_0) in each area as a point of reference to rotate the molecules' alignment, and hence the optical anisotropy, with respect to spatial coordinates.

Rotation angle ϑ, will then be:

$$\hat{\vartheta} = \hat{\varphi} - \tan^{-1}[(x - x_0)/(y - y_0)] \tag{5.5}$$

The resulting rotating angle ϑ varies from 135 to 45 degrees for planar 1 configuration (see Figure 5-20 (b)) and from 45 to -45 degrees for planar 2 configuration (see Figure 5-20(d)), showing a realistic idea of what we expected, as schematically shown in Figure 5-22 (a, b) respectively. Angle φ, defines whether the variation axis symmetry exists at 90° along $n_{\text{planar 1}}$ or at 0° along $n_{\text{planar 2}}$.

5.5 Orientational Optical Nonlinearity of Nematic Liquid Crystals Induced by The Enhanced Light-Matter Interactions with THz Metamaterials

Given that the re-alignment of the nematic LC must occur within the hotspots in simultaneously all metamolecules upon illumination of the sample, it could not be a spontaneous process. I therefore conclude that it was induced by the electric fields of the metamolecules and so the anomalous resonance frequency shift observed experimentally in the positive MM was the manifestation of Kerr (orientational) optical nonlinearity of the LC [2]. Kerr nonlinearity of LCs has not been reported for the intensities accessible with conventional commercial THz-TDS setups (typically built around mW lasers pumping photoconductive emitters) and I argue that the following factors could have enabled the effect in my experiments.

Firstly, I note that the re-orientation of the LC in the configuration described here is equivalent to in-plane electrical switching, which would occur without a threshold for the initial misalignment of the LC of less than 45°, as follows from [264]. Secondly, the electric field enhancement in my structures is dominated by two combined effects. One effect is the amplification of THz fields by the MMs via their high-Q resonant response. This (resonant) effect is relevant to both the negative and positive MMs and allows local fields one order of magnitude stronger than the incident field (as evident from diagrams in Figure 5-14 (b, d)).

The other effect is the concentration of electric fields by sharp geometric features of the metamolecules, the so-called 'lightning rod' effect [265,266]. This second (geometrical) effect, however, ensures further ten-fold enhancement only in the positive MM, where sharp geometric features of the metamolecules and localisations of the resonantly amplified fields (i.e., hotspots) coincide. As a result, the overall field enhancement attainable in the positive MM is likely to exceed two orders of magnitude (see diagram in Figure 5-14 (b)).

I, therefore, argue that the high electric field enhancement in combination with the threshold-less nature of the LC re-orientation make it not unreasonable to expect that the enhancement of the local field in the positive MM would enable optically-induced local switching of the LC even at the intensity levels characteristic of my THz-TDS setup.

5.6 Conclusions

In conclusion, I demonstrate that Babinet complementary patterns of a THz metallic MM do not exhibit the same frequency tuning range when hybridized with a nematic LC. My study suggests that this difference results from a mismatch between the alignment of the LC and the direction of the local electric field induced in the MM patterns. More intriguingly, my experimental observations indicate that it is possible to shift the resonance of the positive MM pattern beyond the limit imposed by theory and to significantly increase its tuning range. Further, the observed anomalous frequency shift results from the orientational optical nonlinearity of the LC enhanced via integration with the metallic MM.

I envisage that these findings can directly lead to the increase of the efficacy of THz modulators and other active optical components exploiting the enhanced nonlinear light-matter interactions in LC-MM hybrid structures. Most importantly, I show that nonlinear effects can be engaged with a low power photoconductive antenna-based THz spectrometer, when combined with resonant amplification and sub-wavelength concentration of THz fields facilitated by MMs. This demonstration enables future studies of nonlinear effects in the THz range, which up to now, where exclusively reserved for high-power THz spectrometers based on complex and often cumbersome, amplified laser systems.

Chapter 6

Analytical Calculation of The All-Optical In-Plane Switching of Liquid Crystals at Terahertz Frequencies Enabled by Metamaterials

This chapter aims to investigate the in-plane switching dynamics of homogeneously aligned nematic liquid crystals cells integrated with metallic resonators (metamaterials). I demonstrate an analytical calculation of the pure twist deformation of liquid crystals caused by the THz electric field enhancement in the vicinity of metamaterials and estimate the critical threshold to induce in-plane switching of liquid crystals. This method offers a combinatorial way to study molecular liquid crystal interactions in the bulk as well as interfacing with resonant structures. My contribution to this work discussed in this chapter is both the analytical and computational calculations.

6.1 Introduction

Liquid crystals (LCs) enable a range of technologies such as smart displays [267,268], smart windows [269,270], flat optics [271-274], and flexible electronics [275-277], not mention the now prevailing LC displays. LCs in such devices are controlled by externally applied electric fields, necessitating the use of transparent electrodes [156,157] which are not easily available at all regions of spectrum e.g. THz. Therefore, tuneable LC displays, or modulators are both of

interest and importance [52,94,278,279]. There are two main advantages of the all-optical control of LC devices: the absence of electrodes and hence externally applied electric field, and the flexible LC alignment patterns [52]. Such systems are also particularly interesting for manipulating light of longer wavelengths, such as THz radiation, where standard conducting electrodes are no longer transparent [3], thus restricting the development of active THz technology.

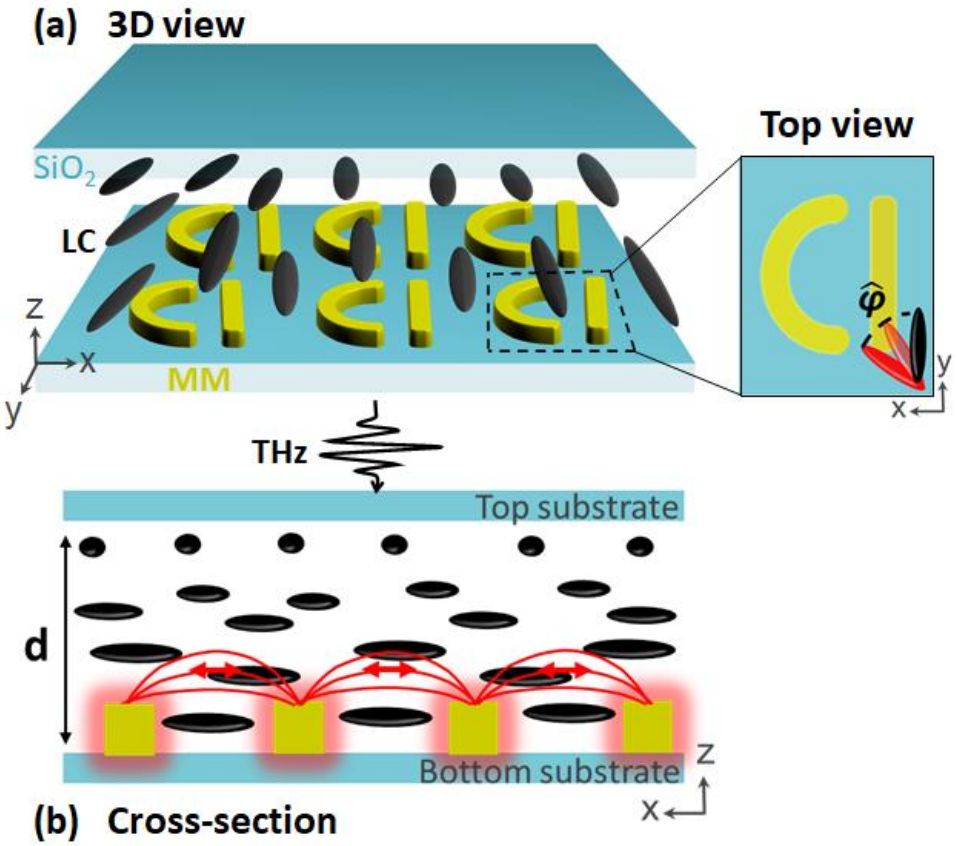

Figure 6-1 (a) 3D view of a homogeneously aligned LC cell, which is integrated with an array of metallic resonators (metamolecules). Magnification shows the geometry of the twist deformation of LC molecules by the in-plane THz electric field. (b) Schematic representation of in-plane switching induced in a homogeneously aligned LC cell, where shaded areas and red arrows show the near-field enhancement and lines respectively.

THz components, because of the long radiation wavelength, normally require thick devices for optimum response. Therefore, compact components are in demand, in particular such as light modulators [240,280], phase shifters [155] for applications in non-disruptive drugs sensing [281,282] and security [159,283,284]. LCs exhibit reduced birefringence in the THz region, the

effect that could be partially remedied by doping [159]. However, the most promising route for manipulating radiation in that region relies on THz resonant structures, the so-called metamaterials (MMs) that allow enhanced light-matter interactions leading to the desirable device response, while maintaining low device footprint (see e.g. [165,240] and references therein).

It has been shown that thin layers of LC integrated with metallic MMs are capable of effective manipulation of THz radiation but, so far, have been controlled by electric fields [161,165,240,243-249]. Moreover, I have recently shown experimentally that such hybrid systems can also be driven optically with a low-power THz beam of a conventional THz-time domain spectrometer (TDS) setup (see 0). The observed optical switching was attributed to local in-plane reorientation of LC molecules induced by incident THz fields, which undergo resonant amplification and sub-wavelength concentration facilitated by MMs. In this work, I provide a comprehensive theoretical analysis of the demonstrated effect based on the analytical model of in-plane LC switching [285], and confirm that engaging orientational optical nonlinearity of LCs at typical THz intensities is possible with the help of metallic MMs.

6.2 Experimental demonstration of optical switching

For the sake of completeness and for the convenience of the reader I provide below a brief account of the study of LC optical switching with THz fields (see 0). It involved the investigation of the transmission spectra of LC cells hybridised with MMs featuring D-shaped metallic resonators (metamolecules), which were measured with a commercial THz-TDS setup in the 0.1-1.4 THz range of frequencies. Each hybrid cell had the thickness of 20 μm and was filled with LC 1825 with induced planar alignment parallel to straight sections of the metamolecules (Figure 6-1(a)). The spectrum simulated for planar LC configuration (blue solid line) appeared blue-shifted with respect to the experimentally measured curve (black dashed line) and displayed larger variation of transmission at the resonance, as evident from Figure 6-2(a). This surprising discrepancy was attributed to local distortions of the initial planar alignment of LC, which could appear near the edges of the metamolecules due to the re-orientation of LC molecules driven there by resonantly amplified near-fields of the MMs (hotspots) (see Figure 6-2(b)).

To this end the numerical model was modified to include the distributions of the refractive index of LC near the edges and in the gaps of D-shaped resonators that reflected the re-alignment of LC molecules in the hotspots along the direction of the local electric field lines, as

shown in the inset to Figure 6-2(a). The transmission spectrum calculated for the MM using the modified numerical model is also depicted in Figure 6-2(a) (red solid line) and shows a good spectral overlap with the experimental data, provided that the maximal deviation from planar alignment in the hotspots did not exceed the twist angle φ of $\pi/4$. The overall field enhancement (E/E_0) attainable in the positive MM is likely to exceed 200 (see 0), indicating that nonlinear effects can be engaged even with a low-power THz spectrometer. Below, I show that such an enhancement would be sufficient for triggering in-plane re-alignment of the LC at the intensity levels characteristic of my THz-TDS setup.

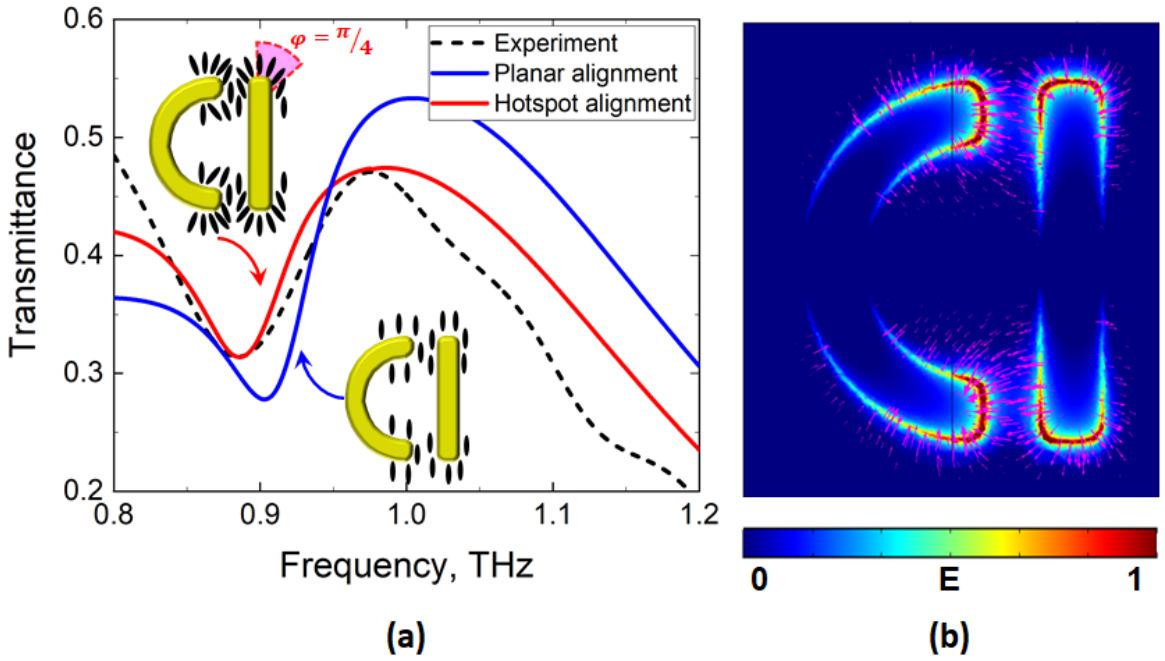

Figure 6-2 (a) Experimental (dash line) and simulated (solid lines) transmission spectra of LC-loaded MM in the case of planar alignment (blue curve) and hotspot alignment (red curve) induced by orientational nonlinearity of LC. Insets illustrate schematically the alignment of LC molecules in the two cases. Twist angle, φ, shows the maximum twist deformation of LC molecules by $\pi/4$. (b) Field map shows the normalised magnitude of electric field at the resonant frequency of the positive pattern. Field localisation appears around the edges of D-shaped MM geometry with electric field lines distributing along the pink arrows.

6.3 Analytical calculation of in-plane switching

I use a mathematical model previously developed for the analysis of the in-plane switching (IPS) of LCs homogeneously aligned between interdigital electrodes [285]. Briefly, IPS technology implies that the electrodes whose electrical field are used to switch the LC molecules, are found in one of the two substrates (see e.g., MMs in Figure 6-1(a)). As a result, a homogeneous electric field aligned parallel to the substrate surface is applied on the LC sample allowing 'in-plane' twist deformation of LCs from 0 rads to $\pi/2$. Similarly, the overall electric field enhancement attainable in the sharp edges of metallic resonators enable optically-induced 'in-plane' switching of the LC molecules towards the direction of the local fields, with only difference being that the initial angle is not 0 but $\pi/4$ (Figure 6-2(b)) [286,287]. Although IPS in [285] was considered in homogeneous field between two parallel electrodes, in this case the field is diverging and produced effectively by one electrode. Therefore, here IPS is considered as a local approximation around MMs hotspots (see Figure 6-3).

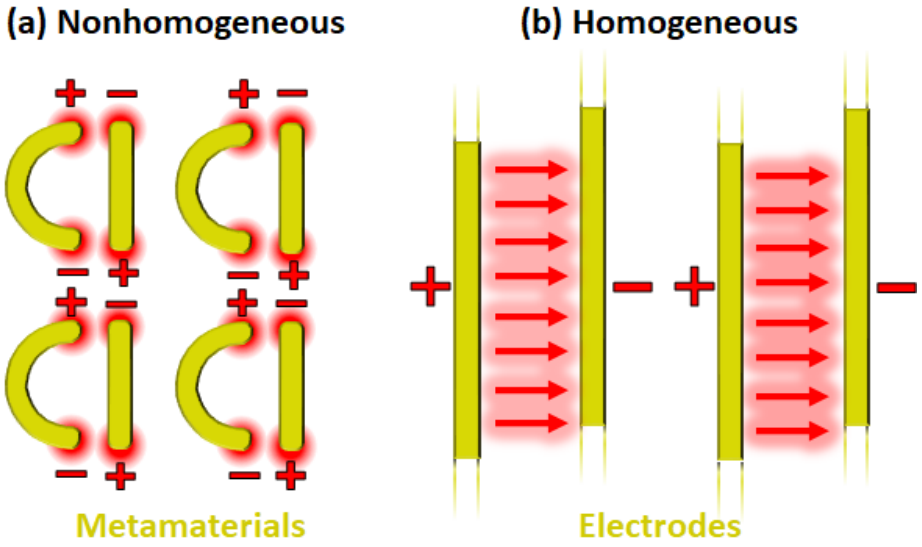

Figure 6-3 Drawing field lines: (a) diverge around the metamaterial edges and (b) extend perpendicularly to the parallel plates as per [285], producing either a nonhomogeneous or a homogeneous electric field, respectively.

This pure twist deformation caused by the THz electric field is considered in the vicinity of the gaps between the constituent elements of D-metamolecules. Following [285], the free energy F of the twist deformation can be described as,

$$F = \frac{1}{2}\int_0^d \left\{ K_2 \left(\frac{d\varphi}{dz}\right)^2 - \varepsilon_0 |\Delta\varepsilon| E^2 sin^2\varphi \right\} dz \tag{6.1}$$

where K_2 is the elastic constant of the twist deformation, φ is the twist angle (in xy-plane), ε_0 is the vacuum dielectric constant, $\Delta\varepsilon$ denotes dielectric anisotropy, and E corresponds to the electric field strength. Then by applying the Euler-Lagrange equation one can obtain,

$$K_2 \frac{d^2\varphi}{dz^2} + \varepsilon_0 |\Delta\varepsilon| E^2 \, sin\,\varphi \, cos\,\varphi = 0 \tag{6.2}$$

In this case, the initial orientation of LC molecules corresponds to $\varphi = {}^{\pi}/_{4}$ (the maximal initial misalignment with respect to the MM local-field lines (see Section 5.5)). Thus, the following substitution can be made: $\varphi = \varphi + {}^{\pi}/_{4}$, where φ now describes the deformation relative to the initial twist.

$$K_2 \frac{d^2\varphi}{dz^2} + \varepsilon_0 |\Delta\varepsilon| E^2 \, sin(\varphi + {}^{\pi}/_{4}) \, cos(\varphi + {}^{\pi}/_{4}) = 0 \tag{6.3}$$

Then, with the assumption that the twist deformation angle is small ($\varphi \to 0$) and the boundary condition $\varphi(0) = \varphi(d) = 0$ (i.e., strong LC anchoring imposed on both sides of the cell by rubbed polyimide), I arrive at the following solution:

$$\varphi(z) = \frac{\varepsilon_0 |\Delta\varepsilon| E^2}{4\, K_2} (d - z) z \tag{6.4}$$

Equation (6.4) indicates that the in-plane re-orientation of LC molecules in this case starts with no threshold on electric field, E, since the expression is valid for any $E \geq 0$. To find the strength of the local electric field needed to re-orient LC molecules in the plane of the MM along the field lines (i.e., to produce an additional twist of ${}^{\pi}/_{4}$), I aim to solve the nonlinear differential Equation (6.2).

To simplify the nonlinear differential equation and solve it analytically, the second term of Equation (6.2) can be written as:

$$\varepsilon_0 |\Delta\varepsilon| E^2 sin\,\varphi \, cos\,\varphi = \varepsilon_0 |\Delta\varepsilon| E^2 \frac{1}{2} sin\, 2\varphi \tag{6.5}$$

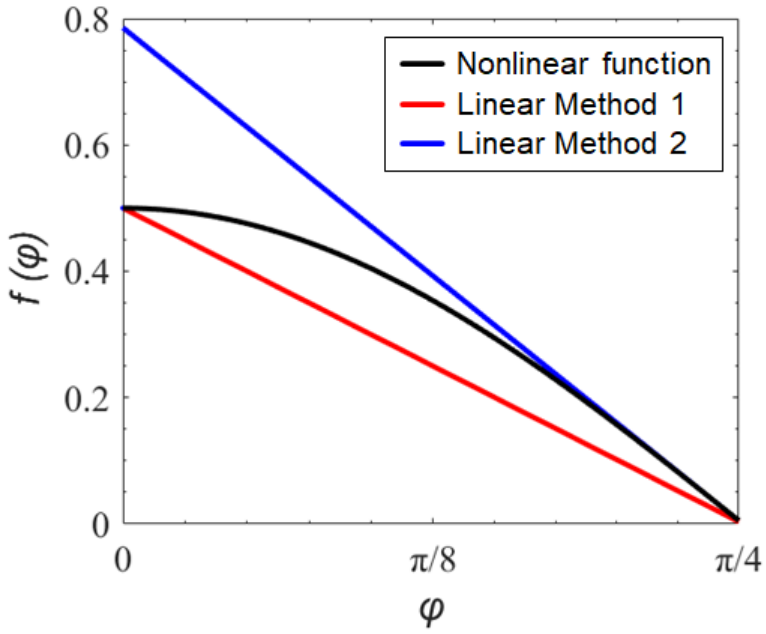

Figure 6-4 The linear approximation of $\frac{1}{2}cos\ 2\varphi$ (black line) obtained with two methods: Method 1 (red line) and Method 2 (blue line).

Although, Fréedericksz critical threshold involves a full re-orientation to $\pi/2$ for the twist angle, in this case the re-orientation occurs around the MM hotspots only to a maximum of $\pi/4$, as justified by my simulations in 0. In addition, from Figure 6-5(b) it is clear that the penetration depth of the near-field enhancement starts from the surface of the substrate (z=0) occupying the maximum strength. Therefore, φ is effectively offset into $\varphi \rightarrow \varphi + \pi/4$, and $\frac{1}{2}sin\ 2\varphi$ in Equation (6.5) is then transformed into $\frac{1}{2}cos\ 2\varphi$.

To solve the differential Equation (6.2) analytically, I approximate $\frac{1}{2}cos\ 2\varphi$ with a linear function using two different methods: the first (see red line at Figure 6-4) overestimates the required electric field strength, while the second (see blue line at Figure 6-4) underestimates it.

6.3.1 Linear approximation – Method 1

I approximate $\frac{1}{2}cos\ 2\varphi$ in Equation (6.2) by a line, which connects points at φ = 0 and φ = π/4 (see red line at Figure 6-4). The corresponding linear function has the form:

$$f_1(\varphi) = \frac{1}{2} - \frac{2\varphi}{\pi} \tag{6.6}$$

Using Equation (6.6) the initially nonlinear differential Equation (6.2) turns into:

$$K_2 \frac{d^2\varphi}{dz^2} - \frac{2\varepsilon_0|\Delta\varepsilon|E^2}{\pi}\varphi + \frac{\varepsilon_0|\Delta\varepsilon|E^2}{2} = 0, \tag{6.7}$$

which can be solved analytically, and its solution is given by:

$$\varphi(z) = \frac{\pi}{4} + k_1 exp\left(-\sqrt{\frac{2\varepsilon_0|\Delta\varepsilon|}{\pi K_2}}Ez\right) + k_2 exp\left(\sqrt{\frac{2\varepsilon_0|\Delta\varepsilon|}{\pi K_2}}Ez\right) \tag{6.8}$$

k_1 and k_2, can determined using boundary conditions, $\varphi(0) = 0$ and $\varphi(d) = 0$. The derived expressions for k_1 and k_2 are:

$$k_1 = -\left(\frac{\pi}{4} + k_2\right)$$

$$k_2 = -\frac{\pi}{4\left(exp\left(\sqrt{\frac{2\varepsilon_0|\Delta\varepsilon|}{\pi K_2}}Ed\right) + 1\right)} \tag{6.9}$$

The constants in Equations (6.8) and (6.9) for LC 1825 are taken from [58] (see Table 6-1).

Table 6-1. Specifications of LC 1825 [58]

Constants	**Values**
$\boldsymbol{\varepsilon_0}$	$8.85 \cdot 10^{-12}$ [N/V²]
$\boldsymbol{\Delta\varepsilon}$	17
$\boldsymbol{K_2}$	$7.4 \cdot 10^{-12}$ [N]

Figure 6-5 (a) presents the variation of the twist angle, φ, with the distance from the MM calculated using Equation (8) for different values of electric field strength. The strength of electric field increases from 10^{-4}V/μm (dark blue color) to 1.6 V/μm (dark brown color) with a step of $5 \cdot 10^{-2}$ V/μm. Varied electric field values were applied until $\varphi(E)$ is saturated at z =

1 μm, since up to this level above the MM the maximum near-field enhancement is localized (see Figure 6-5(b)). The stronger the electric field LC reorientation occurs closer at the MM surface, opposing the initial planar orientation even from the level of 1 μm for an of $E = 1.6$ V/μm.

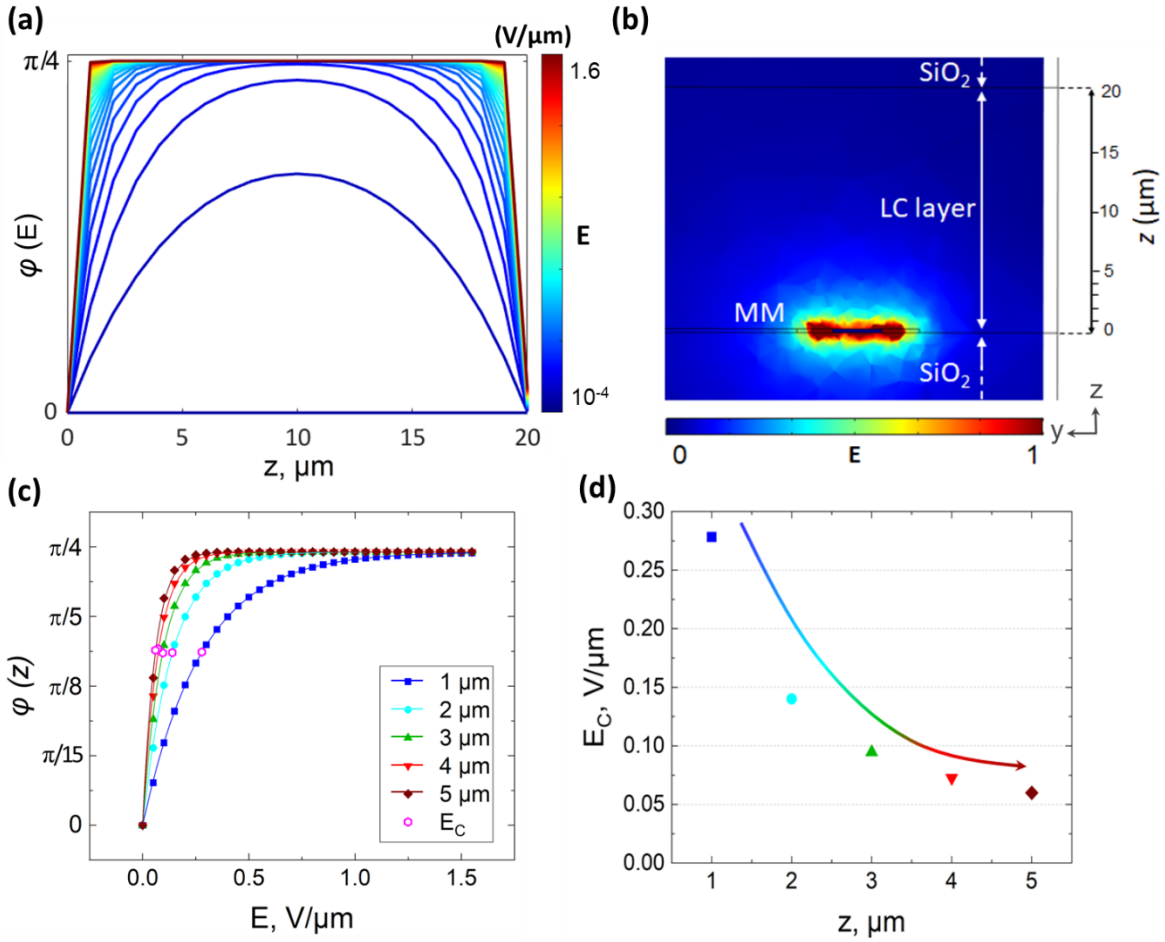

Figure 6-5 (a) The change of twist angle, φ, within LC layer, z, for different electric field, E, values. (b) Electric field map shows the penetration depth of the near-field enhancement of MMs in the LC bulk. (c) The change of twist angle, φ, as a function of the electric field strength, E, for different penetration levels, z, above the metasurface, (z=1-5 μm). The critical electric field strength values, EC, where LC molecules are oriented in between of initial planar and 'hotspot' alignments is shown in magenta open hexagons. (d) The estimated critical electric field strength, EC, as a function of LC thickness height, z, obtained by the linear approximation.

Although, to estimate exactly the value of E I analysed the twisted angle, φ, as a function of the applied electric field as shown in Figure 6-5(c). There, to calculate the threshold electric field I extract the value of $\varphi(z)$ before reaching saturation, which is estimated at 1.44 V/μm. Therefore, an electric field of $E \geq 1.44$ V/μm would be sufficient to reorient LC molecules in-plane by π/4 in the vicinity of MMs.

For longer distance above the MM surface such as 5 μm, the corresponding electric field strength for a twist angle change is smaller than the one needed closer to the MMs, as evident from Figure 6-5(a) and estimated at 0.3 V/μm from Figure 6-5(c). This specific electric field strength will be able to twist the LC molecules by π/4. However, at the level of 5 μm above the MM, LC molecules will not all be aligned at π/4 but lie in between of the initial planar (π/2) and φ(1 μm) i.e., π/4, creating a gradual transition of LC alignment between the metasurface and the LC bulk (see Figure 6-1(b)). There, the critical electric field, E_C, can be calculated by analysing the twisted angle, φ, as a function of the applied electric field (as shown in Figure 6-5(c)). The E_C is then defined at the level 1/e below the saturation of $\varphi(E)$ at 0.06 V/μm with a twist angle reorientation of 0.50 rads (≈ π/6) (see magenta open circles in Figure 6-5(c)). For completeness, I estimated the E_C for $z = 1 - 5\ \mu m$, and data are presented in Figure 6-5(d).

6.3.2 Linear approximation – Method 2

I approximate $\frac{1}{2}cos\,2\varphi$ in Equation (6.2) by a tangential line at φ = π/4 (see blue line at Figure 6-3). The corresponding linear function has the form:

$$f_2(\varphi) = -\varphi + \frac{\pi}{4} \tag{6.10}$$

Thereafter, using Equation (6.10) the initially nonlinear differential Equation (6.2) turns into:

$$K_2 \frac{d^2\varphi}{dz^2} - \varepsilon_0|\Delta\varepsilon|E^2\varphi + \varepsilon_0|\Delta\varepsilon|E^2\frac{\pi}{4} = 0 \tag{6.11}$$

Equation (6.11) can be then solved analytically, and its solution is given by:

$$\varphi(z) = \frac{\pi}{4} + k_1 exp\left(-\sqrt{\frac{\varepsilon_0|\Delta\varepsilon|}{K_2}}Ez\right) + k_2 exp\left(\sqrt{\frac{\varepsilon_0|\Delta\varepsilon|}{K_2}}Ez\right) \tag{6.12}$$

To determine $k_1$and k_2, I used the boundary conditions, $\varphi(0) = 0\ and\ \varphi(d) = 0$, which describe strong anchoring on both side of LC cell induced by rubbed surfaces. The derived expressions for k_1 and k_2 are:

$$k_1 = -\left(\frac{\pi}{4} + k_2\right) \tag{6.13}$$

$$k_2 = -\frac{\pi}{4\left(exp\left(\sqrt{\frac{\varepsilon_0|\Delta\varepsilon|}{K_2}}Ed\right)+1\right)}$$

The constants in Equations (6.12) and (6.13) for LC 1825 are taken from [58] (see Table 6-1).

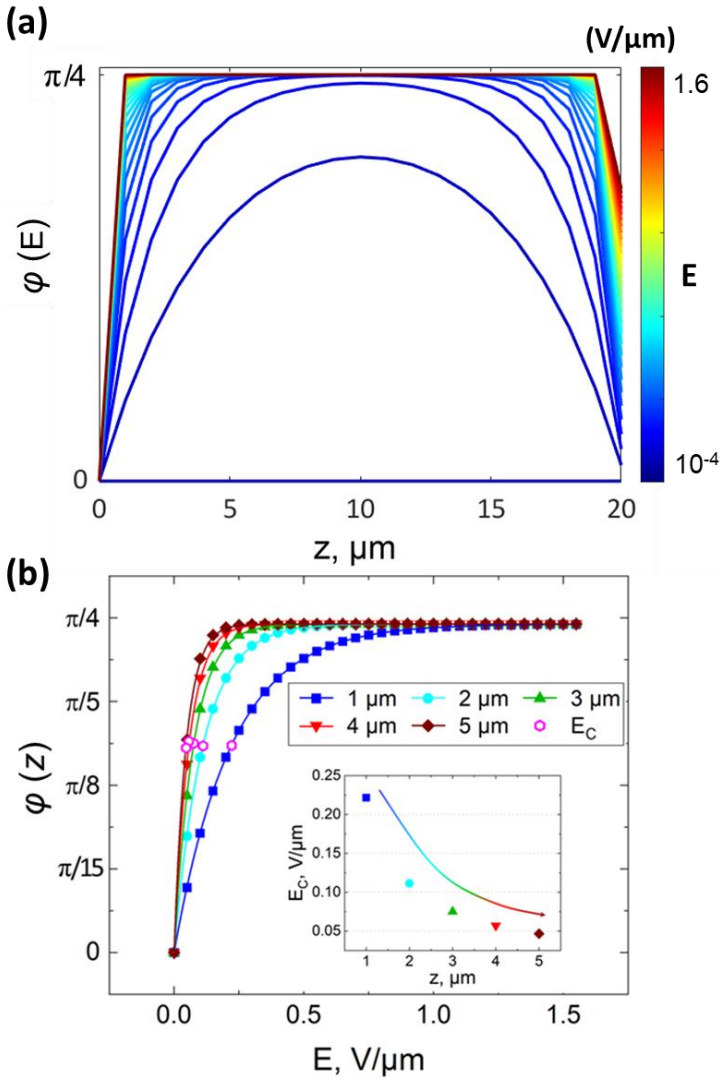

Figure 6-6 (a) The change of twist angle, φ, within LC layer, z, for different electric field, E, values. (b) The change of twist angle, φ, as a function of the electric field strength, E, for different penetration levels, z, above the metasurface, (z=1-5 μm). The critical electric field strength values, EC, where LC molecules are oriented in between of initial planar and 'hotspot' alignments is shown in magenta open hexagons. Inset shows the estimated critical electric field strength, EC, as a function of LC thickness height, z, obtained by the linear approximation.

Figure 6-6(a) presents the change of twist angle, φ, as derived from Equation (6.12), as a function of the distance from the MM, calculated for a range of different electric field strength values. Here I follow the same analysis procedure as in section 6.3.1. The strength of electric field increases from 10^{-4} V/μm (dark blue color) to 1.6 V/μm (dark brown color) with a step of $5 \cdot 10^{-2}$ V/μm and the applied electric field values varied until $\varphi(E)$ is saturated at z = 1 μm. Thus, an electric field of 1.6 V/μm is enough to trigger in-plane reorientation of LCs by π/4 for a distance of 1 μm above the MMs, which further proves that both linear approximation methods coincide. As expected, the tangent line approximation underestimates the electric field threshold in comparison with the first linear approximation method. In fact, the value of the threshold electric field as extracted from Figure 6-6(b) is estimated at 1.05 V/μm. Thus, an electric field of $E \geq 1.05$ V/μm would be sufficient to reorient LC molecules in-plane by π/4 in the vicinity of MMs, according to Method 2.

While for 5 μm above the LC-MM interface, an electric field strength of 0.25 V/μm would be able to induce reorientation of LC molecules by π/4 which is again smaller than the estimation of Method 1 (0.3 V/μm), preserving the underestimation concept. Thereafter, the critical electric field threshold, E_C, is estimated at 0.05 V/μm with a twist angle reorientation of 0.49 rads (≈ π/6) (see magenta open circles in Figure 6-6(b)). Inset of Figure 6-6(b) shows the E_C estimation for $z = 1 - 5\ \mu m$.

6.4 Discussion

The threshold electric field strength which can effectively drive LC molecules to reorient in-plane by π/4 at a distance of 1 μm above the MM, lies between the two estimates presented here. The first gives an estimation of 1.44 V/μm while the second 1.05 V/μm. However, this change of twist angle, $\varphi(z)$, may occur with a lower electric field threshold.

It is known that LCs in the bulk have lower voltage threshold to reorient their molecular axis due to intrinsic dynamics between the molecules [1,2], which is also evident from Figures Figure 6-5(a) and Figure 6-6(a). To better quantify this in this case, I calculate the electric field threshold at a distance of $z = 5\ \mu m$, where the MM near-field drops off (see Figure 6-5(b)). The electric field strength capable of reorienting LC molecules at $z = 5\ \mu m$ will be sufficient to affect LC alignment near the MM too. Therefore, I define the critical electric field threshold between 0.06 V/μm and 0.05 V/μm, as obtained from methods 1 and 2 respectively. The amplitude of the impinging pulsed THz-TDS wave in conjunction with the local field enhancement at the MM suffice to approach that threshold value.

6.5 Conclusions

Here, I demonstrate an analytical method to estimate the IPS mode of nematic, homogeneously aligned, LCs integrated with planar MM resonators. Such LC-MM resonators are found to possess strong near-field intensities exceeding 200 (E/E_0). To prove the switching principle satisfying the IPS mode, the near-field threshold required. I found that the near-field threshold of IPS of the nematic LC is ranging between 0.06 V/μm and 0.05 V/μm for methods 1 and 2, respectively. These electric field strength values lie in the range of most conventional low-power THz apparatuses. Therefore, this proves my initial hypothesis, that light confinement delivered by the hybrid MM LC devices results in all-optical in-plane reorientation of LC molecules by ± $\pi/4$ radians. I argue that this study enables future work investigating non-linearities in THz LC devices allowing the discovery of electrode-free nanostructured patterns for applications such as on-chip waveguides, optical fibres, spatial light modulators, and spectral filters.

Chapter 7

Conclusions and Outlook

7.1 Conclusions

Passing from the 'age' of voltage driven LC integrated devices to the 'smarter' all-optically driven, active photo-addressable ALs and narrowband resonant MMs (MMs) are investigated. This Thesis provided evidence that active control of visible and THz regimes is possible when standard LCs technology is merged with the photosensitive complex dyes (PAAD) or with the exotic properties of planar MMs. More specifically, this Thesis included:

- The development of a fully-automated optical instrument to characterise multi-layered LC devices in one-go and obtain profile maps of their core properties in real time. Integrated LC cells with enhanced, photoactive response, asymmetric by design, need to be monitored for the stability and uniformity, especially in the regions exposed to light. In this work, I report on an integrated, versatile model and technique to characterise these parameters as well as more subtle effects, such as the strength of anchoring energy. The snapshot method also provides two-dimensional maps of the cells' thickness, pretilt angle and uniformity.

- The investigation of the photo-aligning properties of complex azobenzene dyes (PAAD) as AL to the LCs. Here I used the photo-addressable PAAD ALs to control the LC alignment, switching from planar state to the twisted state. Conventionally, UV light is used to address azobenzene-based dyes, however here I proved that this is possible even for visible light.

- The development of an optically addressed bistable LC-based waveplate for efficient control of visible and near-infrared light. Such photo-alignment properties of the layer

enable reversible switching between two perpendicular alignment states at the cell surface. An efficiency of 90% has been reported by switching between a planar and twisted LC configurations. Further, I showed that this process i.e. switching ON/OFF is reversible and reproducible for multiple cycles.

- The integration of LCs with planar MMs for efficient, all-optical control of THz radiation. I experimentally and theoretically demonstrate that intensity modulation of THz radiation using a large-scale planar MM hybridized with a 20 μm thin layer of a LC. I showed that tunable birefringence of an optically thin layer of LC, which is too weak to produce any noticeable transmission effect alone, can yield a very efficient THz radiation control mechanism when functionalised with the sharp Fano resonant response of my metamolecules.

- The observation that Babinet complementary patterns of a spectrally tunable MM incorporating a nematic LC normally do not exhibit the same tuning range, as assumed. Here I demonstrated that for a hybrid, THz LC-MM, the sensitivity of its resonances to the variations of the refractive index differs substantially for the two complementary patterns. This is due to a mismatch between the alignment of the LC and the direction of the local electric field induced in the patterns.

- The first demonstration of an anomalous resonance shift, beyond the limits imposed by theory, due to spatial re-orientation of LC molecules around the MM 'hotspots'. This could have been resulted only from a better match between the direction of the local electric field and the orientation of LC molecules, since that would effectively increase the refractive index of the LC perceived by the resonant electromagnetic mode of the metamolecules.

- The suggestion that electric field enhancement in my structures is dominated by two combined effects. (i) The amplification of THz fields by the MMs via their high-Q resonant response. (ii) The concentration of electric fields by sharp geometric features of the metamolecules, the so-called 'lightning rod' effect. As a result, the overall field enhancement attainable in the positive MM is likely to exceed by several orders of magnitude the field enhancement of the negative MM design.

- The manifestation that Kerr nonlinearity of LCs has not been reported before for the intensities accessible with conventional, commercial THz-TDS setups. This demonstration enables future studies of nonlinear effects in the THz range, which up to now, where exclusively reserved for high-power THz spectrometers based on complex and often cumbersome, amplified laser systems.

- The finding that that the re-orientation of LC molecules in the vicinity of metallic resonators is equivalent to the in-plane electrical switching (IPS mode) of homogeneously aligned nematic LCs.

- A comprehensive theoretical analysis method based on the analytical model of the IPS LC switching mode, which confirms that engaging orientational optical nonlinearity of LCs at typical THz intensities is achievable with the use of metallic MMs.

In conclusion, this Thesis merged the physics of LCs and MMs upon investigating novel, 'smart', THz modulators. The findings reported in this Thesis, can directly lead to the increase of the efficacy of THz modulators and other active optical components exploiting the enhanced nonlinear light-matter interactions in LC-MM hybrid structures.

7.2 Ongoing and Future Work

7.2.1 Investigation of twisted liquid crystal devices integrated with THz metamaterials

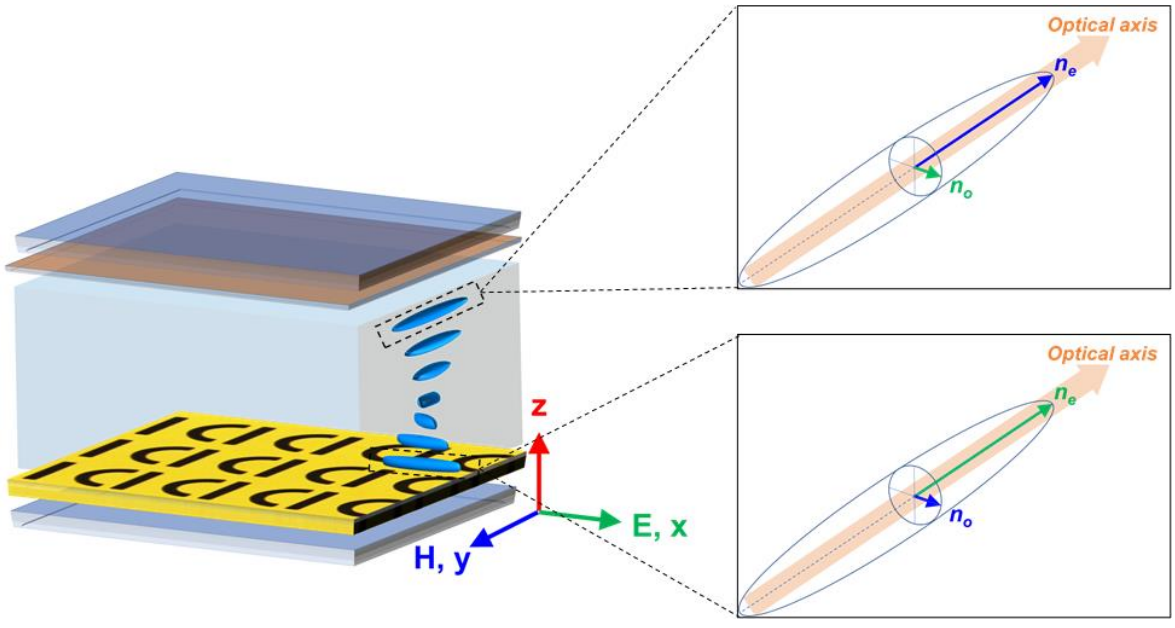

Figure 7-1 Schematic representation of a twisted nematic LC cell.

Complex, asymmetric by design THz MMs, namely D-shaped patterns, enabling high-Q Fano resonances offer a transmission shift up to 45 GHz when two opposite planar alignments are compared. This shift was beyond the limitation imposed by my computational model,

indicating that a nonlinear optical anisotropy of LC occurs due to the enhancement of THz electric field around the 'hotspots' of MMs. However, different designs may offer a larger resonance shift.

Therefore, here I propose to explore a range of different MM designs with the aim to provide a portfolio of different patterns either in the positive or negative designs. In addition, I suggest investigating the effect between a planar LC alignment and a twisted configuration. To the best of my knowledge, modelling a twisted LC configuration has not been presented before.

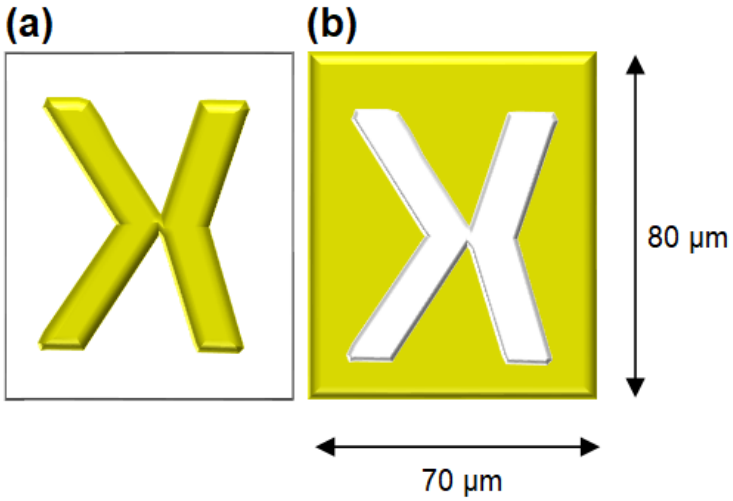

Figure 7-2 Schematic illustration of the X-shaped metamolecules in (a) positive and (b) negative designs. The width of the patches/slits is 10 µm, and the unit cell of the arrays has the dimensions of 70 x 80 µm.

7.2.2 Diffraction Efficiency of Azobenzene Complex Dyes

Photo-aligning azobenzene dyes (PAAD) are proven to control efficiently the alignment of thin LC cells with one-step illumination with UV or visible light (see 0). Here, I aim to exploit their photoinduced properties in order to create bistable THz modulators based on the LC-MMs integrated devices. Instead of the fixed LC geometries emerged from the rubbing technique, switching between LC states will be possible by illuminated the sample with visible light [288,289]. Thereafter, by altering the polarisation of the pump light (i.e. linear, circular, elliptical, etc) different patterns can be written in the surface of PAAD materials and hence extend into LC layer. In addition, PAAD materials offer a smaller anchoring energy with molecules moving more 'freely' on the substrate surface, prompting LC molecules to re-orient even closer to the ALs' level and hence achieve a larger resonant shift with less electric field strength (E_F) [290]. As a result, PAAD material is an excellent candidate for the creation of photo-addressable LC spatial light modulators (SLM) for the THz regime.

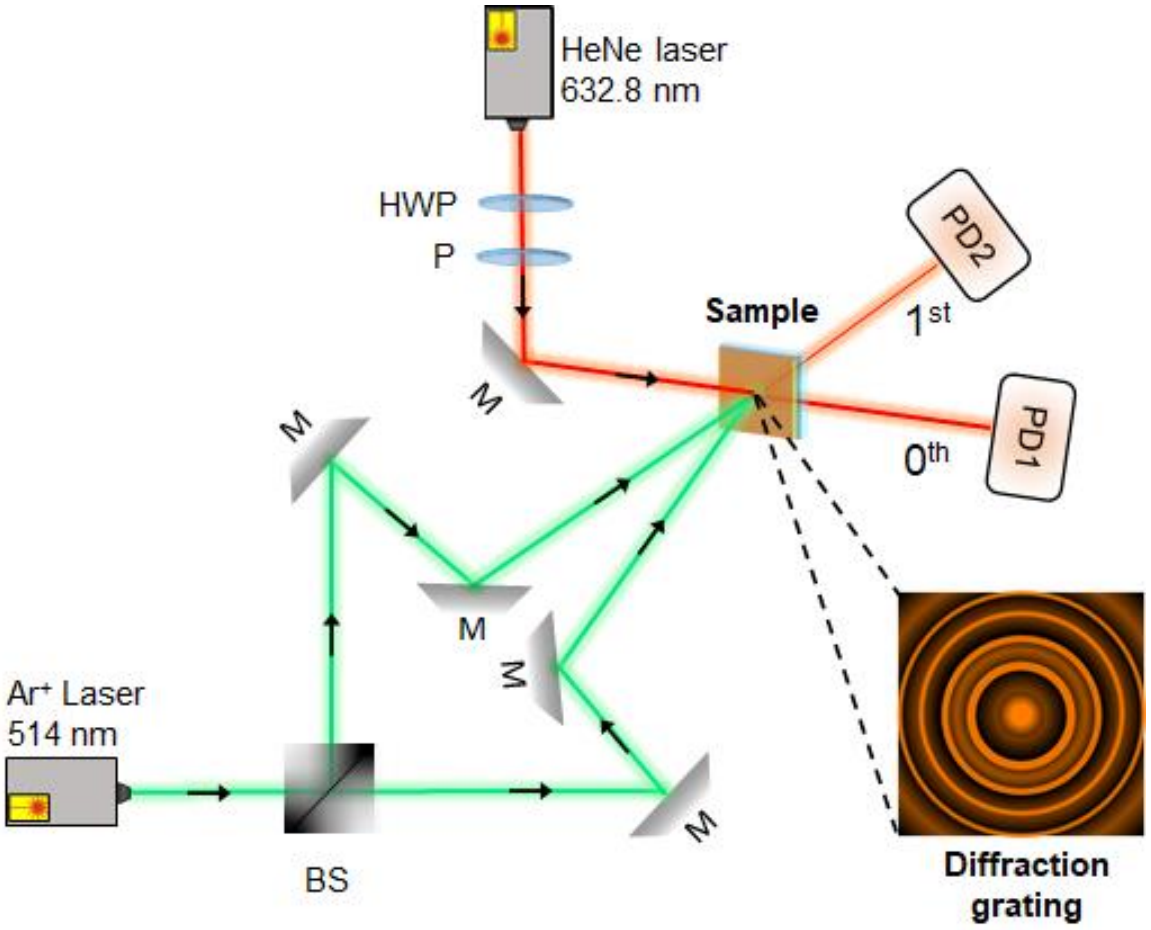

Figure 7-3 A 514.5 nm Ar^+ laser was used for writing the diffraction gratings and a HeNe laser at 632.8 nm was used for monitoring the diffraction efficiency (η).

One of the most astonishing feature of PAAD materials is the fact that high-modulation-depth-relief gratings (SGRs) can be inscribed at the polymer-air interface, when exposed to an interference pattern of light with spatial variation of the intensity and/or polarisation. This effect holds promise for holographic applications, providing an interesting connection between optical alignment techniques and functional hybrid LC-MMs THz modulator.

Here, I present the first step towards understanding the photoinduced properties of PAAD materials by monitoring the diffraction from phase gratings, recorded in thin films by interferometric illumination. A periodic intensity pattern was created by the interference of two mutually coherent Ar^+ laser beams at 514.5 nm, a wavelength strongly absorbed by the PAAD films, using a Michelson interferometric arrangement [291], as shown in Figure 7-3. The angle between the recording beams was 30°, corresponding to a grating period of 1 μm. The pump beam had linear polarisation and perpendicular to the plane of incidence, with a total recording laser power at 10 mW. Photo-induced gratings were probed by a HeNe laser beam

(at 632.8 nm) with a power of 1.4 mW, and incident at the corresponding Bragg angle for this wavelength, which is 18.5°. The polarisation of the probe was controlled with the aid of a polariser (P) and a half-wave plate (HWP). Transmitted and diffracted orders were measured after the gratings recording and with pump beams turned off.

Photoinduced gratings were written on PAAD-22E thin (~35 nm) on 1 mm ITO coated glass substrate. The incident angle and polarisation of the probe beam were varied to monitor the transmittance of the s- and p-polarised outputs (see Inset

Figure 3-11). In order to achieve this, the sample was held in a rotation stage. The stage consisted of a 360° rotating base with a holder to keep the sample cantered on the stage's rotational axis (as depicted in Figure 3-10, the axis points out of the image). In this way, the incident light remained focused on the same spot of the sample as the stage was rotated, enabling us to monitor the transmission of the same spot of the sample for all of the different angles of incidence (as described in Section 3.3). After propagating through the sample, the transmitted light (0th order) was collected by a photodiode, PD1, while positive and negative 1st diffracted orders by PD2, which measured its intensity.

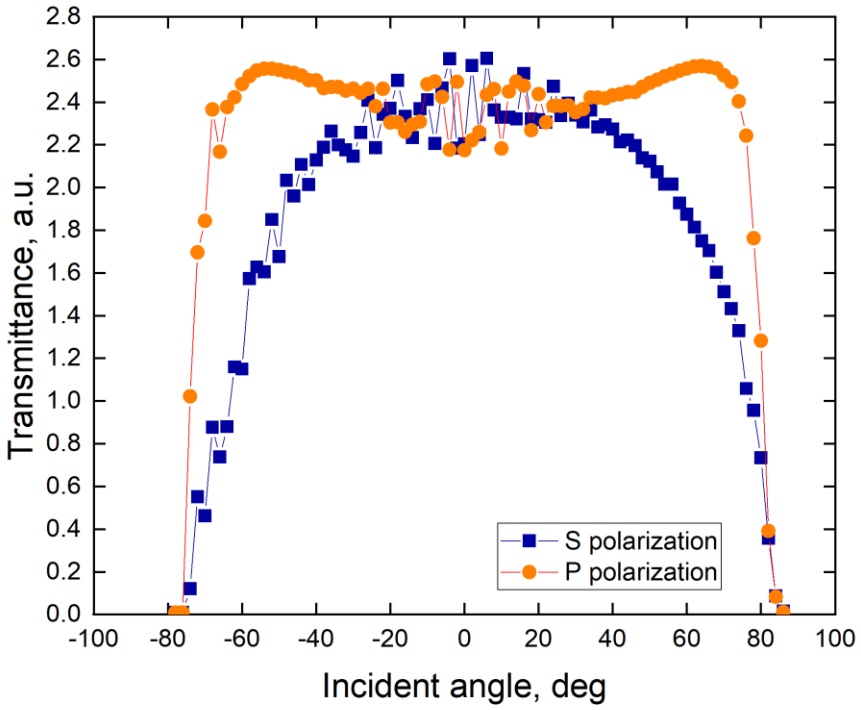

Figure 7-4 Transmitted order is S- and P-polarisation of the reference sample: ITO coated glass.

Figure 7-4 presents, the transmission (0th order) of the reference sample i.e., ITO coated glass, while Figure 7-5 for PAAD-22E on ITO/glass. The diffraction efficiency, η, was measured for

two polarisations of the probe beam, parallel (P) and perpendicular (S) to the plane of incidence, as presented in Figure 7-6. It was calculated by dividing the power of the first order diffracted beam by the power of the 0th order.

While it is not clear to us the behaviour of PAAD gratings yet, the highest diffraction efficiency value of PAAD-22E is estimated at 3×10^{-4} for the S polarisation while of magnitude lower for the P polarisation. Clearly, diffraction efficiency depends strongly on the polarisation of the pump to the probe beam. Further, investigation of both 0th and 1st orders is needed.

The next step is to investigate the formation of gratings with AFM, POM and SEM imaging and understand further their photoinduced properties. Thereafter, we will test their stability over time trying a variety of possible inscription wavelengths. We foresee that the combination of the flexible photoaddressable concept will enable new applications for photo-responsive THz modulators.

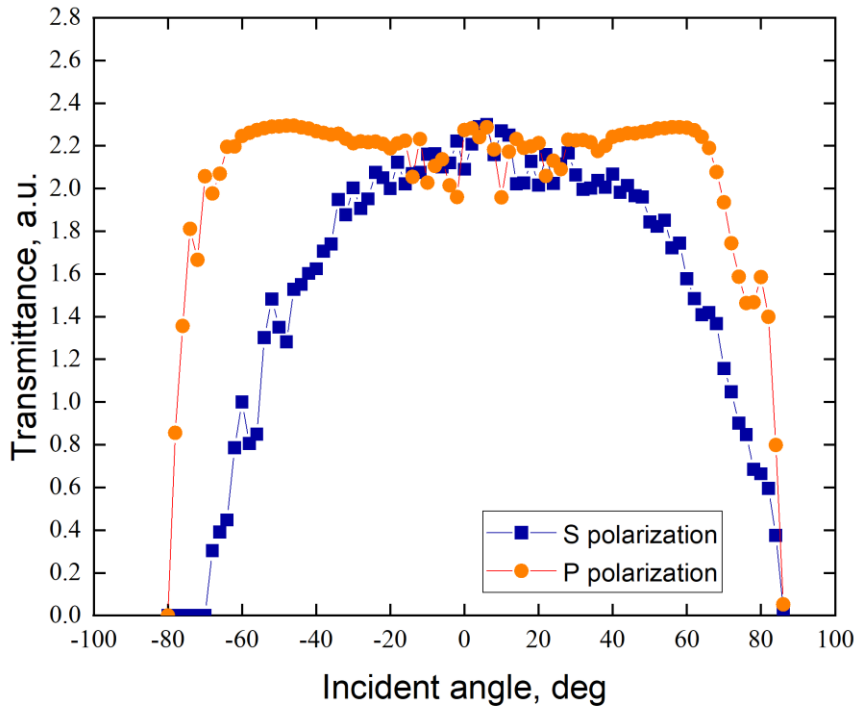

Figure 7-5 Transmitted order is S- and P-polarisation of the sample: PAAD film on ITO coated glass.

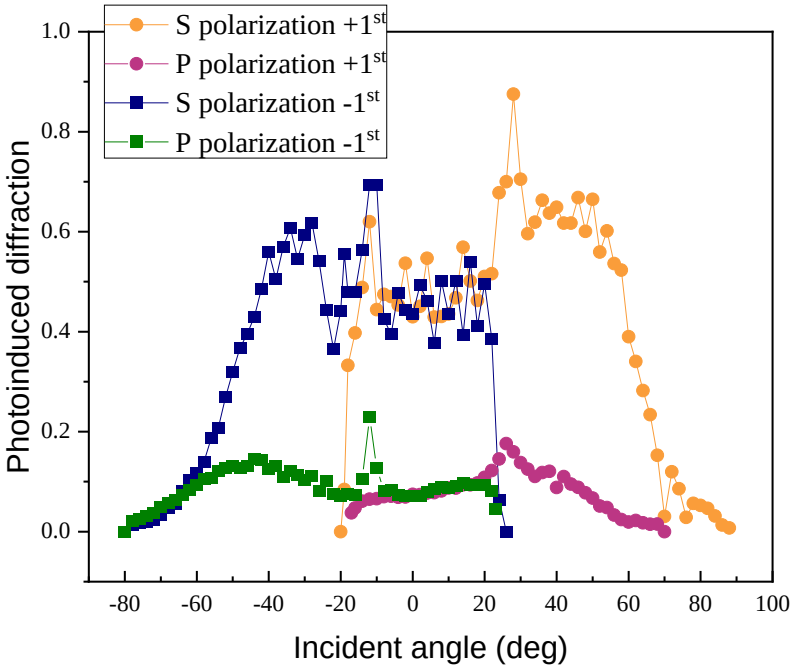

Figure 7-6 1st diffractive orders is S- and P-polarisation of the sample: PAAD film on ITO coated glass.

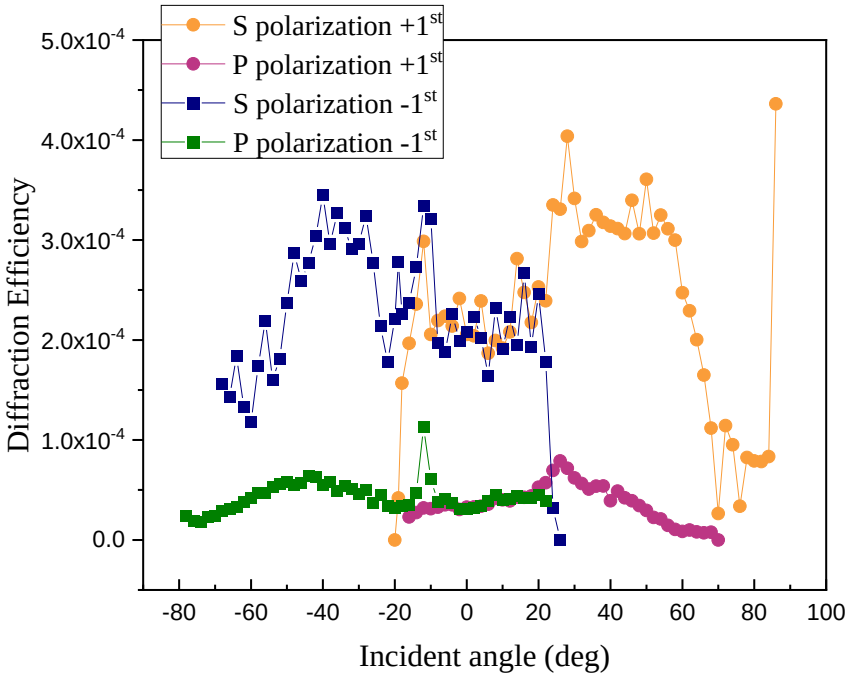

Figure 7-7 Diffraction efficiency as calculated from 1st diffracted orders and from 0th transmitted orders for S- and P-polarisation of the sample: PAAD film on ITO coated glass.

Appendix A

Different LC re-alignment scenarios caused by the near-field enhancement in the vicinity of MM edges

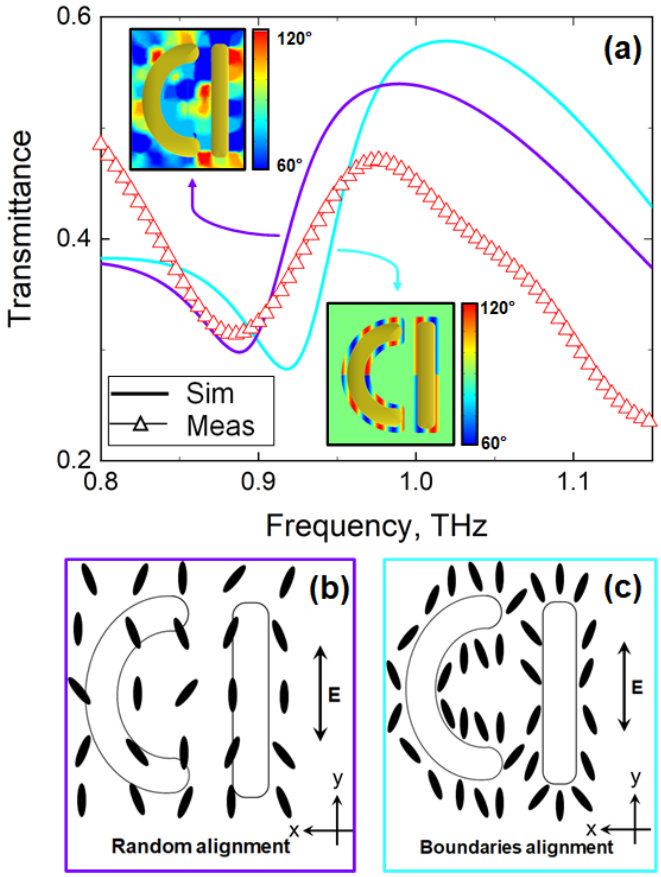

Figure A-1. Apart from the re-alignment scenario of NLC molecules around near-field 'hotspots', we investigated two more re-alignment scenarios; 'random' and 'boundaries' alignment. (a) Transmission spectra of experimental data (scatter) and simulations (solid lines) for NLC-loaded positive THz MM films in planar 1 configuration. (Insets) Calculated angular distribution of NLC molecules when distributed randomly, or locally around the boundaries of metamolecules. Angular distribution ranges from 60° to 120° (±30° from 90° i.e., planar 1 configuration) (b) Schematic representation of 'random' alignment. This scenario is not applicable due to the strong anchoring energy of the rubbing, however, proves the alignment quality of the initial planar 1. (c) Schematic representation of 'boundaries' alignment, where NLC molecules are confined due to the vicinity of metallic nanostructure and rotate around the boundaries of metamolecules.

Here, I present two additional alignment scenarios for LCs in order to explain the anomalous resonance shift observed for the positive MM when hybridised with a thin (20 μm) layer of LC. To better quantify the shifts of the resonant frequency of the MMs with respect to the orientation of LCs, we investigated three different alignment scenarios, which differ from the initial planar configuration. The first scenario i.e., 'random' alignment corresponds to a random spatial variation of LC molecules, where variation occurs all over the unit cell within the range of $\pm\pi/3$ radians from the planar 1 position (parallel to y axis). Then, scenario 2, i.e., 'boundaries' alignment, indicates that there is a variation of LC alignment only around the boundaries of the D-shaped MM, assuming that molecules follow the shape of D MM under confinement in the vicinity of metasurface. Finally, scenario 3 i.e., 'hotspots' alignment, shows that there is a variation of LC alignment only around the edges of the D-shaped MM, caused by the extreme light localization at the hotspots which we discussed in this thesis.

Transmission spectra of these scenarios along with experimental results are shown in Figure A-1. Firstly, to ensure that the large experimental shift is not an artefact of mechanical rubbing and fabrication imperfections, we simulated a random orientation of LC molecules (scenario 1). Alignment of LC molecules varies randomly throughout the unit cell surface, corresponding to higher refractive index and hence red-shifted resonant frequency position. In particular, transmission spectra of 'random' variation is blue-shifted only by 2 GHz from the experiment however it differs at lower frequencies offering a larger amplitude which does not fit the experimental results. Similar results we obtained from 'boundaries' alignment.

Appendix B

B1. Journal and Conference publications

- Perivolari, E., Fedotov, V. A., Kaczmarek, M, and Apostolopoulos, V. (2021). All-Optical Switching of Liquid Crystals at Terahertz Frequencies Enabled by Metamaterials. (submitted)

- Perivolari, E., Fedotov, V. A., Parka, J., Kaczmarek, M, and Apostolopoulos, V. (2021). Anomalous resonance frequency shift in LC-loaded THz metamaterials. (submitted)

- Perivolari, E., D'Alessandro, G., Apostolopoulos, V., Brouckaert, N., Heiser, T., & Kaczmarek, M. (2021). Two-dimensional snapshot measurement of surface variation of anchoring in LC cells. *Liquid Crystals*, 1-11.

- Gill, J. R., Perivolari, E., Kaczmarek, M, & D'Alessandro, G. (2021). Efficient scattering model of multi-layer systems with anisotropic films. *Journal of the Optical Society of America A*, 38(5), 595-605. **[Featured as Editor's Pick]**

- Perivolari, E., Fedotov, V. A., Apostolopoulos, V., Kaczmarek, M. (2019). Optically driven LC modulators integrated with terahertz metafilms *(Conference Proceedings).* Optics of Liquid Crystals-OLC 2019. Université Laval, Quebec, Canada.

- Perivolari, E., Gill, J. R., Podoliak, N., Apostolopoulos, V., D'Alessandro, G., & Kaczmarek, M. Bistable and photo-switchable thin films for efficient visible and near-infrared light manipulation, (2018), Proc. SPIE 10735, Liquid Crystals XXII, 107350D.

- Perivolari, E., Gill, J. R., Podoliak, N., Apostolopoulos, V., Sluckin, T. J., D'Alessandro, G., & Kaczmarek, M. (2018). Optically controlled bistable waveplates. *Journal of Molecular Liquids*, 267, 484-489.

- Bennett, T., Proctor, M., Forster, J., Perivolari, E., Podoliak, N., Sugden, M., Kaczmarek, M. & D'Alessandro, G. (2017). Wide area mapping of LC devices with passive and active command layers. *Applied Optics*, 56(32), 9050-9056.

B2. Conference contributions

- [Oral presentation] Unusually Large Tuning Range in Liquid Crystal-Loaded THz Metamaterials. Perivolari, E., Apostolopoulos, V., Kaczmarek, M, & Fedotov, V. A. 15th International Congress on Artificial Materials for Novel Wave Phenomena – Metamaterials 2021. New York, USA.

- [Oral presentation] Orientational Optical Nonlinearity of Nematic Liquid Crystals Integrated with THz Metamaterials. Perivolari, E., Fedotov, V. A, Apostolopoulos, V., & Kaczmarek, M. SPIE Liquid Crystals 2021. San Diego, USA.

- [Oral presentation] Anomalous Resonance Frequency Shift in Liquid Crystal-Loaded Metamaterials. Perivolari, E., Apostolopoulos, V., Kaczmarek, M, & Fedotov, V. A. CLEO Europe 2021.

- [Oral presentation] Optically driven liquid crystal modulators integrated with terahertz metafilms. Perivolari, E., Fedotov, V. A., Apostolopoulos, V., & Kaczmarek, M. Optics for Liquid Crystals (OLC) 2019. Laval University, Quebec, Canada.

- [Poster] Optically driven waveplates. Perivolari, E., Gill, J. R., Podoliak, N., Apostolopoulos, V., Sluckin, T. J., D'Alessandro, G., & Kaczmarek, M. Quantum Light and Matter (QLM) summer school, Southampton 2019, UK. [**1st place award]**

- [Oral presentation] Bistable photo-induced properties of azobenzene based materials integrated in liquid crystal systems. Perivolari, E., Mavrona, E., Gill, J. R. E. , Podoliak, N., Mailis, S., D'Alessandro, G., Apostolopoulos, V., & Kaczmarek, M. Photoalignment and Photopatterning in Soft Materials (PhoSM) 2018, Tampere University of Technology, Finland.

- [Oral presentation] PAAD films for reversible photo-aligned liquid crystal devices. Gill, J. R. E., Perivolari, E., Podoliak, N., Apostolopoulos, V., D'Alessandro, G., & Kaczmarek, M. British Liquid Crystal Society (BLCS) 2018, Manchester, UK.

- [Poster] Compact optical device for measuring liquid crystal elastic and dynamic properties. Podoliak, N., Perivolari, E., Bennett, T.P., Proctor, M. B., D'Alessandro, G., Regrettier, T., Heiser, T., & Kaczmarek, M. SPIE 2017. San Diego, USA.

Bibliography

[1] De Gennes P-G, Prost J. The physics of liquid crystals. Vol. 83. Oxford university press; 1993.

[2] Khoo I-C, Wu S-T. Optics and nonlinear optics of liquid crystals. Vol. 1. World Scientific; 1993.

[3] Chen C-W, Lin Y-C, Chang C-H, et al. Frequency-dependent complex conductivities and dielectric responses of indium tin oxide thin films from the visible to the far-infrared. IEEE Journal of Quantum Electronics. 2010;46(12):1746-1754.

[4] Collings PJ, Goodby JW. Introduction to liquid crystals: chemistry and physics. Crc Press; 2019.

[5] Kawamoto H. The history of liquid-crystal displays. Proceedings of the IEEE. 2002;90(4):460-500.

[6] Khoo I-C. Liquid crystals. Vol. 64. John Wiley & Sons; 2007.

[7] Blinov LM. Electro-optical and magneto-optical properties of liquid crystals. JOHN WILEY & SONS, INC, 605 THIRD AVE, NEW YORK, NY 10158, USA, 1983, 350. 1983.

[8] Outram B. Liquid Crystals. Bristol, UK: IOP Publishing; 2018 September 2018.

[9] Oseen C. The theory of liquid crystals. Transactions of the Faraday Society. 1933;29(140):883-899.

[10] Frank FC. I. Liquid crystals. On the theory of liquid crystals. Discussions of the Faraday Society. 1958;25:19-28.

[11] Collings PJ. Liquid crystals: nature's delicate phase of matter. Princeton University Press; 2002.

[12] Liquid Crystal Microscopy Blog http://lcmicroscopy.weebly.com/lc-photogallery.html.

[13] Rapini A, Papoular M. Distorsion d'une lamelle nématique sous champ magnétique conditions d'ancrage aux parois. Le Journal de Physique Colloques. 1969;30(C4):C4-54-C4-56.

[14] Blinov LM, Chigrinov VG. Electrooptic effects in liquid crystal materials. Springer Science & Business Media; 1996.

[15] Repiova A, Frederiks V. On the nature of the anisotropic liquid state of mater, J. Russian Phys Chem Soc. 1927;59:183.

[16] Chigrinov VG. Liquid crystal devices: physics and applications. 1999.

[17] Sonin AA. The surface physics of liquid crystals. 1995.

[18] Yang D-K, Wu S-T. Fundamentals of liquid crystal devices. John Wiley & Sons; 2014.

[19] Yaroshchuk O, Reznikov Y. Photoalignment of liquid crystals: basics and current trends. Journal of Materials Chemistry. 2012;22(2):286-300.

[20] Dubois-Violette E, Durand G, Guyon E, et al. Instabilities in nematic liquid crystals. 1955-1999: Overview, Contents, and Authors. 1999:122.

[21] Lee ES, Vetter P, Miyashita T, et al. Orientation of polymer molecules in rubbed alignment layer and surface anchoring of liquid crystals. Japanese journal of applied physics. 1993;32(9B):L1339.

[22] Sato Y, Sato K, Uchida T. Relationship between rubbing strength and surface anchoring of nematic liquid crystal. Japanese journal of applied physics. 1992;31(5A):L579.

[23] Chatelain P. Sur l'orientation des cristaux liquides par les surfaces frottées. Bulletin de Minéralogie. 1943;66(1):105-130.

[24] Zocher H. Über die optische Anisotropie selektiv absorbierender Stoffe und über mechanische Erzeugung von Anisotropie. Naturwissenschaften. 1925;13(49-50):1015-1021.

[25] Shih M, Shishido A, Khoo I. All-optical image processing by means of a photosensitive nonlinear liquid-crystal film: edge enhancement and image addition–subtraction. Optics letters. 2001;26(15):1140-1142.

[26] Dyadyusha A, Kozenkov V, Marusiy T, et al. Light-induced planar alignment of nematic liquid-crystal by the anisotropic surface without mechanical texture. Ukrainskii Fizicheskii Zhurnal. 1991;36(7):1059-1062.

[27] Gibbons WM, Shannon PJ, Sun S-T, et al. Surface-mediated alignment of nematic liquid crystals with polarized laser light. Nature. 1991;351(6321):49-50.

[28] Dyaduysha A, Khizhnyak A, Marusii T, et al. Peculiarity of an oblique liquid crystal alignment induced by a photosensitive orientant. Japanese journal of applied physics. 1995;34(8A):L1000.

[29] Marusii TY, Reznikov YA. Photosensitive orientants for liquid crystal alignment. Mol Mat. 1993;3:161-168.

[30] Voloshchenko D, Khyzhnyak A, Reznikov Y, et al. Control of an easy-axis on nematic-polymer interface by light action to nematic bulk. Japanese journal of applied physics. 1995;34(2R):566.

[31] Ichimura K, Oh S-K, Nakagawa M. Light-driven motion of liquids on a photoresponsive surface. Science. 2000;288(5471):1624-1626.

[32] Ichimura K, Suzuki Y, Seki T, et al. Reversible change in alignment mode of nematic liquid crystals regulated photochemically by command surfaces modified with an azobenzene monolayer. Langmuir. 1988;4(5):1214-1216.

[33] Schadt M, Schmitt K, Kozinkov V, et al. Surface-induced parallel alignment of liquid crystals by linearly polymerized photopolymers. Japanese Journal of Applied Physics. 1992;31(7R):2155.

[34] West J, Wang X, Ji Y, et al., editors. Polarized UV-exposed polyimide films for liquid crystal alignment. SID INTERNATIONAL SYMPOSIUM DIGEST OF TECHNICAL PAPERS; 1995: SOCIETY FOR INFORMATION DISPLAY.

[35] De Sio L, Roberts DE, Liao Z, et al. Digital polarization holography advancing geometrical phase optics. Optics express. 2016;24(16):18297-18306.

[36] Glushchenko A, Kresse H, Reshetnyak V, et al. Memory effect in filled nematic liquid crystals. Liquid crystals. 1997;23(2):241-246.

[37] Nersisyan SR, Tabiryan NV, Mawet D, et al. Improving vector vortex waveplates for high-contrast coronagraphy. Optics express. 2013;21(7):8205-8213.

[38] Priimagi A, Shevchenko A. Azopolymer-based micro-and nanopatterning for photonic applications. Journal of polymer science Part B: Polymer physics. 2014;52(3):163-182.

[39] Priimagi A, Vapaavuori J, Rodriguez FJ, et al. Hydrogen-Bonded Polymer− Azobenzene Complexes: Enhanced Photoinduced Birefringence with High Temporal Stability through Interplay of Intermolecular Interactions. Chemistry of Materials. 2008;20(20):6358-6363.

[40] Bryan-Brown GP, Brown CV, Jones JC. Bistable nematic liquid crystal device. Google Patents; 2001.

[41] Ageev LA, Miloslavsky VK. Photoinduced effects in light-sensitive films. Optical Engineering. 1995;34(4):960-972.

[42] Nersisyan SR, Tabiryan NV, Steeves DM, et al. Study of azo dye surface command photoalignment material for photonics applications. Applied optics. 2010;49(10):1720-1727.

[43] Griffiths J. II. Photochemistry of azobenzene and its derivatives. Chemical Society Reviews. 1972;1(4):481-493.

[44] Nicoletta FP, Cupelli D, Formoso P, et al. Light responsive polymer membranes: A review. Membranes. 2012;2(1):134-197.

[45] Kumar GS, Neckers D. Photochemistry of azobenzene-containing polymers. Chemical Reviews. 1989;89(8):1915-1925.

[46] Blanche P-A, Lemaire PC, Dumont M, et al. Photoinduced orientation of azo dye in various polymer matrices. Optics letters. 1999;24(19):1349-1351.

[47] Dumont ML, Hosotte S, Froc G, et al., editors. Orientational manipulation of chromophores through photoisomerization. Photopolymers and Applications in Holography, Optical Data Storage, Optical Sensors, and Interconnects; 1994: International Society for Optics and Photonics.

[48] Akiyama H, Kawara T, Takada H, et al. Synthesis and properties of azo dye aligning layers for liquid crystal cells. Liquid Crystals. 2002;29(10):1321-1327.

[49] Mavrona E, Mailis S, Podoliak N, et al. Intrinsic and photo-induced properties of high refractive index azobenzene based thin films. Optical Materials Express. 2018;8(2):420-430.

[50] De Sio L, Klein G, Serak S, et al. All-optical control of localized plasmonic resonance realized by photoalignment of liquid crystals. Journal of Materials Chemistry C. 2013;1(45):7483-7487.

[51] Nersisyan S, Tabiryan N, Steeves DM, et al. Axial polarizers based on dichroic liquid crystals. Journal of Applied Physics. 2010;108(3):033101.

[52] Perivolari E, Gill J, Podoliak N, et al. Optically controlled bistable waveplates. Journal of Molecular Liquids. 2018;267:484-489.

[53] Frey L, Kaczmarek M, Jonathan J, et al. Analysis of gratings induced in azo-dye doped liquid crystals. Optical Materials. 2001;18(1):91-94.

[54] Raynes E, Brown C, Strömer J. Method for the measurement of the K 22 nematic elastic constant. Applied physics letters. 2003;82(1):13-15.

[55] Zhou Y, Sato S. A method for determining elastic constants of nematic liquid crystals at high electric fields. Japanese journal of applied physics. 1997;36(7R):4397.

[56] Li J, Wen C-H, Gauza S, et al. Refractive indices of liquid crystals for display applications. Journal of Display Technology. 2005;1(1):51.

[57] Raynes E, Tough R, Davies K. Voltage dependence of the capacitance of a twisted nematic liquid crystal layer. Molecular Crystals and Liquid Crystals. 1979;56(2):63-68.

[58] Chodorow U, Parka J, Garbat K, et al. Spectral investigation of nematic liquid crystals with high optical anisotropy at THz frequency range. Phase Transitions. 2012;85(4):337-344.

[59] Qingdao QY Liquid Crystal Co. L. Available from: http://www.liquidcrystals.cn/

[60] Bennett T, Proctor M, Forster J, et al. Wide area mapping of liquid crystal devices with passive and active command layers. Applied optics. 2017;56(32):9050-9056.

[61] Stewart IW. The static and dynamic continuum theory of liquid crystals: a mathematical introduction. Crc Press; 2019.

[62] Bennett T, Proctor M, Forster J, et al. Wide area mapping of liquid crystal devices with passive and active command layers. Appl Opt. 2017;56(32):9050-9056.

[63] Bennett T, Proctor M, Kaczmarek M, et al. Lifting degeneracy in nematic liquid crystal viscosities with a single optical measurement. J Colloid Interface Sci. 2017;497:201-206.

[64] Rapini A, Papoular M. Distorsion d'une lamelle nématique sous champ magnétique conditions d'ancrage aux parois. J Phys Colloq. 1969;30(C4):C4-54-C4-56.

[65] Trefethen LN. Spectral methods in MATLAB, volume 10 of Software, Environments, and Tools. Soc Ind Appl Math (SIAM). 2000;24.

[66] Beeckman J, Neyts K, Vanbrabant PJ. Liquid-crystal photonic applications. Optical Engineering. 2011;50(8):081202.

[67] Cui C, Bao R, Yu S, et al. Polarizer-free imaging using reference image for liquid crystal lens. Optics Communications. 2015;342:214-217.

[68] Donisi D, Asquini R, d'Alessandro A, et al. Distributed feedback grating in liquid crystal waveguide: a novel approach. Optics express. 2009;17(7):5251-5256.

[69] Peccianti M, Dyadyusha A, Kaczmarek M, et al. Tunable refraction and reflection of self-confined light beams. Nature Physics. 2006;2(11):737-742.

[70] Residori S. Patterns, fronts and structures in a liquid-crystal-light-valve with optical feedback. Physics Reports. 2005;416(5-6):201-272.

[71] Schadt M. Liquid crystal materials and liquid crystal displays. Annual review of materials science. 1997;27(1):305-379.

[72] Srivastava AK, Wang X, Gong S, et al. Micro-patterned photo-aligned ferroelectric liquid crystal Fresnel zone lens. Optics letters. 2015;40(8):1643-1646.

[73] Tocnaye JDBDL. Engineering liquid crystals for optimal uses in optical communication systems. Liquid crystals. 2004;31(2):241-269.

[74] Gardner DF, Evans JS, Smalyukh II. Towards reconfigurable optical metamaterials: colloidal nanoparticle self-assembly and self-alignment in liquid crystals. Molecular Crystals and Liquid Crystals. 2011;545(1):3/[1227]-21/[1245].

[75] Hegmann T, Qi H, Marx VM. Nanoparticles in liquid crystals: synthesis, self-assembly, defect formation and potential applications. Journal of Inorganic and Organometallic Polymers and Materials. 2007;17(3):483-508.

[76] Mertelj A, Lisjak D, Drofenik M, et al. Ferromagnetism in suspensions of magnetic platelets in liquid crystal. Nature. 2013;504(7479):237-241.

[77] Podoliak N, Buchnev O, Herrington M, et al. Elastic constants, viscosity and response time in nematic liquid crystals doped with ferroelectric nanoparticles. Rsc Advances. 2014;4(86):46068-46074.

[78] Evans D, Cook G, Saleh M. Recent advances in photorefractive two-beam coupling. Optical Materials. 2009;31(7):1059-1060.

[79] Herrington M, Daly K, Buchnev O, et al. AC-field–enhanced beam coupling in photorefractive, hybrid liquid crystals. EPL (Europhysics Letters). 2011;95(1):14003.

[80] Proctor M, Bateman J, Daly K, et al. Light-activated modulation and coupling in integrated polymer–liquid crystal systems. JOSA B. 2014;31(12):3144-3152.

[81] Nakano F, Isogai M, Sato M. Simple method of determining liquid crystal tilt-bias angle. Japanese Journal of Applied Physics. 1980;19(10):2013.

[82] Mur U, Čopar S, Posnjak G, et al. Ray optics simulations of polarised microscopy textures in chiral nematic droplets. Liquid Crystals. 2017;44(4):679-687.

[83] Posnjak G, Čopar S, Muševič I. Points, skyrmions and torons in chiral nematic droplets. Scientific reports. 2016;6(1):1-10.

[84] Strömer J, Raynes E, Brown C. Study of elastic constant ratios in nematic liquid crystals. Applied physics letters. 2006;88(5):051915.

[85] Born M, Wolf E. Principles of Optics Pergamon Press. Chap. 1980;3(1):118.

[86] Wang H, Wu TX, Gauza S, et al. A method to estimate the Leslie coefficients of liquid crystals based on MBBA data. Liquid crystals. 2006;33(1):91-98.

[87] Trabi C, Brown C, Smith A, et al. Interferometric method for determining the sum of the flexoelectric coefficients (e 1+ e 3) in an ionic nematic material. Applied Physics Letters. 2008;92(22):223509.

[88] Chen H, Zhu R, Zhu J, et al. A simple method to measure the twist elastic constant of a nematic liquid crystal. Liquid Crystals. 2015;42(12):1738-1742.

[89] Soci C, Hwang IW, Moses D, et al. Photoconductivity of a low-bandgap conjugated polymer. Advanced Functional Materials. 2007;17(4):632-636.

[90] Huang BY, Huang SY, Chuang CH, et al. Electrically-Tunable Blue Phase Liquid Crystal Microlens Array Based on a Photoconductive Film. Polymers. 2020;12(1):65.

[91] Kaczmarek M, Dyadyusha A, Slussarenko S, et al. The role of surface charge field in two-beam coupling in liquid crystal cells with photoconducting polymer layers. J Appl Phys. 2004;96(5):2616-2623.

[92] Kim HW, Choi KS, Mun J, et al. Photo-aligned and photo-conductive polymer layers for photorefractive liquid crystal cells of high transmittance. Opt Mater. 2003;21(1-3):657-662.

[93] Ono H, Kawatsuki N. Orientational holographic grating observed in liquid crystals sandwiched with photoconductive polymer films. Appl Phys Lett. 1997;71(9):1162-1164.

[94] De Sio L, Klein G, Serak S, et al. All-optical control of localized plasmonic resonance realized by photoalignment of liquid crystals. J Mater Chem C. 2013;1(45):7483-7487.

[95] Nersisyan S, Tabiryan N, Steeves DM, et al. Axial polarizers based on dichroic liquid crystals. J Appl Phys. 2010;108(3):033101.

[96] Tsutsumi N. Recent advances in photorefractive and photoactive polymers for holographic applications. Polym Int. 2017;66(2):167-174.

[97] Yaroshchuk O, Reznikov Y. Photoalignment of liquid crystals: basics and current trends. J Mater Chem. 2012;22(2):286-300.

[98] Bushby RJ, Lozman OR. Photoconducting liquid crystals. Curr Opin Solid State Mater Sci. 2002;6(6):569-578.

[99] Kumar M, Kumar S. Liquid crystals in photovoltaics: a new generation of organic photovoltaics. Polym J. 2017;49(1):85-111.

[100] O'Neill M, Kelly SM. Liquid crystals for charge transport, luminescence, and photonics. Adv Mater. 2003;15(14):1135-1146.

[101] Verbunt PP, Kaiser A, Hermans K, et al. Controlling light emission in luminescent solar concentrators through use of dye molecules aligned in a planar manner by liquid crystals. Adv Funct Mater. 2009;19(17):2714-2719.

[102] Ouskova E, Reznikov Y, Shiyanovskii S, et al. Photo-orientation of liquid crystals due to light-induced desorption and adsorption of dye molecules on an aligning surface. Phys Rev E. 2001;64(5):051709.

[103] Weng L, Liao PC, Lin CC, et al. Anchoring energy enhancement and pretilt angle control of liquid crystal alignment on polymerized surfaces. AIP Adv. 2015;5(9):097218.

[104] Chigrinov V, Kwok HS, Takada H, et al. Photo-aligning by azo-dyes: physics and applications. Liq Cryst Today. 2005;14(4):1-15.

[105] Lee SH, Park WS, Lee GD, et al. Low-cell-gap measurement by rotation of a wave retarder. Jpn J Appl Phys. 2002;41(1R):379.

[106] Lien A, Takano H. Cell gap measurement of filled twisted nematic liquid crystal displays by a phase compensation method. J Appl Phys. 1991;69(3):1304-1309.

[107] Tang ST, Kwok HS. Transmissive liquid crystal cell parameters measurement by spectroscopic ellipsometry. J Appl Phys. 2001;89(1):80-85.

[108] Nakano F, Isogai M, Sato M. Simple method of determining liquid crystal tilt-bias angle. Jpn J Appl Phys. 1980;19(10):2013.

[109] Vilfan M, Mertelj A, Čopič M. Dynamic light scattering measurements of azimuthal and zenithal anchoring of nematic liquid crystals. Phys Rev E. 2002;65(4):041712.

[110] Barbero G, Madhusudana N, Durand G. Weak anchoring energy and pretilt of a nematic liquid crystal. J Phys Lett. 1984;45(12):613-619.

[111] Nastishin YA, Polak R, Shiyanovskii SV, et al. Determination of nematic polar anchoring from retardation versus voltage measurements. Appl Phys Lett. 1999;75(2):202-204.

[112] Murauski A, Chigrinov V, Muravsky A, et al. Determination of liquid-crystal polar anchoring energy by electrical measurements. Phys Rev E. 2005;71(6):061707.

[113] Murauski A, Chigrinov V, Kwok HS. New method for measuring polar anchoring energy of nematic liquid crystals. Liq Cryst. 2009;36(8):779-786.

[114] Pezzi L, Veltri A, De Luca A, et al. Model for molecular director configuration in a liquid crystal cell with multiple interfaces. J Nonlinear Opt Phys Mater. 2007;16(02):199-206.

[115] Perivolari E, Gill J, Podoliak N, et al. Optically controlled bistable waveplates. J Mol Liq. 2018;267:484-489.

[116] Dozov I, Stoenescu DN, Lamarque-Forget S, et al. Development of low anchoring strength liquid crystal mixtures for bistable nematic displays. J Inf Disp. 2005;6(3):1-5.

[117] Shiyanovskii S, Lavrentovich O, Schneider T, et al. Lyotropic chromonic liquid crystals for biological sensing applications. Mol Cryst Liq Cryst. 2005;434(1):259/[587]-270/[598].

[118] Sohn HR, Liu CD, Wang Y, et al. Light-controlled skyrmions and torons as reconfigurable particles. Opt Express. 2019;27(20):29055-29068.

[119] Chou TR, Chen SH, Chiang YT, et al. Highly conductive PEDOT: PSS films by post-treatment with dimethyl sulfoxide for ITO-free liquid crystal display. J Mater Chem C. 2015;3(15):3760-3766.

[120] Liu Y, Zhang Y, Oh BY, et al. Super-fast switching of liquid crystals sandwiched between highly conductive graphene oxide/dimethyl sulfate doped PEDOT: PSS composite layers. J Appl Phys. 2016;119(19):194505.

[121] Jeong S, Kwon Y, Choi BD, et al. Effects of nematic liquid crystal additives on the performance of polymer solar cells. Macromol Chem Phys. 2010;211(23):2474-2479.

[122] Wang X, Hu S, Li Q, et al. Inducting effects of ionic liquid crystal modified-PEDOT: PSS on the performance of bulk heterojunction polymer solar cells. RSC Adv. 2015;5(65):52874-52881.

[123] Barla G, editor Some Constitutive Equations for Rock Materials. The 11th US Symp Rock Mech USRMS; 1969: American Rock Mechanics Association.

[124] Ericksen J. Anisotropic fluids. Arch Ration Mech Anal. 1959;4(1):231-237.

[125] Regrettier T, Kaczmarek M, D'Alessandro G, et al., editors. Integrated organic donor-acceptor bulk heterojunctions for self-activated liquid crystal light modulators. Liq Cryst XXII; 2018: International Society for Optics and Photonics.

[126] Raynes E, Brown C, Strömer J. Method for the measurement of the K 22 nematic elastic constant. Appl Phys Lett. 2003;82(1):13-15.

[127] Chen H, Zhu R, Zhu J, et al. A simple method to measure the twist elastic constant of a nematic liquid crystal. Liq Cryst. 2015;42(12):1738-1742.

[128] Wang H, Wu TX, Gauza S, et al. A method to estimate the Leslie coefficients of liquid crystals based on MBBA data. Liq Cryst. 2006;33(1):91-98.

[129] Yang F, Sambles J, Dong Y, et al. Fully leaky guided wave determination of the polar anchoring energy of a homogeneously aligned nematic liquid crystal. J Appl Phys. 2000;87(6):2726-2735.

[130] Brimicombe P, Kischka C, Elston S, et al. Measurement of the twist elastic constant of nematic liquid crystals using pi-cell devices. J Appl Phys. 2007;101(4):043108.

[131] Lin Y-H, Ren H, Wu YH, et al. Pinning effect on the phase separation dynamics of thin polymer-dispersed liquid crystals. Opt Express. 2005;13(2):468-474.

[132] Seo DS, Iimura Y, Kobayashi S. Temperature dependence of the polar anchoring strength of weakly rubbed polyimide films for the nematic liquid crystal (5CB). Appl Phys Lett. 1992;61(2):234-236.

[133] Seo DS, Kobayashi S, Kang DY, et al. Effects of rubbing and temperature dependence of polar anchoring strength of homogeneously aligned nematic liquid crystal on polyimide Langmuir-Blodgett orientation films. Jpn J Appl Phys. 1995;34(7R):3607.

[134] Chigrinov VG, Kozenkov VM, Kwok H-S. Photoalignment of liquid crystalline materials: physics and applications. Vol. 17. John Wiley & Sons; 2008.

[135] Nys I, Chen K, Beeckman J, et al. Periodic Planar-Homeotropic Anchoring Realized by Photoalignment for Stabilization of Chiral Superstructures. Adv Opt Mater. 2018;6(6).

[136] Kiselev AD, Chigrinov V, Huang DD. Photoinduced ordering and anchoring properties of azo-dye films. Phys Rev E. 2005;72(6):061703.

[137] Mavrona E, Mailis S, Podoliak N, et al. Intrinsic and photo-induced properties of high refractive index azobenzene based thin films. Opt Mater Express. 2018;8(2):420-430.

[138] Fox MAM. Optical Properties of Solids. 2 ed. Vol. 3. Oxford University Press, Incorporated; 2010. (Ser. OMSiP, editor. (Oxford Master Series in Physics)).

[139] https://www.beamco.com/Photoalignment-materials.

[140] Gill JR, Perivolari E, Kaczmarek M, et al. Efficient scattering model of multilayer systems with anisotropic films. JOSA A. 2021;38(5):595-605.

[141] Moerland RJ, Hoogenboom JP. Subnanometer-accuracy optical distance ruler based on fluorescence quenching by transparent conductors. Optica. 2016;3(2):112-117.

[142] König TA, Ledin PA, Kerszulis J, et al. Electrically tunable plasmonic behavior of nanocube–polymer nanomaterials induced by a redox-active electrochromic polymer. ACS nano. 2014;8(6):6182-6192.

[143] Auston DH, Cheung K, Valdmanis J, et al. Cherenkov radiation from femtosecond optical pulses in electro-optic media. Physical Review Letters. 1984;53(16):1555.

[144] Mauguin C. Sur les cristaux liquides de M. Lehmann. Bulletin de Minéralogie. 1911;34(3):71-117.

[145] Tonouchi M. Nature Photon. 1, 97–105 (2007). CrossRef| CAS| Web of Science® Times Cited. 2007;726.

[146] Zhong H, Karpowicz N, Xu J, et al., editors. Inspection of space shuttle insulation foam defects using a 0.2 THz Gunn diode oscillator. Infrared and Millimeter Waves, Conference Digest of the 2004 Joint 29th International Conference on 2004 and 12th International Conference on Terahertz Electronics, 2004.; 2004: IEEE.

[147] Castro-Camus E, Johnston MB. Conformational changes of photoactive yellow protein monitored by terahertz spectroscopy. Chemical Physics Letters. 2008;455(4-6):289-292.

[148] Markelz AG, Knab JR, Chen JY, et al. Protein dynamical transition in terahertz dielectric response. Chemical Physics Letters. 2007;442(4-6):413-417.

[149] Vasić B, Zografopoulos DC, Isić G, et al. Electrically tunable terahertz polarization converter based on overcoupled metal-isolator-metal metamaterials infiltrated with liquid crystals. Nanotechnology. 2017;28(12):124002.

[150] Zografopoulos DC, Beccherelli R. Tunable terahertz fishnet metamaterials based on thin nematic liquid crystal layers for fast switching. Scientific reports. 2015;5(1):1-11.

[151] Isić G, Vasić B, Zografopoulos DC, et al. Electrically tunable critically coupled terahertz metamaterial absorber based on nematic liquid crystals. Physical Review Applied. 2015;3(6):064007.

[152] Yan F, Yu C, Park H, et al. Advances in polarizer technology for terahertz frequency applications. Journal of infrared, millimeter, and terahertz waves. 2013;34(9):489-499.

[153] Siles GA, Riera JM, Garcia-del-Pino P. Atmospheric attenuation in wireless communication systems at millimeter and THz frequencies [Wireless Corner]. IEEE Antennas and Propagation Magazine. 2015;57(1):48-61.

[154] Rahm M, Li J-S, Padilla WJ. THz wave modulators: a brief review on different modulation techniques. Journal of Infrared, Millimeter, and Terahertz Waves. 2013;34(1):1-27.

[155] Weis P, Garcia-Pomar JL, Hoh M, et al. Spectrally wide-band terahertz wave modulator based on optically tuned graphene. ACS nano. 2012;6(10):9118-9124.

[156] Lin X-w, Wu J-b, Hu W, et al. Self-polarizing terahertz liquid crystal phase shifter. Aip Advances. 2011;1(3):032133.

[157] Wu H-Y, Hsieh C-F, Tang T-T, et al. Electrically tunable room-temperature 2/spl pi/liquid crystal terahertz phase shifter. IEEE Photonics Technology Letters. 2006;18(14):1488-1490.

[158] Park H, Parrott EP, Fan F, et al. Evaluating liquid crystal properties for use in terahertz devices. Optics express. 2012;20(11):11899-11905.

[159] Mavrona E, Chodorow U, Barnes M, et al. Refractive indices and birefringence of hybrid liquid crystal-nanoparticles composite materials in the terahertz region. AIP Advances. 2015;5(7):077143.

[160] Sengupta K, Nagatsuma T, Mittleman DM. Terahertz integrated electronic and hybrid electronic–photonic systems. Nature Electronics. 2018;1(12):622-635.

[161] Chikhi N, Lisitskiy M, Papari G, et al. A hybrid tunable THz metadevice using a high birefringence liquid crystal. Scientific reports. 2016;6(1):1-10.

[162] Wang R, Li L, Guo T, et al. Graphene/liquid crystal hybrid tuning terahertz perfect absorber. Applied optics. 2019;58(34):9406-9410.

[163] Kleine-Ostmann T, Dawson P, Pierz K, et al. Room-temperature operation of an electrically driven terahertz modulator. Applied physics letters. 2004;84(18):3555-3557.

[164] Kersting R, Strasser G, Unterrainer K. Terahertz phase modulator. Electronics Letters. 2000;36(13):1156-1158.

[165] Buchnev O, Wallauer J, Walther M, et al. Controlling intensity and phase of terahertz radiation with an optically thin liquid crystal-loaded metamaterial. Applied Physics Letters. 2013;103(14):141904.

[166] Buchnev O, Podoliak N, Kaczmarek M, et al. Electrically controlled nanostructured metasurface loaded with liquid crystal: toward multifunctional photonic switch. Advanced Optical Materials. 2015;3(5):674-679.

[167] Schwierz F, editor The frequency limits of field-effect transistors: MOSFET vs. HEMT. 2008 9th International Conference on Solid-State and Integrated-Circuit Technology; 2008: IEEE.

[168] Davies A, Linfield EH, Johnston MB. The development of terahertz sources and their applications. Physics in Medicine & Biology. 2002;47(21):3679.

[169] Wiltse JC. History of millimeter and submillimeter waves. IEEE Transactions on microwave theory and techniques. 1984;32(9):1118-1127.

[170] Siegel PH, editor THz for space: The golden age. 2010 IEEE MTT-S International Microwave Symposium; 2010: IEEE.

[171] Melinger JS, Yang Y, Mandehgar M, et al. THz detection of small molecule vapors in the atmospheric transmission windows. Optics express. 2012;20(6):6788-6807.

[172] Slocum DM, Slingerland EJ, Giles RH, et al. Atmospheric absorption of terahertz radiation and water vapor continuum effects. Journal of Quantitative Spectroscopy and Radiative Transfer. 2013;127:49-63.

[173] Cocker TL, Jelic V, Gupta M, et al. An ultrafast terahertz scanning tunnelling microscope. Nature Photonics. 2013;7(8):620-625.

[174] Yoshida S, Arashida Y, Hirori H, et al. Terahertz scanning tunneling microscopy for visualizing ultrafast electron motion in nanoscale potential variations. ACS Photonics. 2021;8(1):315-323.

[175] Siegel PH. Terahertz technology. IEEE Transactions on microwave theory and techniques. 2002;50(3):910-928.

[176] Borie E. Effect of resonator parameters on frequency and quality factor of gyrotron resonators. International Journal of Infrared and Millimeter Waves. 2008;29(2):113-130.

[177] Whitford BG, Siemsen KJ, Riccius HD, et al. New frequency measurements and techniques in the 30-THz region. IEEE Transactions on Instrumentation and Measurement. 1974;23(4):535-539.

[178] Han P, Tani M, Usami M, et al. A direct comparison between terahertz time-domain spectroscopy and far-infrared Fourier transform spectroscopy. Journal of Applied Physics. 2001;89(4):2357-2359.

[179] Auston DH. Picosecond optoelectronic switching and gating in silicon. Applied Physics Letters. 1975;26(3):101-103.

[180] Lee CH. Picosecond optoelectronic switching in GaAs. Applied Physics Letters. 1977;30(2):84-86.

[181] Yang K, Richards P, Shen Y. Generation of far-infrared radiation by picosecond light pulses in LiNbO3. Applied Physics Letters. 1971;19(9):320-323.

[182] Yajima T, Takeuchi N. Spectral Properties and Tunability of Far-Infrared Difference-Frequency Radiation Produced by Picosecond Laser Pulses. Japanese Journal of Applied Physics. 1971;10(7):907.

[183] Auston DH, Cheung KP, Smith PR. Picosecond photoconducting Hertzian dipoles. Applied physics letters. 1984;45(3):284-286.

[184] Spence DE, Kean PN, Sibbett W. 60-fsec pulse generation from a self-mode-locked Ti: sapphire laser. Optics letters. 1991;16(1):42-44.

[185] DeFonzo AP, Jarwala M, Lutz C. Transient response of planar integrated optoelectronic antennas. Applied physics letters. 1987;50(17):1155-1157.

[186] Van Exter M, Fattinger C, Grischkowsky D. High-brightness terahertz beams characterized with an ultrafast detector. Applied Physics Letters. 1989;55(4):337-339.

[187] Tani M, Matsuura S, Sakai K, et al. Emission characteristics of photoconductive antennas based on low-temperature-grown GaAs and semi-insulating GaAs. Applied optics. 1997;36(30):7853-7859.

[188] Wu Q, Zhang XC. Free-space electro-optic sampling of terahertz beams. Applied Physics Letters. 1995;67(24):3523-3525.

[189] Cole BE, Woodward RM, Crawley DA, et al., editors. Terahertz imaging and spectroscopy of human skin in vivo. Commercial and Biomedical Applications of Ultrashort Pulse Lasers; Laser Plasma Generation and Diagnostics; 2001: International Society for Optics and Photonics.

[190] Woodward RM, Cole BE, Wallace VP, et al. Terahertz pulse imaging in reflection geometry of human skin cancer and skin tissue. Physics in Medicine & Biology. 2002;47(21):3853.

[191] Crawley DA, Longbottom C, Wallace VP, et al. Three-dimensional terahertz pulse imaging of dental tissue. Journal of biomedical optics. 2003;8(2):303-307.

[192] Welch A. Full-Body Scanners: Full Protection from Terrorist Attacks or Full-On Violation of the Constitution. Transp LJ. 2010;37:167.

[193] Pinna D, Galeotti M, Mazzeo R. Scientific examination for the investigation of paintings: a handbook for conservator-restorers. 2009.

[194] Fukunaga K, Hosako I, Picollo M, et al., editors. Application of THz sensing to analysis of works of art for conservation. 2010 IEEE International Topical Meeting on Microwave Photonics; 2010: IEEE.

[195] Jackson JB, Mourou MR, Whitaker JF, et al., editors. Terahertz time-domain reflectometry applied to the investigation of hidden mural paintings. Conference on Lasers and Electro-Optics; 2008: Optical Society of America.

[196] Nagai N, Imai T, Fukasawa R, et al. Analysis of the intermolecular interaction of nanocomposites by THz spectroscopy. Applied physics letters. 2004;85(18):4010-4012.

[197] Buron JD, Mackenzie DM, Petersen DH, et al. Terahertz wafer-scale mobility mapping of graphene on insulating substrates without a gate. Optics express. 2015;23(24):30721-30729.

[198] Yasui T, Yasuda T, Sawanaka K-i, et al. Terahertz paintmeter for noncontact monitoring of thickness and drying progress in paint film. Applied Optics. 2005;44(32):6849-6856.

[199] Dreyhaupt A, Winnerl S, Dekorsy T, et al. High-intensity terahertz radiation from a microstructured large-area photoconductor. Applied Physics Letters. 2005;86(12):121114.

[200] Katzenellenbogen N, Grischkowsky D. Efficient generation of 380 fs pulses of THz radiation by ultrafast laser pulse excitation of a biased metal-semiconductor interface. Applied Physics Letters. 1991;58(3):222-224.

[201] Smith PR, Auston DH, Nuss MC. Subpicosecond photoconducting dipole antennas. IEEE Journal of Quantum Electronics. 1988;24(2):255-260.

[202] Grischkowsky D, Keiding S, Van Exter M, et al. Far-infrared time-domain spectroscopy with terahertz beams of dielectrics and semiconductors. JOSA B. 1990;7(10):2006-2015.

[203] Vieweg N, Fischer B, Reuter M, et al. Ultrabroadband terahertz spectroscopy of a liquid crystal. Optics express. 2012;20(27):28249-28256.

[204] Fischer BM, Helm H, Jepsen PU. Chemical recognition with broadband THz spectroscopy. Proceedings of the IEEE. 2007;95(8):1592-1604.

[205] Jepsen PU, Cooke DG, Koch M. Terahertz spectroscopy and imaging–Modern techniques and applications. Laser & Photonics Reviews. 2011;5(1):124-166.

[206] Fattinger C, Grischkowsky D. Point source terahertz optics. Applied Physics Letters. 1988;53(16):1480-1482.

[207] Naftaly M, Foulds A, Miles R, et al. Terahertz transmission spectroscopy of nonpolar materials and relationship with composition and properties. International Journal of Infrared and Millimeter Waves. 2005;26(1):55-64.

[208] Barnes ME, Berry SA, Gow P, et al. Investigation of the role of the lateral photo-Dember effect in the generation of terahertz radiation using a metallic mask on a semiconductor. Optics express. 2013;21(14):16263-16272.

[209] González-Cardel M, Arguijo P, Díaz-Uribe R. Gaussian beam radius measurement with a knife-edge: a polynomial approximation to the inverse error function. Applied optics. 2013;52(16):3849-3855.

[210] Wallace VP, Fitzgerald AJ, Pickwell E, et al. Terahertz pulsed spectroscopy of human basal cell carcinoma. Applied spectroscopy. 2006;60(10):1127-1133.

[211] Ashworth PC, Pickwell-MacPherson E, Provenzano E, et al. Terahertz pulsed spectroscopy of freshly excised human breast cancer. Optics express. 2009;17(15):12444-12454.

[212] Liu H-B, Zhong H, Karpowicz N, et al. Terahertz spectroscopy and imaging for defense and security applications. Proceedings of the IEEE. 2007;95(8):1514-1527.

[213] Wilk R, Vieweg N, Kopschinski O, et al. Liquid crystal based electrically switchable Bragg structure for THz waves. Optics express. 2009;17(9):7377-7382.

[214] Lin C-J, Li Y-T, Hsieh C-F, et al. Manipulating terahertz wave by a magnetically tunable liquid crystal phase grating. Optics express. 2008;16(5):2995-3001.

[215] Hsieh C-F, Lai Y-C, Pan R-P, et al. Polarizing terahertz waves with nematic liquid crystals. Optics letters. 2008;33(11):1174-1176.

[216] Jewell SA, Hendry E, Isaac TH, et al. Tuneable Fabry–Perot etalon for terahertz radiation. New Journal of Physics. 2008;10(3):033012.

[217] Chen C-Y, Hsieh C-F, Lin Y-F, et al. Magnetically tunable room-temperature 2π liquid crystal terahertz phase shifter. Optics express. 2004;12(12):2625-2630.

[218] Nie X, Xianyu H, Lu R, et al. Pretilt angle effects on liquid crystal response time. Journal of display technology. 2007;3(3):280-283.

[219] Jakeman E, Raynes E. Electro-optic response times in liquid crystals. Physics Letters A. 1972;39(1):69-70.

[220] Chodorow U, Parka J, Kula P, et al. Terahertz properties of fluorinated liquid crystals. Liquid Crystals. 2013;40(11):1586-1590.

[221] Yang C-S, Lin C-J, Pan R-P, et al. The complex refractive indices of the liquid crystal mixture E7 in the terahertz frequency range. JOSA B. 2010;27(9):1866-1873.

[222] Dąbrowski R, Kula P, Herman J. High birefringence liquid crystals. Crystals. 2013;3(3):443-482.

[223] Nowinowski-Kruszelnicki E, Kędzierski J, Raszewski Z, et al. High birefringence liquid crystal mixtures for electro-optical devices. Optica Applicata. 2012;42(1):167-180.

[224] Tkachenko V, Dyomin A, Tkachenko G, et al. Electrical reorientation of liquid crystal molecules inside cylindrical pores for photonic device applications. Journal of Optics A: Pure and Applied Optics. 2008;10(5):055301.

[225] Pan R-P, Hsieh C-F, Pan C-L, et al. Temperature-dependent optical constants and birefringence of nematic liquid crystal 5CB in the terahertz frequency range. Journal of Applied Physics. 2008;103(9):093523.

[226] Chen C-Y, Tsai T-R, Pan C-L, et al. Room temperature terahertz phase shifter based on magnetically controlled birefringence in liquid crystals. Applied physics letters. 2003;83(22):4497-4499.

[227] Fedotov V. Metamaterials. In: Kasap S, Capper P, editors. Springer Handbook of Electronic and Photonic Materials. Cham: Springer International Publishing; 2017. p. 1-1.

[228] Philip E, Güngördü MZ, Pal S, et al. Review on polarization selective terahertz metamaterials: from chiral metamaterials to stereometamaterials. J Infrared Millim Terahertz Waves. 2017;38(9):1047-1066.

[229] Xu W, Xie L, Ying Y. Mechanisms and applications of terahertz metamaterial sensing: a review. Nanoscale. 2017;9(37):13864-13878.

[230] He J, Dong T, Chi B, et al. Metasurfaces for terahertz wavefront modulation: a review. J Infrared Millim Terahertz Waves. 2020:1-25.

[231] Zheludev NI. The road ahead for metamaterials. Science. 2010;328(5978):582-583.

[232] Pendry JB, Holden AJ, Robbins DJ, et al. Magnetism from conductors and enhanced nonlinear phenomena. IEEE Trans Microw Theory Tech. 1999;47(11):2075-2084.

[233] Linden S, Enkrich C, Wegener M, et al. Magnetic response of metamaterials at 100 terahertz. Science. 2004;306(5700):1351-1353.

[234] Shelby RA, Smith DR, Schultz S. Experimental verification of a negative index of refraction. Science. 2001;292(5514):77-79.

[235] Schurig D, Mock JJ, Justice B, et al. Metamaterial electromagnetic cloak at microwave frequencies. Science. 2006;314(5801):977-980.

[236] Fedotov V, Mladyonov P, Prosvirnin S, et al. Asymmetric propagation of electromagnetic waves through a planar chiral structure. Phys Rev Lett. 2006;97(16):167401.

[237] Rogacheva A, Fedotov V, Schwanecke A, et al. Giant gyrotropy due to electromagnetic-field coupling in a bilayered chiral structure. Phys Rev Lett. 2006;97(17):177401.

[238] Fedotov V, Rose M, Prosvirnin S, et al. Sharp trapped-mode resonances in planar metamaterials with a broken structural symmetry. Phys Rev Lett. 2007;99(14):147401.

[239] Papasimakis N, Fedotov VA, Zheludev N, et al. Metamaterial analog of electromagnetically induced transparency. Phys Rev Lett. 2008;101(25):253903.

[240] Buchnev O, Podoliak N, Kaltenecker K, et al. Metasurface-based optical liquid crystal cell as an ultrathin spatial phase modulator for THz applications. ACS Photonics. 2020;7(11):3199-3206.

[241] Zhao Q, Kang L, Du B, et al. Electrically tunable negative permeability metamaterials based on nematic liquid crystals. Appl Phys Lett. 2007;90(1):011112.

[242] Wang X, Kwon D-H, Werner DH, et al. Tunable optical negative-index metamaterials employing anisotropic liquid crystals. Appl Phys Lett. 2007;91(14):143122.

[243] Yang J, Wang P, Shi T, et al. Electrically tunable liquid crystal terahertz device based on double-layer plasmonic metamaterial. Optics express. 2019;27(19):27039-27045.

[244] Wang R, Li L, Liu J, et al. Triple-band tunable perfect terahertz metamaterial absorber with liquid crystal. Optics Express. 2017;25(26):32280-32289.

[245] Yang L, Fan F, Chen M, et al. Active terahertz metamaterials based on liquid-crystal induced transparency and absorption. Optics Communications. 2017;382:42-48.

[246] Li X, Tan N, Pivnenko M, et al. High-birefringence nematic liquid crystal for broadband THz applications. Liquid Crystals. 2016;43(7):955-962.

[247] Wang J, Tian H, Wang Y, et al. Liquid crystal terahertz modulator with plasmon-induced transparency metamaterial. Optics express. 2018;26(5):5769-5776.

[248] Savo S, Shrekenhamer D, Padilla WJ. Liquid crystal metamaterial absorber spatial light modulator for THz applications. Advanced Optical Materials. 2014;2(3):275-279.

[249] Zhao Q, Kang L, Du B, et al. Electrically tunable negative permeability metamaterials based on nematic liquid crystals. Applied physics letters. 2007;90(1):011112.

[250] Zhao J, Zhang C, Braun PV, et al. Large-Area Low-Cost Plasmonic Nanostructures in the NIR for Fano Resonant Sensing. Adv Mater 2012;24(35):OP247-OP252.

[251] Mimura Y, Ohkubo T, Takeuchi T, et al. Deep-UV photolithography. Japanese Journal of Applied Physics. 1978;17(3):541.

[252] Falcone F, Lopetegi T, Laso M, et al. Babinet principle applied to the design of metasurfaces and metamaterials. Physical review letters. 2004;93(19):197401.

[253] Hoogvliet J, Van Bennekom W. Gold thin-film electrodes: an EQCM study of the influence of chromium and titanium adhesion layers on the response. Electrochimica acta. 2001;47(4):599-611.

[254] Coburn JW, Winters HF. Plasma etching—A discussion of mechanisms. Journal of vacuum Science and Technology. 1979;16(2):391-403.

[255] Ordal MA, Bell RJ, Alexander RW, et al. Optical properties of Au, Ni, and Pb at submillimeter wavelengths. Appl Opt. 1987;26(4):744-752.

[256] Naftaly M, Foulds A, Miles R, et al. Terahertz transmission spectroscopy of nonpolar materials and relationship with composition and properties. J Infrared Millim Terahertz Waves. 2005;26(1):55-64.

[257] Luk'yanchuk B, Zheludev NI, Maier SA, et al. The Fano resonance in plasmonic nanostructures and metamaterials. Nat Mater. 2010;9(9):707-715.

[258] Limonov MF, Rybin MV, Poddubny AN, et al. Fano resonances in photonics. Nat Photonics. 2017;11(9):543.

[259] Fano U. Effects of configuration interaction on intensities and phase shifts. Physical Review. 1961;124(6):1866.

[260] Chmielak B, Waldow M, Matheisen C, et al. Pockels effect based fully integrated, strained silicon electro-optic modulator. Optics express. 2011;19(18):17212-17219.

[261] Chodorow U, Parka J, Garbat K, et al. Spectral investigation of nematic liquid crystals with high optical anisotropy at THz frequency range. Phase Transit. 2012;85(4):337-344.

[262] Mavrona E, Chodorow U, Barnes M, et al. Refractive indices and birefringence of hybrid liquid crystal-nanoparticles composite materials in the terahertz region. AIP Adv. 2015;5(7):077143.

[263] Kowerdziej R, Olifierczuk M, Salski B, et al. Tunable negative index metamaterial employing in-plane switching mode at terahertz frequencies. Liq Cryst. 2012;39(7):827-831.

[264] Oh-e M, Kondo K. The in-plane switching of homogeneously aligned nematic liquid crystals. Liq Cryst 1997;22(4):379-390.

[265] Gersten J, Nitzan A. Electromagnetic theory of enhanced Raman scattering by molecules adsorbed on rough surfaces. J Chem Phys. 1980;73(7):3023-3037.

[266] Ermushev A, Mchedlishvili BV, Oleĭnikov VA, et al. Surface enhancement of local optical fields and the lightning-rod effect. Quantum Electron. 1993;23(5):435.

[267] Li C-C, Tseng H-Y, Chen C-W, et al. Versatile energy-saving smart glass based on tristable cholesteric liquid crystals. ACS Applied Energy Materials. 2020;3(8):7601-7609.

[268] Talukder JR, Lin H-Y, Wu S-T. Photo-and electrical-responsive liquid crystal smart dimmer for augmented reality displays. Optics express. 2019;27(13):18169-18179.

[269] Khaligh HH, Liew K, Han Y, et al. Silver nanowire transparent electrodes for liquid crystal-based smart windows. Solar Energy Materials and Solar Cells. 2015;132:337-341.

[270] Oh SW, Kim SH, Baek JM, et al. Optical and thermal switching of liquid crystals for self-shading windows. Advanced Sustainable Systems. 2018;2(5):1700164.

[271] Bosch M, Shcherbakov MR, Won K, et al. Electrically actuated varifocal lens based on liquid-crystal-embedded dielectric metasurfaces. Nano Letters. 2021;21(9):3849-3856.

[272] Gou F, Peng F, Ru Q, et al. Mid-wave infrared beam steering based on high-efficiency liquid crystal diffractive waveplates. Optics express. 2017;25(19):22404-22410.

[273] Kobashi J, Yoshida H, Ozaki M. Planar optics with patterned chiral liquid crystals. Nature Photonics. 2016;10(6):389-392.

[274] Yoshida H, Kobashi J. Flat optics with cholesteric and blue phase liquid crystals. Liquid Crystals. 2016;43(13-15):1909-1919.

[275] Behabtu N, Lomeda JR, Green MJ, et al. Spontaneous high-concentration dispersions and liquid crystals of graphene. Nature nanotechnology. 2010;5(6):406-411.

[276] Gupta RK, Sudhakar AA. Perylene-based liquid crystals as materials for organic electronics applications. Langmuir. 2018;35(7):2455-2479.

[277] Liu Y, Xu Z, Gao W, et al. Graphene and other 2D colloids: liquid crystals and macroscopic fibers. Advanced Materials. 2017;29(14):1606794.

[278] De Sio L, Ouskova E, Lloyd P, et al. Light-addressable liquid crystal polymer dispersed liquid crystal. Optical Materials Express. 2017;7(5):1581-1588.

[279] Lee H-K, Kanazawa A, Shiono T, et al. All-optically controllable polymer/liquid crystal composite films containing the azobenzene liquid crystal. Chemistry of materials. 1998;10(5):1402-1407.

[280] Watts CM, Shrekenhamer D, Montoya J, et al. Terahertz compressive imaging with metamaterial spatial light modulators. Nature Photonics. 2014;8(8):605-609.

[281] Tahhan SR, Aljobouri HK. Sensing of illegal drugs by using photonic crystal fiber in terahertz regime. Journal of Optical Communications. 2020.

[282] Lu J-Y, Chen L-J, Kao T-F, et al. Terahertz microchip for illicit drug detection. IEEE photonics technology letters. 2006;18(21):2254-2256.

[283] Federici JF, Schulkin B, Huang F, et al. THz imaging and sensing for security applications—explosives, weapons and drugs. Semiconductor Science and Technology. 2005;20(7):S266.

[284] Ning B, Chen Z, Chen W, et al., editors. Improving security of THz communication with intelligent reflecting surface. 2019 IEEE Globecom Workshops (GC Wkshps); 2019: IEEE.

[285] Oh-e M, Kondo K. The in-plane switching of homogeneously aligned nematic liquid crystals. Liquid Crystals. 1997;22(4):379-390.

[286] Soref R. Field effects in nematic liquid crystals obtained with interdigital electrodes. Journal of Applied Physics. 1974;45(12):5466-5468.

[287] Oh-e M, Kondo K. Electro-optical characteristics and switching behavior of the in-plane switching mode. Applied physics letters. 1995;67(26):3895-3897.

[288] Koskela JE, Vapaavuori J, Hautala J, et al. Surface-relief gratings and stable birefringence inscribed using light of broad spectral range in supramolecular polymer-bisazobenzene complexes. The Journal of Physical Chemistry C. 2012;116(3):2363-2370.

[289] Priimagi A, Saccone M, Cavallo G, et al. Photoalignment and Surface-Relief-Grating Formation are Efficiently Combined in Low-Molecular-Weight Halogen-Bonded Complexes. Advanced Materials. 2012;24(44):OP345-OP352.

[290] Perivolari E, D'Alessandro G, Apostolopoulos V, et al. Two-dimensional snapshot measurement of surface variation of anchoring in liquid crystal cells. Liquid Crystals. 2021:1-11.

[291] Ying Y, Valdivia C, Sones C, et al. Latent light-assisted poling of LiNbO 3. Optics express. 2009;17(21):18681-18692.